Observation of Energy and Baseline Dependent Reactor Neutrino Disappearance in the RENO Experiment

Wonqook Choi

Under the supervision of
Professor Soo-Bong Kim

A Dissertation submitted to the Graduate
Faculty of Seoul National University
in partial fulfillment of the requirement
for the Degree of Doctor of Philosophy

Department of Physics and Astronomy
Graduate School of Natural Science
Seoul National University
Seoul, KOREA

Febrary 2016

Abstract

The Reactor Experiment for Neutrino Oscillation (RENO) began gathering data in August, 2011. The RENO is designed to measure the neutrino mixing angle θ_{13} and mass squared difference $|\Delta m^2_{ee}|$ which is the $\bar{\nu}_e$ weighted average mass square difference of $|\Delta m^2_{31}|$ and $|\Delta m^2_{32}|$. The experimental site of RENO is the Hanbit nuclear power plant, which is 280 km away from the capital city of Koera, Seoul. There are 6 reactors in the Hanbit nuclear power plant, equally spaced in a single line. The Experiment used two identical detectors. The near detector (far detector) is located at 294 m (1384 m) from the center of this six reactor array. and the flux-weighted average distance between the reactors and the far (near) detector is 408.6 m (1444.0 m). The experimental has analyzed about 500 live days of data in the period between August 2011 and January 2013. In this period, the far (near) detector observed 31541 (290775) electron antineutrino candidate events with a background fraction of 4.9% (2.8%). The measured prompt spectra has an excess of reactor $\bar{\nu}_e$ of approximately 5 MeV relative to the prediction from the most commonly used model. The excess is proportional to reactor thermal output power, therefore the excess is the neutrino signal coming from reactor cores and not a background. To aviod this problem, the data are analysed based on the measured far-to-near ratio of prompt spectra. A clear energy and baseline dependent disappearance of reactor $\bar{\nu}_e$ is observed in the deficit of the observed amount of $\bar{\nu}_e$. From this deficit, we can determine $\sin^2 2\theta_{13} = 0.082 \pm 0.009(stat.) \pm 0.006(syst.)$ and $|\Delta m^2_{ee}| = \left[2.62^{+0.21}_{-0.23}(stat.)^{0.12}_{-0.13}(syst.)\right] \times 10^{-3}\text{eV}^2$ based on a rate and spectra analysis. The precise measurement of θ_{13} would be a important milestone in determination of the leptonic CP phase if combined with a result of an accelerator neutrino beam experiment.

Contents

List of Figures

List of Tables

Chapter 1

Introduction

There have been great advancements in understanding the neutrino physics in the last two decades. The discovery of neutrino oscillation indicate directly a physics beyond the Standard Model, and provides a unique, next milestone for exploration on the Grand Unification energy scale.

1.1 Overview of Neutrino Oscillation

The observation of neutrino oscillation is one of the most important discoveries in particle physics. Neutrino oscillation is a flavor transformation of a neutrino from one type to another. Neutrino mixing, which is the oscillation of flavor states of the neutrino and the nonzero neutrino masses provides insights into the adjustment of the current standard model.

Neutrino oscillation is a consequence of that the neutrino flavor being linear combination of the mass eigenstate. The currently accepted model describing neutrino mixing is a framework of three flavors(ν_e, ν_μ, ν_τ). This phenomenon is expressed by three mixing angles (θ_{12}, θ_{23}, θ_{13}), three mass difference (Δm^2_{21}, Δm^2_{31}, Δm^2_{32}), and one phase angle (δ) [1, 2]. In 1998, the Super-Kamiokande experiment discovered neutrino oscillation and the mixing angle θ_{23} [3]. It is interesting that angle θ_{23} is close to the maximal value. The solar neutrino oscillation was determined by the SNO collaboration in 2001, and the mixing angle θ_{12} was obtained [4, 5].

The last unknown angle, the smallest mixing angle θ_{13}, was found in 2012 in the RENO, Daya Bay and Double-Chooz experiments via the electron antineutrino disappearance from reactor [6, 7, 8]. These reactor neutrino experiments could measure θ_{13} without matter effects and charge parity (CP) violation. The first measurement of θ_{13} by RENO was based on the rate-only analysis to compare expected and observed reactor neutrino rates [6]. In this thesis, we present a more

precise measurement of θ_{13} and the first measurement of $|\Delta m^2_{ee}|$, a mixture of $|\Delta m^2_{31}|$ and $|\Delta m^2_{32}|$, obtained from energy and baseline dependent disappearance of reactor electron antineutrinos.

1.2 Neutrino Oscillation

A neutrino with flavor α and momentum $\overrightarrow{p}$ is combination of different mass eigenstate. Mathematically

$$|\nu_\alpha\rangle = \sum_i U^*_{\alpha i} |\nu_i\rangle \tag{1.1}$$

The massive neutrino states are eigenstate of the hamiltonian. This implies the massive neutrino can evolve in time as plane wave.

$$|\nu_\alpha(t)\rangle = \sum_i U^*_{\alpha i} e^{-iE_i t} |\nu_i\rangle \tag{1.2}$$

inverting equation 1.1, the neutrino flavor states can be expressed in terms of flavor states.

$$|\nu_\alpha(t)\rangle = \sum_{\beta=e,\mu,\tau} U^*_{\alpha i} e^{-iE_i t} U_{\beta i} |\nu_\beta\rangle \tag{1.3}$$

Therefore, The transition probability of ν_α to ν_β $(\alpha, \beta = e, \mu, \tau)$ with Energy E after traveling distance L in vacuum can be calculated as follows:

$$P(\nu_\alpha \to \nu_\beta) = |\langle \nu_\alpha | \nu_\beta \rangle|^2 = \delta_{\alpha\beta} - 2\mathrm{Re} \sum_{j>i} U_{\alpha i} U^*_{\alpha j} U^*_{\beta i} U_{\beta j} \left(1 - \exp\left\{ i\Delta m^2_{ji} L \frac{2}{E} \right\}\right) \tag{1.4}$$

where $\Delta m^2_{ji} \equiv m^2_j - m^2_i$ is the difference between the neutrino masses squared. If the neutrino has 3 flavors and 3 mass eigenstate, matrix U is described by a 3×3 matrix which is called Pontecorvo-Maki-Nakagawa-Sakata matrix [9, 10].

$$\begin{aligned} U &= \begin{pmatrix} 1 & 0 & 0 \\ 0 & c_{23} & s_{23} \\ 1 & -s_{23} & c_{23} \end{pmatrix} \begin{pmatrix} c_{13} & 0 & s_{13}e^{i\delta} \\ 0 & 1 & 0 \\ -s_{13}e^{-i\delta} & 0 & c_{13} \end{pmatrix} \begin{pmatrix} c_{12} & s_{12} & 0 \\ -s_{12} & c_{12} & 0 \\ 0 & 0 & 1 \end{pmatrix} \\ &= \begin{pmatrix} c_{12}c_{13} & s_{12}c_{13} & s_{13}e^{-i\delta} \\ -s_{12}c_{23} - c_{12}s_{23}s_{13}e^{i\delta} & c_{12}c_{23} - s_{12}s_{23}s_{13}e^{i\delta} & s_{23}c_{13} \\ s_{12}s_{23} - c_{12}c_{23}s_{13}e^{i\delta} & -c_{12}s_{23} - s_{12}c_{23}s_{13}e^{i\delta} & c_{23}c_{13} \end{pmatrix} \end{aligned} \tag{1.5}$$

where $c_{ij} = \cos\theta_{ij}$, $s_{ij} = \sin\theta_{ij}$ (θ_{ij} is the mixing angle) , and δ is a Dirac CP violating phase. A further theoretical description of neutrino mixing can be found in Ref. [11].

The current best values of neutrino oscillation parameters with errors of one standard deviation (1σ) are summarized as follows [12]:

$$\begin{aligned}
\sin^2 2\theta_{23} &= 0.999^{+0.001}_{-0.018}\ \text{(normal)}\ \left[^{+0.1}_{-1.8}\%\right] \\
&\text{or}\quad 1.000^{+0.000}_{-0.017}\ \text{(inverted)}\ \left[^{+0.0}_{-1.7}\%\right] \\
\sin^2 2\theta_{12} &= 0.846 \pm 0.021\,[\pm 2.5\%] \\
\sin^2 2\theta_{13} &= 0.093 \pm 0.008\,[\pm 8.6\%] \\
\Delta m^2_{32} &= (2.44 \pm 0.06) \times 10^{-3}\text{eV}^2\ \text{(normal)}\,[\pm 2.5\%] \\
&\text{or}\quad (2.52 \pm 0.07) \times 10^{-3}\text{eV}^2\ \text{(inverted)}\,[\pm 2.8\%] \\
\Delta m^2_{21} &= (7.53 \pm 0.18) \times 10^{-5}\text{eV}^2\,[\pm 2.4\%]
\end{aligned} \tag{1.6}$$

Where, the bracketed values are the fractional errors. Note that disappearance experiments cannot measure the sign of Δm^2_{32} because the dominant term in the Equation 1.6 depends on the square of the sine function. This is called the neutrino mass hierarchy problem.

1.3 Reactor Neutrino Experiment

Nuclear reactors have played crucial roles in experimental neutrino physics. The discovery of the neutrino was made at the Savannah River Reactor in 1956 by Reines and Cowan [13]. KamLAND observed the disappearance of reactor antineutinos and distortion in the energy spectrum because of neutrino oscillations due to mixing angle θ_{12} [14, 15]. Because of low-energy reactor neutrino, the mixing angle can be measured in short baseline experiment without the matter effects and CP phase. A reactor neutrino detector does not need to be large, and construction of a neutrino beam is not needed. In consequence, θ_{13} is measured by RENO, Daya Bay and Double-Chooz experiment via rate-only analysis in 2012 [6, 7, 8].

Past reactor experiments could not observed neutrino disappearance using a single detector located $\sim$ 1 km or less from the reactor, as summarized in Table 1.1. In the early efforts to measure θ_{13} by using reactors, the CHOOZ and Palo Verde experiments had a problem: instability with their Gd-doped liquid scintillator (LS). Palo Verde struggled with the gradual deterioration of Gd-doped LS through precipitation [28, 29]. The Gd-doped LS in the CHOOZ experiment turned yellow a few months after deployment, which reduced the photo-electron collection efficiency [25, 30]. To avoid this problems, researchers have used new recipes to successfully synthesize Gd-doped LS with good optical properties and long-term stability [31, 32, 33]. To measure the rate and energy spectrum of the $\bar{\nu}_e$s, CHOOZ and Palo Verde used a single detector with $\sim$1 km baseline. Such measurements from the single detector are sensitive to systematic issues related

Experiment	Year	Reactor Power (MW_{th})	Baselines (m)	N_{obs}/N_{exp}
ILL [16]	1980-1981	57	8.8	0.96 ± 0.12
Goesgen [17, 18, 19]	1981-1985	2800	37.9	1.02
			45.9	1.05 ± 0.06
			64.7	0.98 ± 0.06
Rovno [20, 21, 22]	1983-1991	1375	18, 25	0.964 ± 0.07
Krasnoyarsk [23]	1987-1994	-	57,231	0.99 ± 0.05
Bugey [24]	1995	2800	15	0.99 ± 0.05
			40	0.99 ± 0.05
			95	0.92 ± 0.14
Chooz [25]	1997	8500	1000	1.01 ± 0.04
Palo Verde [26, 27]	1999	11600	890, 750	1.01 ± 0.10

Table 1.1: Past short-baseline reactor neutrino experiments

to the detector and the reactors. To avoid this problem, current experiments (Daya Bay, Double Chooz, and RENO) are deploying multi identical detectors at different placements in relation to the reactors the reactors, which allow the disappearance of $\bar{\nu}_e$ to be obtained from the ratio of the observed $\bar{\nu}_e$ rates. Because it is a relative measurement, the far-to-near ratio can significantly reduce the systematic uncertainties from the detector and reactor. In 2012, two reactor disappearance experiments Daya Bay [7], Double-Chooz [8], and RENO [6] reported the measurement of the θ_{13} value. The first measurement of θ_{13} by the RENO was based on the rate-only analysis of deficit found (rate only analysis) [6]. In this thesis, A more precisely measured value of θ_{13} will be reported, based on the rate, spectral, and baseline information of reactor neutrino disappearance (rate+shape analysis). Using a shape information of reactor neutrino made it possble the value of θ_{13} with less systematic error than that of the rate only analysis. Because the spectral shape of the backgrounds is different from that of the reactor neutrino, it is easy to distinguish between the backgrounds and the neutrino.

1.3.1 Production of Reactor Neutrino

The electron antineutrinos are produced from β-decay of reactor fuels; ^{235}U, ^{238}U, ^{239}Pu and ^{235}Pu. Figure 1.1 shows the Feynman diagram for β-decay process. A down quark of neutron transform to up quark by weak interaction and emits W^- boson. The W^- boson decays into an electron and antineutrino.

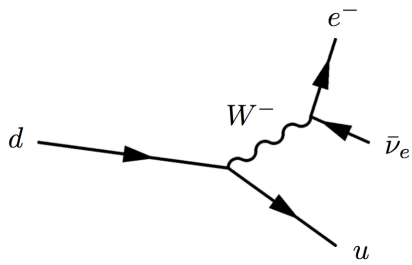

Figure 1.1: Feynman diagram for β-decay of neutron. A neutron decays into a proton, an electron and an electron antineutrino.

Each fission of the four isotopes produces ∼6 electron antineutrino [35, 36, 37, 38]and releases average ∼200 MeV of energy [34]. Based on this information, the neutrino intensity can be estimated to be $\sim 2 \times 10^{20}/(GW_{th} \cdot s)$.

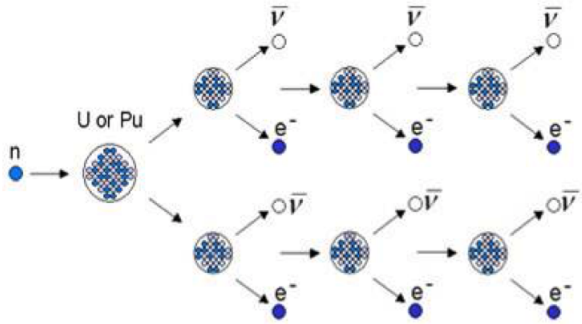

Figure 1.2: Production of neutrino in a fission process of reactor fuel [72].

The energy spectrum of reactor antineutrino is a function of reactor thermal power and the fission fraction of the 4 major isotopes. The thermal output is varies over time and with the reactor status. The fission fraction of the isotopes varies with the fuel burning as shown on the left side plot of Figure 1.3. In addition, the reactor antineutrino energy spectrum per fission of 4 isotopes are differ from each other, as shown on the right side of Figure 1.3. Thus, the expected antineutrino flux and spectrum are calculated by combining these three types of information. More details are given section 3.1.

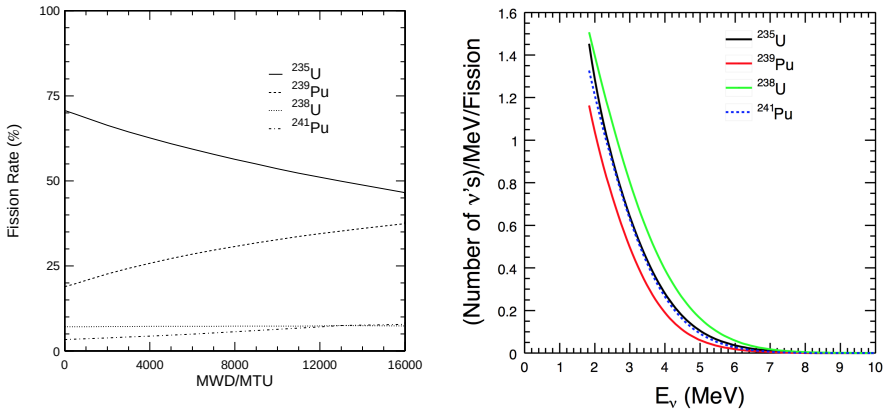

Figure 1.3: The left plot shows evolution of fissile rate of four main isotopes according to burn up. The right plot shows normalized neutrino spectrum from the fission of each isotopes [39, 40].

1.3.2 Detection of Reactor Neutrino

The electron antineutrinos from reactor are obtained via the inverse beta decay(IBD),

$$\bar{\nu}_e + p \rightarrow e^+ + n \tag{1.7}$$

When an electron antineutrino enters matter, it can be captured by a free proton via the inverse neutron decay, producing a positron and a neutron as shown Figure 1.4 and Figure 1.5.

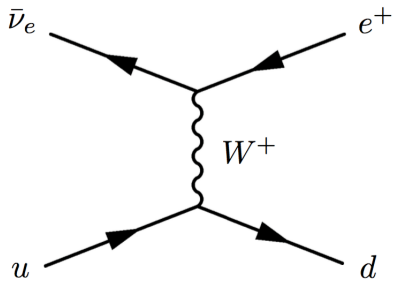

Figure 1.4: Feynman diagram for inverse β-decay. An electron antineutrino interact with u quark of the protons and producing a positron and neutron(= d quark).

The incident antineutrino energy is directly related to the energy of the positron by

$$E_{\bar{\nu}_e} = E_{e^+} + (m_n - m_p) + \mathcal{O}(E_{\bar{\nu}_e}/m_n) \simeq E_{e^+} + 1.293 \text{ MeV} \tag{1.8}$$

where E_{e^+} is the energy of the positron coming out from the inverse neutron decay and $m_n(m_p)$ is the neutron (proton) mass. The positron deposits its energy and then annihilates, yielding two photons, each with 0.511 MeV, thus experimentally visible energy is $(E_{e^+} + 0.511$ MeV) with the minimum energy of 1.022 MeV. The resulting neutron is subsequently captured by a proton in the following process:

$$n + p \rightarrow D + \gamma, \tag{1.9}$$

where D is a deuterium. The mean time for neutron capture is ~ 200 μs.

However, if a neutron is captured by Gd in which a proton is bound, the capture cross section becomes larger and additional gammas are produced, which causes the total energy to be $\sim$8 MeV. The experimental signature for reactor neutrinos is a prompt energy deposit of 1-8 MeV, resulting from the positron kinetic energy and annihilated e^+e^- masses, followed an average of 30 μs later by an 8-MeV energy deposit of gammas from the neutron capture on Gd. Exploiting the delayed coincidence is a key to controlling backgrounds. Figure 1.5 shows both prompt and delayed signals produced by a reactor neutrino.

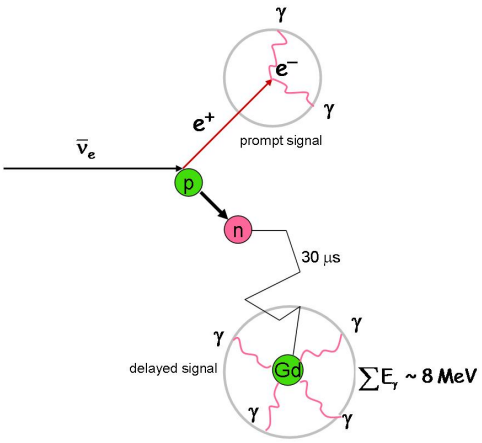

Figure 1.5: Electron antineutrino would be detected by coincidence signals of prompt positron and delayed captured neutron. The neutrino energy is directly related to the measured energy of the outgoing positron.

The inverse neutron decay process has the following cross section of the form [41, 42],

$$\sigma(E_{e^+}) \simeq \frac{2\pi^2\hbar^3}{m_e^5 f \tau_n} p_{e^+} E_{e^+}, \tag{1.10}$$

where p_{e^+} and m_e are the momentum and the mass of the positron,respectively, τ_n is the lifetime of a free neutron, and $f = 1.7152$ is the free neutron decay phase space factor [43].

Figure 1.6 shows the neutrino flux, inverse beta decay cross section, and interaction spectrum at a detector in arbitrary units calculated in Ref. [44]. The most probable neutrino energy interacting at a detector is ~ 3.8 MeV.

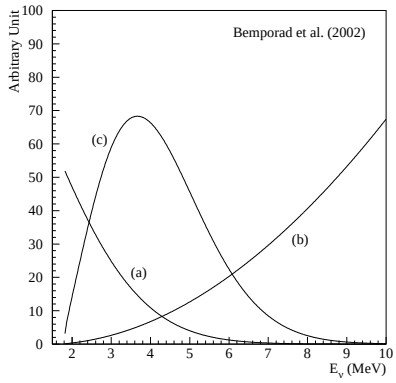

Figure 1.6: Reactor $\bar{\nu}_e$ flux (a), inverse beta decay cross section (b), and interaction spectrum at detector based on this type of reaction (c) from Ref. [44]. The cut-off at 1.8 MeV is due to the minimum neutrino energy required for the inverse beta decay process.

1.3.3 Neutrino Oscillation in Reactor Experiments

The energy of a reactor neutrino is less than 12 MeV. A reactor neutrino cannot have enough energy to produce a muon or tau. Therefore, a reactor experiment should only observe disappearance of reactor neutrino. Thus, survival probability associated with the reactor experiment is only $P(\bar{\nu_e} \rightarrow \bar{\nu_e})$. This survival probability does not consider the CP phase term. Because of the short baseline and low neutrino energy, the matter effect is negligible in the reactor experiment. $P(\bar{\nu_e} \rightarrow$

$\bar{\nu_e}$) is written as [45]

$$
\begin{aligned}
P(\bar{\nu}_e \to \bar{\nu}_e) &= 1 - 4\sum_{j>k} |U_{ej}|^2 |U_{ek}|^2 \sin^2\left(\frac{\Delta m^2_{jk} L}{4E}\right) \qquad (1.11)\\
&= 1 - \cos^4\theta_{13}\sin^2 2\theta_{12}\sin^2\left(\frac{\Delta m^2_{21} L}{4E}\right)\\
&- \sin^2 2\theta_{13}\left(\cos^2\theta_{12}\sin^2\left(\frac{\Delta m^2_{31} L}{4E}\right) + \sin^2\theta_{12}\sin^2\left(\frac{\Delta m^2_{32} L}{4E}\right)\right)\\
&\simeq 1 - \cos^4\theta_{13}\sin^2 2\theta_{12}\sin^2\left(\frac{\Delta m^2_{21} L}{4E}\right) - \sin^2 2\theta_{13}\sin^2\left(\frac{\Delta m^2_{ee} L}{4E}\right)
\end{aligned}
$$

where,

$$\Delta m^2_{ee} = \cos^2\theta_{12}\Delta m^2_{31} + \sin^2\theta_{12}\Delta m^2_{32} \qquad (1.12)$$

Equation 1.11 consists of two components; Δm^2_{21} and Δm^2_{ee}. Figure 1.7 shows the probability as a function of baseline, L (km). The Δm^2_{21} term is a negligible contribution in the few kilometer region. The other term (Δm^2_{ee}) makes a full contribution in this region. The first minimum located ~1.5 km away from the reactor. If the far detector is placed at the distance of ~1.5 km, the value of θ_{13} can be easily measured.

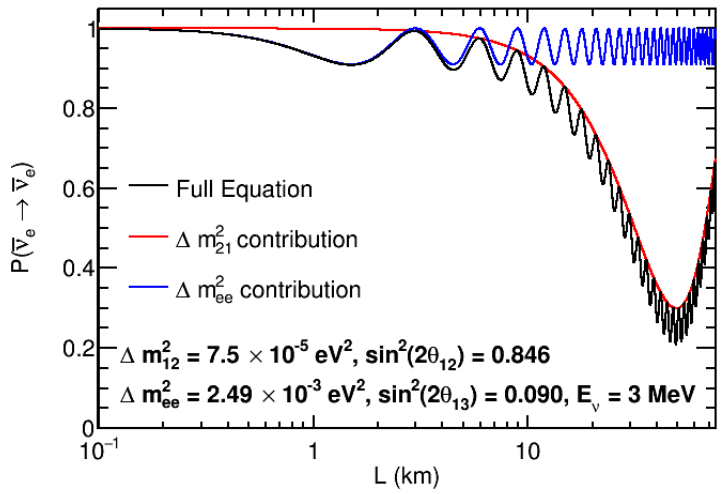

Figure 1.7: Survival probability P($\bar{\nu_e} \to \bar{\nu_e}$) vs the distance. The blue line is the Δm^2_{ee} term in Equation 1.11. The red curve represents the Δm^2_{21}. And the black line shows the sum of the two terms. The first local minimum is located ~1.5 km apart from the reactor core. At this point, Δm^2_{21} contribution is negligible.

1.3.4 Determination of Mixing Angle θ_{13}

As shown in Equation 1.11, mixing angle θ_{13} determine magnitude of the survival probability in the few km region. The measurement of the angle θ_{13} increases our understandings of neutrino oscillation. In addition, the angle θ_{13} can also serve as a guide for determining the neutrino mass hierarchy and CP violation in neutrino oscillation [46, 47, 48]. The ordering of the neutrino masses can be directly measured by a reactor experiment with a large value of θ_{13} and a baseline of ~ 50 km, such as RENO-50 [49] and JUNO [50]. The CP phase angle δ_{CP} is always found in the $U_{e3} = \sin\theta_{13}e^{-i\delta_{CP}}$. Therefore, mixing angle θ_{13} plays an important role in the determination of the phase angle δ_{CP} [51]. In this study, a more precisely θ_{13} is measured, based on the rate, spectral, and baseline information of reactor neutrino disappearance (rate+shape analysis).

1.3.5 Determination of Mass Squared Difference $|\Delta m^2_{ee}|$

The shape of survival probability $\mathrm{P}(\bar{\nu_e} \to \bar{\nu_e})$ is ruled by parameter $|\Delta m^2_{ee}|$ which is the angular frequency of the trigonometric function in the Equation 1.11. The measurement of the mass difference $|\Delta m^2_{ee}|$ also enables further understanding of neutrino oscillation and determination of mass hierarchy.

As shown in Equation 1.12, The mass difference $|\Delta m^2_{ee}|$ has physical meaning that the ν_e weighted average of $|\Delta m^2_{31}|$ and $|\Delta m^2_{32}|$. On the other hand, the mass difference $|\Delta m^2_{\mu\mu}|$ is used in the $\mathrm{P}(\nu_\mu \to \nu_e)$ at the accelerator neutrino appearance experiment T2K [52] and MINOS [53].

$$\begin{aligned} \Delta m^2_{\mu\mu} &= \sin^2\theta_{12}\Delta m^2_{31} + \cos^2\theta_{12}\Delta m^2_{32} \\ &\quad + \cos\delta_{CP}\sin\theta_{13}\sin\theta_{12}\tan\theta_{23}\Delta^2_{21} \end{aligned} \tag{1.13}$$

$|\Delta m^2_{\mu\mu}|$ is also the ν_e weighted average of $|\Delta m^2_{31}|$ and $|\Delta m^2_{32}|$, and has a tiny difference because of δ_{CP}, as shown in Equation 1.13. Therefore, the measurement of Δm^2_{31} and Δm^2_{32} in the reactor experiment is simpler than doing so in the accelerator neutrino experiment.

$|\Delta m^2_{ee}|$ is also shown as following equation.

$$|\Delta m^2_{ee}| = |\Delta m^2_{32}| \pm 5.21 \times 10^{-5}\ \mathrm{eV}^2\ (+\text{: Normal, } -\text{: Inverted}) \tag{1.14}$$

The Equation 1.14 shows the relation between the $|\Delta m^2_{ee}|$ and $|\Delta m^2_{32}|$ [45]. If the value of $|\Delta m^2_{ee}|$ is measured within 3% error, the mass hierarchy of the neutrinos can be determined.

Figure 1.8 shows the probability curve as a function of neutrino energy. The value of $|\Delta m^2_{ee}|$ determines the location of minimum point of the probability. When using spectral information of the reactor neutrino, the RENO could measure $|\Delta m^2_{ee}|$. In thesis will report the first measurement of $|\Delta m^2_{ee}|$ in the RENO.

Recently, similar measurement results of θ_{13} and $|\Delta m^2_{ee}|$ were reported by the Daya Bay experiment [54].

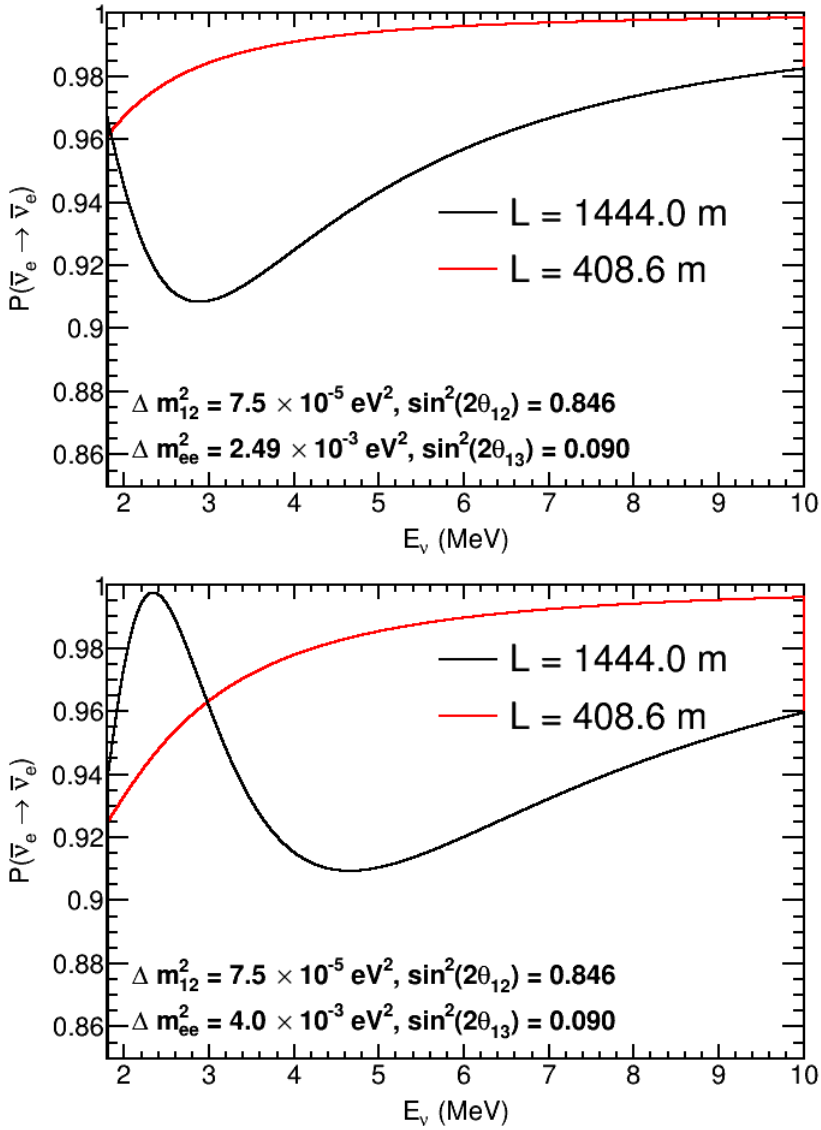

Figure 1.8: Survival probability P($\bar{\nu_e} \to \bar{\nu_e}$) vs the energy. The upper (lower) plot shows the probability with $\Delta m^2_{ee} = 2.49 \times 10^{-3} eV^2$ ($\Delta m^2_{ee} = 4.00 \times 10^{-3} eV^2$).

1.4 The RENO Experiment

The RENO is the reactor based experiment to measure the neutrino mixing angle θ_{13} and and mass squared difference $|\Delta m^2_{ee}|$, It is being conducted near the Hanbit Nuclear Power Plant in Korea. The experiment was suggested in 2005, and obtained ∼1M US dollars in funding in 2006. Civil engineering began in 2007, and the near and far detectors were both constructed in early 2011. Data began to be gathered with both detectors started in August, 2011. In early April 2012, the experiment successfully reported a definitive measurement of θ_{13} by observing the deficit of reactor neutrinos [6]. As of January 2016, the experiment has collected about 1500 days of data with accumulated data-taking efficiency of better than 95%.

We describe experimental arrangement and the RENO detectors in Chapter 2, the expected flux and spectrum of the reactor neutrino in Chapter 3, energy calibration of the near and far detectors in Chapter 4, and Monte-Calro simulation in Chapter 5. From Chapter 6, we present a spectral analysis of 500 day data. We describe IBD event selection criteria in Chapter 6, estimation of backgrounds in Chapter 7, and systematic uncertainties in Chapter 8. A spectral measurement of θ_{13} and $|\Delta m^2_{ee}|$ is presented in Chapter 9. Conclusions and discussions are presented in Chapter 10.

Chapter 2

RENO Experimental Arrangement and Detector

2.1 Overview

The RENO is the experiment to measure the neutrino mixing angle θ_{13} using electron antineutrino emitted from the Habit nuclear power plant in Yonggwang, Korea with world-second largest thermal power output of 16.4 GW. The Hanbit site was chosen due to a large number of anti-neutrinos from the nuclear power plant at the site and a mountainous geography suitable for constructing underground detectors.

The RENO experiment has two identical detectors, one placed at $\sim$ 294 m from the reactor array baseline and another at $\sim$ 1384 m. They are called near detector and far detector, respectively. By using identical design for both detectors, a number of systematic uncertainties cancel out due to normalization of the neutrino flux at the far detector using that of the near detector.

The detectors have a layered structure similar to other reactor neutrino experiments, *i.e.* Daya Bay and Double Chooz experiments. The RENO detectors consist of four cylindrical shape layers. They are, from the center, target, γ-catcher, buffer, and veto, where an outer layer almost enclosing an inner layer. The PMTs for detecting neutrino interaction will be in the buffer layer. The cutaway view of a RENO detector is shown in Fig. 2.1.

The "target" is gadolinium (Gd) doped liquid scintillator contained in a transparent cylindrical vessel made of acrylic plastic. An inverse beta decay event produces a positron and neutron pair. The positron loses energy through scintillating process before converted into two gammas via a pair annihilation. The neutron thermalizes then is captured by Gd nucleus producing several gammas. The gammas produced close to the boundary of target can escape target with-

out completely depositing its energy in scintillator. To contain the energy carried by gammas escaping from the target, the "γ-catcher," another liquid scintillator layer, surrounds target. Unlike the target, the liquid scintillator in the γ-catcher is not loaded with Gd since this layer is intended to augment the target in energy measurement of gammas emitted in target. As with target, a transparent cylindrical acrylic vessel contains γ-catcher liquid.

Surrounding the γ-catcher is a non-scintillating liquid layer called the "buffer." Mineral oil is used as the buffer and is contained in a cylindrical vessel made of stainless steel. The photomultiplier tubes (PMTs) are mounted on the inner surface of the buffer vessel immersed in buffer. The buffer acts as a shield against gammas mainly coming from radioactive isotope contained in PMTs entering the scintillating volume.

The outermost layer of the RENO detector is the "veto," a water Cherenkov detector layer. Its purpose is to reduce background gammas and neutrons from the surrounding environment (such as rocks) inner layers as well as rejecting cosmic muon induced background events. The veto container is constructed with 30 cm thick concrete and the top lid is made of stainless steel. PMTs are mounted on the inner surface of veto container for detecting Cherenkov light from cosmic muons.

The various design parameters have been determined for optimal performance using detailed simulation[]. The simulation includes background γs from PMTs and surrounding rocks, cosmic muons reaching the detector site as well as inverse beta decay from the reactor anti-neutrinos. The detector layers and vessels are summarized in Table 2.1.

Detector Component	Outer Diameter(mm)	Outer Height(mm)	Material	Volume (m^3)	Mass (tons)
Target	2750	3150	Gd-loaded LS	18.70	16.08
Target Vessel	2800	3200	Acrylic	0.99	1.18
γ-catcher	3940	4340	LS	33.19	28.55
γ-catcher Vessel	4000	4400	Acrylic	2.38	2.83
Buffer	5388	5788	Oil	76.46	64.22
Buffer Vessel	5400	5800	SUS	1.05	8.39
Veto	8388	8788	Water	352.61	352.61

Table 2.1: Dimensions of the mechanical structure of the detector.

A RENO DAQ system is designed to record the charge and arrival time of PMT hits. The near and far detectors are designed to have the same PMT configuration and readout system. The RENO DAQ employs a new electronics developed for Super-Kamiokande experiment.

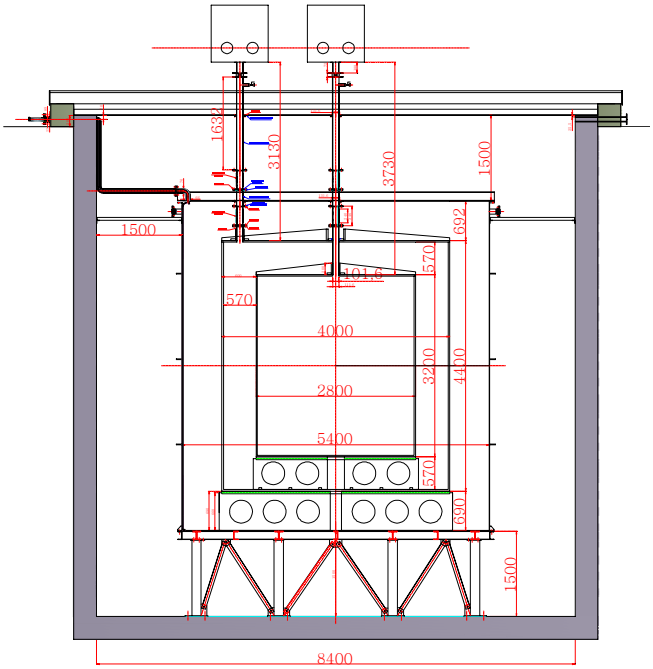

Figure 2.1: RENO detector. From the center, there are liquid scintillator filled target and gamma catcher with transparent acrylic vessel, mineral oil filled buffer with stainless steel vessel, and water filled veto layers. The PMTs for the inner and outer detectors are inwardly mounted on buffer and veto vessels, respectively.

2.2 Experimental Arrangement

2.2.1 Near and Far Detectors

One of the primary sources of systematic error is the uncertainty in the reactor neutrino flux. To minimize this uncertainty, near and far detectors, two identical detectors are needed. Each detector will contain 18.7 m^3 of liquid scintillator target doped with 0.1% of gadolinium (see Chapter **??**).

Figure 2.3 shows the layout of six reactors and two detectors and table 2.2 shows the neutrino flux contributions of reactors at each detector. The near and far detectors are placed 290 m and 1400 m away from the center of the reactors, respectively. The near detector is located under an 70 m (AMSL) ridge with an overburden of $\sim$ 110 mwe whereas the far detector is located under a 260 m mountain with the overburden of $\sim$ 450 mwe as shown in Figs. 2.3 and The

coordinates of the detector center are measured with a total station to a precision of the order of 100 mm (See Appendix F).

Reactor No.	Near Detector (%)	Far Detector (%)
1	7.06	14.24
2	15.54	16.31
3	33.80	17.82
4	26.71	18.28
5	11.37	17.53
6	5.52	15.83

Table 2.2: Fractional reactor neutrino contribution of reactor.

2.2.2 Hanbit Nuclear Power Plant

The Hanbit nuclear power plant is placed in the west coast of the southern part of Korea, about $\sim$ 250 km from Seoul as shown in Fig. 2.2. The reactors in the plant are Pressurized Water Reactors (PWR). These reactors are aligned in roughly equal distances, as shown in Fig. 2.3. Reactor operation cycle varies from 18 months to 24 months and refuelling are done with the plant shutdown. The total thermal output power is 16.4 GW_{th} with six reactor cores generating about equal power. The coordinates of the reactor cores are measured with a GPS to a precision of 30 mm (See Appendix F).

Reactor No.	Thermal power (MW_{th})	Commercial operation
1	2775	Aug. 1986
2	2775	Jun. 1987
3	2815	Mar. 1995
4	2815	Jan. 1996
5	2815	May 2002
6	2815	Dec. 2002

Table 2.3: Thermal power and Commercial operation of Hanbit powerplant

Figure 2.2: Hanbit nuclear power plant. The plant is located Yonggwang away from 250 km south of Seoul. Three other nuclear power plants are placed in the east coast of the southern part of Korea.

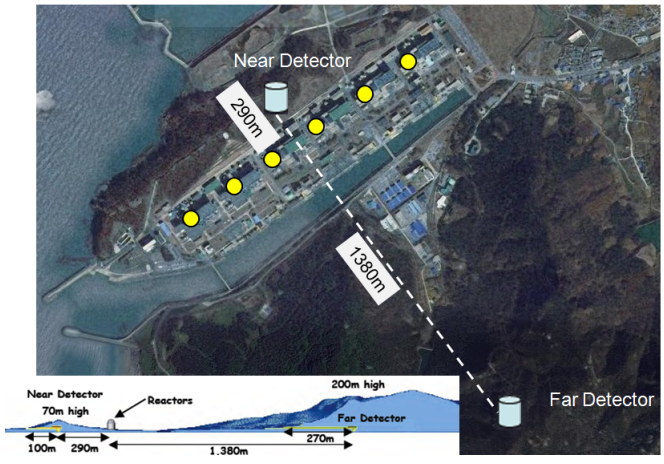

Figure 2.3: Layout of the Hanbit experiment site. The yellow dots and light blue cylinder represent reactors and detectors, respectively. The six reactors are roughly equally spaced in a 1280 m span. The near and far detectors are 290 m and 1380 m away from the reactor array, respectively. The image taken from Google Earth^{TM} and copyrighted therein. Bottom-left plot shows a side view.

2.2.3 Underground Facility and Experiment Halls

The detectors are built with two horizontal tunnels, 100 m long for the near detector and 300 m long for the far detector, as shown in Fig. 2.4. NATM (New Austrian Tunneling Method) is used for constructing the tunnels. The tunnel schematic of experimental hall are shown in Fig. 2.5

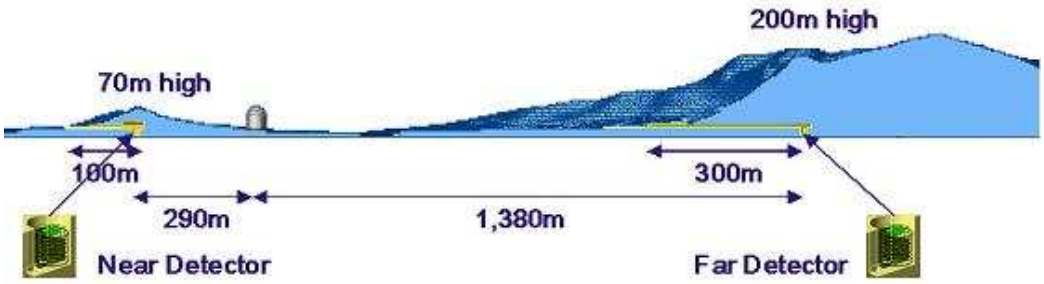

Figure 2.4: Side view of RENO experiment.

The access tunnels are 95 m and 272 m long for near and far detector sites, respectively. The cross section of the access tunnel is shown in Fig. 2.5. The gradient toward the experimental hall is 0.3% for both tunnels for natural drainage. It is designed to accommodate the passage of a 10 ton truck.

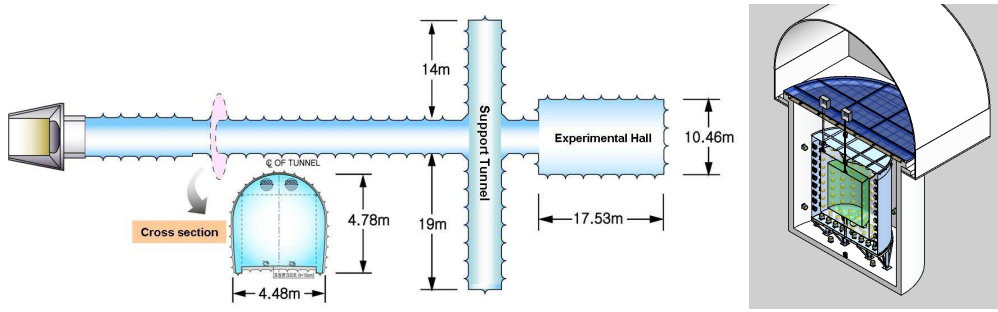

Figure 2.5: Plan of the access tunnel (top) and 3D schematic for experimental hall (bottom). The tunnels are constructed using NATM.

2.3 Detector Components

Both RENO near and far detectors consist of a cylindrical target of 140 cm in radius and 320 cm in height, providing a volume of 18.7 m^3. Identical arrange-

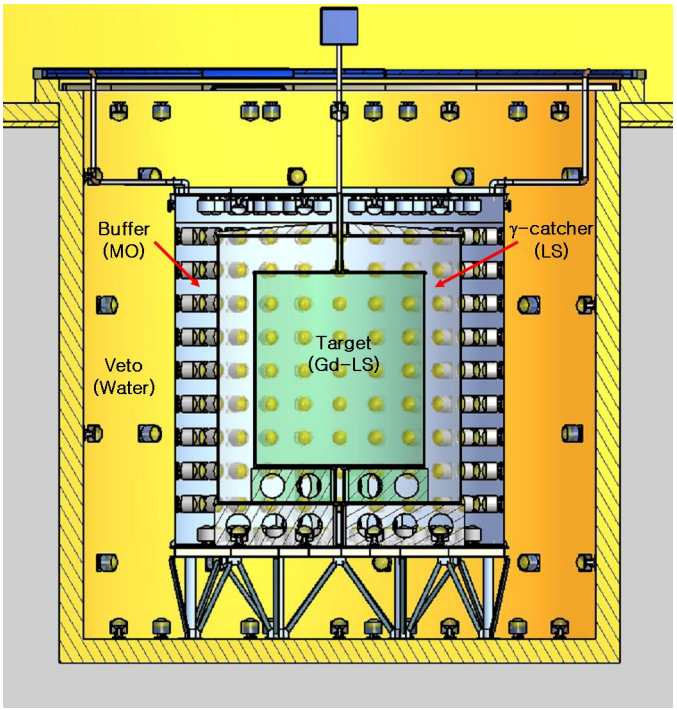

Figure 2.6: A schematic view of RENO detector. A neutrino target of 18.7 m^3 Linear Alkyl Benzene (LAB) based liquid scintillator doped with Gd is contained in a transparent acrylic vessel, and surrounded by 33.2 m^3 unloaded liquid scintillator of gamma catcher and 76.5 m^3 non-scintillating buffer. There are 354 and 67 10-inch PMTs mounted on buffer and veto vessel walls, respectively.

ment of the near and far detectors will significantly reduce the systematic errors of relative normalization to 0.6%. However, they will have different cosmic ray background levels because of unequal overburdens (∼110 mwe *vs.* ∼450 mwe). Although the near detector will suffer from higher cosmic ray background, it will observe much more signal events of reactor anti-neutrinos due to shorter distance from the nuclear cores and thus allows a high signal-to-background ratio.

The RENO detector consists of a neutrino target, a gamma catcher, a buffer and a veto. Target and gamma catcher vessels will be made from acrylic plastic material, having transparency to the light of wavelengths above 400 nm. The acrylic vessels should hold aromatic liquids without leakage and its properties should not change for the duration of the experiment. They should not develop any chemical reaction with the scintillating liquids of neutrino target, gamma catcher and buffer for a long time period.

2.3.1 Target and Gamma Catcher

Structure

The two innermost layers, target and γ-catcher, are contained in vessels made of acrylic plastic. This acrylic plastic is transparent to photons with wavelengths above 400 nm. Two important issues for these layers are considered; chemical compatibility between the contents and the vessel, and mechanical stability.

As for the chemical compatibility, the liquid scintillating material for both the target and γ-catcher should not chemically interact with the vessel for the duration of the experiment. At the same time, the γ-catcher vessel should be chemically inert to the mineral oil in buffer layer. There have already been extensive studies on chemical compatibility of these materials for CHOOZ experiment and others. The RENO collaboration is also conducting various R&D on the chemical interaction of acrylic plastic and other materials used in the experiment.

Mechanically, these vessels are required to withstand the mechanical stresses that they are subjected to during the all phases of the experiment and maintain structural integrity. When loaded with liquids, the volume of the vessels can change slightly from the nominal volume. This change should be within specified tolerances.

The target vessel a cylinder with a height of 3.2 m, a diameter of 2.8 m, and a thickness of 25 mm. The mass of the target vessel is 1.2 tons. The target vessel has a volume of 19.2 m^3 and the combined mass of the target liquid and vessel with supporting structure is 17.3 tons. Inside the γ-catcher vessel, the target vessel is mounted on the supporting structure made of the same acrylic plastic. When both target and γ-catcher are filled, the net load on the target supporting structure would be 328 kg due to buoyancy. At the center of the top of the vessel, a pipe is installed to connect the target volume to the outside of the detector for filling target liquid and inserting calibration sources.

The design of the γ-catcher is similar to that of the target but about three times larger in volume. The γ-catcher vessel is a transparent cylinder with a height of 4.4 m and a diameter of 4.0 m diameter. Its wall is 3 cm thick. The γ-catcher vessel is mounted on the supporting structure made of acrylic plastic and placed inside the buffer vessel. It has a pipe connecting the top of the γ-catcher vessel and the outside of the detector for liquid filling and calibration source insertion. The γ-catcher vessel has a mass of $\sim$ 2.8 tons. The combined mass of the γ-catcher vessel and γ-catcher liquid scintillator is 31.4 tons. When the γ-catcher is immersed in buffer liquid, the total load on the γ-catcher supporting structure would be 2.2 tons.

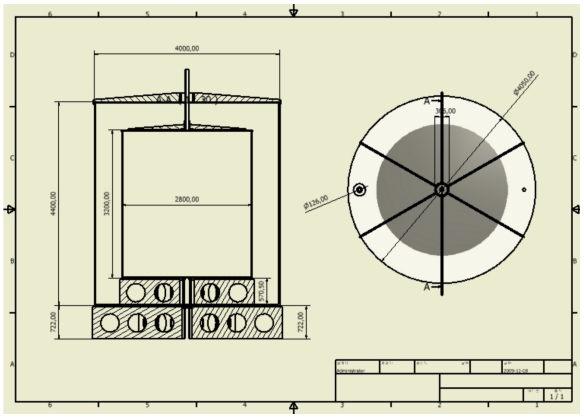

Figure 2.7: Target and gamma catcher vessels with supporting structures. The supporting structures are made with the same transparent acrylic plastic as the vessels.

Acrylic Vessels

The target and γ-catcher vessels are made of transparent acrylic plastic called Polymethyl-methacrylate (PMMA). The molecular formula of PMMA is $(C_5O_2H_8)_n$. PMMA can be found under trade names like Plexiglas, R-Cast, and Lucite. The properties of PMMA are shown in Table 2.4. With additional ingredients in PMMA the UV below 400 nm is absorbed.

The target and γ-catcher vessels are made from cast acrylic sheets (Plexiglass, GS-233) supplied by Degussa GmbH, Germany. The cast acrylic sheet has better mechanical and chemical properties than the extruded acrylic sheet. The production of the vessels is done by KOA Tech in Korea.

The manufacturing precision of the vessels is less than 0.1% in volume (2 mm in 1 dimension), therefore, less than 0.14% difference in target vessel volume between near and far detector could incur.

Properties	Value
Density	1.19 g/cm^3
Melting point	130-140 ^{o}C
Refractive index	1.491
Transmittance	92%

Table 2.4: The mechanical and optical properties of cast acrylic, such as Plexiglas GS-233 from Degussa GmbH, Germany and R-Cast from Reynolds Co., USA.

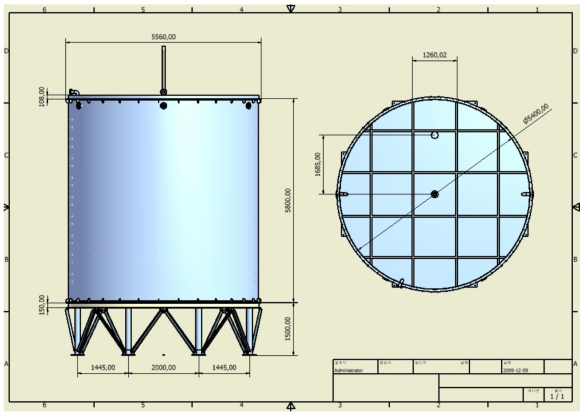

Figure 2.8: External view of the buffer vessel. The vessel is made of stainless steel (304L) and the supporting truss structure is made of nickel plated steel pipes.

Chimney

Each target and γ-catcher has a chimney for filling liquids and transporting calibration sources from the top lid of the veto vessel into and out of either target or γ-catcher. A chimney is made of about 4-inch transparent acrylic tubing with a flexible convoluted PTFE tube connecting the buffer vessel and the acrylic tubing to ease the stress. From the top lid of the buffer the chimney is made of stainless pipes extending to the top lid of the veto vessel.

2.3.2 Buffer

The buffer vessel is a cylinder of 5.8 m height and 5.4 m diameter containing target, γ-catcher, and buffer liquid. The buffer contains non-scintillating oil to shield the scintillating volume within from background sources outside, including radioactivity in PMTs. The buffer vessel also acts as the PMT mounting surface where 354 PMTs are mounted staring inward and optically isolates the these PMTs from the veto volume. The size of the buffer vessel has been determined from the MC simulations.

The buffer vessel should be chemically inert against mineral oil inside and water outside. Also, it should withstand the stress from the loads coming from liquids and structures contained within. The buffer vessel is constructed with 6 mm thick 304L stainless steel for the top lid and barrel section, 8 mm thick for the bottom plate for extra mechanical support. The external view is shown in Fig. 2.8. The surface of the vessel is not polished. When the detector is filled with required liquids, the buffer vessel would experience buoyant force due to the

density difference between the organic liquids inside the buffer vessel and water in veto layer. The buoyant force is estimated to be 11.5 tons and the buffer vessel supporting structure is designed to counter this force.

The buffer vessels are manufactured by Nivak co., Korea. They are transported as segmented pieces to the experiment site and assembled in the experiment halls. The barrel section consists of six segments and top and bottom plates each consists of three segments. The bottom plate is welded to the barrel section and the top plate is bolted to the barrel section.

There are total 354 10-inch PMTs mounted on the inner side walls of the buffer vessel, 234 PMTs mounted on the barrel section, 60 each on the top and bottom plates, as shown in Fig. 2.9. PMTs are mounted upright on the walls using the PMT holding structure described in Sect. 2.3.4.

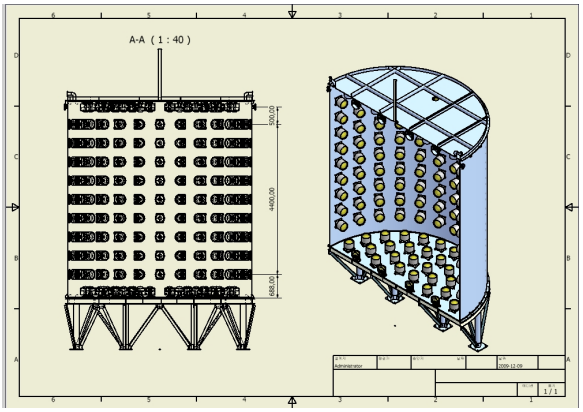

Figure 2.9: Inner detector PMT array on the buffer vessel. The PMTs are mounted on the vessel wall using the PMT holders. There are total 354 10-inch PMTs.

2.3.3 Veto

Design Criteria

The veto system is located just outside of the buffer tank. The main background of the experiment is caused by cosmic muons, and it is very important to identify the entering muons since they can produce neutrons by muon-nucleus interaction in the detector. There also correlated backgrounds by ^{9}Li and ^{8}He in the target and γ-catcher produced by muons. The veto vessel should be chemically compatible with water and strong enough to support all the three inner chambers before filling the liquids.

Structure

The inner diameter and height of the veto vessel are 8.4 m and 8.8 m, respectively. The vessel is constructed with a 40 cm thick concrete vessel , as shown the outermost layer of Fig. 2.10. Inner surface of the concrete vessel was water-proofed with urethane resin. The water is purified at filling and continuously be circulated through a water purification system. There are 67 10-inch water-proof PMTs (R7081 Hamamatsu) attached on the inner surface of the veto vessel. The outer surface of buffer vessel and the inner surface of veto vessel is covered by Tyvek sheet to increase the light collection of Cherenkov photons in the water.

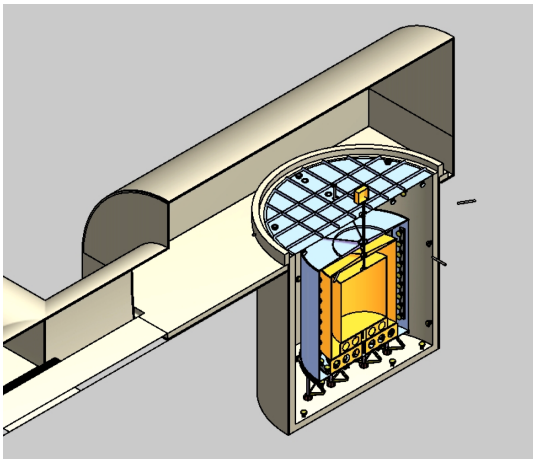

Figure 2.10: Cutaway view of RENO detector. The outermost region is veto and filled with fure water.

2.3.4 PMT

PMT Requirements and Specification

The scintillation lights from target and γ-catcher is detected with PMTs attached on the inner surface of the buffer vessel. The number of photoelectrons detected is estimated to be 150 photoelectrons per MeV for an event occurring at the center of the target. Since the minimum energy deposited in the detector by a positron emitted in the inverse beta decay process is 1.022 MeV, the average number of photoelectron per PMT in the buffer layer is $\sim$0.5. Therefore, the PMTs should be able to measure the single photoelectrons with high efficiency. The peak-to-valley ratio and the single photoelectron resolution of the PMTs are important parameters.

The main reason to isolate PMTs from γ-catcher via non-scintillating buffer region is to shield the γ-catcher from PMT's radioactivity. The radioactivity of PMTs needs to be studied to understand the rate of background originating from PMTs. The PMT background events are mainly in the low energy region of less than 2 MeV and could be misidentified as signals by accidental coincidence with neutron-like background events.

Since the PMTs is immersed in a layer of mineral oil, it is also important that the whole PMT assembly is chemically inert to mineral oil. The oil proofing should be stable for the duration of the experiment.

The quantum efficiency of each PMT is measured We measured the quantum efficiencies of all PMTs with a relative accuracy less than 5%. The outlying PMTs was excluded from installation on the detectors.

Specification of PMT

After considering various performance parameters, such as single photoelectron resolution, afterpulse rate, radioactivity in PMT, and overall detector performance to cost ratio, the RENO use 10-inch low background PMTs by Hamamatsu (R7081-Low). Table 2.5 shows the company specifications and our measurements for the PMT.

	R7081
Gain($\times 10^7$)	1.0 @ 1500 V
QE @ peak (nm)	25% @390
DC (nA)	50
Size (inch)	10
Weight (g)	1150
Rise Time (ns)	4.3
TTS (ns)	2.9
Afterpulse	2%
Peak-to-valley ratio	3.5

Table 2.5: The specifications of PMTs. R7081 is from Hamamatsu

To reduce the background from PMTs, Hamamatsu makes 10-inch PMTs with low background glass (R7081-Low). We measured radioactivities on two sample R7081-Low PMTs. The measured activities for the PMTs tested are summarized in the Table 2.6. The background level of R7081-Low is found to be about 25% of that of the normal glass R7081 PMTs. The measured level of radioactivity of low background glass PMTs would be acceptable for RENO experiment.

PMT	^{238}U	^{232}Th	^{40}K
R7081(Hamamatsu)	4.8 ± 0.07	2.2 ± 0.03	13.1 ± 0.4
R7081(Hamamatsu)-Low	0.72 ± 0.1	0.59 ± 0.07	3.3 ± 0.3

Table 2.6: The radioactivity of 10-inch PMTs from Hamamatsu. The units are Bq/PMT.

PMT Test

To get rid of abnormal behaviors PMT, All PMTs were carefully checked before the installation. By the comparing PMT performance parameters between given by Hamamatsu and measured, the PMT could be selected to employ in the detectors. To test PMTs, a test room was built in the far detector tunnel. The test room consists dark room and DAQ room as shown in Fig. 2.12. The PMT mountable table in the dark room can mount 12 PMTs at once as shown in the left plot of Fig. 2.11, and 1in-12out fiber distribute laser light to 12 PMTs from the laser module in the DAQ room as shown in the right plot of Fig. 2.11. Therefore, 12 PMTs could be tested at once. Two PMTs were always mounted in the table using for a reference, and ten PMTs were tested at once.

Figure 2.11: Photos of PMT test bench.

The check list is summarized as follows:

- appearance
- Peak to Valley
- Time resolution
- Charge linearity

- Transit time

- Dark current

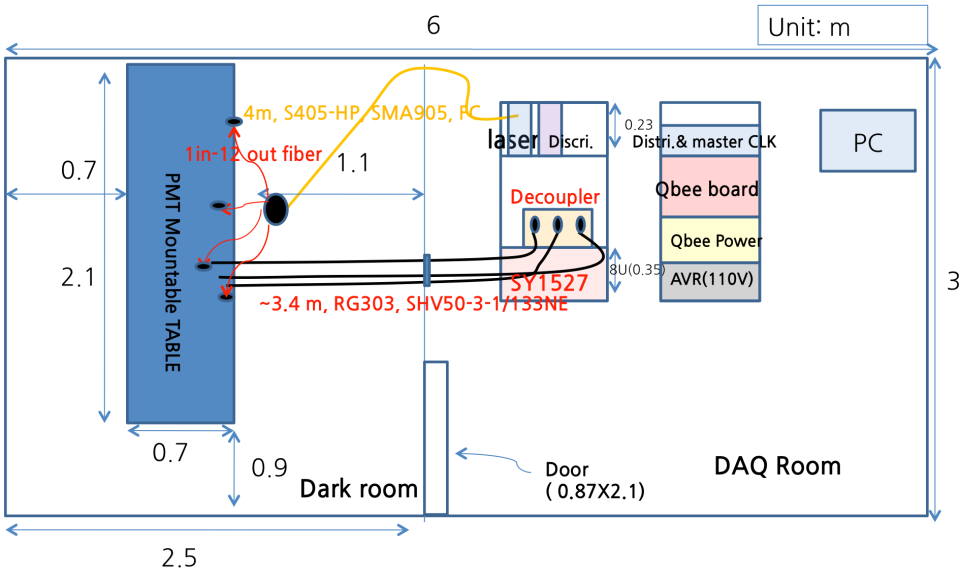

Figure 2.12: PMT test setup block diagram.

PMT Holder

PMTs is mounted on the inner wall of stainless steel buffer vessel. We want to minimize the amount of material while keeping the holding structure as stable as possible. Also the distance between PMT photocathode surface and buffer vessel should be minimized. The PMT holder is made of 1.5∼2 mm thick stainless steel. The schematic is shown in Fig. 2.13. Two rings hold the glass bulb section of the PMT and the front ring defines the photosensitive area. The inner diameter of the rings is 12.3 cm. A mu-metal sheet surrounds the side of the structure to reduce the effects of external magnetic fields. The height of the mu-metal shielding is determined based on the magnetic field survey at the experiment halls.

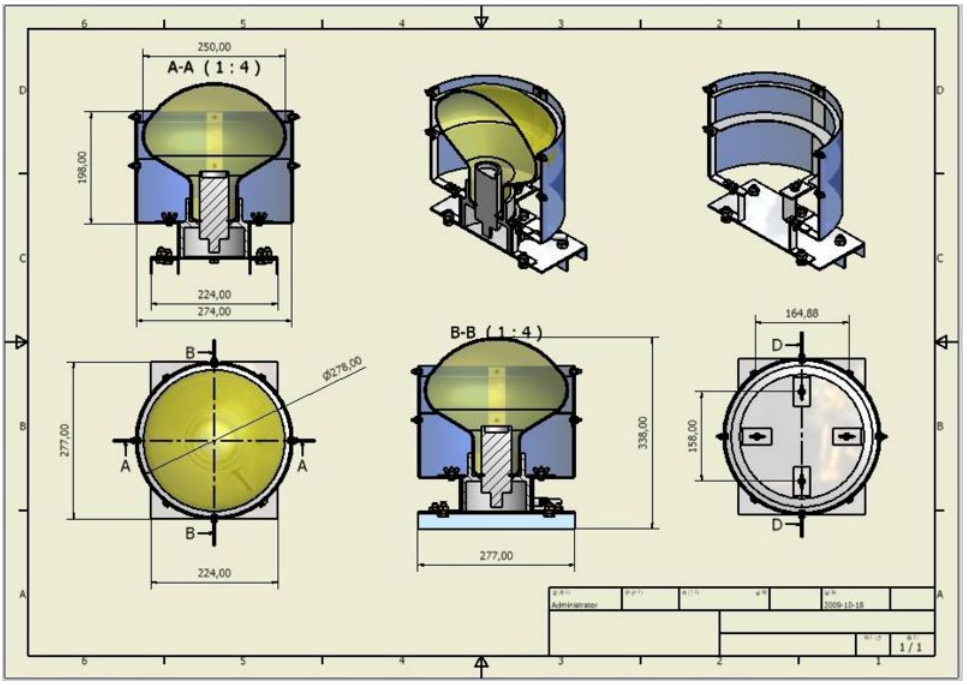

Figure 2.13: A design of PMT holder. Two stainless steel rims hold the glass of 10-inch PMT. A cylinder shape mu metal sheet is outside of the rings surrounding the individual PMT to reduce the effect of the magnetic field.

2.4 Liquid Scintillator

The liquid scintillator(LS) of the RENO experiment is a blend of an organic solvent, a flour, and wavelength shifters. For the previous neutrino experiments, pseudocumene (PC or TMB, C_9H_{12}, 1,2,4-trimethyl-benzene) was commonly used for an organic solvent of LS because it grants a higher light yield compared to others [55]. However, PC is toxic to the human body and the environment. It is harmful to the human body and the environment and has a low flash-point (48 °C). On the other hand, LAB ($C_nH_{2n+1}-C_6H_5$, n = 10−13) is safe material and has a high flash-point (130 °C), a relatively good light yield, high transmittance, and a large attenuation length [56]. Furthermore, LAB could be bought at a sensible price because it is produced by the Isu Chemical Company in South Korea [57].

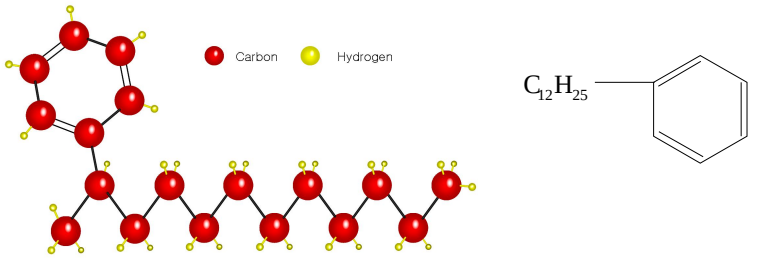

Figure 2.14: Molecular structure of LAB with a linear alkyl chain $C_{12}H_{25}$

	PC	LAB
Molecular formula	C_9H_{12}	C_nH_{2n+1}-C_6H_5, n = 10 ∼ 13
Molecular weight (g/mol)	120.19	233∼237
Flash point (^{o}C)	48	130
Density (g/ml)	0.89	0.85
Compatibility(acrylic)	Bad, need diluent	Good
Cost	Moderate	Low
Fluor dissolution	Very good	Moderate
Domestic availability	No	Yes
Toxicity	Toxic fume	Non toxic

Table 2.7: Comparison between PC and LAB.

2.4.1 Optimization for Liquid Scintillator

Fluor and Wavelength Shifter

The PMTs being used (R7081-low, Hamamatsu) is most sensitive to light at ∼390 nm but retains good sensitivity at 400 − 430 nm, and acrylic vessels of the target and the γcatcher are made of becomes opaque rapidly for light with wavelength below 390 nm. So, it is imperative for the liquid scintillator emitting light at ∼420 nm.

However, the pure LAB solvent shows an emission maximum at 340 nm, as shown in Fig. 2.15. Therefore, the wavelength of the scintillation light from LAB needs to be shifted above 400 nm. This is achieved by using PPO (2,5-diphenyloxazole, $C_{15}H_{11}NO$) as a primary solute and bis-MSB (1,4,-bis(2-methylstyryl)-benzene) as a secondary wavelength shifter. As shown in Fig 2.15, PPO and bis-MSB emit photons at 340 ∼ 440 nm and 380 ∼ 460 nm, respectively.

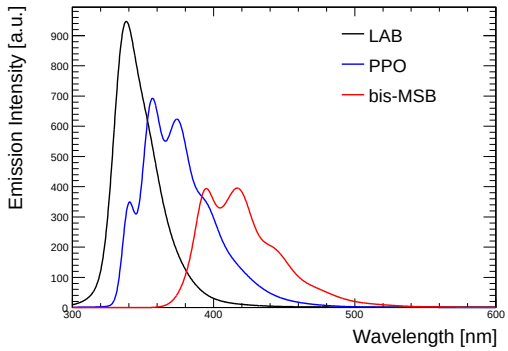

Figure 2.15: Emission spectrum of the solvent LAB (black), the primary fluor PPO (blue), and the wavelength shifter bis-MSB(red).

Optimization of liquid scintillator

We looked for the best concentration of the PPO in the LAB for the maximum light yield(LY). The maximum light yield was obtained at 3 g/l, as shown in the left plot of Fig. 2.16. Then, the light yield was measured at different bis-MSB quantity from 0 to 200 mg/l. The saturation point of the wavelength shifter was found at 30 mg/l, as shown in the right plot of Fig. 2.16. A maximum light yield occurred at a concentration of 3 g/l of PPO plus 30 mg/l of bis-MSB [58].

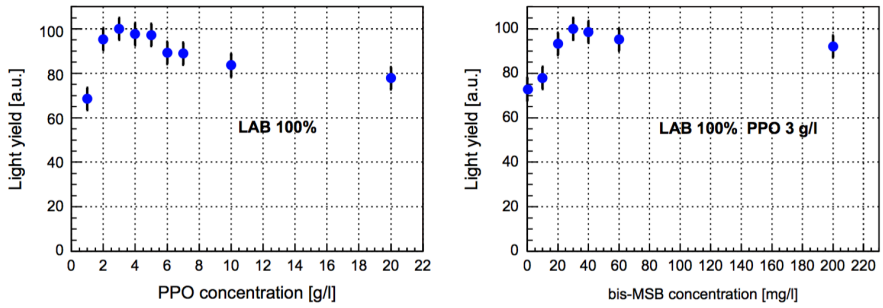

Figure 2.16: The left plot shows relative scintillation light yield of 100% LAB in arbitrary units with varying PPO. The right plot shows light yield of 100% LAB and 3 g/l of PPO with varying bis-MSB concentration [32].

2.4.2 Gd-loaded liquid scintillator

The hydrogen atoms ("free proton") in the liquid scintillator serve as the target for the inverse beta decay reaction. When a neutron is captured by a free proton, γ-rays with a total energy of ~2.2 MeV are emitted. Whereas, a neutron capture on a Gd atom leads to an emission of γ-rays with a total energy of ~8 MeV, much higher than the energies of the gamma rays from natural radioactivities which are normally below 3.5 MeV. The mean thermal neutron capture cross section of Gd isotopes is four orders of magnitude larger than that of proton. Hence the liquid scintillator doped with a small amount of Gd is ideal for detecting inverse beta decay events [56].

Besides the light yield, stability of the Gd loaded scintillator is another crucial matter. Gd-LS should be chemically stable for the duration of the experiment, *i.e.* several years. From Palo Verde and CHOOZ reactor experiments, unexpected problems with Gd-LS had been reported. Palo Verde had problems with precipitation, condensation, and slow deterioration of Gd-LS developing in time [28]. In CHOOZ experiment, Gd-LS turned yellow a few months after deployment. A very rapid decay of attenuation length in Gd-LS had been measured [30].

Gadolinium Loading

It is difficult to add inorganic Gd to organic liquid scintillator to make a stable Gd loaded liquid scintillator. However, two formulations for Gd loaded liquid scintillator have shown promising results; liquid scintillators with Gd binding with carboxylate (CBX) ligands and with β-diketonate (BDK) ligands. Double Chooz and Daya Bay experiments report that both BDK and CBX Gd loaded liquid scintillators have excellent performances [59]. We chose to use CBX as our basis for ligands. There are two steps in synthesizing the Gd-carboxylate compound:

1. $Gd_2O_3 + 6HCl \rightarrow 2GdCl_3 + 3H_2O$

2. $RCOOH + NH_3 * H_2O \rightarrow RCOONH_4 + H_2O$

3. $3RCOONH_4(\text{aqueous}) + GdCl_3(\text{aqueous}) \rightarrow Gd(RCOO)_3 + 3NH_4Cl$

First, we need to make $GdCl_3$ solution from Gd_2O_3 based on step 1. In step 2, 3,5,5-trimethylhexanoic acid (TMHA) is neutralized with ammonium hydroxide. In step 3, two aqueous solutions from steps 1 and 2 are mixed to produce Gd salt. When two solutions are mixed, white Gd-carboxylate compound (Gd-TMHA) precipitates immediately. These reactions are very sensitive to pH. Precipitated Gd-TMHA is thoroughly rinsed with 18 MΩ ultra pure water several times to

remove impurities. Then, liquid–liquid extraction technique was used for the second method as shown in Fig. 2.17. After the reactions, the organic solvent and water will be distinguished due to the density difference.

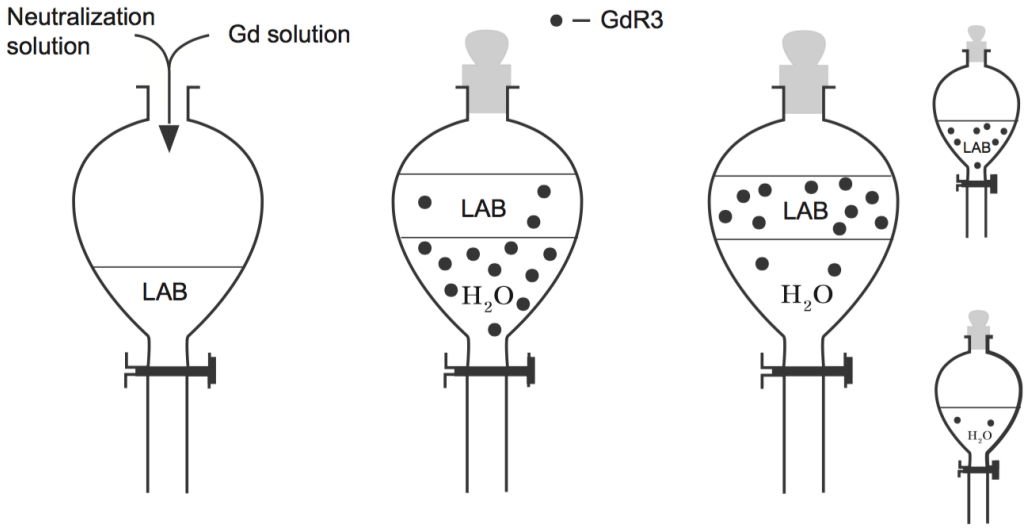

Figure 2.17: Method of liquid–liquid extraction. Neutralization solution and Gd solution are mixed into LAB. Gd complex is directly dissolved in LAB. Two layers between LAB and water are separated due to the density difference between oil and water [32].

Long-term stability

When GdLS filling was completed, GdLS samples were taken out from the targets of the near and far detectors. To evaluate the long-term stability of the GdLS, Gd concentration and transmittance value have been measured. The results of transmittance measurement was routinely acquired by a spectrophotometric technique as shown in Fig. 2.18. All the variation of transmittance values was consistent within the uncertainties. Gd concentration was also routinely measured. It shows stable within the the uncertainties, as shown in Fig. 2.19.

Moreover, in autumn 2012, The second GdLS samples were extracted from the target of the far detector. They were 400 days passed samples. The measured Gd concentration and transmittance of those sample show no degradation in the quality. These points are drawn as a star mark in Figs. 2.18 and 2.19. From these results, we conclude that the GdLS is chemically stable.

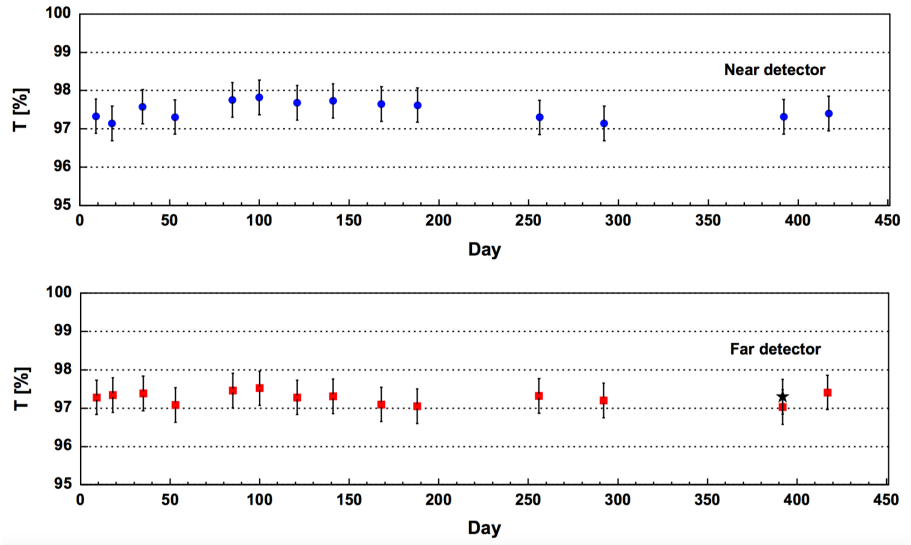

Figure 2.18: Long-term stability of GdLS by measuring the transmittance value at 430 nm as a function of day. A star mark is a value from the sample extracted from detector recently [32].

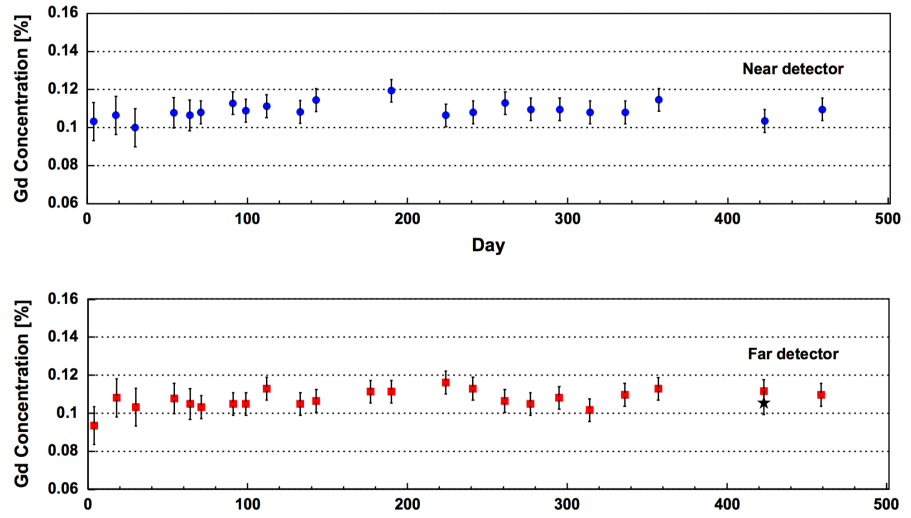

Figure 2.19: Variation of Gd concentration in gadolinium-loaded liquid scintillator by EDTA method as a function of day. A star mark is a value from the sample extracted from detector recently [32].

Dynamic range	$0 \sim 2500$ pC
Self trigger	Built-in discriminator
Number of input channels	3
Processing speed	~ 500 ns/cycle
Gain	1/7/49 (3 settings)
Charge resolution	0.05 p.e. (< 25 p.e.)
(Non-) Linearity (Q)	$< 1\%$
Timing resolution	0.3 ns (1 p.e.$= -3$ mV), 0.2 ns(> 5 p.e.)
Power dissipation	< 200 mW/channel

Table 2.8: Characteristics of QTC chips. p.e. is photoelectron.

2.5 Data Acquisition (DAQ) and Monitoring System

2.5.1 Electronics

The antineutrino interaction in the RENO detector produces scintillation lights, and a part of them are converted into photoelectrons at the PMT. To detect the antineutrino event, the RENO detector has 354 inner PMTs and 67 outer PMTs. A RENO readout system is designed to record the charge and arrival time of PMT hits. Based on the energy and timing information we can select the neutrino events, reject background events, and reconstruct the vertex of antineutrino interaction. The near and far detectors are designed to have the same PMT configuration and readout system.

The RENO DAQ employs a electronics developed for Super-Kamiokande experiment which uses charge-to-time conversion chips to record hits at 60 kHz with no dead time. The following section describes the descriptions of the RENO DAQ electronics.

QBEE Board

The QBEE board is the electronics that has eight charge-to-time conversion chips (QTC), four Time-to-Digital conversion chips (TDC), and onboard ethernet card, developed for Super-Kamiokande experiment. The electronics system are fast enough to record every PMT hits and are guaranteed for stable data acquisition over ten years. The pmt hit information is recorded in the storage and then software trigger criteria are applied. The hit time and charge of the PMT pulse are measured by the QTC chip, and are converted into binary formatted data by the TDC chip. Table 2.8 shows the The characteristics of the QTC chip. And the operation logic diagram of QTC chip is shown in Fig. 2.20.

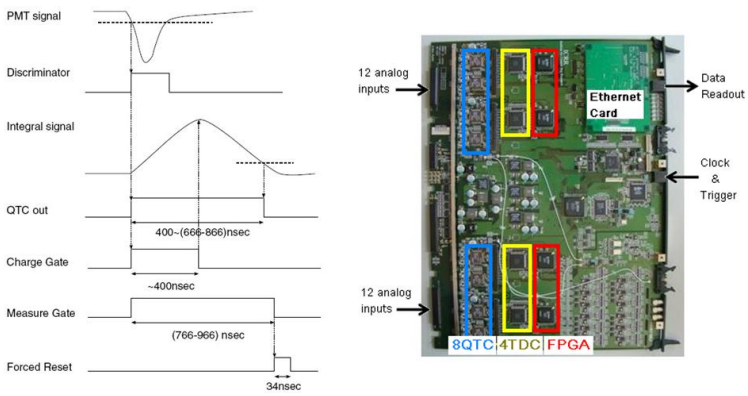

Figure 2.20: Operation logic diagram of QTC chip and QBEE board

The output of QBEE is charge with ADC count. The QBEE board needs calibration to convert ADC count to charge in pC. So, each QBEE board is calibrated with several charge and fitted with 5^{th} polynomial. One of the calibration results are shown in Fig. 2.21.

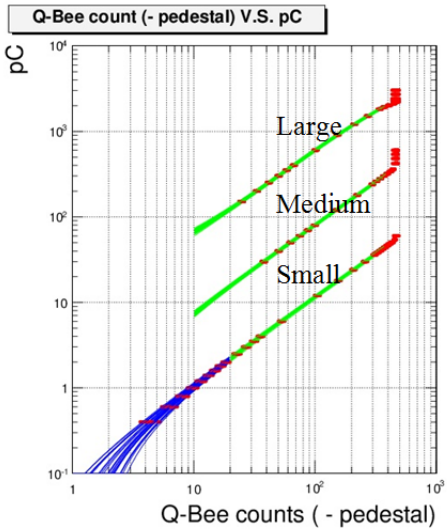

Figure 2.21: The result of QBEE board calibration for each three range using charge-time generator.

2.5.2 Data taking flow

The RENO data acquisition consists of data readout using front-end electronics, event builder, software triggers, data logger and run control. A schematic diagram of the RENO DAQ system is shown in Fig. 2.22 and Fig. 2.23.

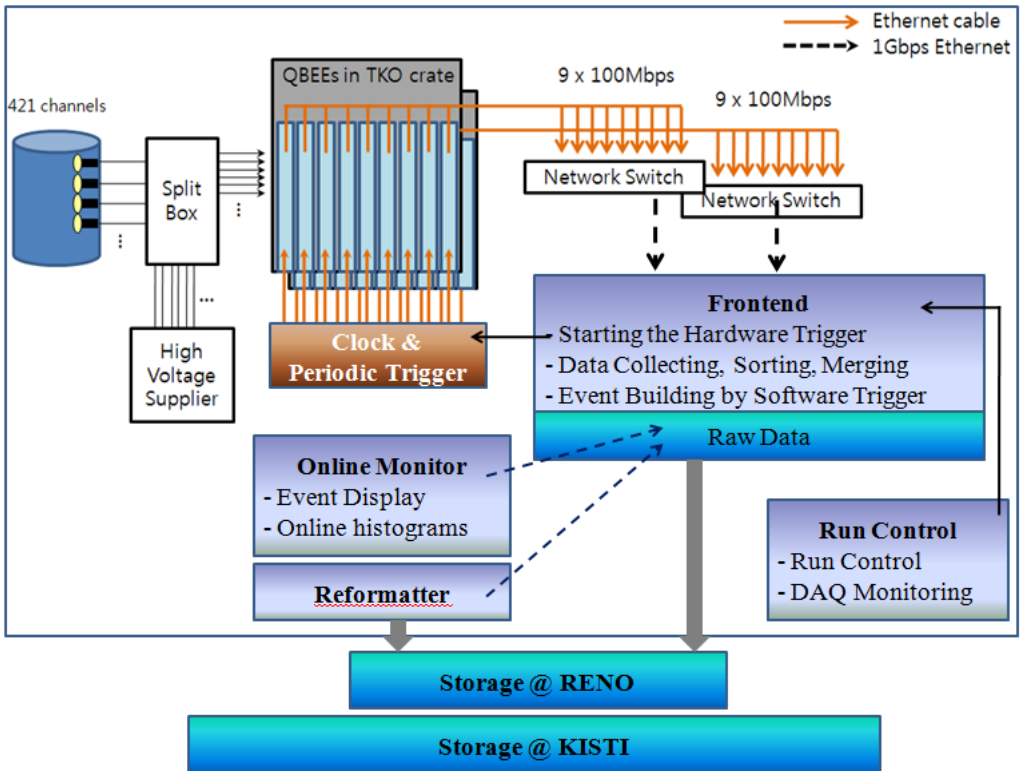

Figure 2.22: Diagram of DAQ system for RENO. There are 18 QBEE boards in two TKO crates collecting the hit signals from 421 PMTs (354 PMTs in inner detector and 67 PMTs in veto). The near and far detectors have the same DAQ architecture.

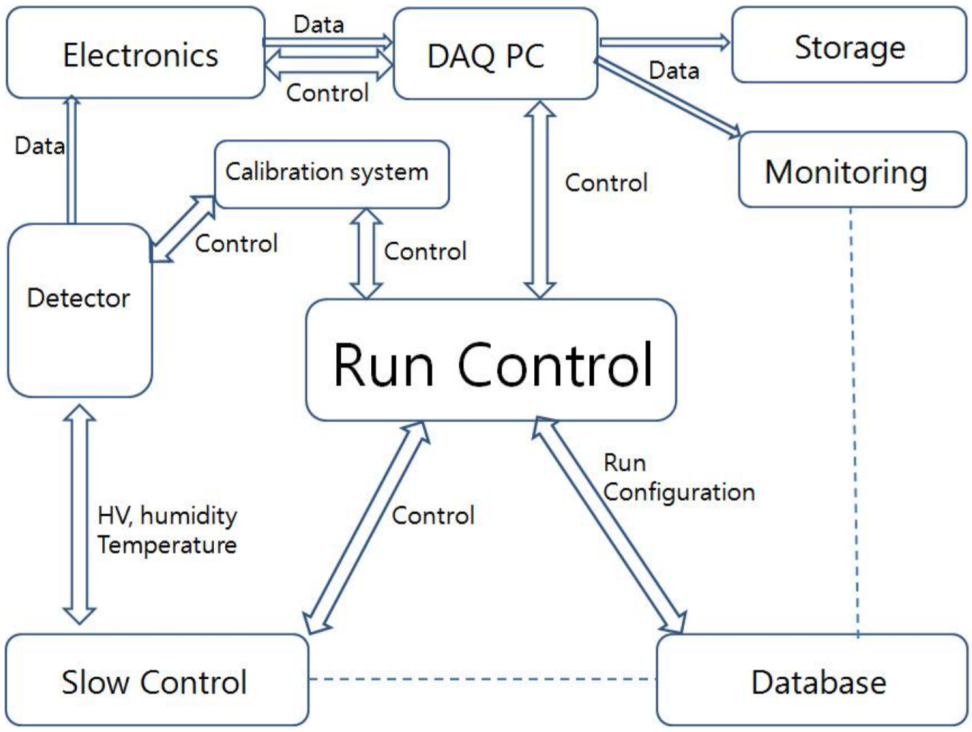

Figure 2.23: Flow diagram of run control for RENO. The run control sends commands to DAQ component and makes run conditions.

Data Readout and Run Control

The front-end electronics for data readout are based on QBEE boards in the TKO crate and ethernet cards on QBEE. A QBEE board receives 24 analog PMT inputs, digitizes them, and sends the signal outputs to the online computer through an 100 Mbps ethernet card. RENO uses 18 QBEE boards for 421 channels per detector, and data throughput rate is about 1.8 Gbps per detector. The near and far detectors have the same DAQ architecture.

The run control sends command to DAQ components and makes run conditions, as shown in Fig. 2.24. Shift crew will use an integrated GUI, which can be used to select run mode, trigger type, and detector parameter.

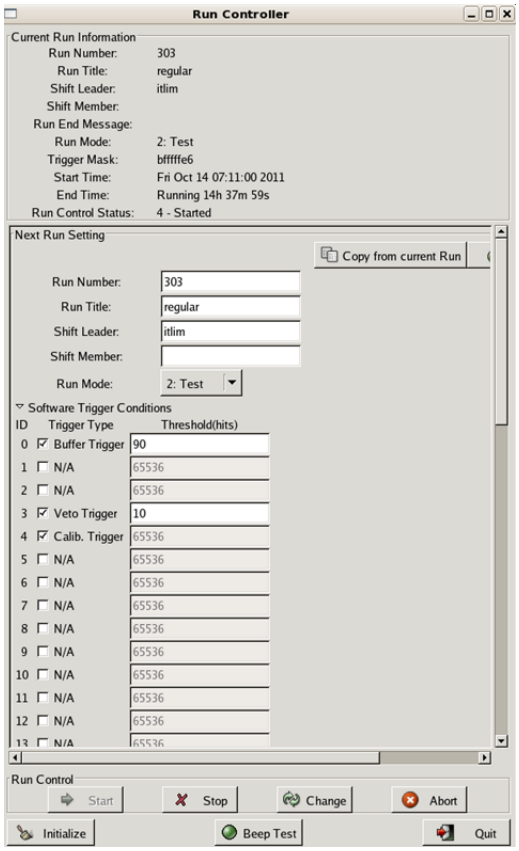

Figure 2.24: Display of run control panel. We can choose run mode and data taking condition.

Event Builder

All the QBEE boards are driven by a common 60 MHz master clock (MCLK). A 60 kHz periodical trigger and a serialized 32-bit event number are generated by a trigger module, and fanned out via a distributor to all the QBEE boards through network cables. All the hit data are sorted and merged according to the trigger event number and the timing information.

A periodic trigger of 60 kHz makes a data block of hits. The order of the data blocks is made according to the event number. The hits in a data block are sorted by their hit time and merged. The hit data in the same block are merged, sorted by hit time, and stored with an event number. An event builder constructs events by applying software trigger to the merged hit data.

Software Trigger

The software triggers are applied to the events constructed by the merger for identifying neutrino candidate events, cosmic muon events, or calibration events. The software trigger calculates the total number of hits (multiplicity) within 50 ns time window and constructs event if the hit sum exceeds a certain threshold number; 90 hits for ID trigger and 10 hits for OD trigger. The moment of satisfaction trigger condistion is set to T_0, and time windows before and after T_0 determine an event gate by software triggers. All of PMT hits within this event gate makes an event and calculate charge sum in time gate (-100 ns $-$ 50 ns).

2.5.3 Monitoring System

An online monitoring computer located in the control room reads data from the DAQ host computer via network. It provides event display, online history histograms to monitor detector performance, and variety of additional tasks needed to e silently monitor detector performance parameters and diagnose troubles of detector and DAQ system. The slow control monitors the status of the HV systems, the temperatures of the electronics crates and detectors, the fluids levels, and humidity. And the slow control is able to set up high voltage for each channel and turn on and off HV remotely. The slow control scheme is shown in Fig. 2.25. The data collected by the slow control system are sent to online monitoring system and database.

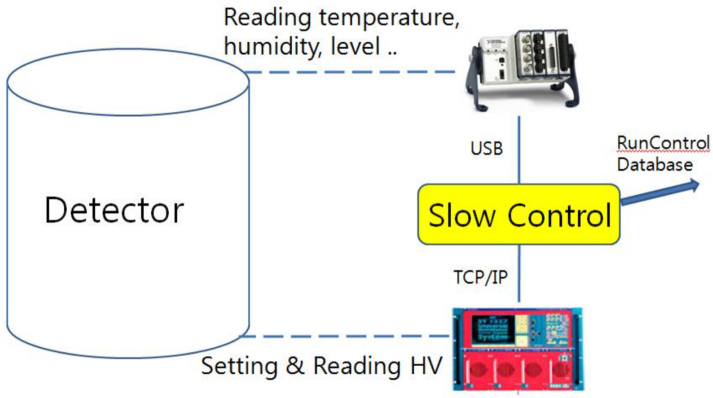

Figure 2.25: Diagram of slow control. The slow control system monitors detector conditions and controls PMT HV power supplies.

Event display and online histograms

Online monitoring system immediately shows the obtained trigger. Event display gives us the condition of a individual trigger. Event display shows the charge and hit time information of trigger for a individual PMT. Figure 2.26 shows event display. Center of the circle indicates hit PMT, size of the circle is proportional to charge of the hit, and color corresponds hit time.

The accumulated condition of the DAQ system is displayed online histograms; ID and OD hit PMT channel, number of hit of trigger, and trigger histograms. Shift crew can recognize any problem in the DAQ system from this online histograms. Figure 2.27 shows the online histogram panel.

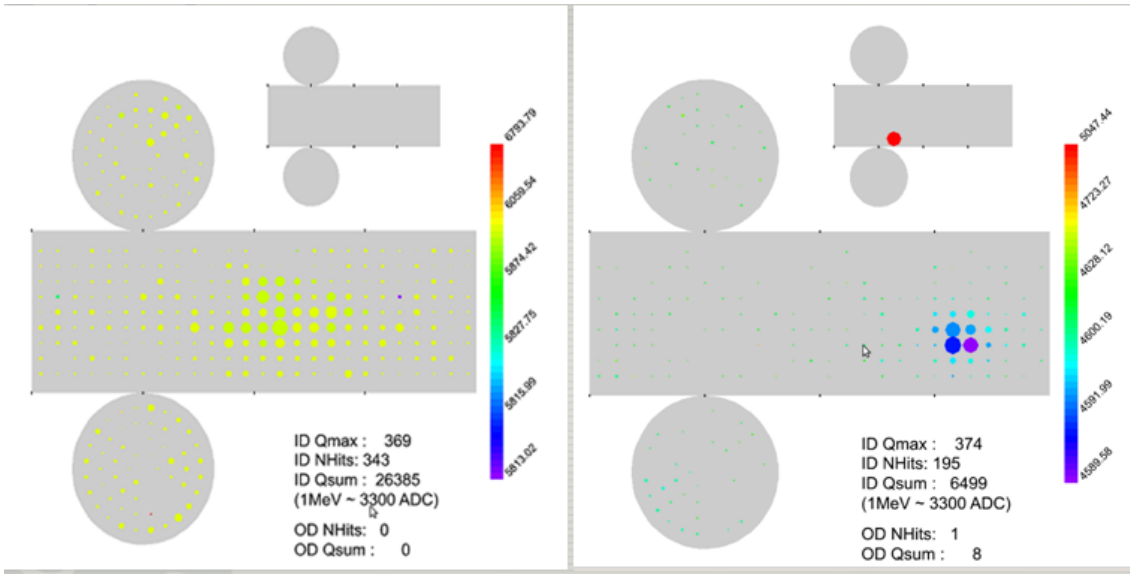

Figure 2.26: RENO event display. Center of the circle indicates hit PMT, size of the circle is proportional to charge of the hit, and color corresponds hit time

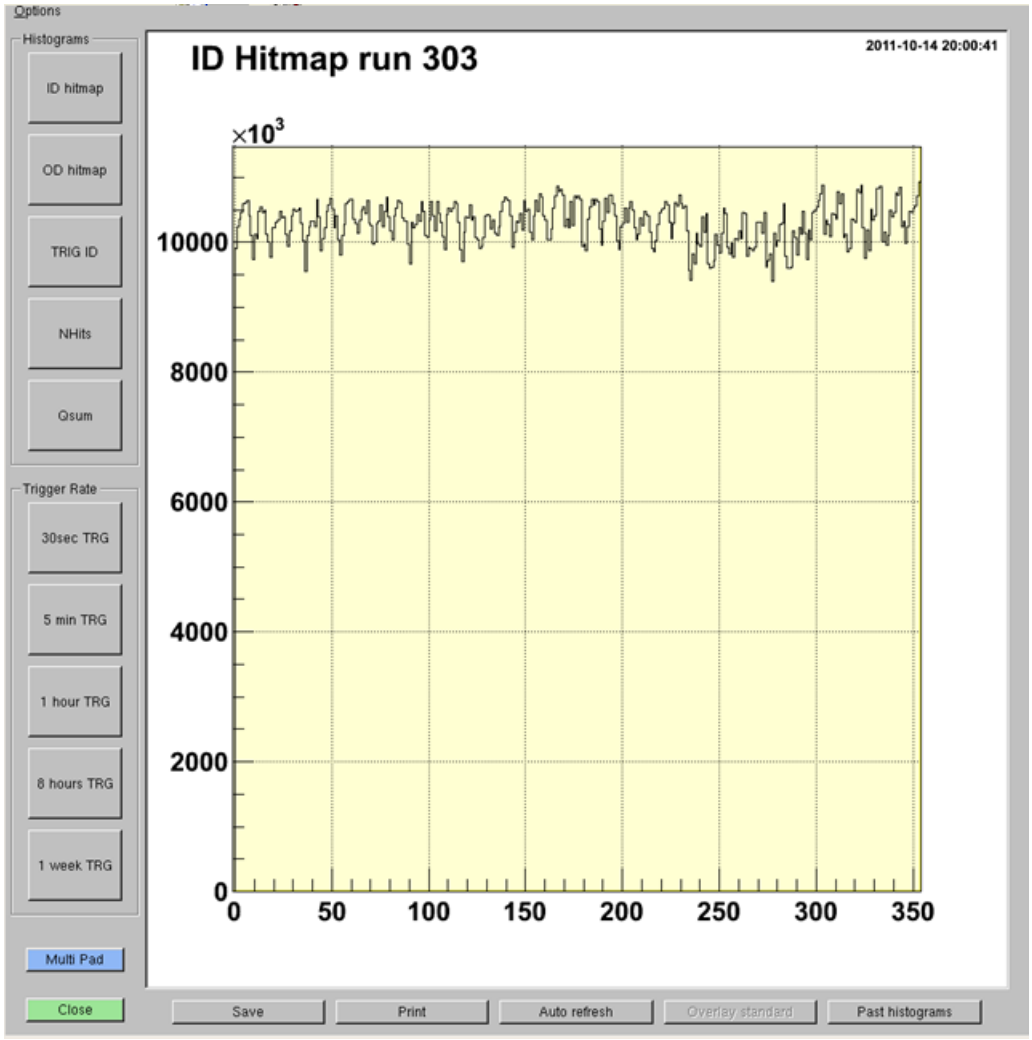

Figure 2.27: Online histogram panel.

High Voltage Monitoring

PMT need to supply high voltage (∼1700 V). Nine 48-channel power supply module (A932AP) in two crates (SY1527), purchased by CAEN are used at each two detector. The supplied high voltage value should be stable and be checked by shift crew. In this needs, the high voltage monitoring system is developed using Labview as shown in Fig. 2.28. The status of each high voltage channel is displayed by colors.

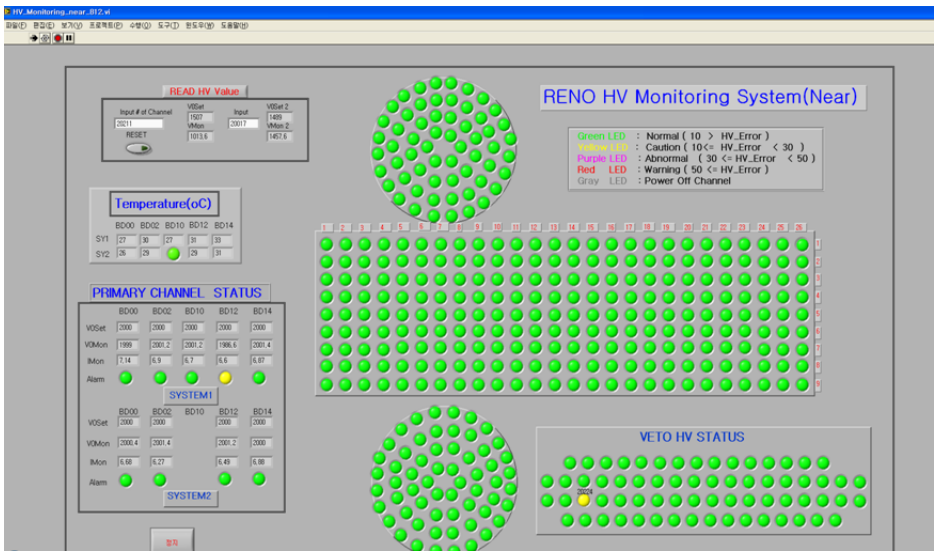

Figure 2.28: RENO high voltage monitoring system.

Slow Monitoring

Experimental environments such as temperature and humidity should be stable during the data taking. To prevent damage of the electronics from the humidity and temperature, a air conditioner and a dehumidifier are installed in the experimental hall, electronics hut and control room. To check the temperature, three thermocouple inside the detector, two thermocouple in the electronics hut and control room are installed. The humidity is also watched with sensor. And for safety reason, O_2, CO_2, and Radon sensor are installed.

Veto is filled with pure water for a Cherenkov radiation. The water needs to be purified to prevent the the deteriorate of quality. So the level of filled water is also monitored with sensor. If the water level is the high setting threshold, water circulation and purify system pump out water in the veto region automatically and re-filled with purified water.

Shift crew can check all these environmental statuses by the slow monitoring system, as shown in Fig. 2.29.

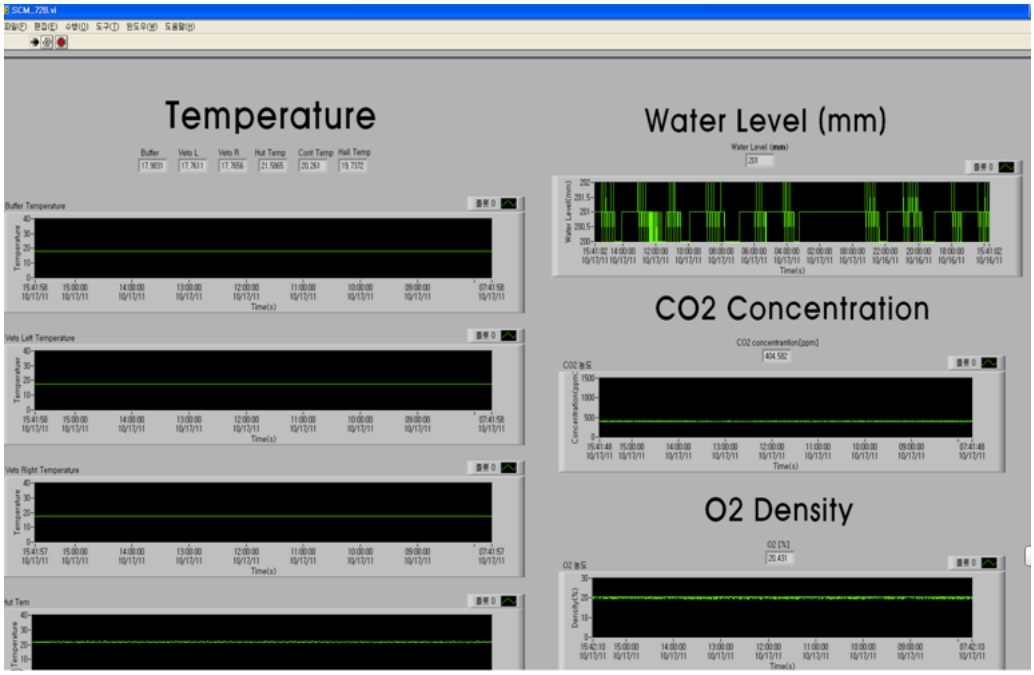

Figure 2.29: RENO slow monitoring system. The temperature, humidity, O_2, CO_2, and Water level in the OD are monitored.

Chapter 3

Expected Flux and Spectrum of Reactor Neutrino

3.1 Reactor Neutrino Production

Reactor neutrinos emitted through the decays of fission products of fissile isotopes in the reactor core (Figure 3.1). The fissile material in the reactors mainly consists of ^{235}U, ^{238}U, ^{239}Pu, and ^{241}Pu, which undergoes thermal neutron fission. and other fissile isotopes contribute only at the 0.1% level.

The dominant ^{238}U is fissile only for fast neutrons but also undergoes fission process by thermal neutron capture and produces ^{239}Pu,

$$n +^{238}\mathrm{U} \rightarrow^{239}\mathrm{U} \rightarrow^{239}\mathrm{Np} \rightarrow^{239}\mathrm{Pu}. \tag{3.1}$$

Similarly, ^{241}Pu is generated from ^{239}Pu,

$$n +^{239}\mathrm{Pu} \rightarrow^{240}\mathrm{Pu} \rightarrow^{241}\mathrm{Pu}. \tag{3.2}$$

The electron antineutrino is emitted from these β decay of isotopes.

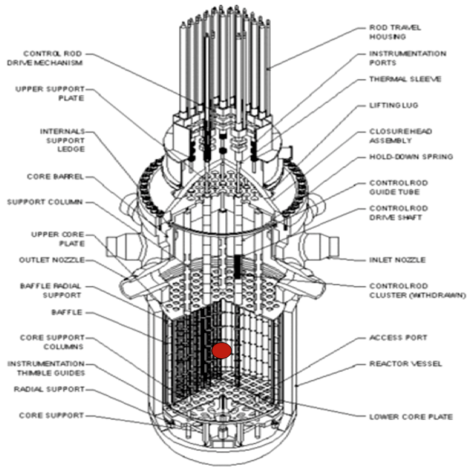

Figure 3.1: A pressurize water reactor core. Red dot is the center of reactor fuel.

The fission rates of the fissile isotopes are shown in Figure 3.2. These four isotopes release similar energy, as shown in Table 3.1, when they undergo fission [34].Therefore, even though the make up of the fissile material in the reactor changes over a refuelling cycle, the average mean energy per fission does not changes significantly.

These four components of reactor fuel β-decay at various energy and the neutrino spectra from these isotopes are difference from each other as shown Figure 3.3. The neutrino energy spectra from fission processes are parameterize in Refs. [60, 61] using

$$\phi_\nu^{(j)} = exp\left(\sum_{i=0}^{5} a_i^{(j)} E_\nu^i\right) \tag{3.3}$$

where $a_i^{(j)}$ are the fit parameters for the jth isotope and E_ν is a neutrino energy in MeV. The results are shown in Table 3.2 and Figure 3.3.

The fission rate in a reactor with a power P_{th} is

$$n_f = \frac{P_{th}}{\sum_i f_i \bar{E}_{fi}}, \tag{3.4}$$

where f_i and $\bar{E}_{fi}$ are the fission fraction in the nuclear fuel and the mean energy released per fission of isotope i, respectively. The number of fission per second is related to the reactor power by

$$n_f = \left(6.24 \times 10^{18}\right) \cdot \frac{P_{th}}{\sum_i f_i \bar{E}_{fi}} \tag{3.5}$$

where the reactor power P_{th} is given in Watts and E_{fi} in eV (6.24×10^{18} is J to eV conversion factor). The number of neutrinos from the fission process from the ith isotope is

$$N_{\nu}^{(i)} = N_{fi} \cdot \int_{E_{min}}^{E_{max}} \phi_{\nu}^{(i)} dE_{\nu} \tag{3.6}$$

Where, N_{fi} is the number of fission of the ith isotope. And the neutrino flux is isotropic about the source.

$$\Phi_{\nu}|_{r} = \frac{1}{4\pi r^2} \sum_{i} N_{fi} \phi_{\nu}^{(i)} \tag{3.7}$$

Assuming ~ 200 MeV per fission, there are 3.1×10^{19} fission per GW_{th}. Since six neutrino are emitted one fission above ~ 2 MeV on average [35, 36, 37, 37] , the neutrino intensity can be estimated to be $\sim 2 \times 10^{20}$ $/(\mathrm{GW}_{th} \cdot \mathrm{s})$.

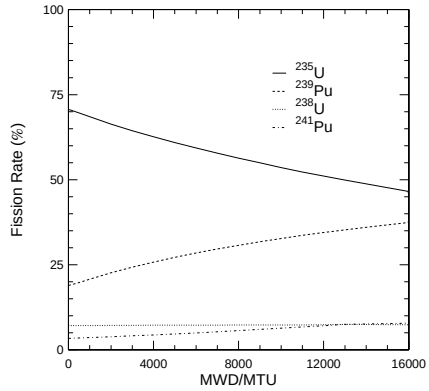

Figure 3.2: Evolution of fissile rate of four main isotopes according to burn up.

Isotope	Mean Energy Per Fission (MeV)
^{235}U	201.7 ± 0.6
^{238}U	205.0 ± 0.9
^{239}Pu	210.0 ± 0.9
^{241}Pu	212.4 ± 1.0

Table 3.1: Mean energy released per fission [34]

Parameter	^{235}U	^{238}U	^{239}Pu	^{241}Pu
a_0	4.367	4.757	4.833×10^{-1}	2.990
a_1	-4.577	-5.392	1.927×10^{-1}	-2.882
a_2	2.100	2.563	-1.283×10^{-1}	1.278
a_3	-5.294×10^{-1}	-6.596×10^{-1}	-6.762×10^{-3}	-3.343×10^{-1}
a_4	6.186×10^{-2}	7.820×10^{-2}	2.233×10^{-3}	3.905×10^{-2}
a_5	-2.777×10^{-3}	-3.536×10^{-3}	-1.536×10^{-4}	-1.754×10^{-3}

Table 3.2: Parameters of the polynomial of order of 5 for the neutrino flux from dominant isotopes in nuclear fuel. Parameters for isotopes ^{235}U, ^{239}Pu, and ^{241}Pu are from Ref. [61]and ^{238}U from Ref. [60]. The resulting distributions are shown in Figure 3.3

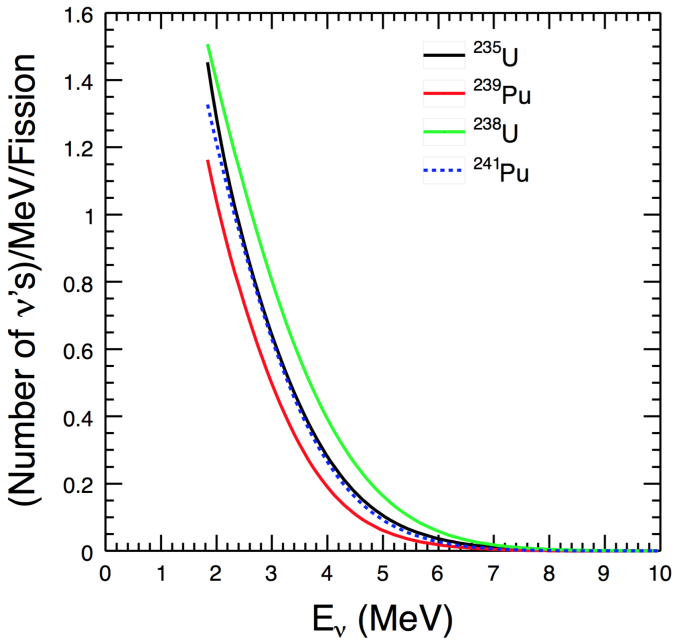

Figure 3.3: The Neutrino spectra from fisson of four isotopes

3.2 Calculation of the Flux and the Spectrum

3.2.1 Calculation of Expected Antineutrino Flux

The equation to calculate the number of antineutrinos observed in the detector d is like following [62]

$$N_\nu^d = \frac{N_p}{4\pi R^2} \frac{\sum_i \alpha_i \bar{\sigma}_i}{\sum_i \alpha_i E_i} P_{th} = \frac{N_p}{4\pi R^2} \frac{\bar{\sigma}_5 \left[1 + \sum_i \alpha_i \left(\bar{\sigma}_i/\bar{\sigma}_5 - 1\right)\right]}{E_5 \left[1 + \sum_i \alpha_i \left(E_i/E_5 - 1\right)\right]} P_{th} \tag{3.8}$$

where,

- N_p : the number of target proton.
- R : the distance between the detector and the reactor.
- α_i : fission fraction of the ith isotopes. (^{235}U, ^{238}U, ^{239}Pu, ^{241}Pu))
- $\bar{\sigma}_i = \int \sigma\left(E_\nu\right) \phi_\nu^{(i)} dE$: The cross section of ith isotope averaged over the antineutrino spectrum per fission.
- $\bar{\sigma}_5$: $\bar{\sigma}$ for the ^{235}U.
- E_i : energy released per fission for the ith isotope.
- E_5 : energy released per fission for the ^{235}U.
- P_{th} : reactor thermal power generated.

Above expression is represented the another form

$$N_\nu^d = \gamma \left(1 + k\right) P_{th} \tag{3.9}$$

where, $\gamma = \frac{N_p \bar{\sigma}_5}{4\pi R^2 E_5}$ is a constant for a given detector and geometry; $1 + k = \left[1 + \sum \alpha_i \left(\bar{\sigma}_i/\sigma_5 - 1\right)\right] / \left[1 + \sum \alpha_i \left(E_i/E_5 - 1\right)\right]$. $1 + k$ is time-dependent as the fission fraction of the 4 isotopes evolve as time.

Number of Target Proton N_p

Target free proton number is decided by the amount of LAB(Linear Alkyl Benzene) in the target detector. The molecular structure of LAB is $C_nH_{2n+1} - C_6H_6$ with n = 10 $\sim$ 13. The composition of each structure is different from manufacturer. The free proton number of RENO LAB molecule is 30 and the molecular weight is 240.7 from the composition analysis sheet provided by the manufacturer. The density of LAB is 0.85 g/L measured by densitometer with 0.001 resolution. Target volume is slightly different between near and far detector. The measured

target volume is 18641 ± 5 L at the near detector and 18637 ± 5 L at the far detector. So that the number of free proton is calculated by following equation,

$$N_p = \rho N_A V \frac{30}{M_A} \tag{3.10}$$

where ρ is the density of LAB, N_A is Avogadro's number, V is the measured volume of target detector, M_A is the molecular weight of LAB and 30 is free proton number of LAB molecule. The calculated number of target proton is 1.189×10^{30} both near and far detector. the correlated uncertainty is 0.5 % and the uncorrelated uncertainty is 0.1 %. These uncertainty is explained later.

The Distance of The Detector and The Reactor R

The neutrino flux is isotropic about the source. So that the flux diminish at a rate inverse square of the distance. The distance between the detector and the reactor is from the detector target center and the center of the reactor fuel array. The Coordinate of reactor core center and detector target center is determined by survey from the national cadastral control points near the power plant and blue print of the reactor and detector. The uncertainties of the baselines are order of cm. Their uncertainties are negligible. because the distance of reactor and detector is order of km.

	Near	Far
R1	660.06	1563.77
R2	444.73	1460.83
R3	301.56	1397.81
R4	339.26	1380.06
R5	519.97	1409.39
R6	746.16	1483.00

Table 3.3: The distance between each detector and each reactor in meters.

Fission Fraction of Isotopes α

As described in section 2.1, the fission fraction of the 4 isotopes evolve as time and it cause $1+k$ changes in time. The isotope fraction also changes the expected reactor neutrino energy spectrum. The average fission fractions of each reactor are summarized in the below table.

Reactor	U235	U238	Pu239	Pu241
1	0.579	0.075	0.293	0.052
2	0.575	0.076	0.296	0.053
3	0.552	0.072	0.314	0.061
4	0.583	0.072	0.292	0.053
5	0.575	0.073	0.297	0.056
6	0.565	0.073	0.304	0.059

Table 3.4: The average fission fraction of 4 isotopes for far detector

Reactor	U235	U238	Pu239	Pu241
1	0.584	0.075	0.290	0.051
2	0.572	0.076	0.299	0.054
3	0.548	0.072	0.318	0.062
4	0.585	0.072	0.290	0.053
5	0.577	0.073	0.295	0.055
6	0.561	0.073	0.307	0.060

Table 3.5: The average fission fraction of 4 isotopes for near detector

The Cross Section Averaged over The Antineutrino Spectrum Per Fission $\bar{\sigma}$

The cross section averaged over the antineutrino spectrum is the convolving the IBD cross-section with the antineutrino energy spectrum. It is the expected energy spectrum of antineutrinos per fission from the each isotopes, as shown Figure 1.6.

Energy Released Per Fission E

The mean energy emitted per fission has been calculated in Ref. [34]. and is summarized in Table 3.1.

Reactor Thermal Power Generated P_{th}

The maximum thermal power is 2.900 GW_{th} for the reactor $1 \sim 2$ and 2.815 GW_{th} for the reactor $3 \sim 6$. However, the thermal output of the reactors are not constant for time. The daily mean thermal output for the 6 reactors are provided by KHNP. Then the thermal power can be calculated by considering the thermal output like maximum $P_{th}\times$ thermal output(%).

Reactor	Near	Far
1	88.82	88.46
2	88.30	87.58
3	97.42	99.83
4	89.29	88.79
5	89.21	91.82
6	98.31	98.33

Table 3.6: The average thermal power

Flux Variation Coming from Fuel Burning $1 + k$

$1 + k$ is time-dependent as the fission fraction of the 4 isotopes evolve as fuel burning. Since we are provided with the values of the fission fraction and cycle burnup, which are determined by reactor core simulation of ANC with about 1 month interval from KHNP (Korea Hydro & Nuclear Power Co), the daily $1 + k$ can be predicted by fitting. Figure 3.4 shows the fitting of $1 + k$ for reactor 1 and cycle 20, for example. The elapsed time (x-axis in Figure 3.4) is calculated dividing cycle burnup by mean daily burnup.

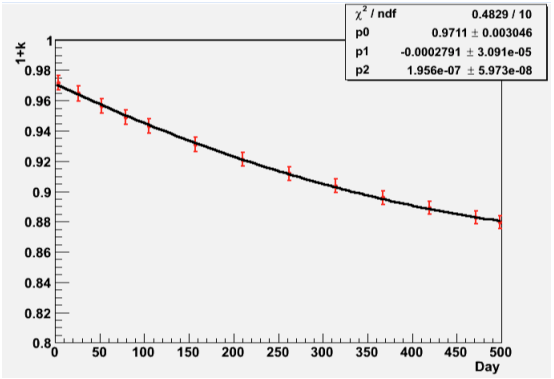

Figure 3.4: Fitting of $1 + k$ factor for reactor 1, cycle 20

Expected Number of Antineutrino Flux N_ν^d

By calculation Equation 3.9 with the quantities obtained above, the expected number of antineutrino event detected at the detector is constructed. The results of the expected flux is summarized Table 3.7.

Reactor	Far	Near
1	7854.65	41165.41
2	8957.33	90241.63
3	8652.48	170306.79
4	9907.65	155050.13
5	8359.33	56501.16
6	8251.18	30063.38

Table 3.7: Expected flux for far and near detector. Visible energy range is 1.0∼ 8 MeV

3.2.2 Expected Interaction Antineutrino Spectrum

The expected interaction antineutrino spectrum in each detector d, can calculated using the following equation,

$$S_\nu^d = N_\nu^d \left(\sum_i I_i s_\nu^i \right) \tag{3.11}$$

where,$N_\nu^d \left(= \sum_i N_{\nu,i}^d \right)$ is the expected number of antineutrino obtained above (where $N_{\nu,i}^d$ is the expected number of antineutrino of ith isotope at the detector d), $I_i \left(= \frac{N_{\nu,i}^d}{\sum_i N_{\nu,i}^d} \right)$ is the fraction of neutrino interaction at the target by neutrino produced by the isotope species i. The average interaction fractions of each reactor are summarized in the Table 3.8 and 3.9. And $s_\nu^i \left(= \sigma\left(E_\nu\right) \phi_\nu^{(i)} / \int \sigma\left(E_\nu\right) \phi_\nu^{(i)} dE_\nu \right)$ is the normalized interaction spectrum by the ith isotope, as shown left side plot of Figure 3.5. From the Equation 3.11, the expected interaction antineutrino spectra are shown middle and right side plot of Figure 3.5 and Figure 3.6.

Reactor	U235	U238	Pu239	Pu241
1	0.624	0.123	0.204	0.050
2	0.613	0.124	0.210	0.053
3	0.593	0.120	0.225	0.061
4	0.627	0.118	0.204	0.051
5	0.619	0.119	0.208	0.054
6	0.605	0.120	0.217	0.059

Table 3.8: The average interaction fraction of 4 isotopes for near detector

Reactor	U235	U238	Pu239	Pu241
1	0.619	0.123	0.206	0.051
2	0.616	0.124	0.209	0.052
3	0.597	0.119	0.223	0.060
4	0.625	0.118	0.205	0.052
5	0.617	0.119	0.210	0.054
6	0.608	0.119	0.215	0.058

Table 3.9: The average interaction fraction of 4 isotopes for far detector

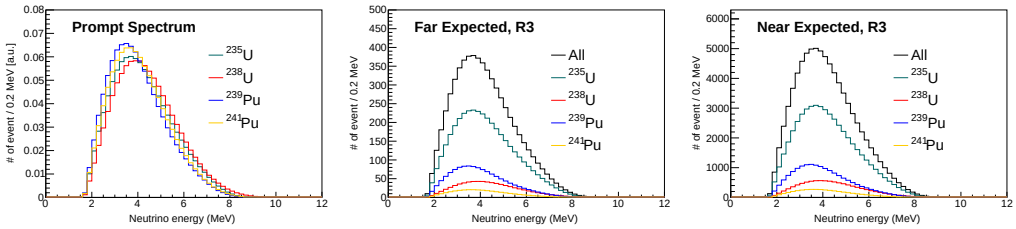

Figure 3.5: Expected interaction spectrum of neutrino. Left side is the normalized interaction spectrum for each isotope. Middle one is the expected interaction spectrum of reactor 3 for the far detector and right side is for the near detector.

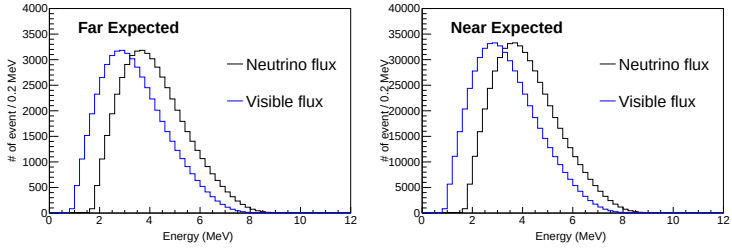

Figure 3.6: Expected neutrino and visible energy spectrum. The left plot shows the far detector, and the right plot shows the near detector. The black line shows the expected interaction spectrum of neutrino at the detector. Blue line shows the expected visible spectrum of neutrino at the detector.

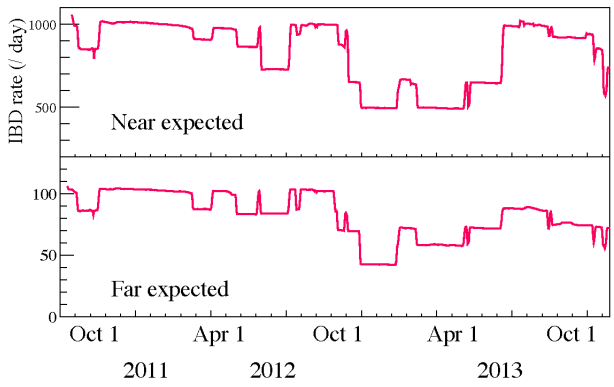

Figure 3.7: Daily expected neutrino flux

3.3 Systematic Uncertainties of Expected Flux and Spectrum

The systematic uncertainties consist of two kinds: correlated and uncorrelated. The correlated systematic uncertainties are same direction and same amount in the data of both detector. By using two identical detectors, These correlated systematic uncertainties could be canceled out. And the uncorrelated systematic uncertainties are independent of each other. These uncorrelated systematic uncertainties could not be canceled out. These two kind of uncertainties are summarized below.

Parameter	Uncorrelated	Correlated
Baseline	0.03%	-
Thermal Power	0.5%	-
Fission fraction	0.7%	-
Fission reaction cross section	-	1.9%
Reference energy spectra	-	0.5%
Energy per fission	-	0.2%
Combined	0.9%	2.0%

Table 3.10: Systematic uncertainties of Expected Flux

The combined uncorrelated uncertainty is 0.9 %

Baseline

The distance from the detector center to reactor fuel center has been precisely measured with below 10cm uncertainty. The shortest baseline which is between the reactor 3 and the near detector is 301.56 m. Therefore, the maximum systematic uncertainty is $0.1/301.56 \rightarrow 0.03\%$. It is too smaller than others and could be negligible.

Thermal Power

The thermal power of reactor is measured indirect way that is calculation with the total power supplied at the secondary side of steam generators. And Uncertainties of thermal power output is usually less than 0.5% per core and fully correlated among the reactor, from the reference [63]. We attached 0.5 % for the uncorrelated uncertainty of thermal power.

Fission Fraction

The uncertainties of fission fraction is summarized Table 3.11 and shown Figure 3.8. These uncertainties are result from using the Westinghouse ANC reactor simulation code [64]. To understand the antineutrino flux varying due to uncertainty of fission fraction, A pseudo experiment was performed. 1,000 pseudo experiment data sets are generated. Each isotope's fission fraction is randomly shaken within it's error. And the sum of four isotope's fission fraction must be 100 % by definition. Therefore each pseudo experiment data sets are normalizing procedure. But normalizing process cause unwanted side effects that reduce RMS of generated fission fraction distribution. This problem is summarized Table 3.12. The neutrino flux calculated from pseudo data set vary 0.5 %. But normalization problem is not solved. So that we attached 0.7 % for the uncorrelated uncertainty of fission fraction instead of 0.5 %.

Isotope	Fractional uncertainty of fission fraction
^{235}U	3.3 %
^{238}U	6.5 %
^{239}Pu	4.0 %
^{241}Pu	11.0 %

Table 3.11: Fractional uncertainties of fission fraction

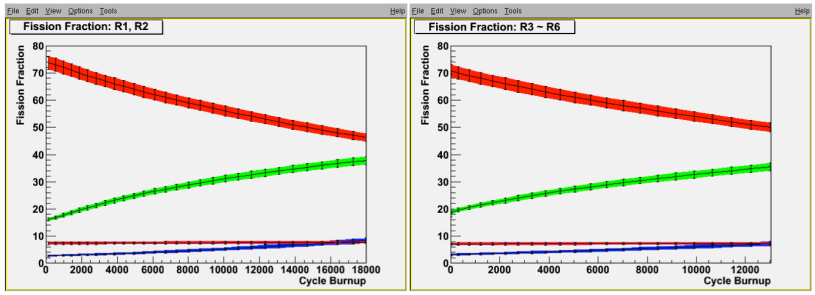

Figure 3.8: The fission fraction varying due to fuel burnup and its uncertainties. Reactor 1 $\sim$ 2 are different reactor type than Reactor 3 $\sim$ 6. The fission fraction varying is small difference between Reactor 1 $\sim$ 2 and Reactor 3 $\sim$ 6. The highest Red is ^{235}U. Green is ^{239}Pu. Blue is ^{241}Pu. And lower Red is ^{238}U.

Isotope	Pseudo Data before normalization [Mean $\pm$ RMS]	Pseudo Data after normalization [Mean $\pm$ RMS]
^{235}U	58.56 $\pm$ 1.97	58.56 $\pm$ 1.13
^{238}U	7.53 $\pm$ 0.48	7.53 $\pm$ 0.47
^{239}Pu	28.76 $\pm$ 1.16	28.76 $\pm$ 1.04
^{241}Pu	5.15 $\pm$ 0.56	5.15 $\pm$ 0.55

Table 3.12: Pseudo fission fraction data set

Fission Reaction Cross Section and Reference Energy Spectra

Associated anti-electron neutrino flux gives 1.9 % correlated uncertainty,calculated from the neutrino yield per fission and fission spectra.

Energy per fission

As shown Table 3.1, The thermal energy released per fission gives 0.2 % correlated uncertainty.

Chapter 4

Energy Calibration

RENO detector observe events (signal or background) collecting scintillation light via PMTs. Through the PMT lines, QBEE board takes this signal. and return the ADC values at each PMT channel. Calibration is the process that converting ADC values collecting from events to energy (MeV). First step is adjusting supplying high voltage value of PMT for the same gain values of each PMTs from one photo electron. this step make possible to convert pC to photo electron. Second step is converting photo electron to MeV from the several radioactive source data.

The energy response of the detector has varied with time. The detector need to be monitored for response. So that the calibration source run has been taking regularly. And delayed signal is used daily monitoring data and obtaining the daily charge correction factor.

4.1 Energy Calibration System

The detector can not take regular run data which is used for IBD analysis during time that radioactive source data is in the detector. The event rate of source data is too higher than event rate of the regular run data. So the detector need the source driving system. So that a 1D/3D source driving system were developed and is operated with custom computer software in the windows os.

The 1D system was setting up for the target region. The wire is moving along the z-axis exactly the center of target vessel, The 1D system consists of a stepping motor, pulley and polyethylene wire. At the end of wire, The encapsulated source container is connected. At the end of the container,a weight made by teflon is connected to countering buoyant force of liquid scintillator[]. The 1D system have an order of a few mm for the z-position accuracy that is much smaller than the vertex resolution(a few cm) of the detector. The design of 1D driving system is shown in Figure 4.1.

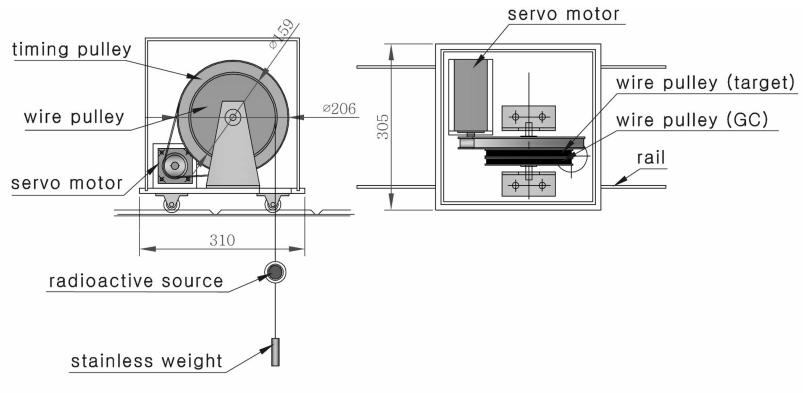

Figure 4.1: Design of 1D source driving system.

The 3D driving system can place the calibration source in the target region only. The system employs four rods to enable moving continuously the z direction of cylindrical coordinate. and uses a robot arm clinging to end of the rod to allow moving all ϕ direction and three ρ points of cylindrical coordinate as shown in Fig. 4.2. Figure 4.3 shows the 1D/3D calibration system installed at the detector.

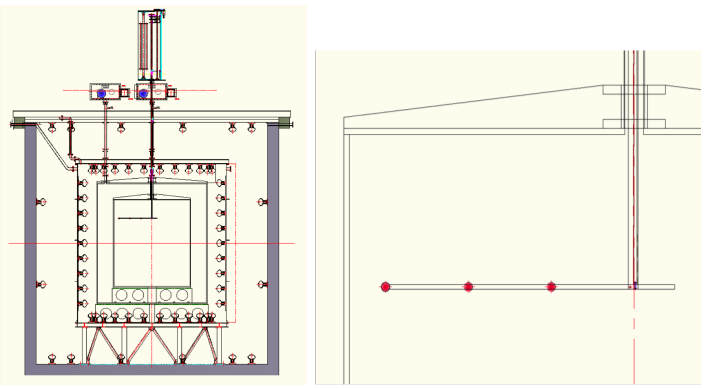

Figure 4.2: Design of 3D calibration system. The left plot shows cutaway view of 3D calibration system installing in the detector. The red dot in the right plots corresponds the position of the calibration source in the robot arm.

Figure 4.3: Installed 3D system. Two installed 1D system is also shown.

4.2 Energy Reconstruction

The threshold value of QBEE board is needed to separate noise and event. So, single photon electron responses are compared with different threshold value. Figure 4.4 shows the charge distributions of each threshold value. But the figure shows no noticeable difference between the distributions. So the highest value is chosen, -1.0 mV, to lower background.

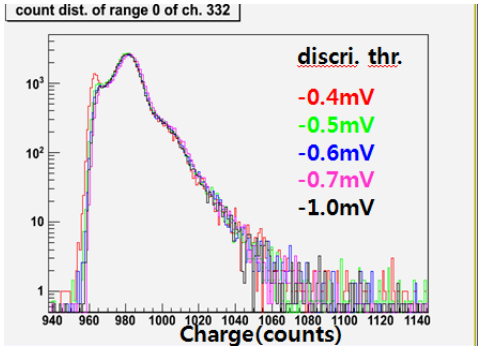

Figure 4.4: Charge distribution of single photo-electron. Different threshold shows almost similar shape.[]

The PMT gain value is set to 1.0×10^7. When one photo electron come in to PMT, the QBEE board get 1.6 pC from the PMT. For setting gain value, ^{137}Cs

radioactive source is taken in the detector center. Because The detector has 354 PMTs in buffer and ^{137}Cs source gives 120∼130 hits, so the events from the ^{137}Cs source is expected single photo-electron response at each PMTs.

To determine the proper high voltage value for the PMT gain, ^{137}Cs source data is taken with 4 different high voltage, 1400, 1500, 1600, and 1700 V. And then the results are fitted together with gain function

$$\text{PMT Gain} = A \cdot V^N \tag{4.1}$$

where, V is the voltage. A and N is fitting parameter. From the fitting result, the proper voltage that gives 1.0×10^7 gain is chosen. The left plot of Figure 4.5 shows the example of fitting result. After fit all the PMT channel, The proper high voltage value was set at each channel. And then ^{137}Cs source data was taken to check the gain setting. The right plot of Figure 4.5 shows the PMT gain distribution after gain matching. X axis is converted to PMT gain. It shows gain variation among PMTs are below 3% level[]. from the PMT gain matching and ^{137}Cs source data, pC to photo-electrons conversion factors are derived with the gain table at each channel.

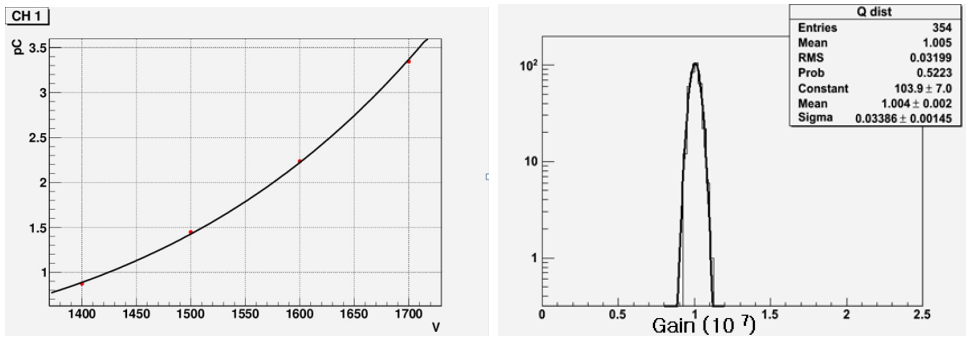

Figure 4.5: The left plot shows fitted curve with four data points. X axis of the left plot is the PMT high voltage value and the Y axis is the output value converted to pC. 1.6 pC is desirable gain value.[] The right plot shows result of PMT gain matching. The variation among PMTs below 3% at the near and far detector.

4.3 Radioactive sources

Four radioactive sources are used for the energy response monitoring. The characteristics of radioactive sources are summarized in Table 4.1. These sources are used regularly to check the energy response and resolution, as shown in Fig. 4.6. The ^{252}Cf source is important that it is neutron source. From the ^{252}Cf source,

we could check the neutron capture by Gadolinium in the target region. As time goes on, the p.e. response of detector is getting lower and lower. So that the PMT charge adjusting is needed as described Appendix A.

type	sources	energy (keV)	calibration
e^+	^{68}Ge	511(2)	position E threshold
γ	^{137}Cs	662	gamma
	^{60}Co	1173+1333	multiple gamma
neutron	^{252}Cf	neutron + ~10 MeV	neutron efficiency

Table 4.1: A list of radioactive sources for RENO detector calibration.

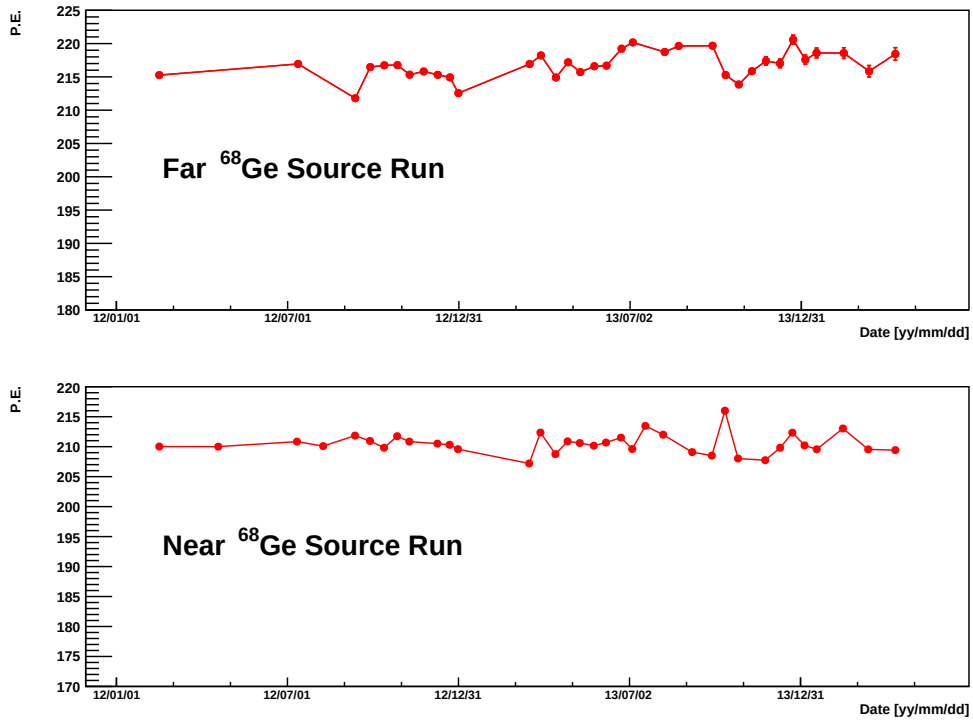

Figure 4.6: Regular ^{68}Ge source run results. The red dot is the peak value of the source run after charge correction.

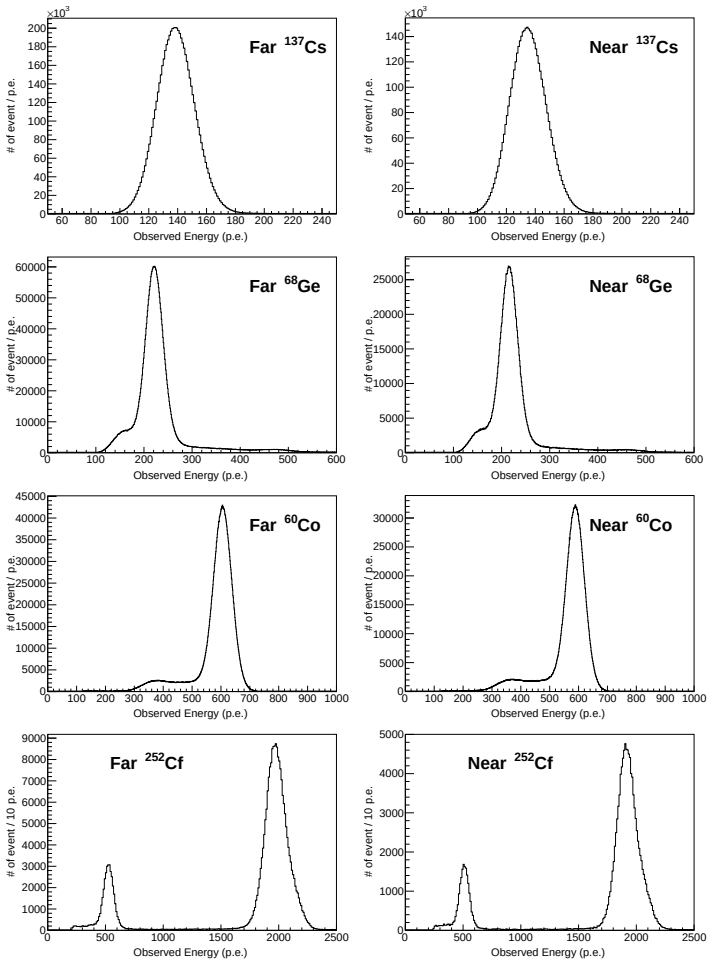

Figure 4.7: Spectra of source data at the far detector. Left side is far and right side is near.

4.4 Energy Conversion Function

In the previous section, the source data and IBD candidates are well controlled for the time variation. From the these corrected data, the p.e. values and corresponding MeV are known. So that p.e. to MeV conversion is possible from the these data. Figure 4.9 shows the relation between p.e. and MeV of the each point. The n-H point is selected from the ^{252}Cf source data. The n-C point is added to obtain energy conversion function which is from ^{210}Po^{9}Be source data as shown Figure 4.8. This n-C point was taken once on the April 2012. And the n-Gd point

is from delayed signal of IBD candidates. Each points are converted to uniformly distributed positron event which is prompt signal of the IBD candidates from the center distributed source data except n-Gd point as following equation.

$$\text{P.E./MeV} = \frac{\text{mean p.e. of source data} \cdot C_{center-to-Uniform} \cdot C_{\gamma-to-e^+}}{\text{MeV value of source data}} \quad (4.2)$$

where, mean p.e. of source data is from the charge corrected and additional corrected source data or charge corrected delayed of IBD candidates. $C_{center-to-Uniform}$ is the values at the November 2012 that is reference date, as shown Figure A.6 and summarized Table 4.2. and $C_{\gamma-to-e^+}$ is the correction factor for the conversion to positron to γ-ray from the source data. this correction factors are derived by comparing positron MC and source MC. The $C_{\gamma-to-e^+}$ are summarized in Table 4.3. Lastly, The results of Equation 4.2 are summarized Table 4.4.

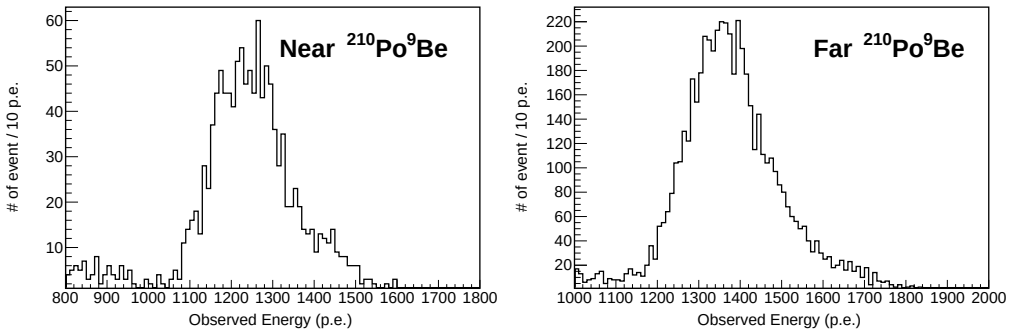

Figure 4.8: Photo-electron distribution of carbon captured event of ^{210}Po^{9}Be source data. Left side is near detector. And right side is far detector.

	far	near
Center-to-Uniform correction factor	1.0050 ± 0.0014	1.0060 ± 0.0006

Table 4.2: Center-to-Uniform correction factor at the November 2011.

γ-to-e^+ correction factor	far	near
^{137}Cs	0.9647 ± 0.0004	0.9643 ± 0.0004
^{58}Ge	1.0199 ± 0.0003	1.0190 ± 0.0003
n-H	0.9745 ± 0.0002	0.9743 ± 0.0002
^{60}Co	1.0223 ± 0.0002	1.0234 ± 0.0002
n-C	0.9896 ± 0.0001	0.9895 ± 0.0001
n-Gd	1.0257 ± 0.0002	1.0256 ± 0.0002

Table 4.3: γ-to-e^+ correction factor from MC.

p.e./MeV	far	near
^{137}Cs	209.49 ± 1.16	203.95 ± 1.07
^{58}Ge	217.66 ± 2.10	211.77 ± 1.75
n-H	237.73 ± 1.07	231.10 ± 1.04
^{60}Co	241.67 ± 1.45	234.95 ± 1.29
n-C	251.35 ± 2.85	244.06 ± 2.58
n-Gd	261.10 ± 0.11	254.63 ± 0.05

Table 4.4: p.e./MeV values of each calibration source data

The LS and Gd-LS have quenching effect. So that energy response of the detector is not linear. The energy conversion function model have to take into account quenching effect. The energy conversion function model are chosen empirically such as following equation.

$$\text{Function of P.E. / MeV (MeV)} = P_0 - \frac{P_1}{1 - \exp(-P_2 \cdot \text{MeV} - P_3)} \tag{4.3}$$

where, P_0, P_1, P_2 and P_3 are fitting parameters. The fitting results are shown in Figure 4.9 and Table 4.5.

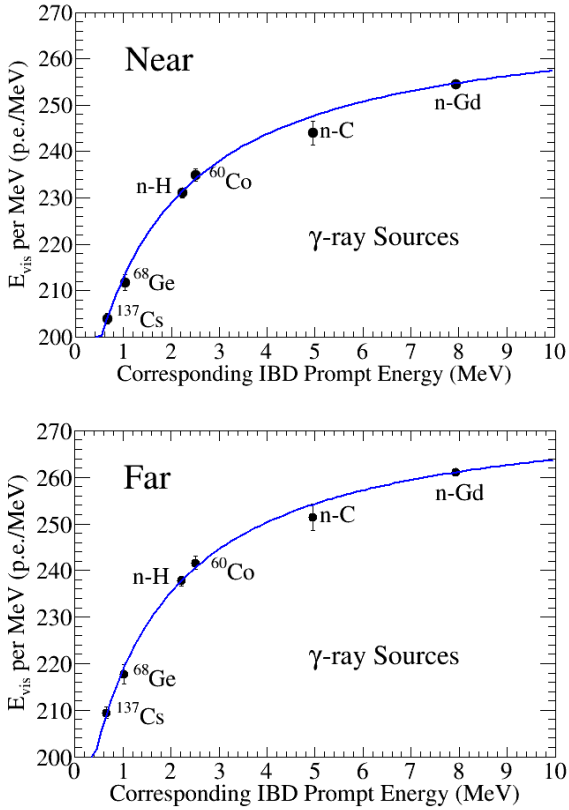

Figure 4.9: Energy conversion function. The top plot shows the near detector. And bottom plot shows the far detector. The point of n-H is from ^{252}Cf source data. The point of n-C is from ^{210}Po^{9}Be source data. and The point of n-Gd is from the delayed of IBD candidates.

Parameter	far	near
P_0	275.9 ± 1.0	270.1 ± 1.3
P_1	0.0170 ± 0.0015	0.0170 ± 0.0025
P_2	0.000123 ± 0.000012	0.000116 ± 0.000012
P_3	0.000174 ± 0.000018	0.000179 ± 0.000030

Table 4.5: The fitting results of energy conversion function

To check energy conversion function, the far and near spectra of the ^{12}B and

^{12}N events are compared as shown Figure 4.10. From the this plot, The energy conversion function seems does not have a problem.

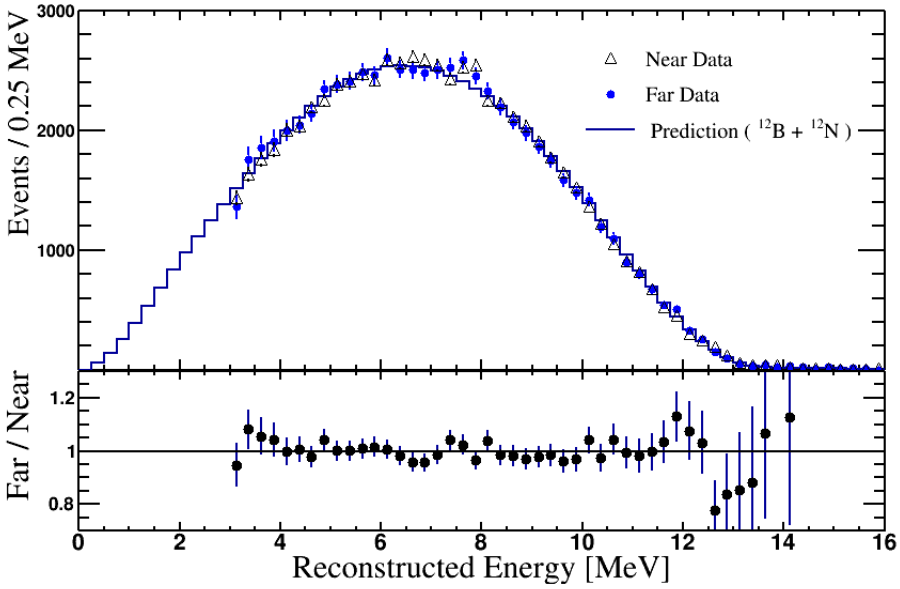

Figure 4.10: Spectra of the ^{12}B and ^{12}N events. Upper plot is comparing between far, near and prediction. The prediction is MC. bottom plot is far to near ratio of the spectra. It shows well behaved.

4.5 Energy Resolution

The energy resolution is obtained from the fit of ^{68}Ge, ^{60}Co, n-Gd data. The fitting model is defined as following equation.

$$\text{Resolution(E)} = \sqrt{\frac{P_0}{E} + P_1} \tag{4.4}$$

where, E is the visible energy, P_0 and P_1 are the fitting parameter. The fitting results are summarized Table 4.6 and Figure 4.11.

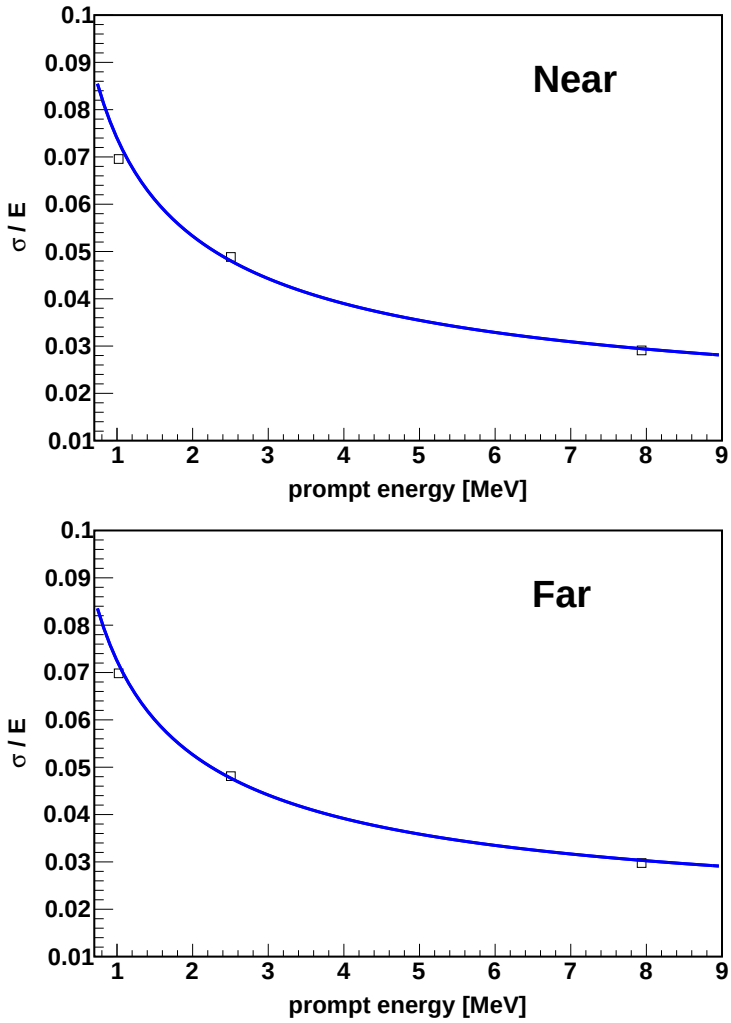

Figure 4.11: Energy resolution of far and near detector. The top plot shows the near detector and the bottom plot shows far detector. Open square is data point for the ^{68}Ge, ^{60}Co, n-Gd. And Blue line is the fitting result curve.

Parameter	far	near
P_0	$4.956\times10^{-3} \pm 8.023\times10^{-6}$	$5.267\times10^{-3} \pm 1.013\times10^{-5}$
P_1	$2.951\times10^{-4} \pm 2.748\times10^{-6}$	$2.031\times10^{-4} \pm 2.656\times10^{-6}$

Table 4.6: The fitting results of energy energy resolution function

Chapter 5

Monte Carlo Simulation

Monte-carlo simulation is commonly utilized in the particle experiments and it provides the guidance to optimize various parameters of the detector. And it enables to check detector performance and to estimate some systematic uncertainties. Simulation of RENO detector is from modified GLG4SIM, GEANT4-based code for liquid scintillator detector. We can obtain the expected flux of the detector with oscillation from the MC. And the expected is used for obtaining θ_{13} and $|\delta m^2_{ee}|$.

5.1 Detector Simulation

The detector simulation is used as a data analysis tool. The RENO detector is designed to have four concentric cylindrical modules, two active inner modules called target and γ-catcher and two inert outer modules called buffer and veto as shown in Fig. 5.1. Compared to the past reactor neutrino experiments, an additional active layer, γ-catcher, is added to the detector design to surround the target to contain gamma rays escaping from target. There are 354 and 67 10-inch PMTs mounted on the buffer vessel wall and veto wall, respectively, pointing inward normal to the wall surfaces.

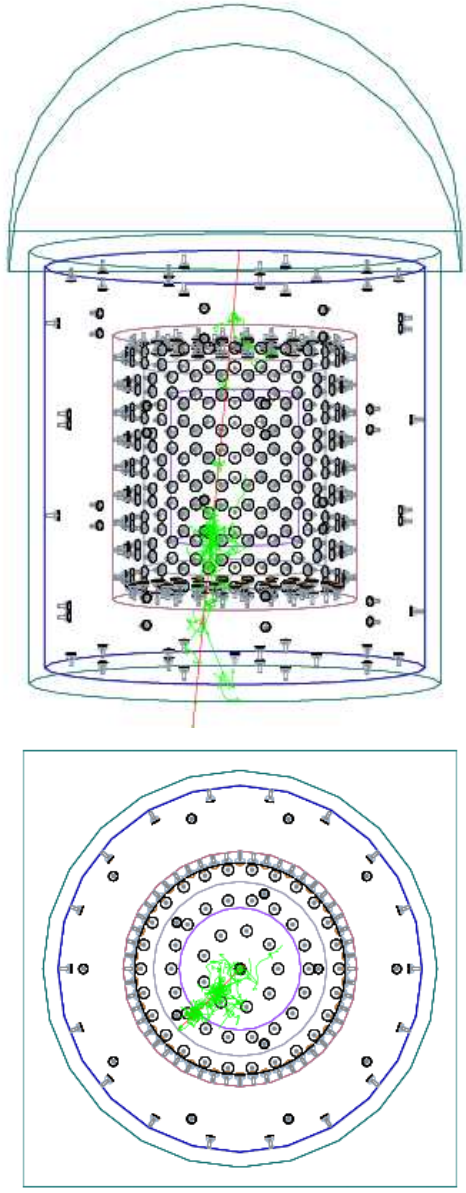

Figure 5.1: Side and top view of the RENO detector simulation with a muon (red line) passing through the target and leaving showers (green lines).

5.1.1 Software Tools

The primary software tool for modelling the RENO detector response is GLG4SIM, a GEANT4-based simulation package for liquid scintillator detectors provided from KLG4SIM of KamLAND collaboration. This software is designed for simulation of the detailed detector response to particles moving through and interacting with a large volume of liquid scintillator detector.

GEANT4 Simulation

The RENO detector has four concentric cylindrical sub-detectors each filled with Gd-loaded liquid scintillator, liquid scintillator without Gd, mineral oil, and water, respectively. The GEANT4 toolkits are applied for simulating the physics processes involving particles with energies above a few keV propagating through the materials in the detectors. However, the optical photon production and propagation through liquid scintillator, including processes like absorption, re-emission, and elastic collisions, are handled by specifically written codes in GLG4SIM.

In the detector simulation, the liquid scintillator consists of LAB for the organic solvent, 1.5 g/l of PPO as a fluor, and 0.3 mg/l of Bis-MSB as a secondary wavelength shifter. In the target region, 0.1% Gadolinium (Gd) is loaded. GEANT4 Neutron Data Library (NDL) version 3.8 gives a reasonable approximation for the continuum gamma spectrum after neutron capture on Gd. However, the discrete lines of high-energy gammas are not included in the NDL version 3.8. Fortunately, an update is available for GLG4SIM for an additional Gd support for a proper modelling of discrete lines of high energy gamma. The resulting distributions of the neutron capture distance and capture time are shown in Fig. 5.2.

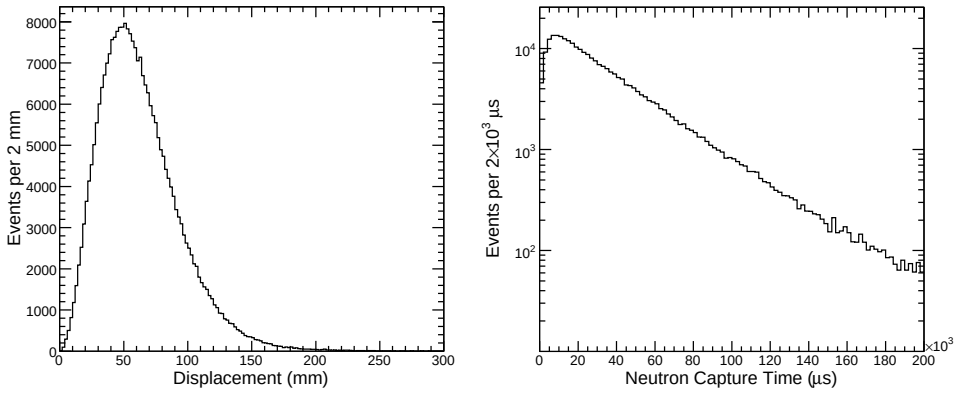

Figure 5.2: Neutron capture distance from inverse beta decay events (left) and neutron capture time (right).

5.1.2 Optical Photon Processes

Each photon generated in the simulation is tracked while in the detector until it either reaches a PMT or is lost. The simulation accounts for several light propagation phenomena while tracking the photons. Photons can experience absorption or elastic scattering (Rayleigh scattering) by solvent and fluor molecules, in the scintillator.

Attenuation length, λ_{att}, of the liquid scintillator is defined as

$$\frac{1}{\lambda_{att}} = \frac{1}{\lambda_{scat}} + \frac{1}{\lambda_{abs}}, \tag{5.1}$$

where λ_{scatt} and λ_{abs} are the scattering length and the absorption length, respectively. The reciprocal value of the liquid scintillator attenuation length, $1/\lambda_{att}^{LS}$, is equal to the sum of those of scattering lengths and absorption lengths,

$$\frac{1}{\lambda_{att}^{LS}} = \frac{1}{\lambda_{scat}^{LS}} + \frac{1}{\lambda_{abs}^{LS}} = \frac{1}{\lambda_{scat}^{LS}} + \frac{1}{\lambda_{abs}^{solvent}} + \frac{1}{\lambda_{abs}^{fluors}}. \tag{5.2}$$

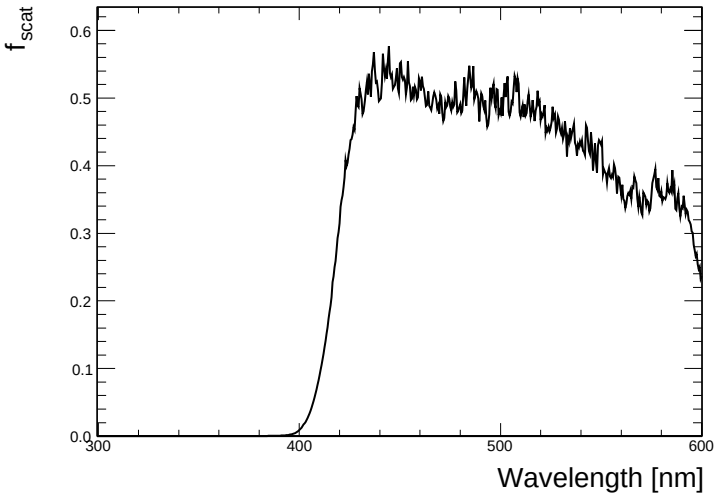

Figure 5.3: Measured scattering fraction of the LAB based liquid scintillator.

In the simulation photons can be either scattered or absorbed by the solvent and fluors according to appropriate fractions. Because a large fraction of liquid scintillator is the solvent, photons are scattered mostly by LAB. It has to be noted that the band gap for the lowest-energy electronic transitions in the LAB molecules is at 320 nm, and thus the absorption by LAB below 320 nm is strong. At wavelengths longer than 320 nm the absorbance by LAB drops rapidly and the measured extinction coefficient roughly obeys a λ^{-4} dependence, as expected in Rayleigh scattering. The scattering fraction, f_{scatt}, can be obtained from

$$f_{scatt} = \frac{\lambda_{att}^{LS}}{\lambda_{scatt}^{LAB}}. \tag{5.3}$$

Figure 5.3 shows the measured scattering fraction of an optical photon in the liquid scintillator. If a photon undergoes elastic scattering, its wavelength remains unchanged but its direction is altered. The direction of a photon after elastic scattering has an $(1+\cos^2\theta)$ dependence, where θ is the photon scattering angle. Absorption of a photon by fluors can be followed by their re-emission, but there is a chance for a absorbing molecule undergoing non-radiative relaxation process depending on its quantum yield efficiency. The non-radiative relaxation results in the loss of the photon, and tracking in the simulation is terminated in that case. The absorption probability of LAB, PPO, and bis-MSB can be

calculated by

$$P^i_{abs} = \frac{\lambda^{LS}_{abs}}{\lambda^i_{abs}}, \tag{5.4}$$

where i represents LAB, PPO, or bis-MSB. Figure 5.4 shows the measured absorption probability for each component in the liquid scintillator. Re-emission occurs isotropically and a longer wavelength than that of the absorbed photon, based on the emission spectrum, is assigned to the re-emitted photon.

The absorption of photons within the acrylic medium (vessel walls) is simulated according to the absorption probability calculated with medium's attenuation length. Also, the reflection and refraction of photons at the surface of the acrylic vessel are simulated using the Fresnel's law. The refractive indices of all dielectric materials in the detector are measured at different wavelengths and implemented in the simulation. The measured refractive indices of some of detector materials are shown in Fig. 5.5. After a photon enters a PMT and is absorbed by the photocathode, tracking is terminated, and a hit is made depending on the quantum efficiency of the photocathode.

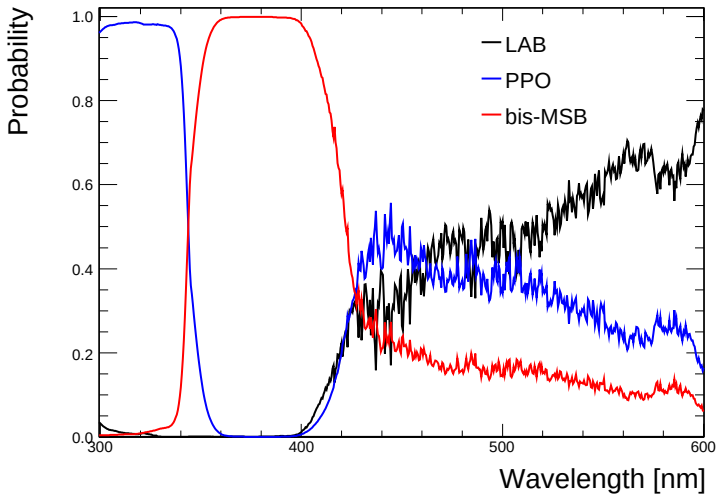

Figure 5.4: Measured absorption probabilities of LAB, PPO, and bis-MSB. These are used in the detector simulation.

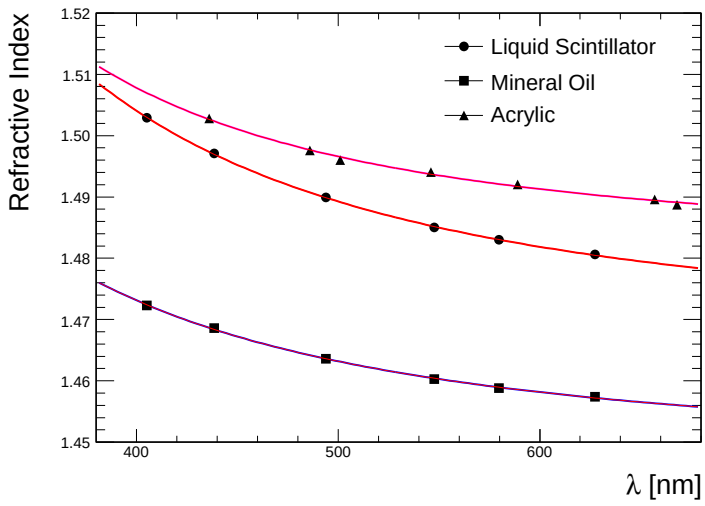

Figure 5.5: Measured refractive indices of liquid scintillator, mineral oil, and acrylic.

5.1.3 Quenching at low energy

When charged particle move in the LS, the LS take a energy from the particle and then emit scintillating light. If the particle have high energy, the relation between light yield of LS and transfered energy from particle is

$$\frac{dL}{dx} = S\frac{dE}{dx}, \tag{5.5}$$

where, L is the light yeild, $\frac{dE}{dx}$ is the energy loss of the particle per path length. However, $\frac{dE}{dx}$ of low energy particle is greater then that of the high energy particle. So the Equation 5.5 need some modification. The modified equation is named Birks low, an empirical formula to explain relation between the light yeild of LS and particl energy loss per path length, as following equation,

$$\frac{dL}{dx} = \frac{S\frac{dE}{dx}}{1 + k_B\frac{dE}{dx}}. \tag{5.6}$$

where, k_B is Birks constant, quenching parameter, which depends on the material. A schematic view of the experimental setup to measure k_B is shown in Fig. 5.6. The γ-ray from the ^{137}Cs source transfer energy to electron via compton scattering, and then remaining energy of γ is measured by Ge-detector. The

recoiled electron move and transfer energy to the LS. The scintillating from the LS is measured by PMT to obtain the light yield of LS. The energy of recoiled electron is calculated from following equation,

$$E_e = E_\gamma - E_{\gamma'} = 662\text{KeV} - E^{Ge-det.}_{measured}, \tag{5.7}$$

where, E_γ (= 662 KeV) is well known energy of the γ-ray from ^{137}Cs. and $E_{\gamma'}$ is the energy of the γ-ray after compton scattering. and $E^{Ge-det.}_{measured}$ is the γ-ray energy measured by Ge-detector. By comparing E_e and Light yield measured from the PMT, the k_B can be measured. The measured k_B of LS and Gd-LS are summarized in Table 5.1. More details are described in Appendix H.

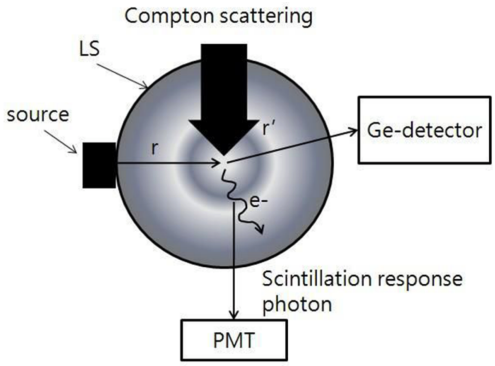

Figure 5.6: Experimental setup for Birks constant.

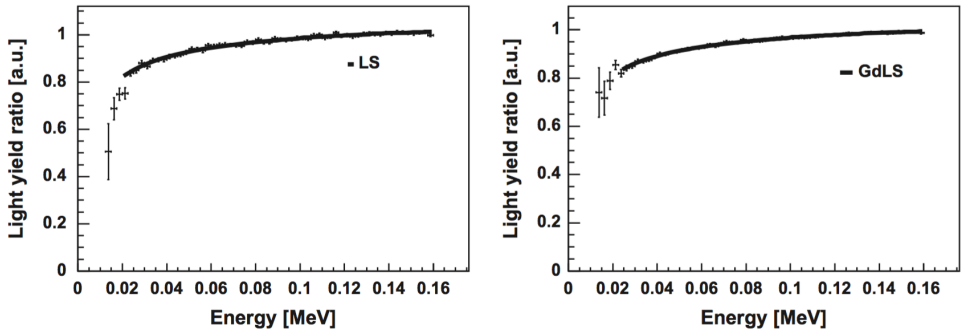

Figure 5.7: Fraction of measured light yield and energy as a function of energy in LS and GdLS. The left plot shows the LS. And the right plot shows the GdLS. The black line shows the fitting result [32].

	k_B (cm/MeV)
LS	0.0117±0.0003
GdLS	0.0124±0.0004

Table 5.1: Measured birks constant of LS and GdLS

5.2 Energy Calibration of Monte Carlo

5.2.1 Energy Conversion Function for Monte-Carlo

To convert photo electron (p.e.) to prompt energy (MeV) for IBD events, we derive the conversion function using the same procedure as data. That is, first we obtain raw p.e. from ^{137}Cs, ^{68}Ge, H-capture, ^{60}Co, C-capture and Gd-capture, which are located at target center as show Figure 5.8. Then we apply gamma-to-positron correction and uniform-to-uniform correction as summarize Table 4.3 since we need p.e. from uniformly distributed positrons. And we also apply center-to-uniform correction factor. Center-to-uniform correction factors are obtained as described in previous section. The measured values for far and near MC is 1.004831 ± 0.00019 and 1.00773 ± 0.00019. As for H-capture and C-capture, we generate 2.223 MeV single gamma and 4.95 MeV single gamma for MC. The other procedure and the fitting function are exactly same as data. The following table shows the source raw p.e., which are used for MC energy conversion. 1 M events are used for n-Gd and 400 k events are used for the other sources.

Source	Range	Fitting Function	Far raw p.e.	Near raw p.e.
^{137}Cs	−2RMS - +2RMS	Single Gauss	147.63 ± 0.14	143.45 ± 0.14
^{68}Ge	−4RMS - +3RMS	7^{th} poly. + Gauss	223.37 ± 0.94	216.45 ± 0.94
nH	−2RMS - +2RMS	Single Gauss	538.26 ± 0.28	522.86 ± 0.28
^{60}Co	−4RMS - +3RMS	7^{th} poly. + Gauss	583.10 ± 1.00	565.94 ± 1.00
nC	−2RMS - +2RMS	Single Gauss	1226.31 ± 0.61	1191.89 ± 0.61
nGd	−4RMS - +3RMS	7^{th} poly. + two Gauss	1931.63 ± 0.95	1880.64 ± 0.95

Table 5.2: MC raw photo electron of calibration sources, which is used for conversion function.

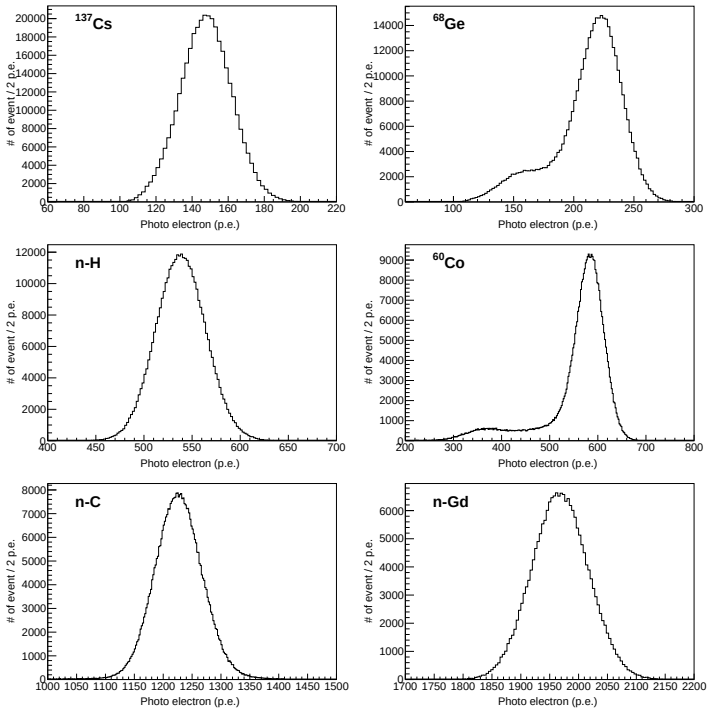

Figure 5.8: Monte-Carlo simulation result of calibration sources at the far detector.

Based on corrected raw p.e., we obtain pe-to-MeV conversion function by fitting with the following function.

$$\text{Function of P.E. / MeV (MeV)} = P_0 - \frac{P_1}{1 - \exp(-P_2 \cdot \text{MeV} - P_3)} \tag{5.8}$$

where, p.e. is photoelectron, MeV is prompt energy (MeV) and P_0, P_1, P_2, P_3 are fitting parameters. The fitting results are shown in Figure 5.9 and Table 5.3.

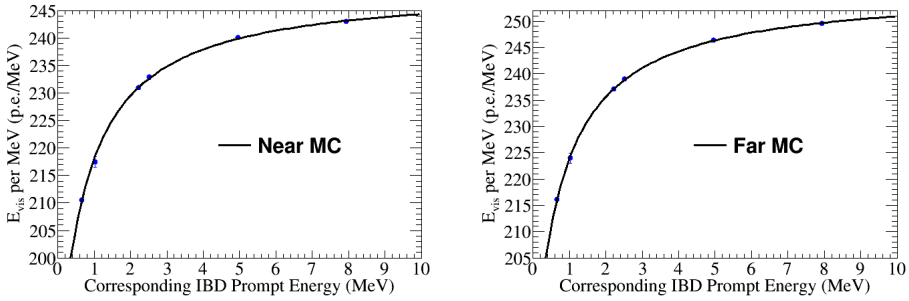

Figure 5.9: Energy conversion function for MC. Left side is near detector. And right side is far detector.

Parameter	far	near
P_0	256.19 ± 0.26	249.46 ± 0.26
P_1	0.0118 ± 0.0014	0.0100 ± 0.0090
P_2	0.000208 ± 0.000023	0.000184 ± 0.000166
P_3	0.000156 ± 0.000019	0.000136 ± 0.000121

Table 5.3: The fitting results of energy conversion function

5.2.2 Correction of Energy Resolution for MC Prompt Energy Spectrum

Energy resolution between MC and data are compared using ^{68}Ge, ^{60}Co and n-Gd sample, which are taken in target center. In case of n-Gd, as data have no sample taken at center, we obtain it by correcting from IBD n-Gd, which is uniform. Table 5.4 show energy resolution (σ/E) for both data and MC and its ratio. As you can see in the tables, data resolution is more worse than MC except near Ge sample. So we need to apply energy resolution correction to MC by the difference between data and MC.

Source	Far σ / mean	
	Data	MC
^{68}Ge center	0.0698 ± 0.0001	0.0639 ± 0.0002
^{60}Co center	0.0481 ± 0.0001	0.0461 ± 0.0001
n-Gd center	0.0298 ± 0.0003	0.0270 ± 0.0001
n-Gd uniform	0.0344 ± 0.0004	0.0312 ± 0.0002
Source	Near σ / mean	
	Data	MC
^{68}Ge center	0.0696 ± 0.0001	0.0720 ± 0.0002
^{60}Co center	0.0488 ± 0.0001	0.0470 ± 0.0001
n-Gd center	0.0291 ± 0.0001	0.0273 ± 0.0001
n-Gd uniform	0.0334 ± 0.0001	0.0314 ± 0.0002

Table 5.4: Energy resolution ($\sigma/mean$) for data and MC, respectively.

Figure 5.11 and Figure 5.10 show σ/E vs. Energy (left) and the difference (%) between data and MC resolution (right) for far detector and near detector, respectively. σ/E vs. Eneargy graph is fitted using the following function.

$$\sigma/E = \text{sqrt}(A/E + B) \tag{5.9}$$

Using the fitted functions, we calculate the difference of energy resolution between data and MC for any given energy. The resolution correction for any given energy is calculated as

$$\sigma^2_{cor} = \sigma^2_{data} - \sigma^2_{MC} \tag{5.10}$$

Then, we do Gaussian smearing of MC energy event-by-event like following

$$E_{new} = GaussianRandom(E_{old}, \sigma_{cor}) \tag{5.11}$$

One thing to take into account is that the energy resolution differences between data and MC shown in Figure 5.11 and Figure 5.10 are what we obtained from center source. So its difference cannot be applied to MC absolutely since our resolution correction is for uniform IBD events. Therefore, we just take the relative difference from the center source and derive σdata for uniform source like following.

$$\sigma_{data} = \sigma_{MC} \times \text{relative difference} \tag{5.12}$$

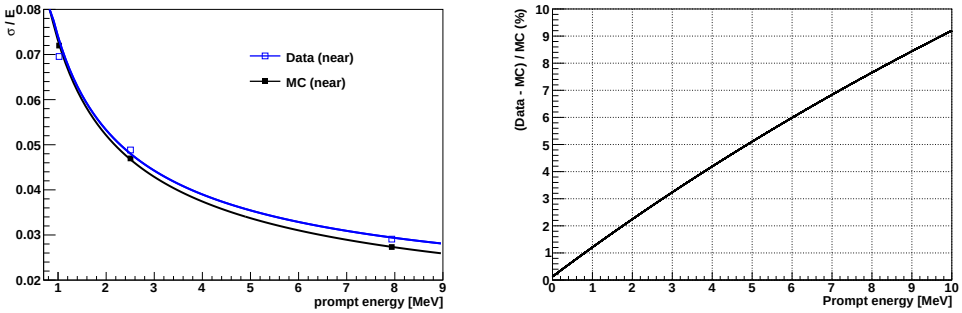

Figure 5.10: σ/E vs. E (left) and difference (%) between data and MC resolution for near detector

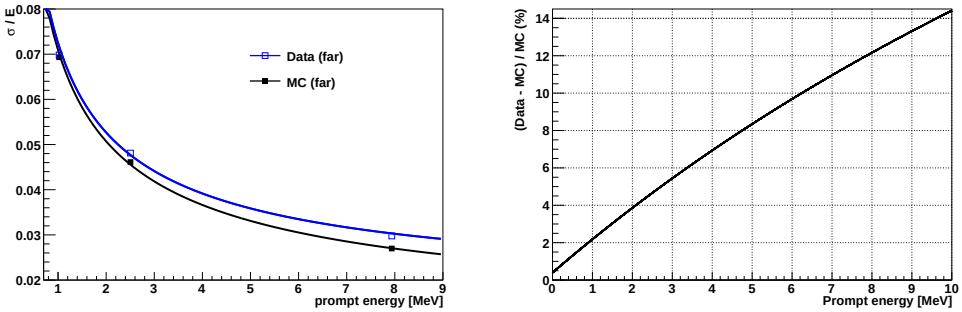

Figure 5.11: σ/E vs. E (left) and difference (%) between data and MC resolution for far detector

5.2.3 MC prompt energy spectrum

We have tuned MC parameters and obtained MC conversion for near and far, respectively. Energy resolution correction factor is also obtained. Then now we can make MC energy spectrum to compare with data. Figure 5.12 shows finally reconstructed MC spectrum without oscillation effect.

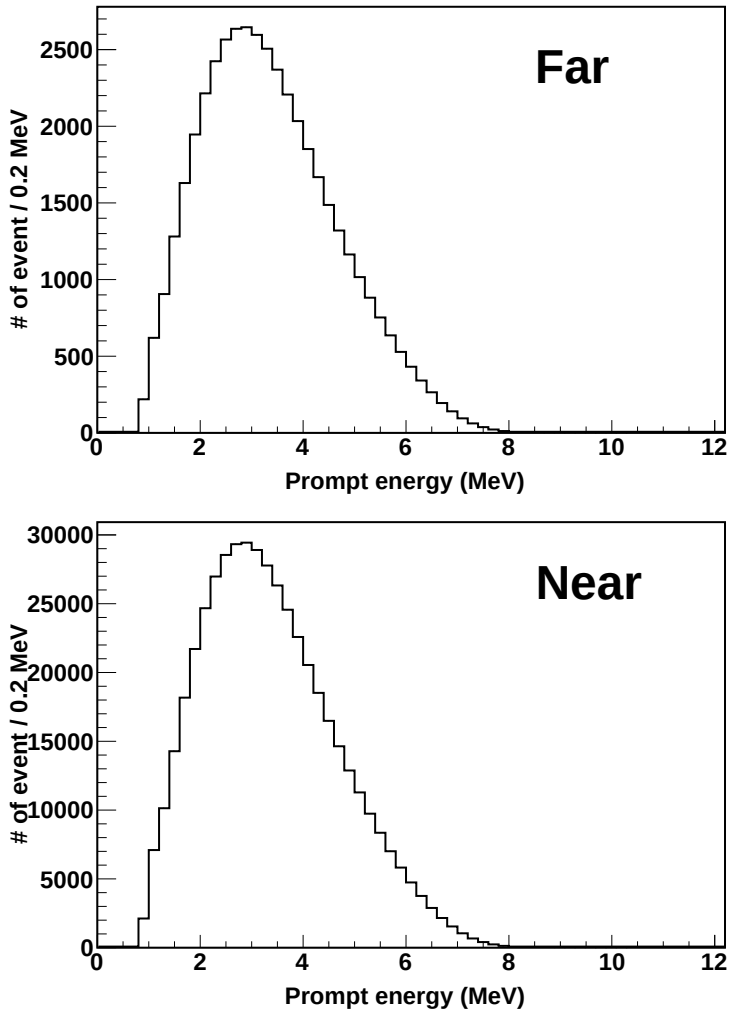

Figure 5.12: MC prompt energy spectrum without oscillation effect, which are reconstructed finally after applying energy resolution correction. Far MC spectrum is shown in the top side. Near MC spectrum is shown in the bottom side.

Chapter 6

Data Sample and Event Selection for IBD Candidates

Data taking began on Aug. 1^{st}, 2011 with both near and far detectors. The Data have been being taken. The data samples contain 800 day data and are divided into 3 sets : Set A, Set B, Set C : Set A contains 400 day data and the normal physics run. It has no any problems. Set B contains 100 day data and is contaminated with ^{252}Cf. Finally, Set C contains 300 days data and is also contaminated with ^{252}Cf,too. In addition, set C exhibits DAQ inefficiency due to UPS noise. This thesis focuses on the results from Set A and Set B, and the results from Set C are briefly reported on. The RENO data acquisition system has the power to take all triggered events without no electronics dead time. The triggered event rate is of the order of a hundred Hertz and the system produces 450 GB per day. On the other hand, the expected rate of observed neutrino events is of the order of ten per day (hundred per day) at the far detector (near detector).As the data consists mostly of backgrounds, IBD signal reconstruction has been developed in consideration of the higher the selection efficiency and lower backgrounds. The IBD selection criteria are different at the far and near detectors for the high efficiency.

6.1 Data Sample

Data taking began on Aug. 1^{st}, 2011 with both near and far detectors being commissioned. The physics data acquisition began on Aug. $11^{s}t$, 2011 (Aug. $19^{t}h$, 2012) at the far (near) detector. This data has no calibration source data and contains bad data. Bad data is identified by abnormal behavior in the hit map, charge distribution and event rate. Data taking efficiency is 96.65% (94.78%) at the far (near) detector. Fig. 6.1 shows three data sets and daily detection

efficiency of both detectors.

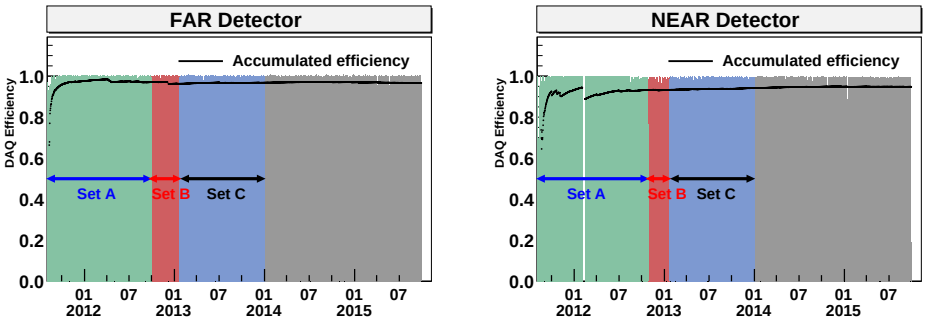

Figure 6.1: Data set and Data Taking efficiency of RENO. The left image shows the far detector and the right image shows the near detector.

Detector	Data Set	Date	DAQ Live time (days)
Far	Set A	11^{th} Aug, 2011 $\sim$ 28^{th} Sep, 2012	384.47
	Set B	28^{th} Sep, 2012 $\sim$ 21^{st} Jan, 2013	105.46
	Set C	21^{st} Jan, 2013 $\sim$ 31^{st} Dec, 2013	304.79
Near	Set A	19^{th} Aug, 2011 $\sim$ 27^{th} Oct, 2012	379.66
	Set B	27^{th} Oct, 2012 $\sim$ 21^{st} Jan, 2013	78.83
	Set C	21^{st} Jan, 2013 $\sim$ 31^{st} Dec, 2013	302.62

Table 6.1: Three sets of data sample

The physics Data consist of three sets: Set A, Set B and Set C. Set A contains the normal run data. Set B contains the ^{252}Californium (^{252}Cf) source data during the contaminated period. A tiny fraction of the ^{252}Cf calibration source was dissolved into Gd-LS during the source run on Sep. 28^{th},2012 at the far detector and Oct. 27^{th}, 2012 at the near detector. To remove the backgrounds from the ^{252}Cf contamination, Cf removal cuts were applied to the set B. Lastly, Set C has DAQ inefficiency due to UPS noise at the near detector. The UPS was installed both detector on Jan. 22^{th}, 2013. Unfortunately the UPS in the near detector caused electric noise, which negatively affected the data taking. The noise gets a place in the data instead of signals. Fig. 6.2 shows the effects of UPS noise effects on the data. So that the detector loss a event or some energy of event. In this thesis, the main analysis is coming from the Set A and Set B.

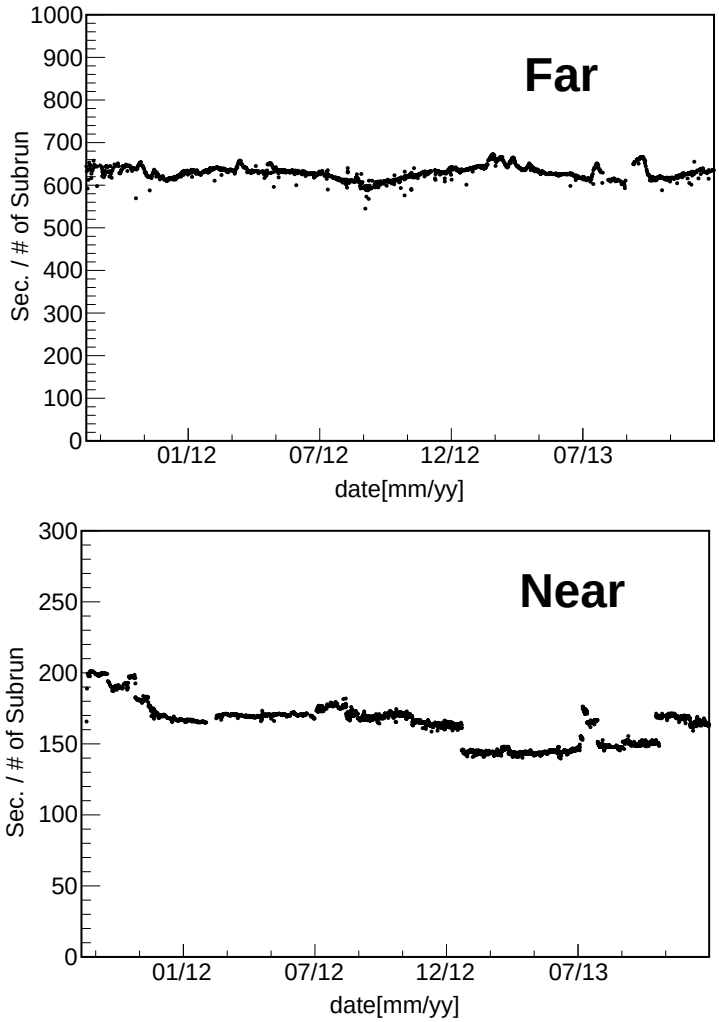

Figure 6.2: Live time per subrun distribution. The top image shows the far and the bottom image shows the near detector. The subrun is generated with every 500 MB of raw data. Set C of the near detector contains UPS noise. The data production rate with UPS noise (Set C) is faster than that without UPS noise (Set B or Set A). Live time per subrun of the near detector suddenly dropped after the installation of the UPS. This means that the noise was taken in the data and the data production rate was increased.

6.2 Backgrounds

6.2.1 Accidental Background

Accidental backgrounds are caused by uncorrelated events accidentally coinciding and mimicking the IBD process. As mentioned in section 6.4.1, the events from gamma and electron emission can be prompt and the single neutron events induced by cosmic muons can be indicated by delayed signal of the inverse beta decay. These backgrounds are completely statistical accidents, such that the prompt and delayed signal of accidental backgrounds have no temporal and spatial correlations, as shown in Fig. 6.3. From this property, the accidental backgrounds are removable.

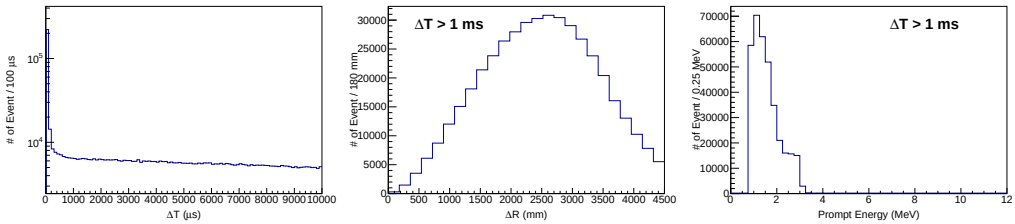

Figure 6.3: Properties of accidental background. The left plot shows the time difference(=ΔT) between the prompt and delayed. There are only Accidentals in the $\Delta T > 1$ ms region. The gentle-sloped component is accidental. The middle plot shows distance(=ΔR) between prompt and delayed accidental. The peak is around 2500 mm. A difference can be seen between accidental backgrounds and IBD which have the spatial correlation between the prompt and delayed signals, as shown Fig. 6.16.The right plot shows the prompt energy spectrum of the accidental background.

6.2.2 Fast Neutron Background

The fast neutron produced by a cosmic muon in surrounding rock or in the detector can mimic an inverse beta decay signal in the detector in three ways. First, the fast neutrons with an energy over 10 MeV can be scattered elastically from protons in the target or the γ-catcher many times and be captured in the target volume. The quenched proton recoil scintillation signals can be detected as the prompt signal with an energy between 1 and 50 MeV and the moderated neutrons can be captured with the same time distribution as the neutrino signal.

Second, some neutrons are produced by cosmic muons without recoil protons and are captured in the detector within 100 μs. A single neutron capture

signal has some probability of falling accidentally within the time window of a preceding signal caused by natural radioactivity in the detector, producing an accidental background. In this case, the prompt and delayed signals are from different sources, forming an uncorrelated background.

Third, multiple neutrons are produced within a short period of time. Multiple neutrons are captured by hydrogen or gadolinium within short time (order of ~ 10 μs). The first captured neutron event could be prompt and the next gadolinium captured neutron event could be delayed. Therefore, this type of fast neutron background has two peaks around 2.2 MeV and 8 MeV.

For these reasons, the prompt and delayed pair of fast neutrons have occurring before or after the prompt event. Using this property of fast neutrons, the fast neutron background could be reduced.

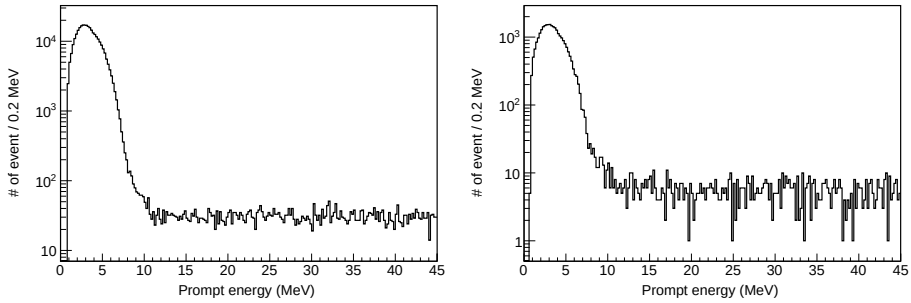

Figure 6.4: Spectra of fast neutrons. The energy spectrum of fast neutron shows a flat shape in the region that where the energy > 10 MeV.

6.2.3 ^{9}Li/^{8}He

From the experiences of previous reactor neutrino experiments such as KamLAND [14, 15] and CHOOZ [25, 30], we know there are irreducible background events from the decay of cosmogenic isotopes. Most prominent radioactive isotopes are ^{8}He and ^{9}Li. ^{8}He decays by $\beta^- + n$ (16%, $Q_{\beta^-} = 10.653$ MeV) with a half-life time of 119 ms. ^{9}Li decays by $\beta^- + n$ (49.5%, $Q_{\beta^-} = 13.606$ MeV) with a half-life time of 178.3 ms. The $\beta^- + n$ decay gives a prompt and delayed signal similar to an IBD events. The production rates of these long-lived cosmogenic isotopes were studied initially by rock dating group. There is a lot of data available on the production rates of ^{10}Be and ^{26}Al from silicon and oxygen by cosmic muons. The production cross section of ^{8}He and ^{9}Li in carbon has been measured with accelerator muon beams at an energy of 190 GeV at CERN [65]. Their combined cross section is $\sigma(^{9}\text{Li} +^{8} \text{He}) = (2.12 \pm 0.35)$ μb. The energy

dependent production cross section is estimated as $\sigma_{tot} = E_{\mu}^{0.73}$, where E_{μ} is the muon energy given in giga electronvolts.

The KamLAND experiment reported that their ^{8}He and ^{9}Li backgrounds are correlated with showering muons, which has more than 10^{6} photoelectrons, and they applied a 2 s veto for the muons. For RENO experiment, we plan to apply a 1 ms veto for non-showering muons and around the order of 100 ms for showering muons. This veto on the showering muons will further reduce the ^{8}He and ^{9}Li background rate by about 70%.

6.2.4 Backgrounds from ^{252}Cf contamination

The physics Data are consist of three sets: Set A, Set B and Set C. Set B contains contaminated with the ^{252}Californium (^{252}Cf). A tiny fraction of ^{252}Cf calibration source was dissolved into GdLS during the source run on Sept. 28^{th},2012 at the far detector and Oct. 27^{th}, 2012 at the near detector. Fig. 6.5 shows the ^{252}Cf source and its package. The package is not perfectly sealed, and the O-ring in the source container has a limited lifetime. The loose O-ring permits GdLS into the container, and the ^{252}Cf remains at the target after the source run.

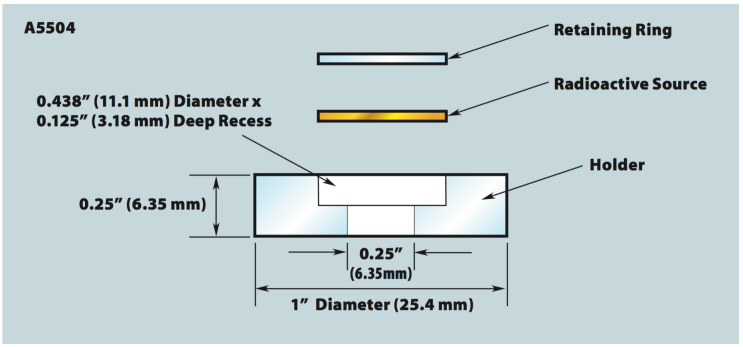

Figure 6.5: The ^{252}Cf source is mounted in a plastic holder, in which it can be separated from and exposed to GdLS [66].

^{252}Cf decay by alpha emission (96.91 %) and spontaneous fission (3.09 %). Half-life time is 2.65 years. The neutron produced from ^{252}Cf energy spectrum is shown Figure 6.29 with most probable energy of 0.7 MeV and an average energy of 2.1 MeV. And ^{252}Cf emits an average of 3.7 neutrons per fission[][]. The fission neutron is also captured by Gd and can be delayed signal. So that The ^{252}Cf have cause colossal backgrounds. To remove these backgrounds from ^{252}Cf contamination, the Cf removal cuts are applied to Set B.

6.3 Removal of γ-Rays from Radioactivity, Noise and Flashers

6.3.1 Removal of γ-Rays from Radioactivity and Noise

As mentioned in the previous section, energetic gamma rays and particles coming from the radioactive decay of isotopes in the inner detector can create accidental as well as correlated backgrounds. Some of these backgrounds come from surrounding rocks, the detector vessels, the PMT glasses and the mineral oil in the buffer, and can be reduced by using properties of the event at the border. These border events have a large ratio value of the maximum PMT charge (Q_{max}) to the total charge (Q_{tot}) ((*i.e.* Q_{max}/Q_{tot})), because the events deposit energy at the buffer, near the PMT, and the PMT nearest to the events receives a much larger number of photoelectrons than the other PMTs. Therefore, the Q_{max}/Q_{tot} ratio is useful for reducing such radioactive backgrounds, but has an energy-dependent efficiency. The lower the energy of the event, the lower the number of photoelectron that hit the PMT. In addition the Q_{max}/Q_{tot} of high energy events is relatively larger than that of low energy events. In other words, the lower the energy of the event, the lower the efficiency. The energy dependent efficiency of the Q_{max}/Q_{tot} cut is shown in Fig. 6.6. This efficiency affects the spectra analyses, as it could be a large systematic uncertainty for measuring $|\Delta m^2_{ee}|$. To avoid this uncertainty, the Q_{max}/Q_{tot} cut efficiency has to be almost 100 %. Fig. 6.7 shows an almost 100% efficiency when the cut threshold is 0.07.

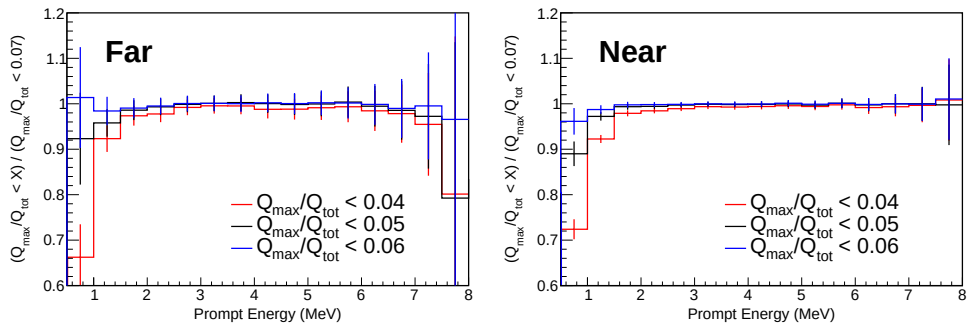

Figure 6.6: IBD Spectrum w.r.t the case in which the $Q_{max}/Q_{tot} < 0.07$ case. The left image shows the far detector and the right image shows the near detector. Under the assumption that the efficiency of $Q_{max}/Q_{tot} < 0.07$ is 100 %, this plot shows the Q_{max}/Q_{tot} cut efficiency has energy dependence.

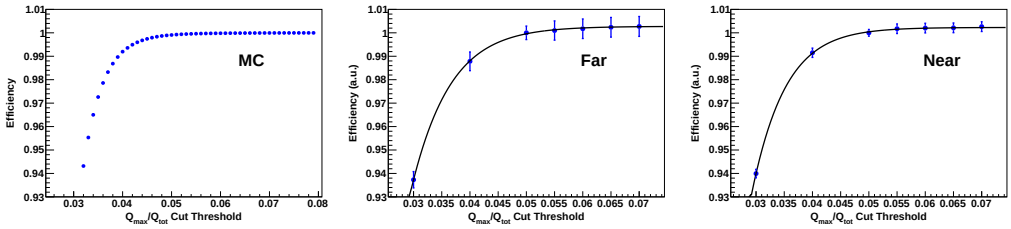

Figure 6.7: Q_{max}/Q_{tot} cut efficiency. The left image shows MC. The middle shows the far detector. The right image shows the near detector. The black line is the fitting result of a logistic function. The cut efficiency at 0.07 is 99.99 ± 0.02% at both detectors, according to the fitting results.

6.3.2 Removal of Flasher

Sometimes PMTs spontaneously emit lots of light and this light from PMT can be triggers. This event is called a flasher and is not yet a fully understood mechanism. The flasher rate is monitored as shown in Fig. 6.8. For purity of signals, when a PMT with a high flash rate exists, the PMT is removed from the DAQ system.

Where the discharge of flasher events is suspected in PMTs. and the flasher event has a particular hit time and charge pattern, so the flasher can be removed without signal loss. Typically, flasher events occur before the hit-time 0 (t_0) with large charge that is shown in Fig. 6.9. To remove flashers, it is more efficient to use the time and charge information between -400 − 800 ns than -100 − 50 ns, so that the flasher removal cut uses same Q_{max}/Q_{tot} of the γ-rays from radioactivity removal cut. However a difference between two cuts is that flasher removal uses a wider time-window. For the 100 % efficiency, the flasher removal cut threshold is also 0.07. Therefore, The flasher removal cut also includes the γ-ray from radioactivity removal cut.

- γ-ray and flasher removal Q_{max}/Q_{tot} (-400 − 800 ns) < 0.07

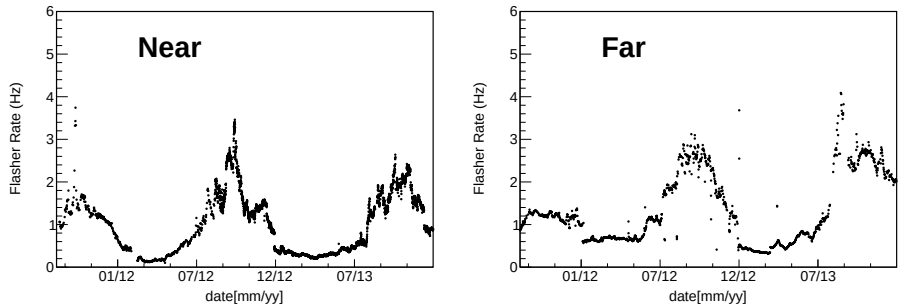

Figure 6.8: Daily flasher event rate. The left image shows the near detector and the right image shows the far detector. The flasher rate during summer is higher than the rate during winter at the both detectors.

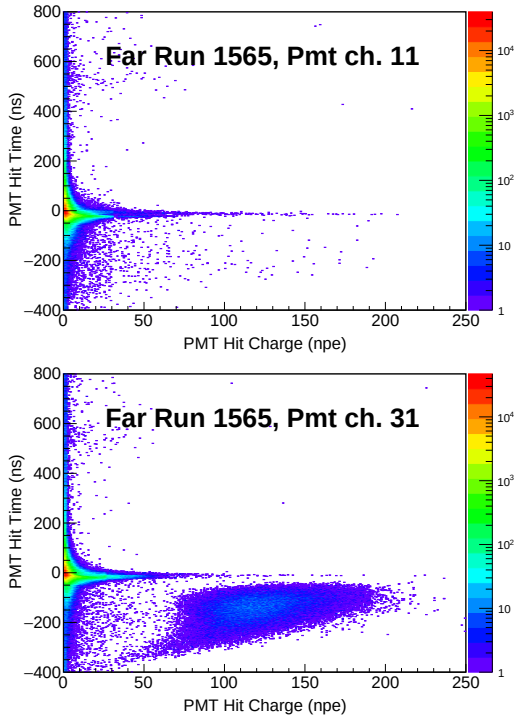

Figure 6.9: PMT hit time and charge distribution. The top image shows the normal PMT and the bottom image shows flasher PMT. The flasher PMT has an abnormal structure (high hit charge and early hit time) compared with that of the normal PMT.

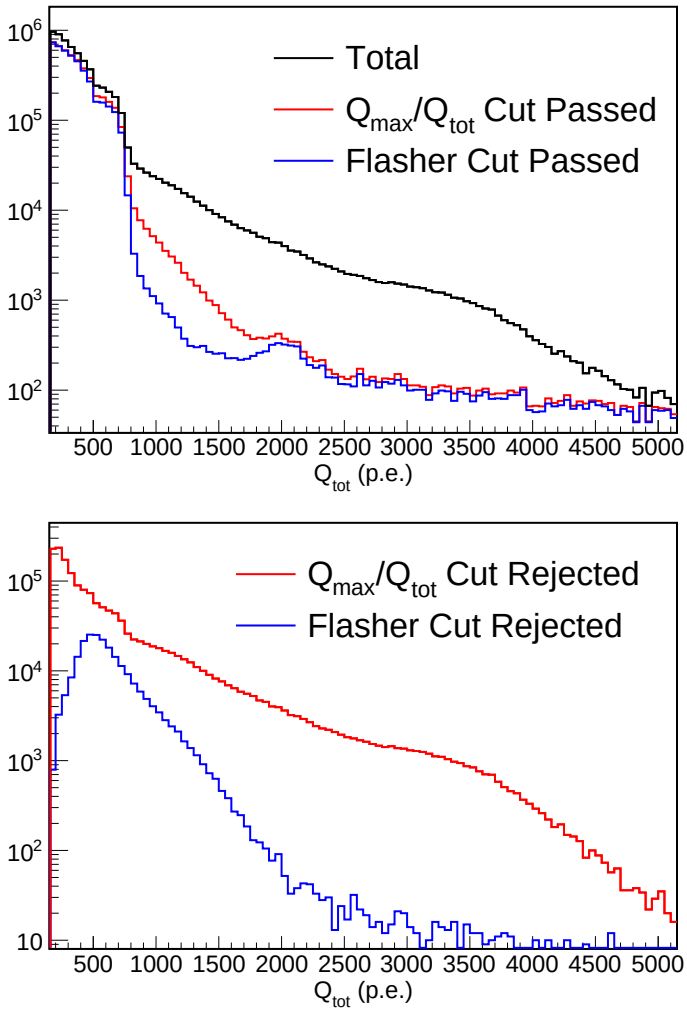

Figure 6.10: The event spectra before and after the Q_{max}/Q_{tot} cut. The top image is before the cut and cut passed. The bottom image shows the cut rejected. The red line is between -100 − 50 ns, and the blue line is between -400 − 800 ns.

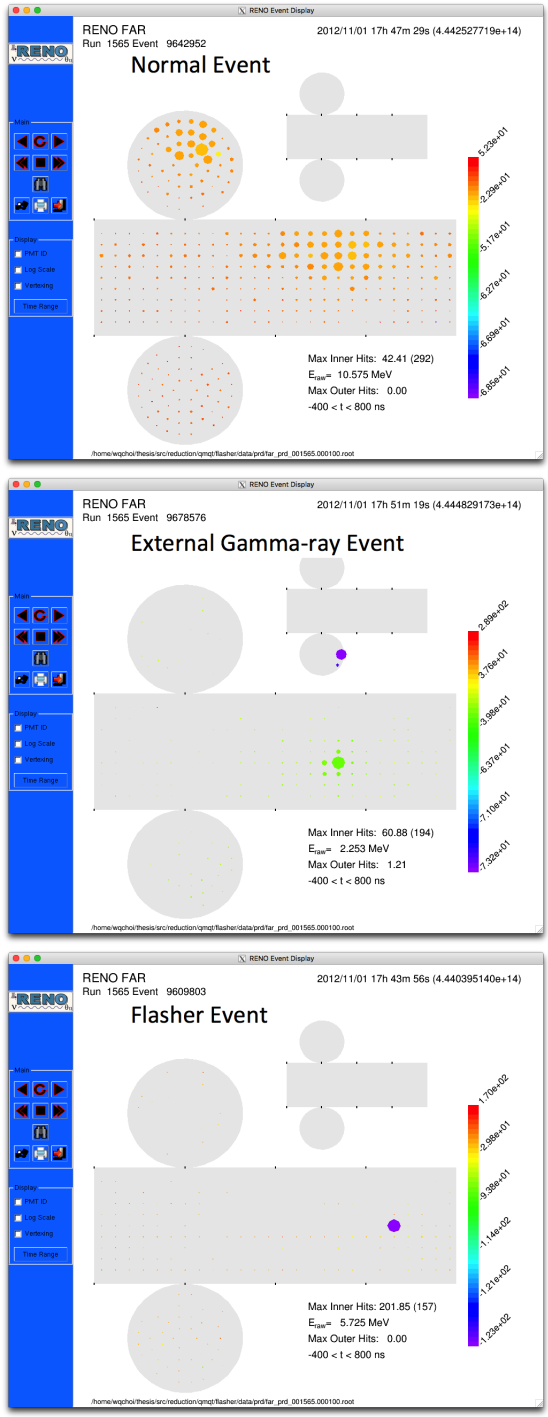

Figure 6.11: Event diplay plot. The top image shows the normal event. The middle image shows external γ-ray event(Q_{max}/Q_{tot} cut rejected). The bottom image shows the flasher event (flasher cut rejected).

6.4 Removal of Accidental Backgrounds

6.4.1 Radioactive Backgrounds

A radioactive isotope (*i.e.* radionuclide) is an atom with an unstable nucleus. They undergoes radioactive decay, and emits a gamma(s) and/or subatomic particles such as alpha, electron and position, *etc.* Some radioactive isotopes, such as ^{40}K, ^{60}Co, ^{232}Th and ^{238}U, are naturally abundant in detector materials and rocks around the detector hall. Energetic gammas and particles coming from the radioactive decay of isotopes in inner detector can create accidental as well as correlated backgrounds. Especially signal made by radioactive gamma rays and electrons can mimic the prompt signal of the inverse beta decay. This background can form an accidental (uncorrelated) background with the single neutron events induced by cosmic muons.

Radioactive background can come from a variety of sources, mainly form inner detector materials and surrounding rock. In this study, we consider the K, Th, and U isotopes as the radioactive sources that exist in the following materials.

- rocks surrounding the detector hall
- liquid scintillators
- acrylic vessels
- buffer oil
- stainless steel vessel
- PMT glasses

Most radioactive isotopes do not decay directly to a stable state, but rather undergo a series of decays until a stable isotope is eventually reached. Fig. 6.12 shows the decay chains of ^{238}U and ^{232}Th. Fig. 6.13 shows the energy level diagram for ^{40}K decay. Gamma radiation emission occurs not only when a radioactive isotope undergoes gamma decay, but also beta decay, where gammas emission often follow the emission of a beta particle. To take into account probability of decay and coincidence of a generated particle, a decay chain generator is developed.

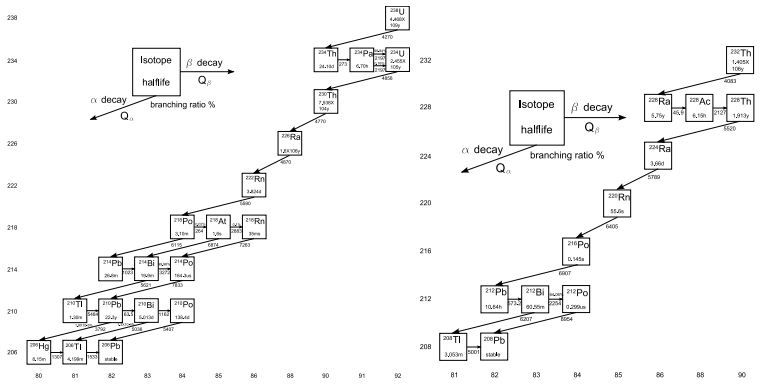

Figure 6.12: Decay chains of ^{238}U and ^{232}Th.

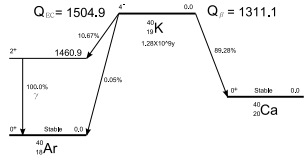

Figure 6.13: Level diagram for ^{40}K.

Using the radioactive decay chain generator, radiations from the three dominant decay chains are generated at the detector subsystem. We apply a 1 MeV threshold to the reconstructed energy. Table 6.2 shows the detector acceptance of the radiation from each radioactive isotope decay chain.

	^{40}K	^{232}Th	^{238}U
Target LS	0.20	1.34	1.25
Target Acrylic	0.09	0.67	0.79
GC LS	0.23	1.29	1.25
GC Acrylic	0.04	0.28	0.35
Buffer Oil	0.007	0.05	0.05
Buffer Vessel	0.0005	0.007	0.004
PMT	0.01	0.04	0.04

Table 6.2: Detector acceptance of the radioactive radiations from each detector subsystem with 1 MeV threshold.

The concentration of isotopes in the inner detector material is measured us-

	^{40}K ppt	^{232}Th ppt	^{238}U ppt	Single Event Rate Hz
Rock	4.33(ppm)	7.58(ppm)	2.32(ppm)	9.2
Target LS	< 0.32	17.7	13.9	< 5.6
Target Acrylic	8	206.8	167.5	0.95
GC LS	< 0.32	17.7	13.9	< 8.4
GC Acrylic	8	206.8	167.5	0.87
Buffer Oil	10	19.7	5.0	1.07
Buffer Vessel	60	900	900	0.33
PMT	10.8	125.9	50.3	8.19
Total				< 34.6

Table 6.3: Concentrations of ^{40}K, ^{232}Th, and ^{238}U in surrounding rock and the main components of RENO detector, and their event rates.

ing an ICP-MS and HPGe detector. With the concentration and the detector acceptance values from the full simulation, the single event rates caused by each detector subsystems are calculated. Table 6.3 shows the results. The most dominant contribution comes from the liquid scintillator in the target and gamma catcher. However, if we control the concentration of the isotopes under 10^{-12}g/g, these rates are negligible compared to that from PMT glass.

6.4.2 Removal of Accidental Backgrounds

The rate of signals resulting from radioactive gamma and electron emission, which can mimic the prompt signal of the IBD process is $\sim$50 Hz. However, the expected IBD rate is around 70 per day in the far detector and 700 per day in the near detector. Therefore, reducing non-relevant events is important to obtained IBD process from the reactor neutrino. IBD candidates are selected according to the following criteria using 3 properties of the IBD process : temporal correlation, spatial correlation between the prompt and delayed signal, and the energy.

Energy Threshold

The prompt signal of the IBD process is from the positron. No matter how small, It will have an energy of at least 1.022 MeV, which is the pair annihilation energy. As seen in the expected prompt energy spectrum Fig. 3.5, the prompt positron will not often be 12 MeV or higher. The delayed signal, which is a Gd captured neutron has a narrow gaussian distribution around 8 MeV. So far, these conditions are for an ideal case. The RENO detector has some inefficiencies. e.g., γ-rays can

escape the LS region, and the detector can not observe their full energy. For these reasons, the energy threshold for the positron signal has been decided to be higher than 0.75 MeV and lower than 12 MeV, and the energy threshold for the delayed signal have been decided to be higher than 6 MeV and lower than 12 MeV. From the required energy threshold, the IBD candidate is reduced by the order of 10^{-2}.

- 0.75 MeV < Prompt signal energy (E_p) < 12 MeV
- 6 MeV < Delayed signal energy (E_d) < 12 MeV.

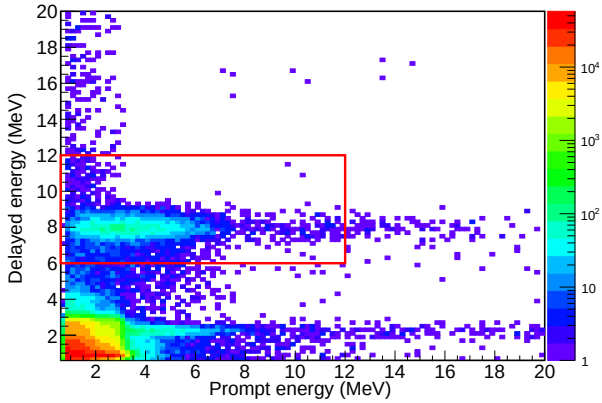

Figure 6.14: The prompt and delayed spectra with no energy threshold condition. The energy threshold for IBD events are indicated by the red box.

Time coincidence

For the neutrino detection, the IBD reaction is commonly used. This IBD reaction produces a positron and a neutron. During the IBD process, the positron immediately deposits kinetic energy and is annihilated with the electron. The neutron undergoes thermalization before the capture process; hence there should be a time difference between the positron event and neutron capture event (Δt). The neutron capture cross-section increases as the neutron kinetic energy decreases by thermalization. Therefore, Δt can be modeled as an exponentially decreasing function. Fig. 6.15 shows the Δt of both detectors. The mean Δt is almost same, at $\sim$ 27 μsec. In this picture, the time coincidence cut has been decided to be 3 times of the mean time difference (2 μs $-$ 100 μs). The prompt and delayed candidate signal is reduced by 0.5% because of the time coincidence cut and assuming event rate which can be prompt of IBD process is 50 Hz.

- 2 μs < Time difference between prompt and delayed signal (Δt) < 100 μs

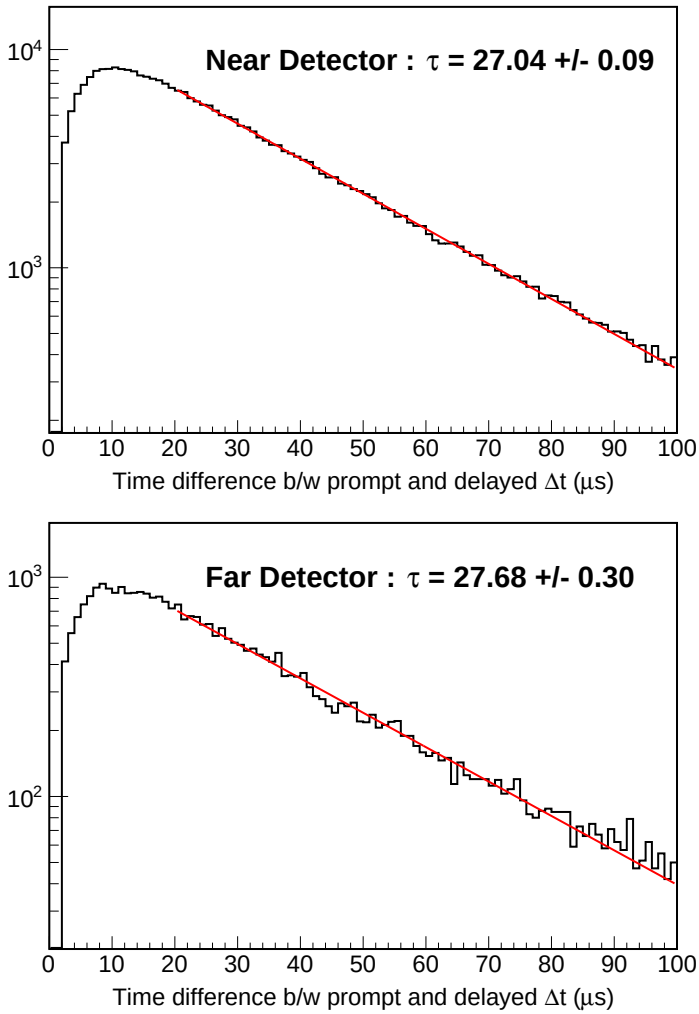

Figure 6.15: Time difference between the prompt and delayed signal. The top image shows the near detector and the bottom image shows the far detector. The red Line is a fit of the simple exponential function. The two detectors have a similar mean time difference $\sim$ 27 μsec.

Spatial Correlation

The neutron from the IBD process is in the order of KeV. For this reason, the neutron can not go far from the IBD point of occurrence. Therefore, spatial correlation would exist between the prompt and delayed signals. However, accidental backgrounds (such as when uncorrelated prompt-like events and delayed-like event pairs accidentally pass the IBD selection cuts) have no spatial correlation and can have a greater distance between the prompt and delayed than IBD pairs. To remove accidental background, this spatial information can be a useful tool.

Fig. 6.16 shows the ΔR distributions of the near detector data. The tight accidental cut sample has almost zero event that have $\Delta R > 2.5$ m (0.001%). Therefore, the ΔR cut has been decided to be lower than 2.5 m with almost zero signal loss.

- Distance between the prompt and delayed signal (ΔR) < 2.5 m

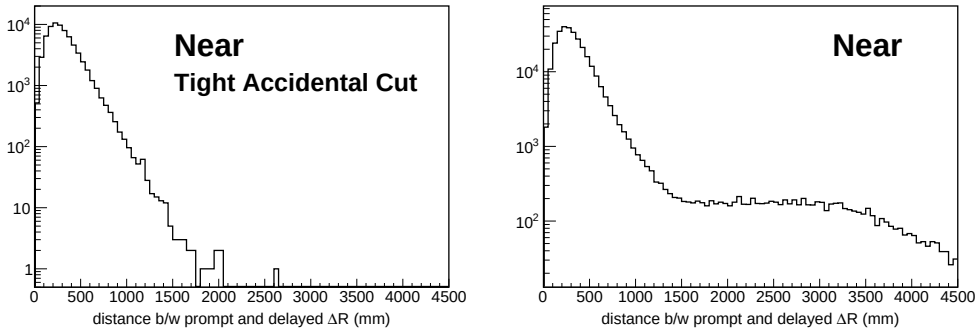

Figure 6.16: Distance between the prompt and delayed signal. The left image shows the tight accidental cut sample at the far detector and the right image shows no tight accidental cut sample at the near detector. According to the left plot, the signal with $\Delta R > 2.5$ m is 0.001% of the total sample. The right plot shows the data has many backgrounds ($\Delta R > 2.5$ m).

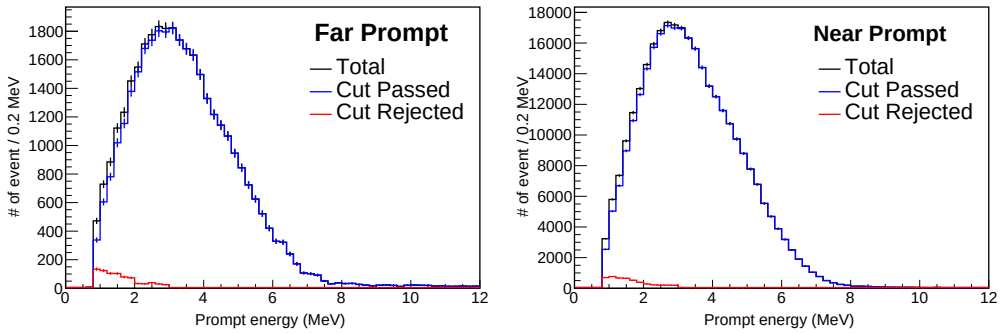

Figure 6.17: The prompt spectra before and after the ΔR cut. The left image shows the far detector and the right image shows the near detector.

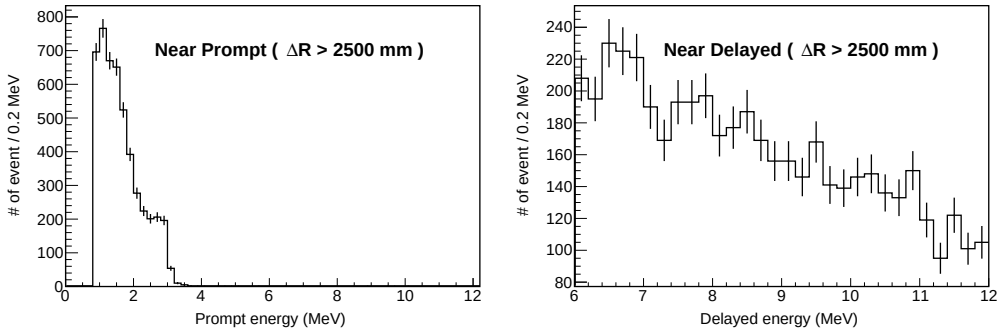

Figure 6.18: ΔR cut rejected prompt and delayed spectra of near detector. The left image shows the prompt signal and the right image shows the delayed signal. The delayed signal of the rejected data does not have the 8 MeV Gd captured event. This means the ΔR cut rejected signal is not relevant to the neutron process.

Fig. 6.18 shows the prompt and delayed signals of ΔR cut rejected. The delayed single of ΔR cut rejected does not show the 8 MeV Gd captured neutron event. This means the delayed signal of ΔR cut rejected is not neutron event, while the prompt signal of the rejected is similar to spectrum of accidental background (see Fig. 7.1).

Buffer and Veto trigger Veto Cut

There are some components that have a buffer and veto trigger following the prompt signal. There are a few events after 200 μs from prompt signal. According to Fig. 6.19, we decided to reject pairs that have a buffer and veto trigger within 200 μs of the prompt. The rejected signals by this veto cut are shown in Fig. 6.20. They consist of mainly low-energy backgrounds of $\sim$2 MeV.

- Zero Buffer and Veto trigger within (0 μs, 200 μs) of prompt signal

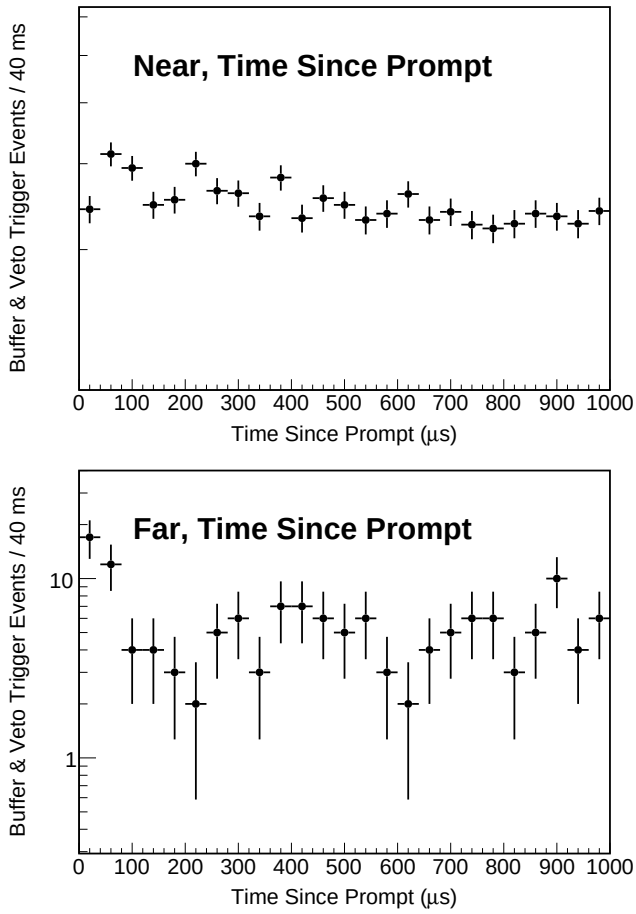

Figure 6.19: Buffer and veto trigger time distribution since prompt. The top image shows the near detector and the bottom image shows the far detector.

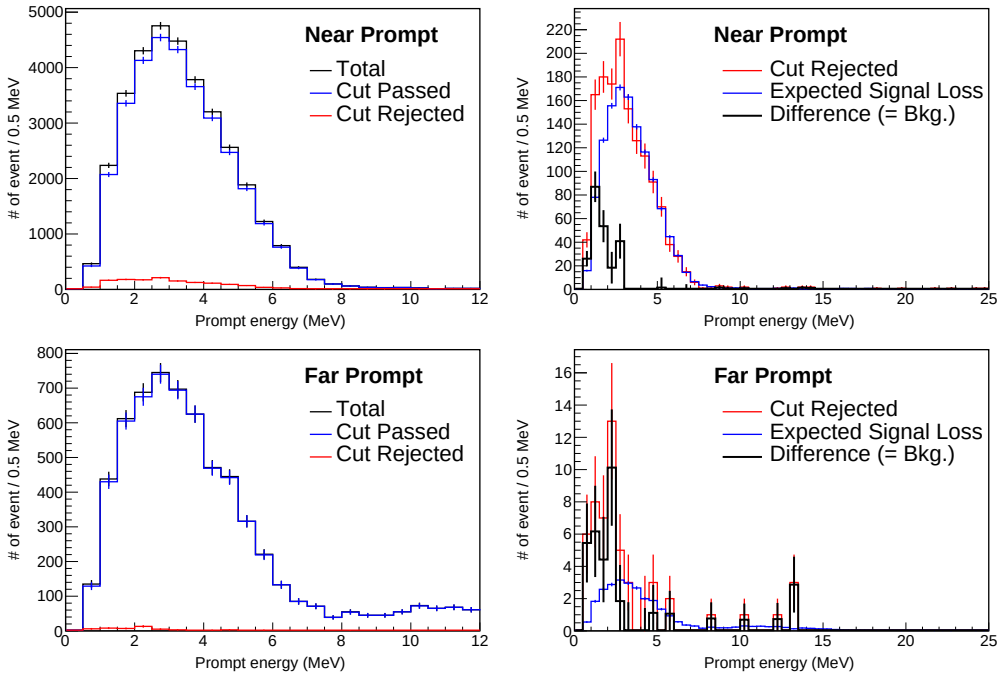

Figure 6.20: Prompt spectra before and after buffer and veto trigger after 200 μs veto cut. Of the upper plots, the left image shows the near detector and the right image shows the far detector. The right plots are before the cut (black), after the cut (blue), and rejected by the cut (red). The left plots are rejected by the cut (red), expected signal loss due to the cut (blue) and the difference between these two histograms (black). The black histogram in the left plots shows the rejected background by the cut.

6.5 Removal of Background associated with cosmic-rays

Neutrons can be produced as result of interactions between muons and the protons inside or outside the detector. Such neutrons could enter the detector, be captured, and mimic the prompt or delayed signals of IBD candidates. Therefore these events from the muon need to be cut. We chose to reject events within 1 ms after the muon event. The veto time window (1 ms) was decided in consideration of efficiency. Muons consist of two kinds : one which passes through the Buffer (muon1), and one shortly passes through the veto region then deposits a large amount of energy in the veto (muon2).

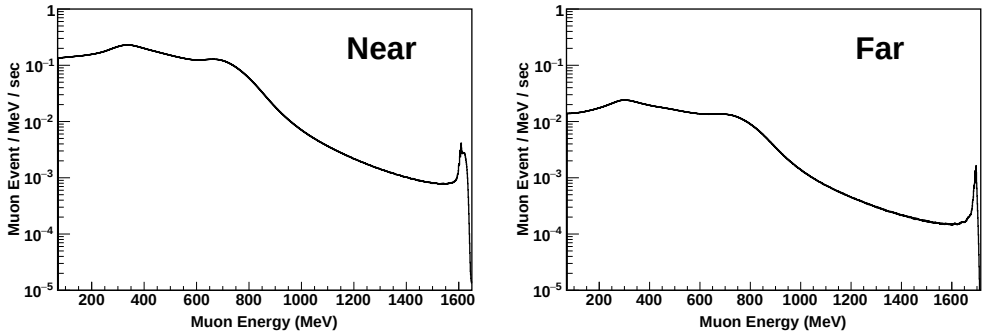

Figure 6.21: Muon visible energy spectra. The left image shows the muon spectrum of the near detector and the right image shows the muon spectrum of the far detector. The spectrum shows a peak at near 1600 MeV. The muon deposit energy is directly proportional to the length of trajectory in the detector. Therefore, the maximum muon energy has a dependence on detector size.

The observed energy of the reactor neutrino events is below 12 MeV. However, muon1 deposited large energy at the buffer region. We defined the muon1 event to be that which deposited energy of more than 70 MeV at the buffer. Muon2 deposited large energy at the veto region and small energy at the buffer. The criteria for muon2 is a deposition of more than 20 MeV at the buffer and a number of hits in the veto region is greater than 50. Muon1 can deposit very high energy. If muons have enough energy, it can make ^{9}Li or ^{8}He. As mentioned in the previous section, ^{9}Li/^{8}He decay with a long lifetime also emits neutron, can mimic the IBD process and give severe background. To reduce ^{9}Li and ^{8}He backgrounds, the cut time range has to be much longer than that of any other veto cuts. Because the half-life of ^{9}Li (^{8}He) is 119.1 ms (178.3 ms), the ^{9}Li and ^{8}He events are timely correlated with the muons. They can be selected by the time distribution since the last muon (t) for all IBD candidate events, and the time distribution can be modeled by a combination of two exponential functions [67].

$$f(t) = B \cdot \exp\left(-\frac{t}{\lambda}\right) + S \cdot \exp\left(-\frac{t}{T}\right), \ \frac{1}{\lambda} = \frac{1}{\tau} + \frac{1}{T} \tag{6.1}$$

where B and S are the magnitudes of ^{9}Li and ^{8}He and other IBD candidates, T is the mean time interval between two adjacent muons, and the inverse of the muon rate, τ is the lifetime of ^{9}Li and ^{8}He, and λ is the effective lifetime of ^{9}Li and ^{8}He due to interruption by the muons. Fig. 6.21 shows the muon rate per megaelectronvolt which is increased as muon energy decreases. The faster the muon rate, the faster the ^{9}Li and ^{8}He effective decay time. According to the

Fig. 6.22, Muon1 is separated by type A, B, and C, which each have different muon visible energy ranges each other. Depending on the muon visible energy, different ranges of time windows for rejecting muon-associated events are used. The ranges are determined such that the efficiency on the signal does not change significantly for each range.

Muon	Far		Near	
Type	Energy	Rate (Hz)	Energy	Rate (Hz)
A	> 1.5 GeV	0.047	> 1.6 GeV	0.107
B	$1.2 \sim 1.5$ GeV	0.081	$1.5 \sim 1.6$ GeV	0.081
C	$1.0 \sim 1.2$ GeV	0.157	$1.4 \sim 1.5$ GeV	0.091
1	$0.07 \sim 1.0$ GeV	12.854	$0.07 \sim 1.4$ GeV	117.193
2	$20 \sim 70$ MeV	0.258	$20 \sim 70$ MeV	0.759

Table 6.4: Rate of muons. Muon rate of the near detector is higher than that of the far detector. Since, the near site's mountain is 70 m high, and the far site's mountain is 200 m high, muon shielding is more powerful at the far site than near site.

- Far Muon A (> 1.5 GeV) : Veto all events within a 700 ms window following muon A at the far detector.
- Far Muon B ($1.2 - 1.5$ GeV) : Veto all events within a 500 ms window following muon B at the far detector.
- Far Muon C ($1.0 - 1.2$ GeV) : Veto all events within a 200 ms window following muon C at the far detector.
- Near Muon A (> 1.6 GeV) : Veto all events within a 700 ms window following muon A at the near detector.
- Near Muon B ($1.5 - 1.6$ GeV) : Veto all events within a 400 ms window following muon B at the near detecter.
- Near Muon C ($1.4 - 1.5$ GeV) : Veto all events within a 200 ms window following muon C at the near detector.
- Muon 1 (Far : $0.07 - 1.0$ GeV, Near : $0.07 - 1.4$ GeV) : Veto all events within a 1 ms window following muon 1.
- Muon 2 (Far, Near :$20 - 70$ MeV, the number of hits in the outer detector > 50): Veto all events within a 1 ms window following muon 2.

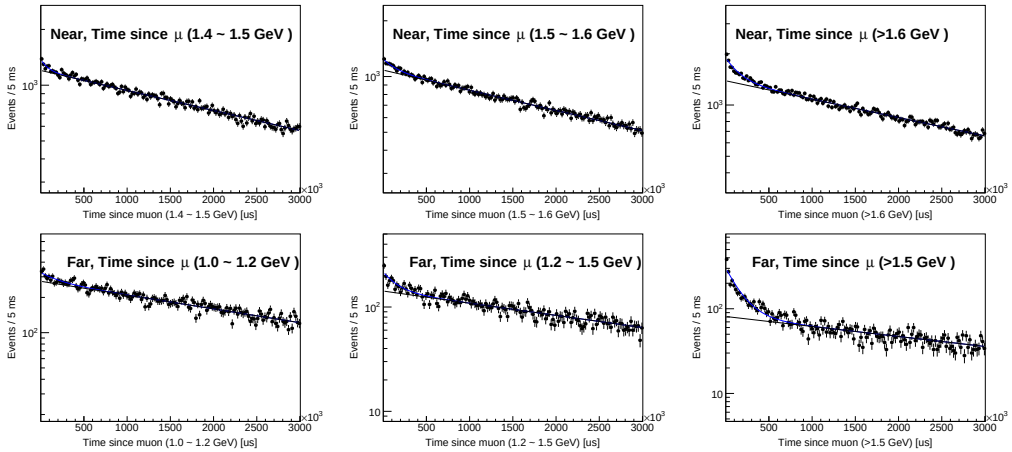

Figure 6.22: Time since muon. The plots are fitted by two exponential function(Eq. 6.1). The black line is the signal component and the red line is the ^{9}Li/^{8}He component. These plots show lower muon energy, fewer observable ^{9}Li/^{8}He events, and a shorter effective ^{9}Li/^{8}He lifetime. Because of the muon rate, it is difficult to find observable ^{9}Li/^{8}He that has below 1.0 GeV (1.4 GeV) muon visible energy at the far (near) detector.

6.6 Removal of Fast Neutron Backgrounds

The IBD event is just a pair of one prompt and one delayed signal. If the pair has multiple prompt or delayed signals, it is not an IBD event. However IBD candidates from fast neutrons have signals before and after the prompt signal with high probability. From this, fast neutron background is rejected using triggers in the vicinity of an IBD candidate pair. For the cut efficiency, 3 types of trigger cuts are used.

- No any trigger within (-100 μs, 0 μs) of prompt signal
- Zero Buffer trigger within (0 μs, 200 μs) of prompt signal
- No prompt-like trigger (-300 μs, 0 μs) of prompt signal (near data only)

6.6.1 Any Trigger Veto Cut

Fig. 6.23 shows the component, which has time correlated with prompt signal. If the pair is a true IBD, It has no signal before the prompt, so this component is not an IBD signal and is a background. According to Fig. 6.23, we decided to

reject a pair which has any trigger within 100 μs before the prompt. The rejection by this veto cut is shown in Fig 6.24. The rejected signals consist of mainly 2.2 MeV hydrogen captured and 8 MeV gadolinium captured event. This means that the rejected signals by this cut are the event from multiple neutron events.

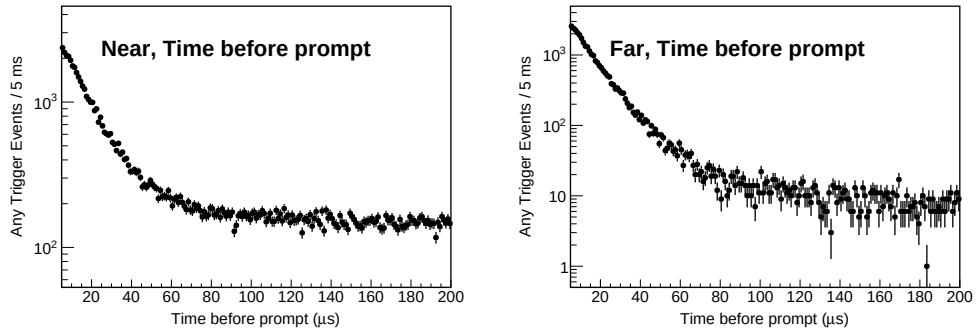

Figure 6.23: Any trigger time distribution before prompt. The left image shows the near detector and the right image shows the far detector.

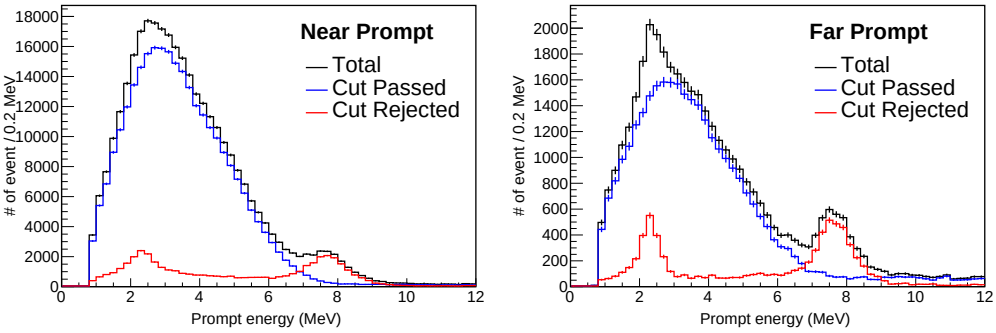

Figure 6.24: The prompt spectra before and after any trigger before the 100 μs veto cut. The left image shows near and the right image shows the far detector. The black histogram shows IBD candidates before the cut. Blue shows after the cut. Red shows rejected by the cut. The red line consists mainly of hydrogen and gadolinium captured neutron events.

6.6.2 Buffer Trigger Veto Cut

There are some components that have a buffer trigger following the prompt signal apart from the delayed neutron signal, as shown in Fig. 6.25. There are a few

events after 200 μs from the prompt signal. According to Fig. 6.25, we decided to reject pair that have buffer triggers within 200 μs after the prompt. The rejected signals by this veto cut are shown in Fig. 6.26. The rejected signals consist of mainly the flat component (= fast neutron, as discussed in chapter 7) and some background which is gaussian distributed around 10 MeV.

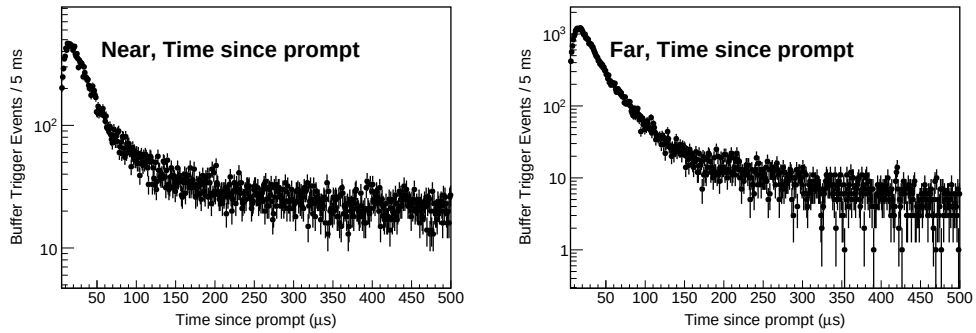

Figure 6.25: Buffer trigger time distribution since prompt. The left image shows the near detector and the right image shows the far detector.

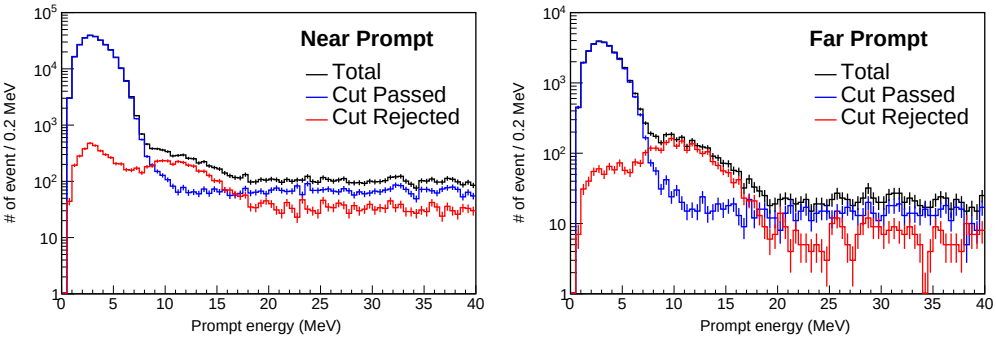

Figure 6.26: The prompt spectra before and after buffer trigger after the 200 μs veto cut. The left image shows the near detector and the right image shows the far detector. The black histogram shows the IBD candidates before the cut. Blue shows after the cut. Red shows rejected by the cut. The red line consists mainly of fast neutron events and unknown component around 10 MeV.

6.6.3 Prompt-like Trigger Veto Cut

The prompt-like trigger is the buffer trigger that is after the muon veto cuts, Qmax/Qtot cut and flasher cut, but with no energy cut applied. As shown Fig. /refsigletdiff, the component which is time correlated with the prompt-like trigger is smaller than that which is buffer trigger correlated and any trigger correlated. We decided to rejected pairs of the near detector that had a prompt-like trigger within 300 μs before the prompt, because it is difficult to find a time correlated with the prompt-like trigger in the far detector. The rejected signals by this veto cut are shown Fig. 6.28. The rejected events seem like hydrogen captured neutron events, But are too small to be identified.

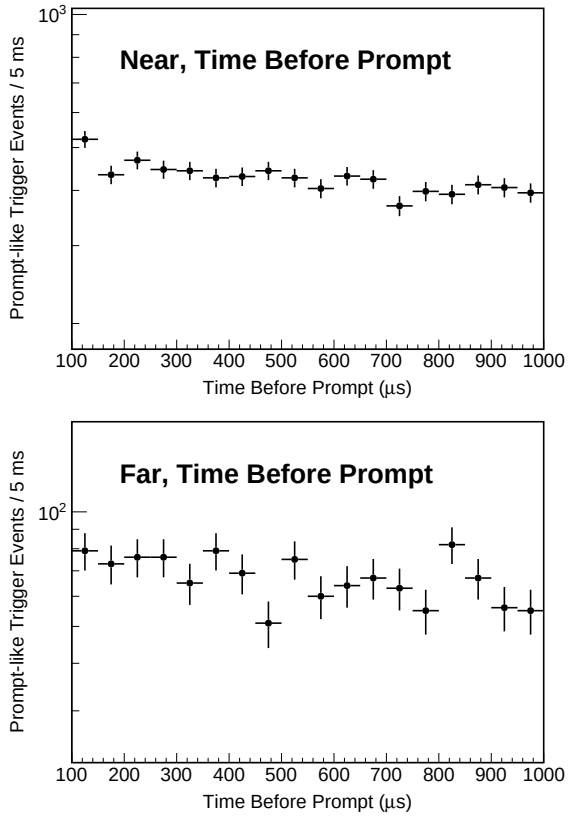

Figure 6.27: Prompt-like trigger time distribution before prompt. The top image shows the near detector and the bottom image shows the far detector.

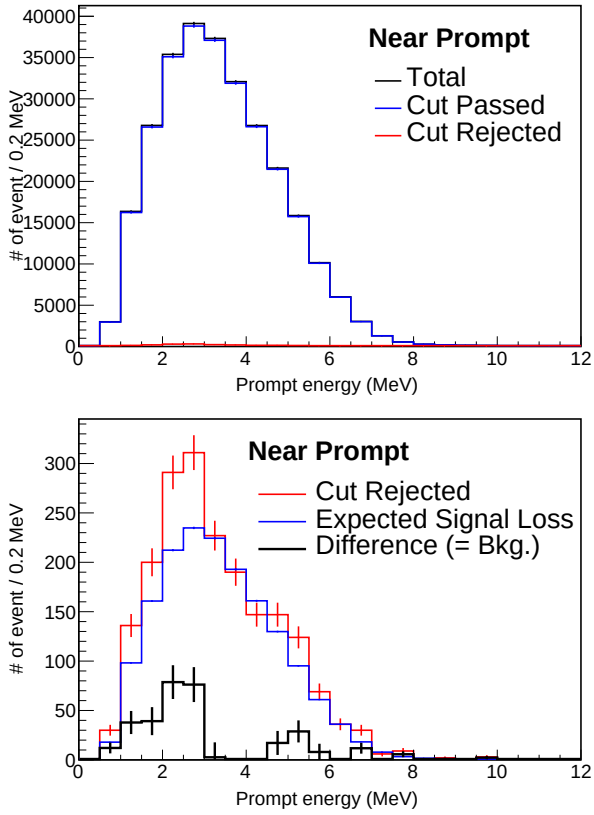

Figure 6.28: Prompt spectra before and after prompt-like trigger before 300 μs veto cut. The bottom plots are before the cut (black), after the cut (blue), and rejected by the cut (red). The top plots are rejected by the cut (red), expected signal loss due to the cut (blue) and the difference of these two histograms (black). The black histogram in the top image indicates the rejected background by the cut.

6.7 Removal of ^{252}Cf contamination

As mentioned in the previous section, ^{252}Cf emits an average of 3.7 neutrons per fission[][]. Using these properties, the Cf removal cuts were developed. The Cf removal cuts consist of three kinds: time correlated, spatial correlated and time and spatial correlated veto cuts. The after and rejection of the cf removal cuts are shown in Fig. 6.30. By the Cf removal cut, the backgrounds due to the ^{252}Cf contamination are reduced by 75%.

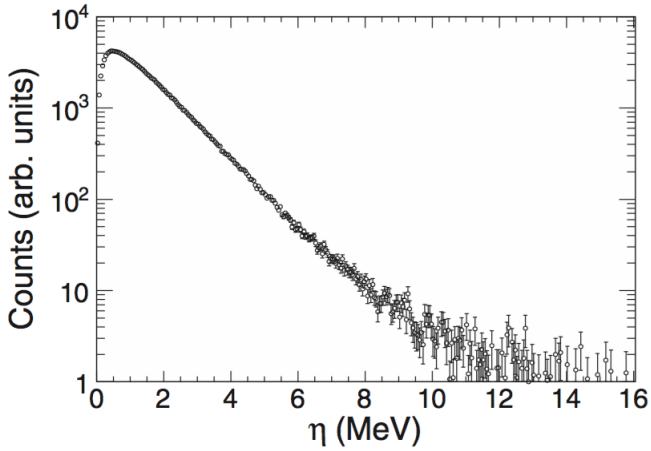

Figure 6.29: Neutron energy spectrum from ^{252}Cf[]

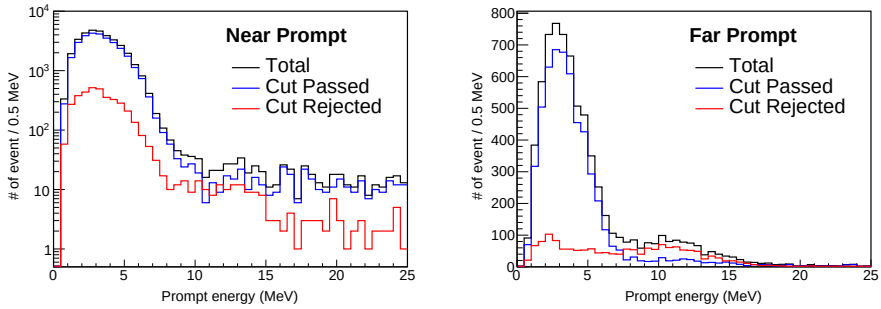

Figure 6.30: Prompt spectra before and after Cf removal cut. The right image shows the far detector, and the left plot shows the near detector. Black shows before the cut, blue shows after the cut, and red shows rejected by the cut.

6.7.1 Time Correlated Veto Cut

The time correlated veto cuts use trigger information before and after the prompt signal. The time correlated veto cut consists of 1 kind: the prompt-like trigger veto cut.

- No prompt-like trigger within (-300 μs, 1000 μs) of prompt signal

Prompt-like Trigger Veto Cut

To remove ^{252}Cf, the prompt-like triggers before and after prompt signal are used. According to Fig. 6.31 and Fig. 6.33, we decided to reject pair which has a prompt-like trigger within 300 μs before the prompt and 1 ms after the prompt. The rejected signals by the before 300 μs cut consist of mainly 2.2 MeV hydrogen captured neutron events, and the rejected by the after 1 ms cut consist of backgrounds are around 8 MeV, 10 MeV and the low energy region.

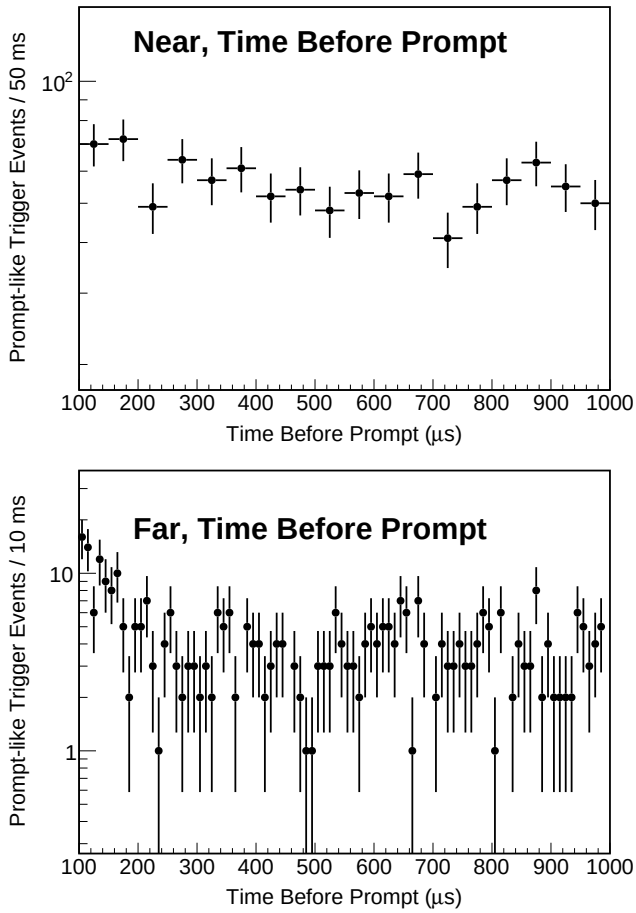

Figure 6.31: Prompt-like trigger time distribution before prompt. The top image shows the near detector and the bottom image shows the far detector.

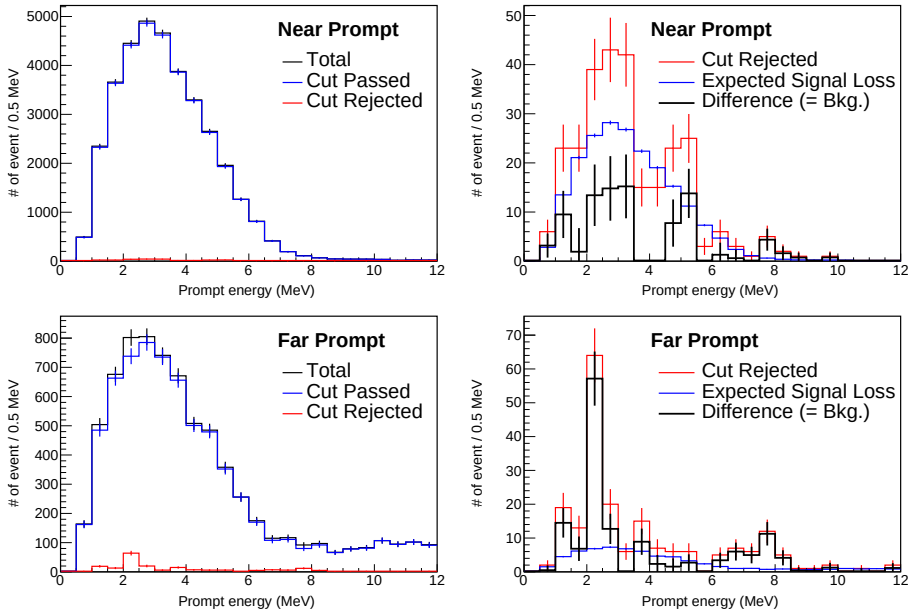

Figure 6.32: Prompt spectra before and after prompt-like trigger before the 300 μs veto cut. Of the upper plots, the left image shows the near detector and right image shows the far detector. The right plots are before the cut (black), after the cut (blue), and rejected by the cut (red). The left plots are rejected by the cut (red), expected signal loss due to the cut (blue), and the difference between these two histograms (black). The black histogram in the left plots shows the rejected background by the cut.

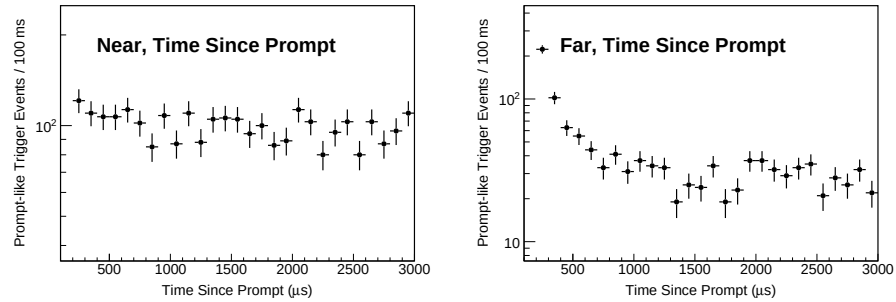

Figure 6.33: Prompt-like trigger time distribution since prompt. The left image shows the near detector and and right image shows the far detector.

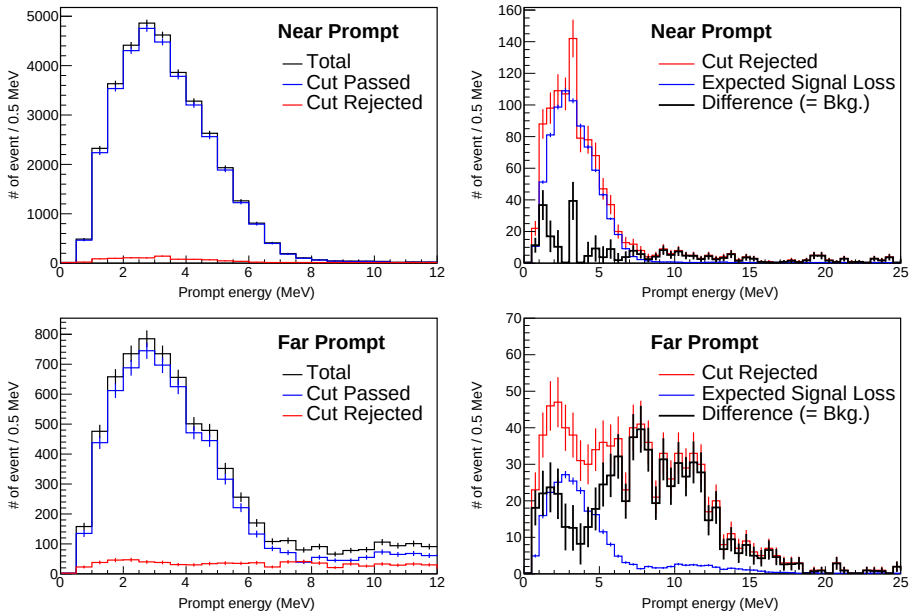

Figure 6.34: Prompt spectra before and after prompt-like trigger after the 1000 μs veto cut. Of the upper plots, the left image shows the near detector and the right image shows the far detector. The right plots are before the cut (black), after the cut (blue), and rejected by the cut (red). The left plots are rejected by the cut (red), expected signal loss due to the cut (blue), and the difference between these two histograms (black). The black histogram in the left plots shows the rejected background by the cut.

6.7.2 Spatial Correlated Veto Cut

As shown in Fig. 6.35, There is a hotspot in the center of the bottom of the far target. However, the near target has no hotspot. Because, ^{252}Cf has a heavier mass than that of the Gd-LS, some fragments of ^{252}Cf were drowned at the center of the bottom of the far target. Fig. 6.36 shows the sinking process of the ^{252}Cf fragments. To remove these backgrounds, as shown in Fig. 6.37, we decided to remove the IBD candidates which the prompt signal of the IBD candidate is in the region $\sqrt{(X-125)^2+(Y-125)^2} < 300$ mm and - 1700 mm $<$ Z $<$ -1200 mm for the far detector only.

- No prompt signal in the region $\sqrt{(X-125)^2+(Y-125)^2} < 300$ mm and - 1700 mm $<$ Z $<$ -1200 mm.

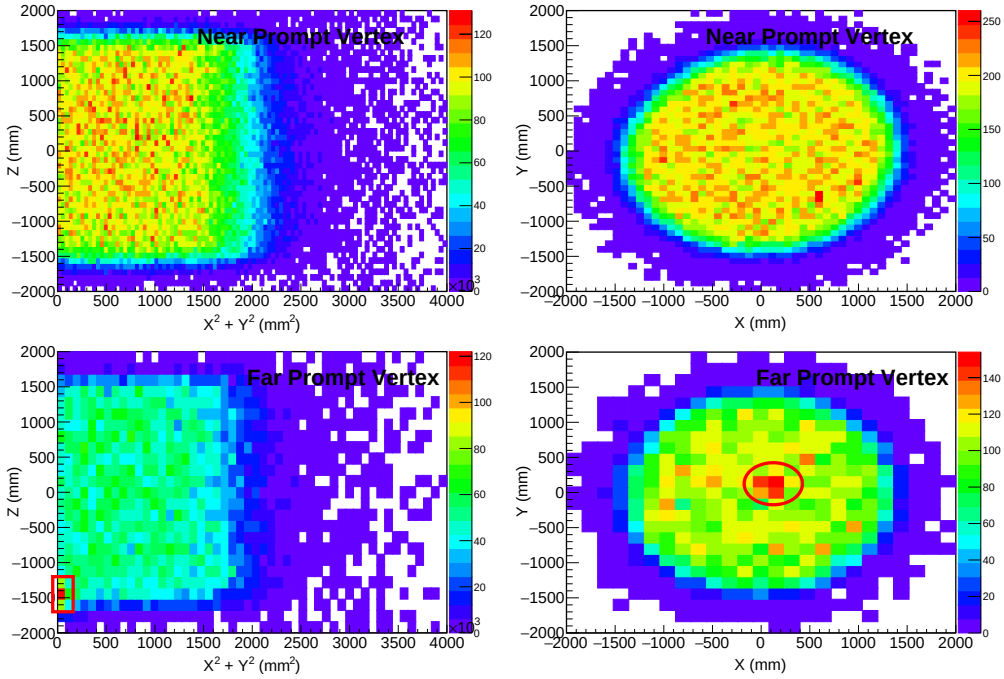

Figure 6.35: Vertex distribution of prompt. Upper plots are from the near detector and the lower plots are from the far detector. The left plots are vertex distributions of Z and $X^2 + Y^2$ plain. The right plots are vertex distributions of X and Y plain. There is a hotspot in the bottom center of the far target. and The near detector does not show a hotspot.

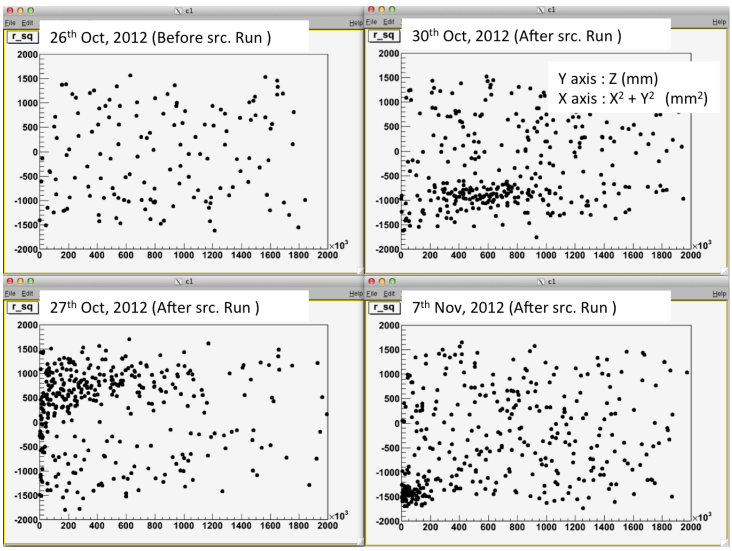

Figure 6.36: ^{252}Cf sinking to the bottom of the far target. Before the ^{252}Cf contamination, there was no hotspot as shown in the upper left plot. After taking the ^{252}Cf source run, the Backgrounds from ^{252}Cf were in target center and upper side as shown in the lower left plot. Three days after the source run day, the ^{252}Cf events sank as shown in the upper right plot. Lastly, the ^{252}Cf events were gathered at the center of the bottom of the target, as shown in the lower right plot.

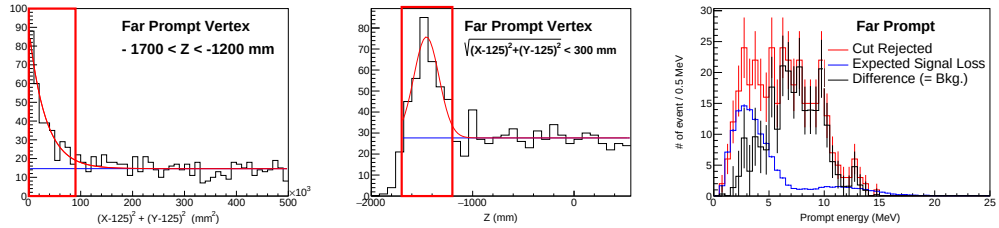

Figure 6.37: Criteria of hot spot removal cut and cut rejected spectrum. The left image is the $(X-125)^2+(Y-125)^2$ distribution of the prompt in the condition -1700 mm $<$ Z $<$ -1200 mm. The middle plot is the Z distribution of the prompt in the condition $\sqrt{(X-125)^2+(Y-125)^2} < 300$ mm. The right image is the spectra of cut rejected (red), the expected signal loss (blue) and the rejected background (black). The right plot shows the rejected backgrounds by the hotspot removal cut are 8 MeV with a gaussian component.

6.7.3 Time and Spatial Correlated Veto Cut

Since ^{252}Cf emits multiple neutron and other particles, the backgrounds due to ^{252}Cf contamination have many temporally and spatially correlated prompt-like triggers near the prompt. Fig. 6.38 shows the time and spatial correlation between the prompt and prompt-like triggers. However, the prompt-like trigger rate is too high to be able to use an entire energy range. Fig. 6.39 shows the prompt-like trigger consists of mainly low energy events. For the efficiency, prompt-like triggers less than 3 MeV are dropped out. Fig. 6.40 and Fig. 6.41 clearly show a correlation of shorter than 400 mm and less than 10 sec. We decided to remove IBD candidates with prompt-like triggers greater than 3 MeV within the time range from -10 to 10 s and a of distance 400 mmmm; we called this cut ΔR-Cf Cut.

- No prompt-like trigger greater then 3 MeV within (-10 s, 10 s) and (0, 400 mm) of prompt signal

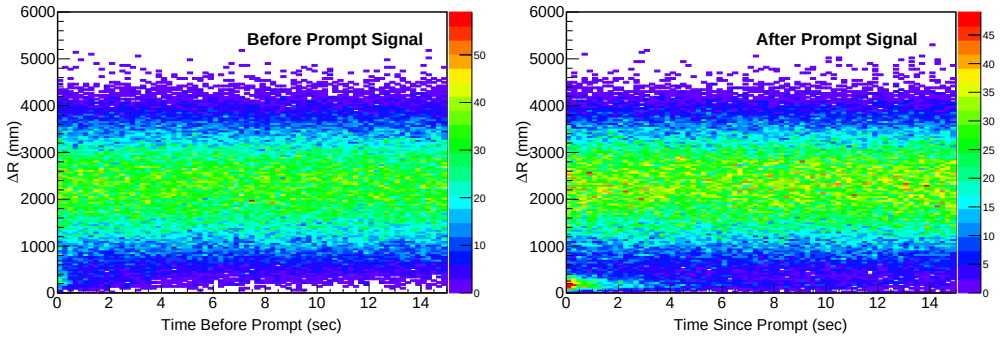

Figure 6.38: ΔR and ΔT distribution between prompt-like trigger and prompt. The left image shows the relation of the prompt and prompt-like trigger occurring before the prompt. The right image shows the relation of the prompt and prompt-like trigger occurring after the prompt. There are some correlated components in the region $\Delta R < 400$ mm.

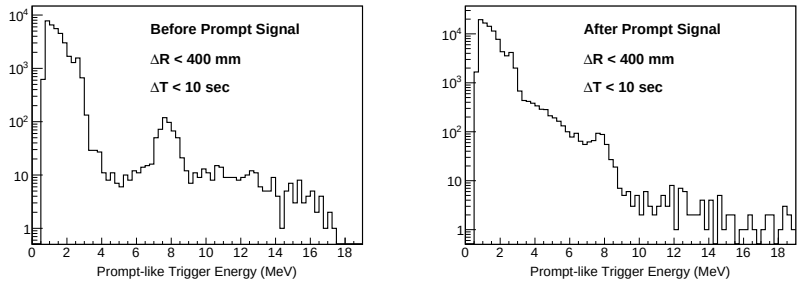

Figure 6.39: Spectrum of the prompt-like trigger with $\Delta R < 400$ mm and $\Delta T < 10$ s. The top image shows the prompt-like trigger spectrum occurring before the prompt. The bottom image shows the prompt-like trigger spectrum occurring after the prompt.

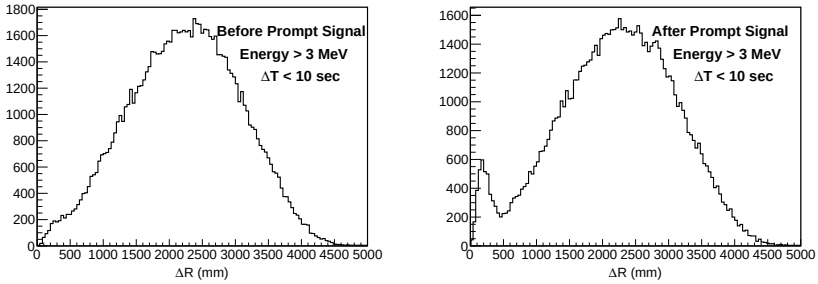

Figure 6.40: ΔR distribution between prompt and prompt-like trigger greater than 3 MeV with $\Delta T < 10$ s.

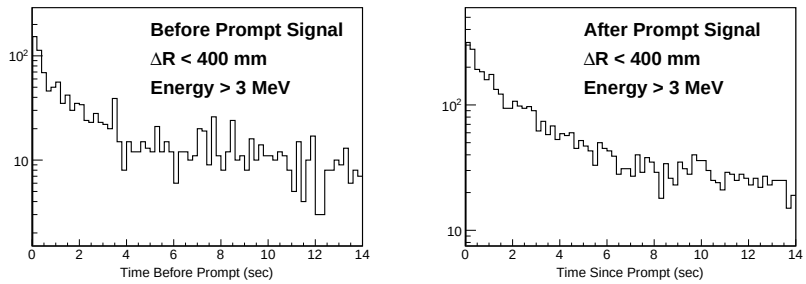

Figure 6.41: ΔT distribution between prompt and prompt-like trigger greater than 3 MeV with $\Delta R < 400$ mm.

Events rejected by the ΔR-Cf cut consist of 2 kinds: low energy peaked and around 12 MeV peaked. The low energy peaked has correlated prompt-like trigger before prompt. On the other hand, the 12 MeV peaked is correlated with prompt-like trigger after prompt, as shown in Fig. 6.42 and Fig. 6.43. For this reason, The ΔR-Cf cut is divided into 2 kinds : before cut and after cut.

- ΔR-Cf before cut: No prompt-like trigger greater than 3 MeV within (-10 s, 0 s) and (0, 400 mm) of prompt signal
- ΔR-Cf after cut: No prompt-like trigger greater then 3 MeV within (0 s, 10 s) and (0, 400 mm) of prompt signal

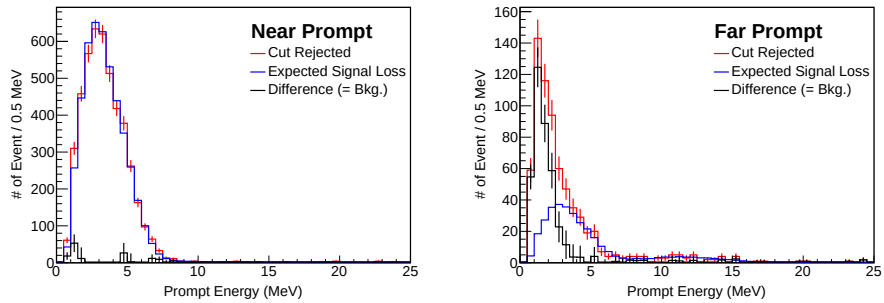

Figure 6.42: Prompt spectra rejected by ΔR-Cf before cut. The left image shows the near detector and the right shows the far detector.

ΔR-Cf After 10 sec Cut

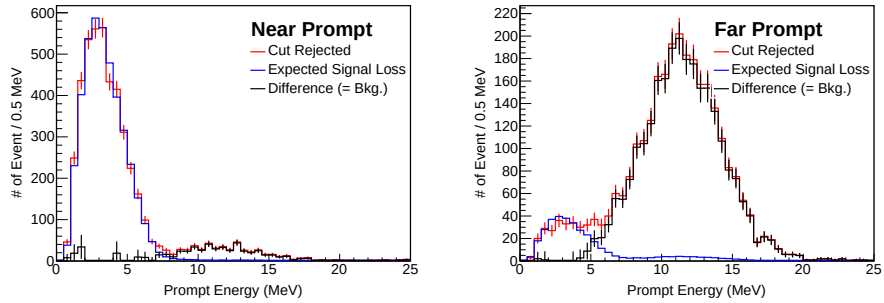

Figure 6.43: Prompt Spectra rejected by ΔR-Cf after cut. The left image shows the near detector and the right shows the far detector.

ΔR-Cf cut is applied to both the far and near detectors although the cut has more efficiency for the far detector than the near detector, as shown in Fig. 6.42 and Fig. 6.43. Because backgrounds from ^{252}Cf are not yet fully understood, they must be removed as much as possible. The expected signal loss of the ΔR-Cf cut is $1 \sim 2$ %. It does not affect statistics of the entire data set.

6.8 Signal Loss from IBD Selection

6.8.1 Signal Loss from Time Coincidence

We require the coincidence time window for the prompt and delayed event to be 2μsec $\sim$ 100μsec. The mean lifetime of neutron capture by Gd is $\sim 30\mu$sec; hence, lifetimes longer than 100μsec are negligible. If we increase the coincidence time window to be more than 100μsec, the increased events will be negligible and accidental background will increase. The efficiency for this coincidence time window is 96.20%.

There is one more inefficiency. The capture time distribution should be exponentially decrease. However, Figure B.1 shows that both the Monte-Carlo simulation and final data sample have a rapidly increase structure between the $2-13$ μsec region. The inefficiency between the $2-13$ μsec capture time is 13.04% for the data and 8.81% for the Monte-Carlo simulation. The difference is 4.23%, so we subtract this difference to the original efficiency to compensate for the difference between the data and the Monte-Carlo simulation. The final calculated efficiency is therefore 91.07%, and signal loss from the time coincidence is 8.93%.

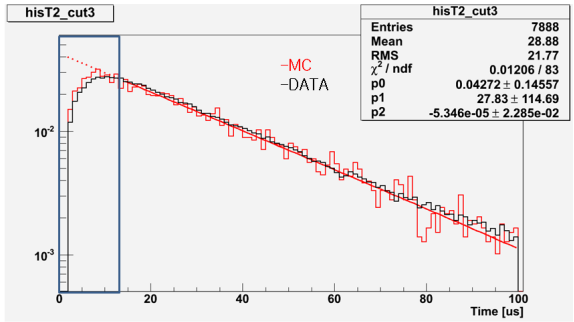

Figure 6.44: Capture time distribution of final data sample and Monte-Carlo simulation. There is a rapidly increasing structure between $2-13\mu$sec and the dashed line is the extrapolation curve of exponential fitting of the greater than 13μsec region. The difference of the extrapolation curve and capture time distribution is considered to be the inefficiency.

6.8.2 Signal Loss from Energy Threshold

Prompt Energy Threshold

The threshold energy of the prompt signal for the inverse beta decay event is 1.022 MeV, or ∼250 photo-electrons. However in the experiment, we must consider the energy resolution and discriminator efficiency, and so on. The efficiency of the prompt energy cut is 100%, with no signal Loss.

Delayed Energy Threshold

The criterion for the delayed energy cut is 6 MeV−12 MeV. However, Fig. 8.1 shows that there is a long tail below 6 MeV. This portion of the event cannot be selected to the inverse beta decay events. Considering this fractional loss, the efficiency for the delayed energy cut is 94.14%. and the loss from the delayed energy cut is 5.86%.

6.8.3 Signal Loss from Spatial Correlation and Removal of γ-Rays from Radioactivity and Flashers

In the section 6.3, the γ-ray and flasher removal cut ($Q_{max}/Q_{tot} < 0.07$) does not have any signal loss.

6.8.4 Signal Loss from Timing Veto with Muon or Trigger Information

If the trigger is within the cut time range [0,Δt] relative to the prompt of the IBD event, the IBD event is lost by the cut. Because there is no correlation between the prompt of the IBD event and adjacent trigger, signal loss is just the probability that at least one of the triggers is within the cut time window [0,Δt] relative to the prompt of the IBD event and It can be calculated by the Poisson probability distribution. The equation is as follows.

$$P(0, \Delta t) = 1 - e^{-R_{trg}\Delta t}. \tag{6.2}$$

The signal loss from the timing veto cut with muon or trigger information is calculated by equation 6.2. However, there is some modification case by case in the equation 6.2. More details are given in the Appendix.

6.8.5 Signal Loss from Cf Removal

The Cf removal cuts consist of 3 kinds : time correlated , spatial correlated and time and spatial correlated. The time correlated Cf removal cuts also can be calculated by Equation 6.2. The spatial correlated Cf removal cut (hotspot removal

cut) is calculated from signal loss at Set A which does not contain ^{252}Cf contamination. If the hotspot is applied to Set A, the rejected signals are not background from ^{252}Cf contamination, but the IBD and other backgrounds. Therefore, the loss from the hotspot removal cut can be easily estimated. Lastly, the loss from time and spatial correlated (ΔR-Cf cut) is estimated to be a spectral fit to the rejected with IBD candidate. The fitting result is the number of IBD candidates in the rejected. This fitting result is assumed as signal loss. More details are given in the Appendix.

6.9 Summary

Applying IBD event selection criteria, observed IBD candidate events are 290775 (31541) at the near (far) detector from Set A and B, which have a total live time of 458.49 (489.93) days in the near (far) detector. Below is a summary of observed IBD candidate for Set A and Set B.

NEAR		
Data Set	Observed IBD Candidate	DAQ live time (days)
A	261338	379.66
B	29437	78.83
A+B	290775	458.49
FAR		
Data Set	Observed IBD Candidate	DAQ live time (days)
A	26579	384.47
B	4962	105.46
A+B	31541	489.93

Table 6.5: Event rate of the observed IBD candidates at $1.2 < E_p < 8.0$ MeV

The signal losses could be divided into two kinds: one is common signal losses of the two detectors and two data set. The other one is uncommon signal losses of the two detectors and two data sets. Common signal losses are from time coincidence, energy cuts of the prompt and delayed signals, the spatial correlation cut and incoming γ-ray and flasher cuts. The common signal losses are assumed to be the same at the far and near detector with time. Uncommon signal losses are from the other selection criteria. The differences are from the event rate varying with time and the difference between the far and near detector environments, such as overburdens. Below is a summary of the signal loss for Set A and Set B. More details are given in Appendix B.

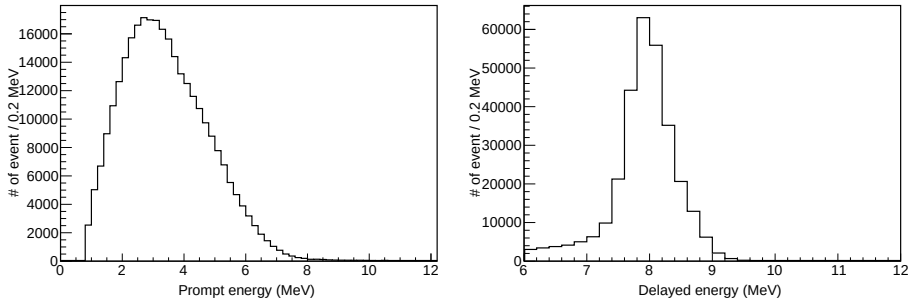

Figure 6.45: Prompt and Delayed Signal Spectrum of Observed IBD candidates

detector	Near		Far	
Data Set	Set A	Set B	Set A	Set B
Common	13.42 ± 0.09%			
Uncommon	13.62 ± 0.00%	20.12 ± 0.10%	26.61 ± 0.00%	33.42 ± 0.04%

Table 6.6: Signal Loss

Chapter 7

Background Estimation

Unfortunately, backgrounds in experimental measurements still remain after applying many selection criteria. The backgrounds can be separated by two major properties: uncorrelated background (accidentals) and correlated background (fast neutrons produced by muons outside the buffer and β-n decay of ^{9}Li/^{8}He also produced by muons, and backgrounds from ^{252}Cf). Each background has two kinds of uncertainties: shape uncertainty and magnitude uncertainty. Shape uncertainty is uncertainty of the backgrounds shape that arises from statistics of the background sample. Magnitude uncertainty is the uncertainty of the amount of background that arises from the background estimation.

7.1 Accidental

A random coincidence of both a prompt-like signal and a delayed-like signal can accidentally survive the applying of several selection cuts. An accidental background is characterized by temporally spatially uncorrelated coincidences between prompt and delayed signals. The ΔT, ΔR (= distance between prompt and delayed signals), and the energy distribution of accidentals are shown Figure 7.1.

The remaining amount of accidental background in the final sample is estimated by a ΔR fitting method. The data has accidental and other backgrounds. They are distinguished by a ΔR distribution, so that the accidental background can be estimated by fitting a ΔR distribution over a large ΔR region. The χ^2 fitting function for estimation of the accidental background is

$$\chi^2 = \sum_i \left(\frac{\Delta R^i_{IBD} - \gamma \cdot \Delta R^i_{Acci.}}{\sqrt{\Delta R^i_{IBD}}} \right)^2 . \tag{7.1}$$

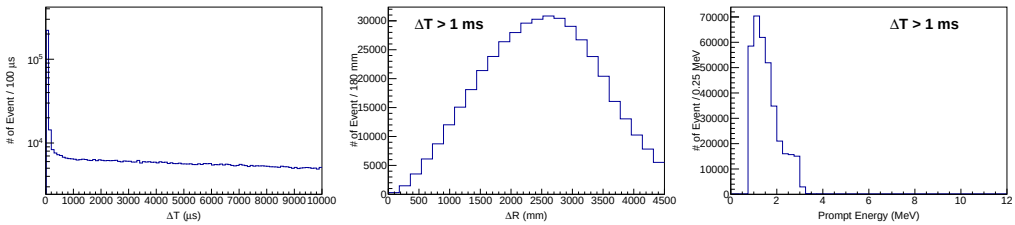

Figure 7.1: Properties of accidental background. The left side plot is the time difference between prompt and delayed signals (=ΔT). There are only accidentals in the $\Delta T > 1$ ms region. The slow sloped component is accidental. The middle plot shows the distance between prompt and delayed signals (=ΔR) of accidental. The peak is around 2500 mm. It shows the difference between other backgrounds and IBD, which has a spatial correlation between prompt and delayed signals, as shown in Figure 6.16. The right plot shows the prompt energy spectrum of the accidental background.

where, $\Delta R^{i}_{IBD,(Acci.)}$ is ith bin of IBD (Accidental) ΔR distribution. The fitting parameter γ represents a normalization factor between the ΔR distribution of the accidental sample and the ΔR distribution of the accidental background in the IBD sample. The obtained accidental background in the final IBD sample is

$$\text{Accidental}(1.2 \sim 8MeV, \Delta R < 2.5m) = \gamma \cdot \Delta R^{(1.2\sim 8MeV, \Delta R<2.5m)}_{Acci.} \tag{7.2}$$

The shape uncertainty of the obtained accidental background is

$$\delta^{Shape}_{Acci.} = \gamma \cdot \Delta R^{(1.2\sim 8MeV, \Delta R<2.5m)}_{Acci.} \cdot \delta n^{1.2\sim 8MeV}_{Acci.} \tag{7.3}$$

where $\delta n^{1.2\sim 8MeV}_{Acci.}$ is the uncertainty of the normalized accidental spectrum. The magnitude uncertainty obtained is $\delta^{Magnitude}_{Acci.} = \delta\gamma \cdot \Delta R^{(1.2\sim 8MeV, \Delta R<2.5m)}_{Acci.}$. The results of accidental estimation are summarized in Table 7.7.

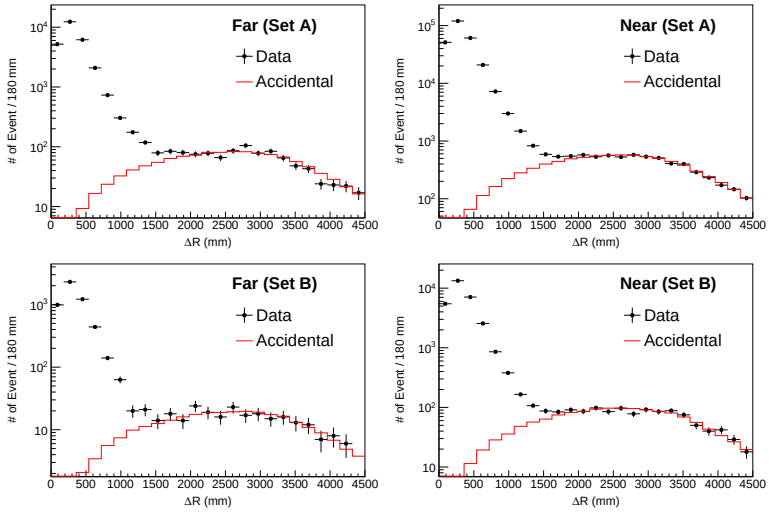

Figure 7.2: Fitting results of accidental estimation.

Detector	Data Set	Rate	Shape Uncert.	Mag. Uncert..	Total Uncert..
Far	Set A	0.989	0.009	0.033	0.035
	Set B	0.919	0.015	0.061	0.063
	Set A+B	0.974	0.008	0.029	0.030
Near	Set A	7.127	0.024	0.092	0.095
	Set B	5.769	0.046	0.179	0.185
	Set A+B	6.893	0.021	0.082	0.085

Table 7.1: Estimated rate of accidental background in per day, Energy Range: $1.2 - 8$ MeV.

7.2 Fast Neutron

An energetic neutron produced from a muon can travel many meters transmitting energy to a proton by elastic scattering and finally being captured by Gd or H. The recoil proton due to neutron scattering can be prompt, and the Gd captured neutron can be delayed of IBD candidate. To estimate the fast neutron rate, when extending the prompt energy criteria up to 60 MeV, the IBD candidates under the extended prompt energy criteria have a flat high energy tail above 12 MeV and 22 MeV (= data set B) as shown Figure 7.3.

The estimation method for fast neutrons involves extrapolating the flat fitting result from the high energy region into the IBD energy region. The results of the fast neutron estimation are summarized in Table 7.7.

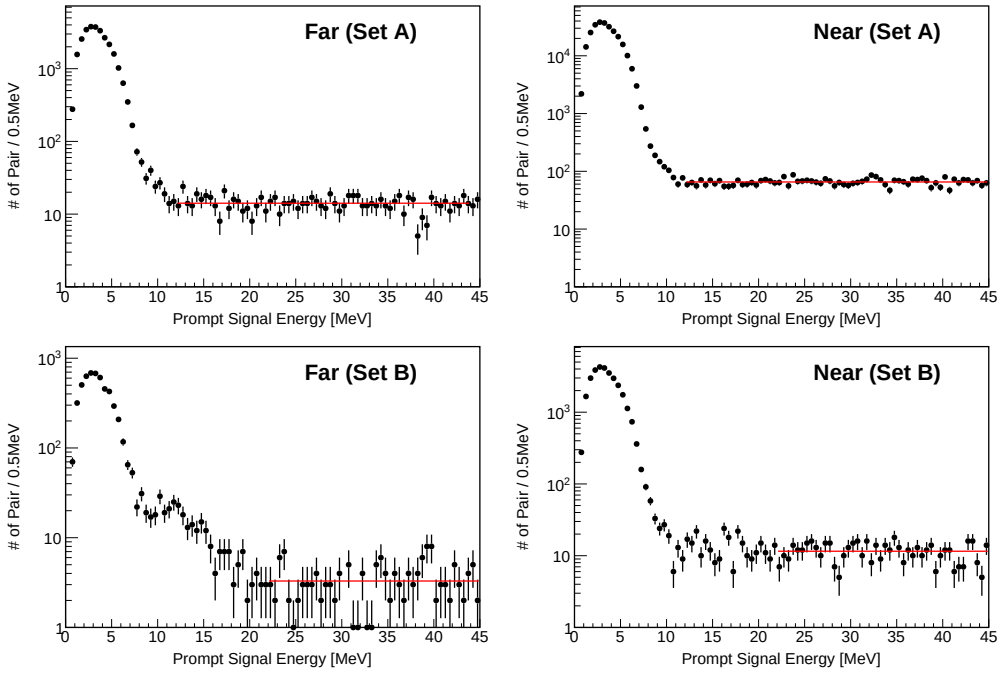

Figure 7.3: Fitting results of the fast neutron estimation

The spectrum of a fast neutron is usually described by a flat distribution. However, since we do not know the real spectrum of the fast neutron, we add an uncertainty from a model (= shape uncertainty). The difference between the fitting result of a fast neutron dominant sample with fitting model consisting of the 0^{th} polynomial and $1st$ polynomial is treated as a shape uncertainty of fast neutrons. The estimated fractional shape uncertainty of fast neutron is 1.25% for the far detector and 1.20% for the near detector. More details concerning the shape uncertainty of fast neutron are given in Appendix C.

Detector	Data Set	Rate	Shape Uncert.	Mag. Uncert..	Total Uncert..
Far	Set A	0.500	0.006	0.017	0.018
	Set B	0.425	0.005	0.034	0.034
	Set A+B	0.483	0.005	0.015	0.016
Near	Set A	2.342	0.028	0.036	0.045
	Set B	1.991	0.024	0.085	0.088
	Set A+B	2.282	0.023	0.033	0.040

Table 7.2: Estimated rate of the fast neutron background in per day, Energy Range: $1.2 - 8$ MeV.

7.3 ^{9}Li / ^{8}He

^{9}Li/^{8}He are produced by interaction between cosmic muons and carbon in the detector. These isotopes have β and neutron cascade decay modes. Since ^{9}Li has a half life time of 0.178 sec and a Q value of 13.6 MeV, and ^{8}He has a half life time of 0.119 sec and a Q value of 10.7 MeV, these isotopes are hard to distinguish from the IBD process.

The spectrum of ^{9}Li/^{8}He is obtained from the time difference distribution between IBD candidate events and high energy muons,as shown in Figure **??**. there are 3 components: Mu-accidental, ^{9}Li/^{8}He and other IBD and backgrounds. The spectrum of ^{9}Li/^{8}He through the fitting with three exponential function models is shown in Figure 7.5. More details are the Appendix D.

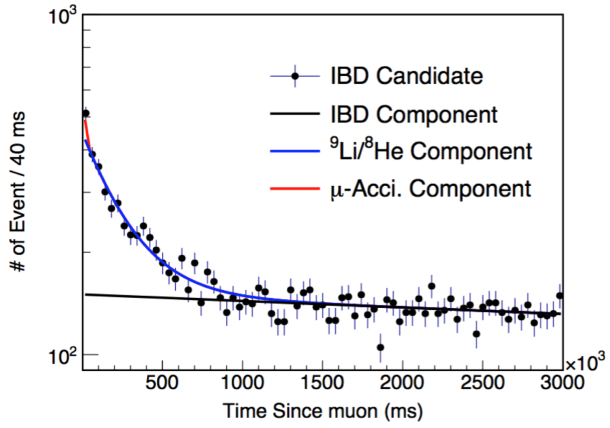

Figure 7.4: Time difference between IBD candidate and adjacent high energy Muon ($>$ 1.5 GeV).

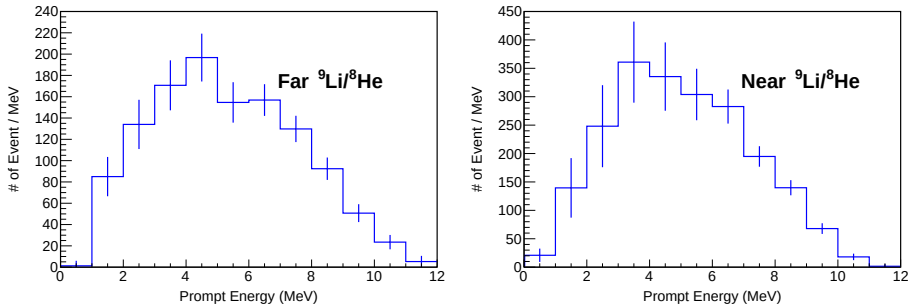

Figure 7.5: Spectrum of ^{9}Li/^{8}He

The ^{9}Li/^{8}He background rate in the final sample is obtained by the measured rate in the background dominant region of prompt Energy > 8 MeV. Since ^{9}Li/^{8}He, fast neutrons and small IBD in the region greater than 8 MeV, the amount of ^{9}Li/^{8}He is estimated by a spectral fit. The spectral fitting function is

$$\chi^2 = \sum_{i=8\sim12MeV} \left(\frac{O_i - E_i}{\sqrt{O_i}}\right)^2 + \left(\frac{f}{\sigma_f}\right)^2 + \sum_i \left(\frac{f_{s_i}}{\sigma_{f_{s_i}}}\right)^2 \tag{7.4}$$

where, O_i is IBD candidate data. $E_i = \alpha \cdot n^i_{LH} + n^i_{IBDMC} + (1 + f + f_{s_i}) \cdot n^i_{FN}$. n_{LH}, n_{FN} and n_{IBDMC} represent it's shapes. The fitting parameter α represent the amount of ^{9}Li/^{8}He. The IBD component is borrowed the expected flux from MC. The fast neutron component is constrained by the magnitude uncertainty $(=f)$ and shape uncertainty$(=f_{s_i})$.

The ^{9}Li/^{8}He obtained in the final sample is

$$^9Li/^8He(1.2 \sim 8MeV) = \alpha \cdot n^{1.2\sim8MeV}_{LH}. \tag{7.5}$$

The shape uncertainty of the obtained ^{9}Li/^{8}He is $\alpha \cdot \delta n^{1.2-8MeV}_{LH}$ and the magnitude uncertainty of the obtained ^{9}Li/^{8}He is $\delta\alpha \cdot n^{1.2\sim8MeV}_{LH}$. The results of the ^{9}Li/^{8}He estimation are summarized in Table 7.7.

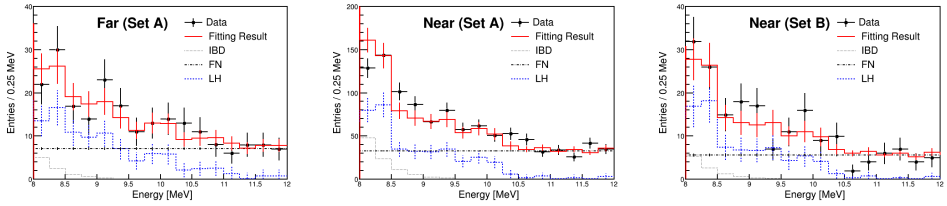

Figure 7.6: Fitting results of ^{9}Li/^{8}He estimation

Detector	Far		
Data Set	Set A	Set B	Set A+B
$n_{LH}^{1.2\sim8MeV}$		1013.5 ± 50.8	
α	0.55 ± 0.08	0.16 ± 0.07	0.71 ± 0.11
^{9}Li/^{8}He rate (per day)	1.52 ± 0.231	1.613 ± 0.64	1.542 ± 0.228
Detector	Near		
Data Set	Set A	Set B	Set A+B
$n_{LH}^{1.2\sim8MeV}$		1856.4 ± 138.8	
α	1.66 ± 0.13	0.35 ± 0.05	2.01 ± 0.14
^{9}Li/^{8}He rate (per day)	8.342 ± 0.861	8.470 ± 1.405	8.364 ± 0.820

Table 7.3: Estimated rate of ^{9}Li/^{8}He estimation in per day, Energy Range: 1.2 − 8 MeV. The estimated ^{9}Li/^{8}He of the far set B is mentioned in the next section.

7.4 Backgrounds due to ^{252}Cf Contamination

Multiple neutron events come from the ^{252}Cf contamination. They could easily mimic IBD candidate pairs. Most of these backgrounds are eliminated by Cf removal cuts so that, backgrounds from ^{252}Cf are small and enough to be ignored in the near detector. However, there still remain a few background events in the far detector. The reconstructed backgrounds shape is shown Figure 7.7(More details are in the Appendix E).

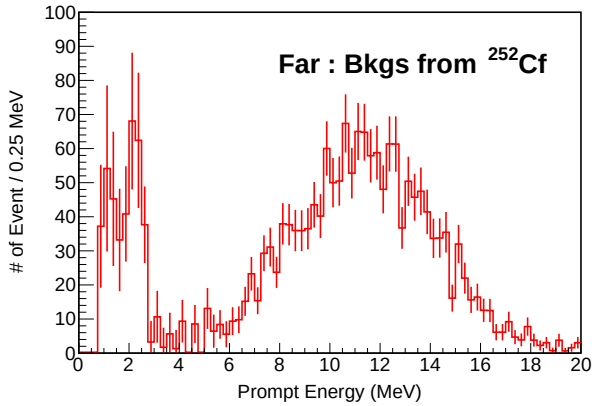

Figure 7.7: Spectrum of backgrounds from ^{252}Cf

The estimation method is the same ^{9}Li/^{8}He. The fitting function for ^{252}Cf

adds an extra term $\beta \cdot n_{cf}^{i}$ to the function for ^{9}Li/^{8}He, so that backgrounds from ^{252}Cf and ^{9}Li/^{8}He are obtained at the same time. The calculation of the amount, shape uncertainty and magnitude uncertainty is similar to that using the ^{9}Li/^{8}He equations. However there is a correlation between the obtained ^{9}Li/^{8}He and the backgrounds from ^{252}Cf. This correlation is taken into account at the magnitude uncertainty of ^{9}Li/^{8}He. The obtained backgrounds from ^{252}Cf in the final sample are

$$\text{Backgrounds from } {}^{252}Cf(1.2 \sim 8MeV) = \beta \cdot n_{Cf}^{1.2\sim 8MeV}. \tag{7.6}$$

The shape uncertainty of the obtained backgrounds from ^{252}Cf is $\beta \cdot \delta n_{Cf}^{1.2\sim 8MeV}$ and the magnitude uncertainty of the obtained backgrounds from ^{252}Cf is $\delta\beta \cdot n_{Cf}^{1.2\sim 8MeV}$. The results of backgrounds from the ^{252}Cf estimation are summarized in Table 7.7.

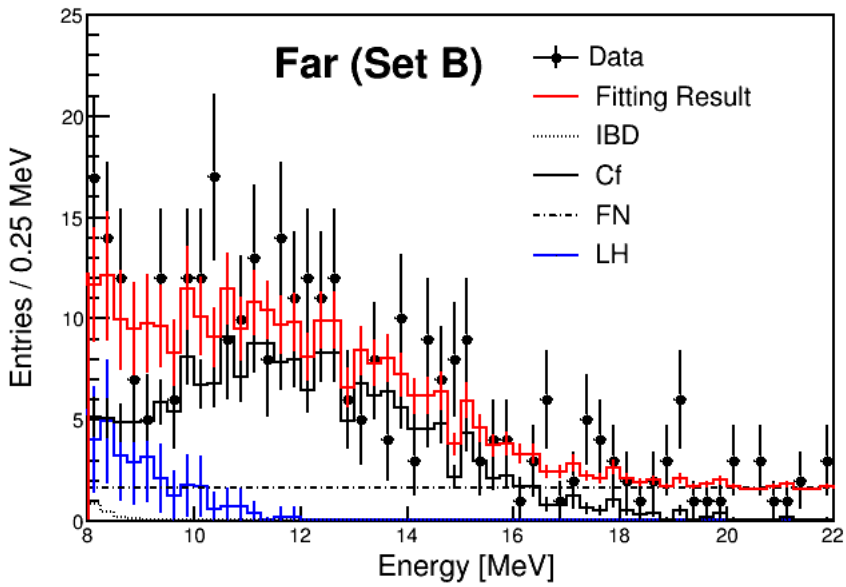

Figure 7.8: Fitting results of backgrounds from the ^{252}Cf and ^{9}Li/^{8}He estimation

Detector	Far
Data Set	Set B
$n_{LH}^{1.2\sim 8MeV}$	1013.5 ± 50.8
α	0.16 ± 0.07
^{9}Li/^{8}He rate (per day)	1.61 ± 0.64
Correlation Coefficient $\rho_{\alpha\beta}$	-0.47
$n_{Cf}^{1.2\sim 8MeV}$	523.2 ± 91.2
β	0.14 ± 0.01
^{252}Cf rate (per day)	0.67 ± 0.14

Table 7.4: The result of ^{9}Li/^{8}He and ^{252}Cf estimation of far data set B, The correlation coefficient between α and β is -0.47. The correlation is taken into account in the magnitude uncertainty of ^{9}Li/^{8}He ($= \sqrt{\left(\delta\alpha \cdot n_{LH}^{1.2\sim 8MeV}\right)^2 + 2 \cdot \rho_{\alpha\beta} \cdot \delta\alpha \cdot n_{LH}^{1.2\sim 8MeV} \cdot \delta\beta \cdot n_{Cf}^{1.2\sim 8MeV}}$

7.5 Summary

The results of the background estimation are summarized in the following tables.

7.5.1 Summary for Data Set A

Background	Far Set A			
	Rate	Shape Uncert.	Mag. Uncert.	Total Uncert.
Accidental	0.989	0.009	0.033	0.035
Fast Neutron	0.500	0.006	0.017	0.018
Li/He	1.522	0.072	0.213	0.231
Total	3.011	0.073	0.216	0.234
Background	Near Set A			
	Rate	Shape Uncert.	Mag. Uncert.	Total Uncert.
Accidental	7.127	0.024	0.092	0.095
Fast Neutron	2.342	0.028	0.036	0.045
Li/He	8.342	0.607	0.610	0.861
Total	17.811	0.608	0.618	0.867

Table 7.5: Summary of estimated background rate in per day for set A. Unit: per day, Energy Range : $1.2 - 8$ MeV.

7.5.2 Summary for Data Set B

Background	Far Set B			
	Rate	Shape Uncert.	Mag. Uncert.	Total Uncert.
Accidental	0.919	0.015	0.061	0.063
Fast Neutron	0.425	0.005	0.034	0.034
Li/He	1.613	0.079	0.634	0.639
Cf	0.671	0.117	0.072	0.137
Total	3.628	0.142	0.642	0.658
Background	Near Set B			
	Rate	Shape Uncert.	Mag. Uncert.	Total Uncert.
Accidental	5.769	0.046	0.179	0.185
Fast Neutron	1.991	0.024	0.085	0.088
Li/He	8.470	0.617	1.263	1.405
Total	16.230	0.619	1.278	1.420

Table 7.6: Summary of estimated background rate in per day for set B. Unit: per day, Energy Range : $1.2 - 8$ MeV.

7.5.3 Summary for Data Set A+B

Background	Far Set A+B			
	Rate	Shape Uncert.	Mag. Uncert.	Total Uncert.
Accidental	0.974	0.008	0.029	0.030
Fast Neutron	0.483	0.005	0.015	0.016
Li/He	1.542	0.074	0.216	0.228
Cf	0.144	0.030	0.025	0.015
Total	3.144	0.079	0.219	0.232
Background	Near Set A+B			
	Rate	Shape Uncert.	Mag. Uncert.	Total Uncert.
Accidental	6.893	0.021	0.082	0.085
Fast Neutron	2.282	0.023	0.033	0.040
Li/He	8.364	0.609	0.550	0.820
Total	17.539	0.610	0.557	0.826

Table 7.7: Summary of estimated background rate in per day for set A+B. Unit: per day, Energy Range : $1.2 - 8$ MeV.

Chapter 8

Systematic Uncertainty

8.1 Detector Efficiency

The signal losses are an inevitable part of signal selections. Additionally, detection efficiency is not a 100%, because RENO detectors are not perfect detectors. Detector efficiency consist of these signal lost from signal selections and detection efficiency. In this section, Detector efficiency is mentioned before the comment about systematic uncertainties.

8.1.1 Efficiency from IBD selection

The Efficiency from IBD selection is calculated with the following equation.

$$\text{Efficiency from IBD selection} = 1 - \text{Signal loss from IBD selection} \tag{8.1}$$

where, the signal loss from IBD selection was summarized in section 6.9.

The efficiency from IBD selections can be sorted into two groups, common and uncommon between the far and near detectors. The common efficiencies between the far and near detectors are listed below.

- Efficiency from time coincidence
- Efficiency from prompt Energy cut
- Efficiency from delayed Energy cut
- Efficiency from spatial correlation cut
- Efficiency from External γ-ray and Flasher cut

Uncommon efficiencies are listed below.

- Efficiency from muon veto cut
- Efficiency from timing veto cut
- Efficiency from Cf removal cut

The common efficiencies are treated as component of the detection efficiency, and the efficiencies are treated independently for each detector and data set.

8.1.2 Detection efficiency

The many causes of detection efficiency are calculated individually in the Monte-Carlo simulation. Descriptions of the each causes are described below.

Trigger Condition

The DAQ device for RENO experiment is the QBEE board. It requires 400 ns for charging time and 560 ns for dead time. These properties of the QBEE board affects Detection efficiency. The buffer trigger condition, which is more than 90 hit within 50-ns time window, is also taken into account. The detection efficiency obtained from the trigger condition is 98.8% from the Monte-Carlo simulation.

Gd Neutron Capture

A Neutron can be captured by either H and Gd. So that the delayed signal of the IBD process has a 2.2 MeV peak due to H capture and a 8 MeV peak due to Gd capture. IBD Candidates of H capture were abandoned for the purity of the IBD sample. because, the delayed signal of H capture is hard to distinguish from the background. The fraction of neutron captures on H is evaluated to be 14.4% and that from Gad is 85.6%. Figure 8.1 shows the energy spectra of the neutron captured by H and Gd.

Spill in

A neutron captured by Gd, not H, is selected as a delayed signal of an IBD event. The Gd is located only at the target region of the detector, so that the events where a neutron was captured by Gd occurred at the target region, only. however, a neutron produced in the target could travel to the outside of target, and be captured by H only. The detection efficiency decrease due to this phenomena that is named spill-out. In the opposite case, a neutron produced in the γ-catcher region could move to the target and be captured either H or Gd. When this neutron is captured by Gd, the number of observed IBD candidates is increased and affects the detection efficiency. This phenomena is named spill-in. The spill-out events

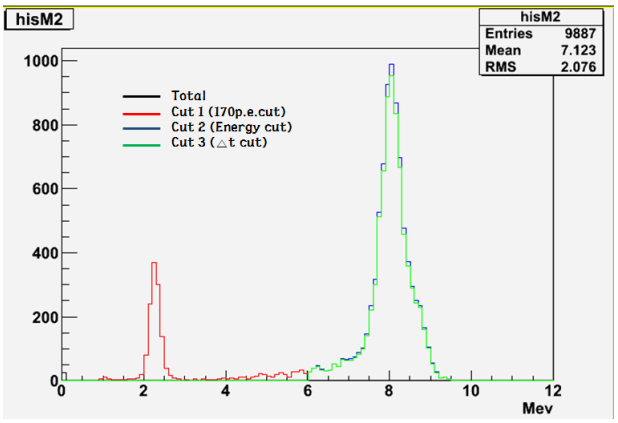

Figure 8.1: Neutron capture by H and Gd. 2.2 MeV peak is H capture and discards this fraction of the event.

are only H captured. and the spill-in events are either H and Gd captured. So that the detection efficiency due to spill-out is unequal to the detection efficiency due to spill-in. From the Monte-Carlo simulation, the excess amount of spill-in is 3.1 %.

Summary of Detection Efficiency

So far, the detection efficiencies of each part are calculated based on the Monte-Carlo simulation and statistics, and are summarized in Table Table 8.2. These detection efficiencies are common in the near and far detectors and the combined common detection efficiency is 75.5±1.4%.

Trigger condition	98.8%
Prompt energy	100.0%
External γ-ray and flasher cut	100.0%
Spatial Correlation	100.0%
Gd neutron capture	85.6±0.7%
Delayed energy $>$ 6 MeV	94.1±0.5%
100μsec coincidence	92.0±0.5%
Spill in	103.1%
Detection efficiency	75.5±1.4%

Table 8.1: Detector efficiency of inverse beta decay events. The calculation is based on the RENO Monte-Carlo simulation.

The final detector efficiency is combined with uncommon efficiency from the IBD selection and summarized in following table.

	Far		Near	
	Set A	Set B	Set A	Set B
Detection Efficiency	75.5 ± 1.4	75.5 ± 1.4	75.5 ± 1.4	75.5 ± 1.4
Efficiency from Selection	86.4 ± 0.0	79.9 ± 0.2	73.4 ± 0.0	66.6 ± 0.04
Total Detection Efficiency	65.2 ± 1.2	60.3 ± 1.1	55.4 ± 1.0	50.3 ± 0.9

Table 8.2: Total efficiency of inverse beta decay events. unit: %

8.2 Detector Related Uncertainty

8.2.1 Common Systematic Uncertainties Related with Detector

IBD cross section

The inverse beta decay cross-section is calculated from the theory. Hence, the uncertainty from the IBD cross-section can be also from the theory, and have no dependence with detectors. Consequently, the uncertainty of the IBD cross-section is only the correlated uncertainty. The value of correlated uncertainty is taken from reference [42], and the value is 0.2%.

Target Protons

The free proton number of the target is 1.189×10^{30}. This value is determined from the measured density of the LAB(=0.85 gL) and target volume measurement with 0.5% correlated uncertainty. The uncorrelated uncertainty of the free proton number is due to the difference of the liquid filled target and the target volume. To reduce the uncertainty from the liquid filled target, 2000 L of the liquid, which is a Gd-Loaded liquid scintillator was produced divided into two 1000 L tanks and filled the targets of the near and far detectors. The measured target volume of the far and near detectors are differ by less than 0.1%, and the uncertainty from the liquid is minimized. From this, we set the uncorrelated uncertainty of free proton number at 0.1%.

Gd capture ratio

The Gd capture ratio depends on the Gd concentration of the Gd-LS. As mentioned in the previous section, the target volume difference between far and near detector is less than 0.1%, so that the difference in Gd concentration between the

far and near detector can be also below the 0.1% level. To derive the systematic uncertainty from the Gd capture ratio, Monte-Carlo simulations were performed with various Gd concentrations. A 0.4% difference in the Gd capture ratio came from a 1% change of Gd concentration according to Monte-Carlo simulations. Since a 0.1% change of in the Gd concentration causes a 0.04% change of Gd capture ratio. We concluded that the uncorrelated uncertainty of Gd capture ratio is 0.1%. and the correlated uncertainty is 0.7% from the neutron capture cross-section.

Delayed Energy Cut

The energy scale affects the observed number of IBD pairs, because it changes the delayed energy cut range in p.e. units. and leads to a systematic error coming from the delayed energy cut. To obtain the uncertainty from the delayed energy selection range, Monte-Carlo simulations are performed within 2% changes of the lower threshold of the delayed energy range. The results of this simulation are summarized in Table 8.3, normalized by the number of events when the lower threshold is 6 MeV. As a result, the uncertainty coming from delayed energy cut is below 0.5% (0.05%) when energy selection range is changed by 2% (0.2%).

Energy cut change	Ecut(MeV)	Event(%)
-2.0%	5.880	100.41
-0.2%	5.988	100.05
0%	6.0	100
+0.2%	6.012	99.95
+2.0%	6.120	99.54

Table 8.3: The change of event with respect to the energy scale difference.

The uncertainty in the energy scale can be calculated from the energy scale difference of the peak value difference of several radioactive isotopes measured between the near and far detectors. The calculated energy scale difference is at ∼0.15% level, so it gives less than ∼0.05% of uncorrelated uncertainty. We determined that the uncorrelated uncertainty from the delayed energy cut is 0.1%, and the correlated uncertainty from the energy scale is below 2%. Therefore, we determined that the correlated uncertainty from delayed energy cut is 0.5%.

Spill in

The neutrons produced outside of the target must penetrate the acrylic vessel to be spill-in events. So that the target acrylic thickness of the target affects the

number of spill-in event, and could be a source of uncertainty of spill-in events. The thickness of the acrylic vessel of the target is 25mm. The uncertainty of the target volume is less than 0.1%. Consequently, the uncertainty in the thickness should be below 1mm. To obtain the uncertainty from spill-in, Monte-Carlo simulations were performed with 1mm changes of acrylic thickness. The result from the Monte-calro shows 0.03% changes of spill-in due to a 1mm change of the acrylic thickness. Therefore, we determined that the uncorrelated uncertainty of spill in is 0.3%.

The Others

The systematic uncertainties from others causes are less than 0.01%. The common systematic uncertainties related to the detectors are summarized in Table 8.4. The overall common uncorrelated systematic uncertainty is 0.2%.

Detector related	Uncorrelated	Correlated
IBD cross section	-	0.2%
Target protons	0.1%	0.5%
Prompt energy cut	0.01%	0.1%
Flasher cut	0.01%	0.1%
Gd capture ratio	0.1%	0.7%
Delayed energy cut	0.1%	0.5%
Time coincidence cut	0.01%	0.5%
Spill-in	0.03%	1.0%
Combined	0.2%	1.5%

Table 8.4: Common Detector related systematic uncertainties.

8.2.2 Uncommon Systematic uncertainties from IBD Selection

The uncommon efficiencies of each detectors and each data sets are different, since these efficiencies came from the difference of signal loss due to the IBD selection. These efficiencies need to be separate from the detection efficiency. The uncertainties of uncommon efficiencies from the IBD selection are given in the Appendix B. Summary of these efficiency uncertainties is shown following table.

Criteria	Far		Near	
	Efficiency	Uncertainty	Efficiency	Uncertainty
Muon Veto Cut	88.80	0.00	78.36	0.00
Timming Veto Cut	97.28	0.00	6.33	0.00
Combined	86.38	0.00	73.39	0.00

Table 8.5: Uncommon Efficiencies from IBD Selection for data set A(%)

Criteria	Far		Near	
	Efficiency	Uncertainty	Efficiency	Uncertainty
Muon Veto Cut	89.22	0.00	79.14	0.00
Timming Veto Cut	97.30	0.00	93.77	0.00
Cf Removal Cut	92.02	0.20	89.72	0.05
Combined	79.88	0.17	66.58	0.04

Table 8.6: Uncommon Efficiencies from IBD Selection for data set B(%)

8.3 Reactor Related Uncertainty

The systematic uncertainties related with the reactor is came from various sources. Expected reactor neutrino flux depends on the fission fraction of four major isotopes, the mean energy released per fission, the thermal power of the reactor and the cross section of fission reaction. The main sources of reactor related uncertainty are the thermal power of the reactor and the fission fraction of four isotopes. The thermal power of the reactor is the measured in an indirect way. at the secondary steam generator of reactor with a 0.5% uncertainty provided from reference [63]. The uncertainty from the fission fraction of the four isotopes is calculated from pseudo experiment. The routine of the pseudo experiment and its results are mentioned in section 3.3. The flux change due to the uncertainty of fission fraction is 0.5% from the pseudo experiment. The maximum difference with the varying fission fraction is 0.6%. Therefore we determined the systematic uncertainty from the fission fraction to be 0.7%.

The systematic uncertainties related with the reactor are not from the difference between the far and near detectors. Even though their origin is from the reactor only, the systematic uncertainties related with the reactor are not from canceled out by comparing the far and near detectors, because the flux contributions of each reactor are different at the far and near detectors due to

the difference in baseline, as summarized in Table **??**. Further details of these uncertainties are in section 3.3.

Reactor related	Uncorrelated	Correlated
Thermal Power	0.5%	-
Fission fraction	0.7%	-
Fission reaction cross section	-	1.9%
Reference energy spectra	-	0.5%
Energy per fission	-	0.2%
Combined	0.9%	2.0%

Table 8.7: Reactor related systematic uncertainties.

8.4 Energy Scale Uncertainty

The energy scale uncertainty is estimated from the energy scale difference between the far and near detectors. The energy scale difference is obtained from spectral comparison of the calibration sources, as shown in Figure 8.2. All energy scale difference points of source data are under 0.15%. We attached 0.15% for the energy scale uncertainty.

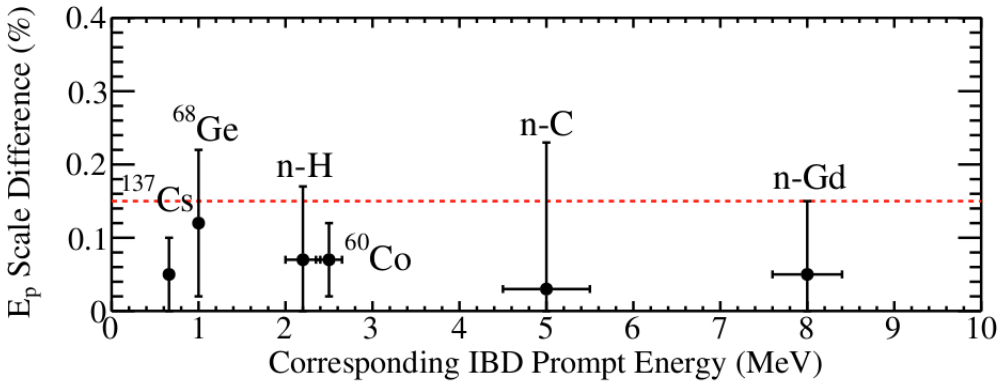

Figure 8.2: Energy scale difference. The red line is 0.15% line, which is treated as the energy scale uncertainty.

The energy scale is assumed to be linear in the energy value, *i.e.* $E(\epsilon) = E_0(1+\epsilon)$, and therefore the expected energy distribution with the energy scale

offset ϵ^d can be written as

$$T_i^d(1+\epsilon^d) \simeq T_i^d + \epsilon^d \left(\frac{\partial T_i^d}{\partial \epsilon^d}\right)_{\epsilon^d=0}, \tag{8.2}$$

following the prescription given in Ref. [68]. The differential is not easy to obtain from the histograms of the expected energy distribution due to limited statistics. Instead, a function is used to fit T_i^d distribution and the differential is obtained from it. The energy distribution from each reactor-detector pair is fitted with the following function

$$f(E) = \exp\left(\sum_{i=0}^{6} p_i\, E^{(i-3)}\right). \tag{8.3}$$

The fit is performed from $E = 1.0$ to 8 MeV as shown in Fig. 8.3.

The differential is approximated by the finite difference as

$$\frac{\partial T_i^d}{\partial \epsilon^d} \simeq \frac{f_+(E(1+\epsilon^d)) - f_-(E(1-\epsilon^d))}{2\,\epsilon^d}, \tag{8.4}$$

where

$$f_\pm(E(1\pm\epsilon^d)) = f(E(1\pm\epsilon^d))\frac{\int f(E)\,dE}{\int f(E(1\pm\epsilon^d))\,dE} \tag{8.5}$$

and $\epsilon = 0.0015$. The fit to an MC positron energy spectrum and its differential with respect to ϵ are shown in Fig. 8.3.

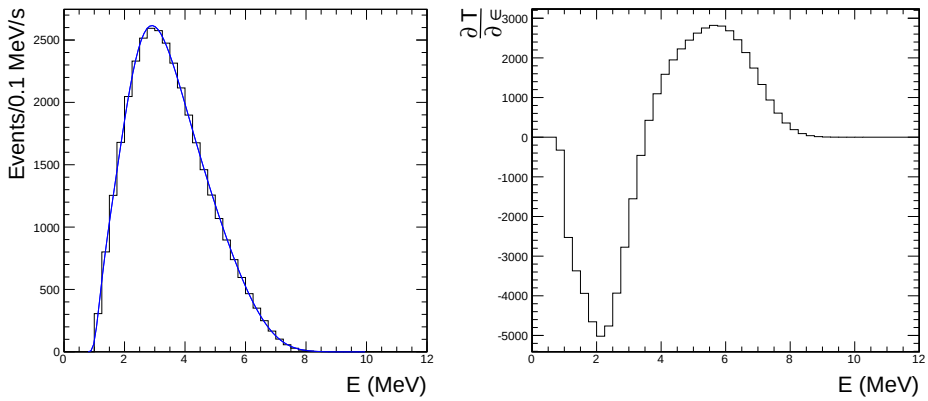

Figure 8.3: The positron energy spectrum is fitted with the function in Eq. 8.3 (left). The differential $\partial T/\partial\epsilon$ of the positron energy spectrum constructed with the fit function (right).

8.5 Background Uncertainty

The uncertainties in the background were described in Chapter 7. The uncertainties in the background consist of 2 kinds: shape uncertainty and magnitude uncertainty. These are summarized Table 7.7. The uncertainties of backgrounds are the dominant component for the systematic errors of $\theta_1 3$ and $|\Delta m^2_{ee}|$. The background uncertainty inputs for measuring $\theta_1 3$ and $|\Delta m^2_{ee}|$ are summarized in the following plots. The Backgrounds from ^{252} consist of many components, each estimated independently, so that the shape uncertainties of the backgrounds from ^{252}Cf need to be considered for each component. For simplicity, The shape uncertainties of the backgrounds from ^{252}Cf are divided into 2 components: a 1 MeV-b component that has the largest shape uncertainty and a combined shape uncertainty of other components. More details for shape uncertainties of Backgrounds from ^{252}Cf are Appendix E.

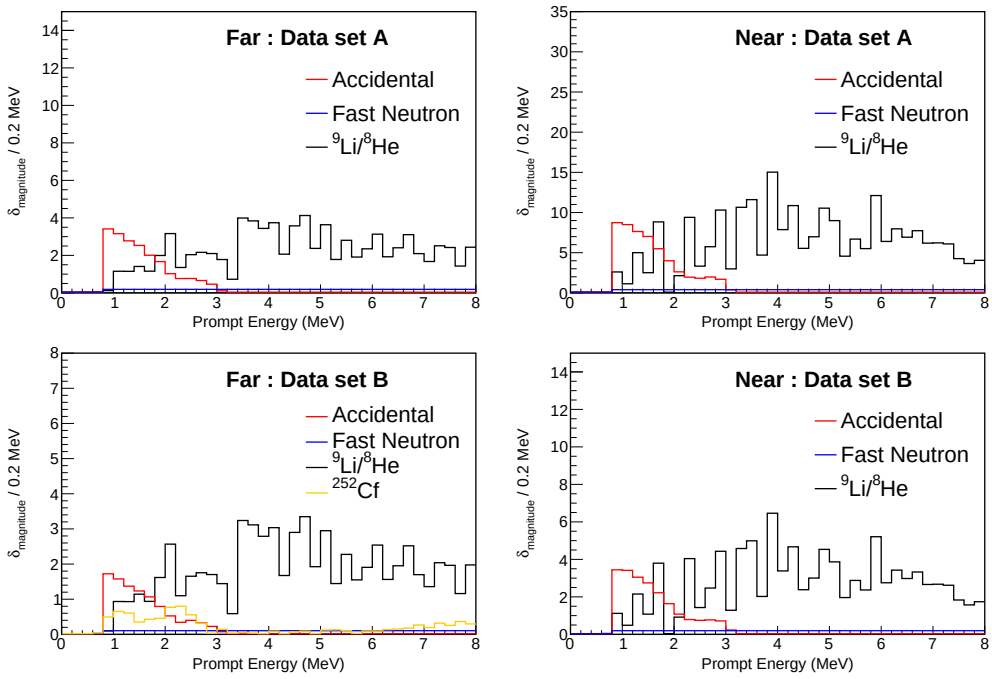

Figure 8.4: Magnitude uncertainties of the backgrounds

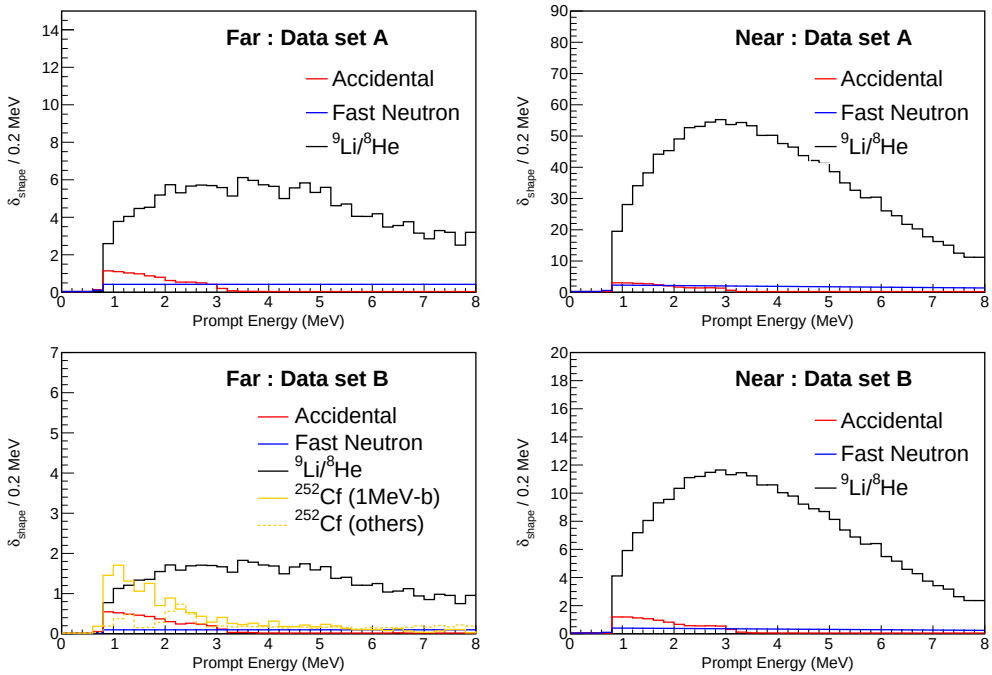

Figure 8.5: Shape uncertainties of the backgrounds

Chapter 9

Measurement Results of θ_{13} and $|\Delta m^2_{ee}|$

Now we have all inputs to determine θ_{13} and $|\Delta m^2_{ee}|$. In Chapter 2, the expected neutrino flux and spectrum is calculated and in the Chapter 5 and Chapter 8, the detector effects and efficiencies are applied in the expected flux and spectrum. The observed are prepared with IBD selection developed in Chapter 6 and background estimation in Chapter 7. To measure θ_{13} and $|\Delta m^2_{ee}|$, χ^2 fitting methods with pull terms are used [68]. The χ^2 fitting methods are of three 3 kinds: the first one is Rate-Only, which uses the number of events information only, the second one is Rate + Shape, which uses magnitude and spectra, and the last one uses spectral information only.

9.1 Observed IBD Candidate and Backgrounds

Physics data was acquired with the far and near detectors from August 2011. During the calibration source data taking, ^{252} Cf contamination occurred on October 2012. Therefore, the data set is divided into two groups: set A (before ^{252}Cf contamination) and set B (after ^{252}Cf contamination). IBD candidate events are obtained by applying the IBD selection criteria in data sets A and B. The IBD candidates obtained from data sets A and B are 31541 events for a 489.93-day dataset in the far detector and 290775 events for a 458.49-day dataset in the near detector with a prompt energy range (1.2−8 MeV). IBD candidate events obtained include both the signals and small amounts of backgrounds. The backgrounds in the final IBD candidate sample are either uncorrelated or correlated IBD candidates. An accidental background has no correlation between prompt and delayed signals so that accidentals could be estimated by comparing the distribution of distance between prompt and delayed signals(=ΔR). Correlated

backgrounds are fast neutrons from out side the detector and muon followers, ^{9}Li/^{8}He induced from cosmic muons and ^{252}Cf contamination. All of these correlation backgrounds are estimated by comparing the energy spectrum between backgrounds and IBD candidates at a greater than 8 MeV region. The total background fraction is 4.9 $\pm$ 0.3% in the far detector and 2.8 $\pm$ 0.1% in the near detector for data sets A and B. IBD candidate events less than 1.2 MeV are abandoned for this analysis because they include a prompt signal that has an observed energy of 1.02 MeV. These 1.02 MeV events are occurring in the acrylic vessel. Consequently, the event loses most of its kinetic energy in the acrylic vessel, not the liquid scintillator. The IBD candidate events and backgrounds are summarized in the following table and figures.

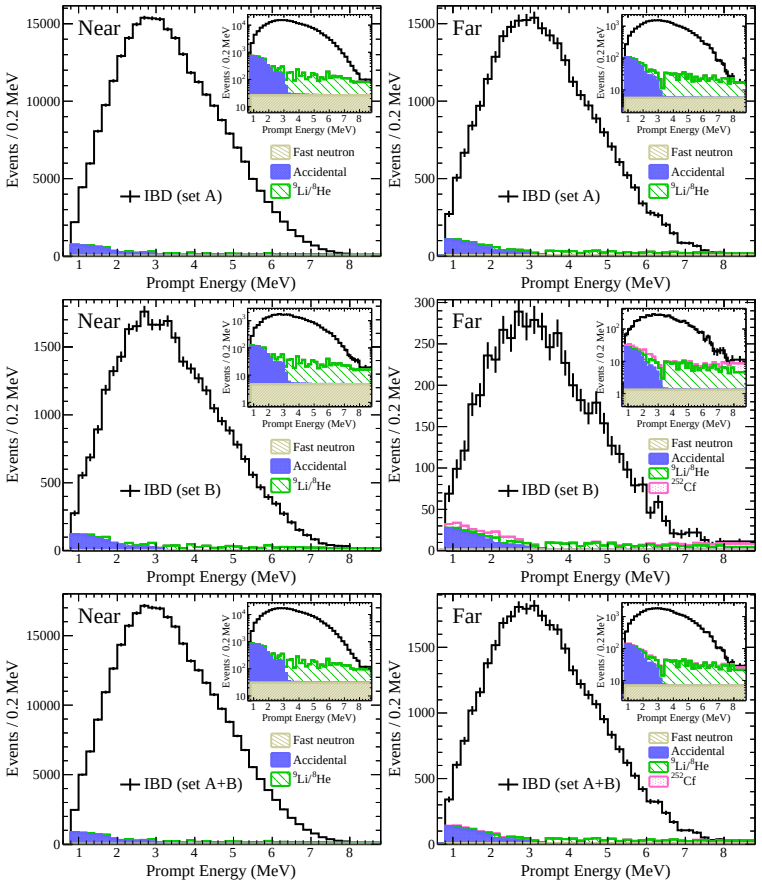

Figure 9.1: Prompt energy spectra of observed IBD candidates and backgrounds

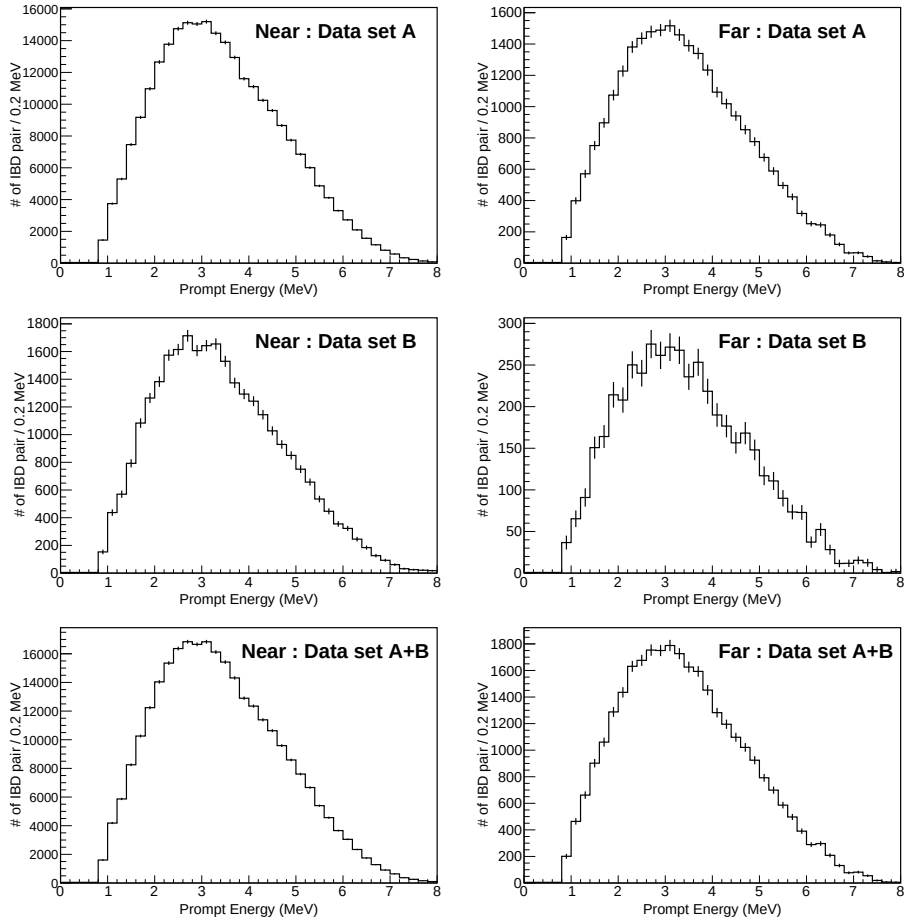

Figure 9.2: Prompt energy spectra of background subtracted IBD candidates

Data Set A : before ^{252}Cf contamination		
Detector	Near	Far
Number of selected events	261338	26579
Total Background Rate (per day)	17.81 ± 0.87	3.01 ± 0.23
IBD rate after background subtraction	670.53 ± 1.60	66.12 ± 0.48
DAQ live time (days)	379.66	384.47
Accidental rate	7.13 ± 0.09	0.99 ± 0.03
^{9}Li/^{8}He rate	8.34 ± 0.86	1.52 ± 0.23
Fast neutron rate	2.34 ± 0.05	0.50 ± 0.02
Data Set B : after ^{252}Cf contamination		
Detector	Near	Far
Number of selected events	29437	4962
Total Background Rate (per day)	16.23 ± 1.47	3.63 ± 0.62
IBD rate after background subtraction	357.22 ± 2.60	43.43 ± 0.91
DAQ live time (days)	78.83	105.46
Accidental rate	5.77 ± 0.19	0.92 ± 0.06
^{9}Li/^{8}He rate	8.47 ± 1.41	1.61 ± 0.64
Fast neutron rate	1.99 ± 0.09	0.43 ± 0.03
^{252}Cf contamination rate	-	0.67 ± 0.14
Data Set A + Set B		
Detector	Near	Far
Number of selected events	290775	31541
Total Background Rate (per day)	17.54 ± 0.83	3.14 ± 0.23
IBD rate after background subtraction	616.67 ± 1.44	61.24 ± 0.42
DAQ live time (days)	458.49	489.93
Accidental rate	6.89 ± 0.09	0.97 ± 0.03
^{9}Li/^{8}He rate	8.36 ± 0.82	1.54 ± 0.23
Fast neutron rate	2.28 ± 0.04	0.48 ± 0.02
^{252}Cf contamination rate	-	0.14 ± 0.03

Table 9.1: Event rate of the observed IBD candidates and the estimated background at $1.2 < E_p < 8.0$ MeV. Rates are given in per day.

9.2 Expected Neutrino Oscillation Templates

9.2.1 Expected IBD Prompt Spectrum

The expected prompt spectrum of IBD in the detector d could be calculated by Equation 9.1 and shown Figure 9.3.

$$N^d_{exp}\left(E_p\right) = \epsilon^d \cdot \left[\sum_{r=1}^{6} P_{surv}\left(E_\nu, L_{d,r}, \theta_{13}, |\Delta m^2_{ee}|\right) \cdot S^{d,r}_p\left(E_p\right)\right] \tag{9.1}$$

where, ϵ^d is detection efficiency of detector d, which is summarized in Table 8.2, $P_{surv}\left(E_\nu, L_{d,r}, \theta_{13}, |\Delta m^2_{ee}|\right)$ is the antineutrino survival probability with neutrino energy E_ν, distance between detector d and reactor r ($=L_{d,r}$), θ_{13} and $|\Delta m^2_{ee}|$. $S^{d,r}_p\left(E_p\right)$ is the expected prompt events of detector d with visible energy E_p from the reactor r, which can be expressed by the following equation,

$$S^{d,r}_p\left(E_p\right) = N^{d,r}_\nu \cdot \left(\sum_{i=iso} I_i \cdot s^i_p(E_p)\right). \tag{9.2}$$

where, $N^{d,r}_\nu = \sum_{i=iso} N^d_{\nu,i}$ is the expected number of interacting neutrinos in the detector d from the reactor r that was summarized in Table 3.7. $I_i = N^d_{\nu,i} / \left(\sum_{i=iso} N^d_{\nu,i}\right)$ is the interaction fraction of the i^{th} isotope which is summarized in Table 3.8 and 3.9. In addition, $s^i_p(E_p)$ is the normalized prompt energy spectrum from the i^{th} isotope's neutrino with prompt energy E_p. The relation between the prompt energy of IBD and the neutrino energy is following equation.

$$\begin{aligned} E_p &\sim E_{e^+} + 1.022 \text{ MeV } (\text{ pair anihillation energy}) \\ &\sim E_{\bar{\nu}} - (m_n - m_p) + 0.511 \text{ MeV} \sim E_{\bar{\nu}} - 0.8 \text{ MeV} \end{aligned} \tag{9.3}$$

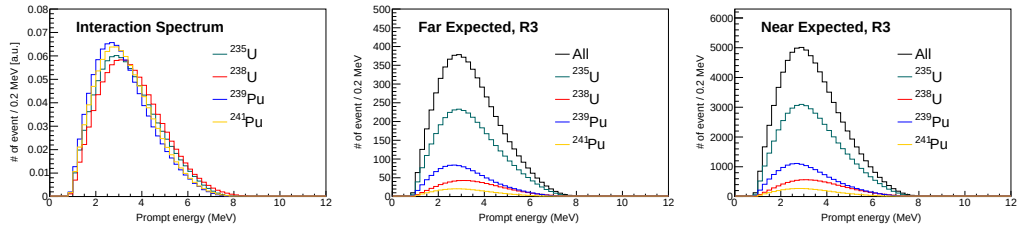

Figure 9.3: Expected prompt spectra of IBD. The left side is the normalized prompt spectrum for each isotope. The middle one is the expected prompt spectrum of reactor 3 for the far detector and right side is the expected prompt spectrum for the near detector.

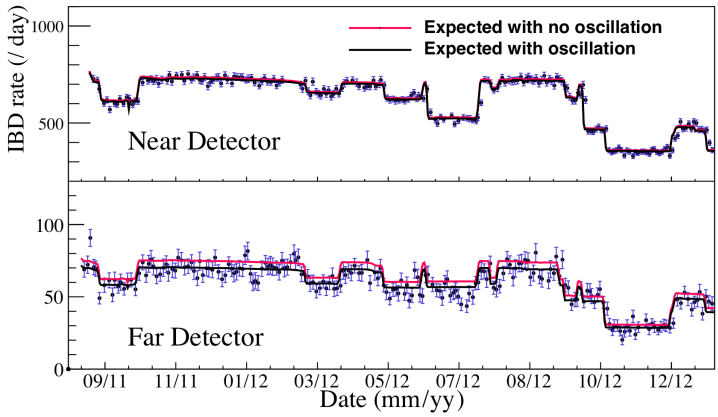

Figure 9.4: Observed and expected daily-average rate of reactor neutrino. The red (black) line shows the expected reactor neutrino rate for no oscillation (the best fit oscillation).

Figure 9.4 shows the daily rate of expected IBD event and background subtracted IBD candidate. We can easily find the strong correlation between the observed and expected reactor neutrino fluxes. It could be a new telemeter for reactor thermal power.

9.2.2 5 MeV Excess

Figure 9.5 shows the difference between the observed background subtracted IBD (Figure 9.2) and the prediction (Figure 9.3) normalized by spectral fitting excluding the $3.5 < E_p < 6.6$ MeV region. The observed background subtracted IBD is greater than the prediction at 5 MeV that constitutes 3 % of the total observed IBD rate in the both the detectors.

When the excess was found at first, we could not assure that it was from reactor neutrino events. The excess could be from miscalibration of energy , background. However, all these studies of these excess events confirmed that the excess is not background or due to the miscalibration of energy. The excess is proportional to the reactor power as shown in Figure 9.6, which means that the excess is from a reactor neutrino. So that the current reactor neutrino model [60, 61] is in need of reevaluation and modification. Because of the excess, the θ_{13} and $|\Delta m^2_{ee}|$ are determined from comparison of the far-to-near ratio between observed and expected events.

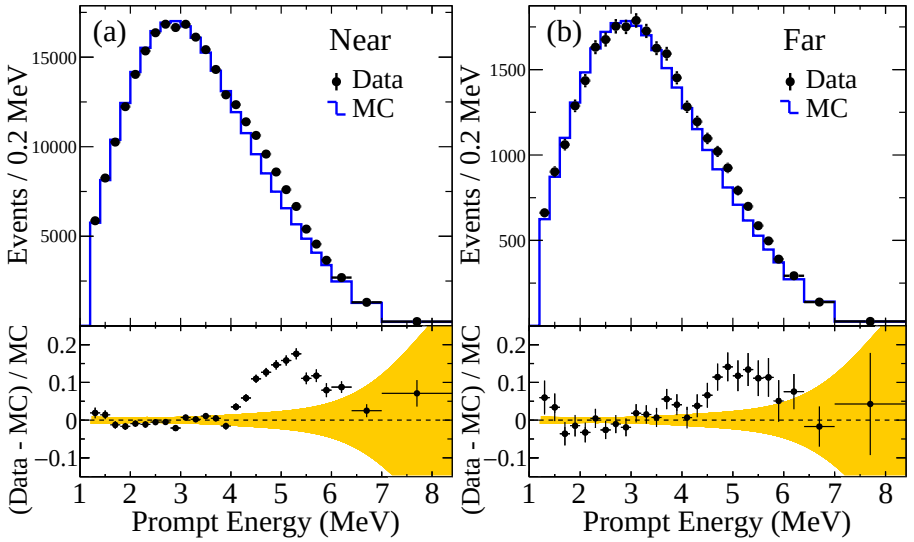

Figure 9.5: Spectral Comparison of observed and expected IBD prompt events in the (a) near and (b) far detectors. A shape difference is clear seen at 5 MeV. The observed excess is correlated with the reactor power, and corresponds to 3 % of the total observed reactor $\bar{\nu}_e$ flux. A spectral deviation from the expectation is larger than the uncertainty of an expected spectrum (shaded band)

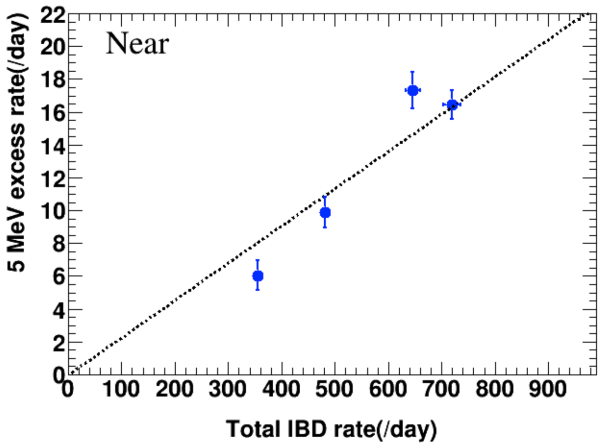

Figure 9.6: Correlation of 5 MeV excess with reactor power. The excess is proportional to the reactor power.

9.2.3 Oscillation Templates

To measure θ_{13} and $|\Delta m^2{}_{ee}|$, Expected IBD templates are prepared with various oscillation parameters, as shown in Figure 9.7. Each template that is shown as a point in the Figure 9.7 represents the expected oscillated prompt spectra at the far and near detectors. The measured θ_{13} and $|\Delta m^2{}_{ee}|$ are points in the template sets, which have minimum χ^2 values calculated between the events observed and the expected templates. There are a total of 6331 expected templates in the region bounded by $0.004 < \theta_{13} < 0.19$ and $0.0003 < |\Delta m^2{}_{ee}| < 0.0043$ eV^2.

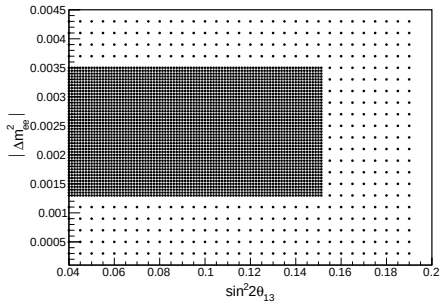

Figure 9.7: Oscillation parameters set for the expected templates, The expected neutrino oscillation templates are prepared with oscillation parameters from these points.

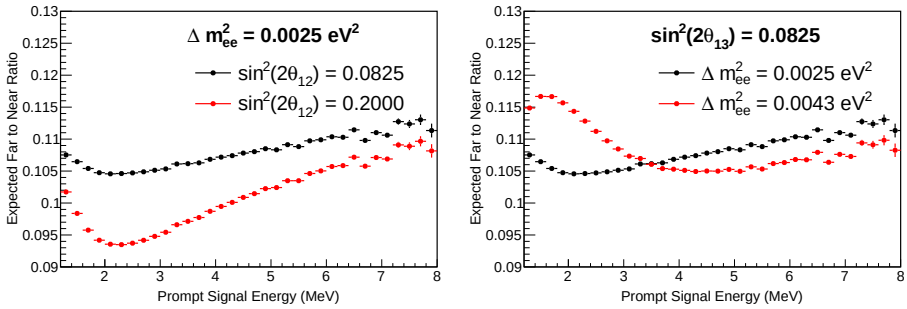

Figure 9.8: Expected far to near ratio of the prompt spectra with oscillations from the expected template.

9.3 Systematic Uncertainties

As described in the chapter 8, the systematics uncertainties are came from detector, reactor, energy scale, and backgrounds and affects the measurement of θ_{13} and $|\Delta m^2_{ee}|$. In this section, the systematics uncertainties are summarized by these four categories. The correlated systematic uncertainties are omitted in this section. because the correlated systematic uncertainties are canceled out in the ratio analysis.

9.3.1 Uncertainties of Detection Efficiency

The uncertainties of detection efficiency are came from detector and signal selections as shown Table 8.4 and Table 8.6. These are divided into 2 categories: common uncertainties to the detector and data set, and those uncommon. The total common uncertainties are 0.2% with respect to the IBD signal. The total uncommon uncertainties derive mostly from Cf removal cuts, and are applied only to data set B and neglected on data set A.

detector	Near		Far	
Data Set	Set A	Set B	Set A	Set B
Common	0.20%			
Uncommon	0.00 %	0.17 %	0.00 %	0.04 %

Table 9.2: Uncertainties of detection efficiency

9.3.2 Reactor Related Uncertainties

The reactor related uncertainties are came from the reactor thermal power and fission fraction of fuels, as shown Table 8.7. The uncertainty from the reactor is 0.5% with respect to the IBD signal, and the uncertainty from the fission fraction is 0.7%. The combined uncertainty is 0.9% ($=\sqrt{0.5^2 + 0.7^2}$).

9.3.3 Energy Scale Uncertainties

The energy scale uncertainties are estimated by the difference between far and near source data distributions,as shown in Figure 8.2 and are attached 0.15%. This uncertainty was calculated assuming half of the difference between the 0.15% left and right shifted templates, as shown in Figure 8.3.

9.3.4 Background Uncertainties

The background uncertainties are the main systematic error of θ_{13} and $|\Delta m^2_{ee}|$. The background uncertainties are divide into 2 categories: shape uncertainty mostly from the statistics uncertainty of background sample and magnitude uncertainty from the fitting error from the magnitude parameter, as shown in Figure 8.4 and 8.5. The values of the uncertainties are summarized in Table 7.7.

9.4 Rate Only Analysis

9.4.1 χ^2 Fitting of Rate Only Analysis

The χ^2 for the rate only analysis is based on the pull method described in Ref. [68], which takes care of correlations between various systematics, and is written as

$$\chi^2 = \sum_{P=SetA,SetB} \left\{ \frac{\frac{N^{F,P}_{obs}}{N^{N,P}_{obs}} - \frac{N^{F,P}_{exp}}{N^{N,P}_{exp}}}{U^P} \right\}^2 + \chi^2_{penalty} \tag{9.4}$$

where

$$N^{F,P}_{exp} = \sum_{r=1}^{6} \left[\left(1 + \xi + \xi^{SetB}_F + f_r\right) \cdot N^{F,P,r}_{exp} \right] - b^P_F - \beta^P_F \cdot S^F_{LH} \tag{9.5}$$

$$N^{N,P}_{exp} = \sum_{r=1}^{6} \left[\left(1 + \xi^{SetB}_N + f_r\right) \cdot N^{N,P,r}_{exp} \right] - b^P_N - \beta^P_N \cdot S^N_{LH} \tag{9.6}$$

$$U^P = \frac{N^{F,P}_{obs}}{N^{N,P}_{obs}} \sqrt{\frac{N^{F,P}_{obs} + N^{F,P}_{bkg}}{\left(N^{F,P}_{obs}\right)^2} + \frac{N^{N,P}_{obs} + N^{N,P}_{bkg}}{\left(N^{N,P}_{obs}\right)^2}} \tag{9.7}$$

and

$$\chi^2_{penalty} = \left(\frac{\xi}{\sigma_\xi}\right)^2 + \sum_{d=F,N} \left(\frac{\xi^{SetB}_d}{\sigma_{\xi_d}}\right)^2 + \sum_{r=1}^{6} \left(\frac{f_r}{\sigma_{f_r}}\right)^2 + \sum_{P,d} \left(\frac{b^P_d}{\sigma^P_{b_d}}\right)^2 + \sum_{d} \left(\frac{S^d_{LH}}{\sigma^d_{LH}}\right)^2 \tag{9.8}$$

Here, the parameters are defined as follow.

- $N^{d,P}_{obs}$: Number of background subtracted IBD, d = detector (far, near), P = data set (Set A, Set B)

- $N_{exp}^{d,P}$: Number of expected IBD, d = detector (far, near), P = data set (Set A, Set B)
- $N_{bkg}^{d,P}$: Number of total background, d = detector (far, near), P = data set (Set A, Set B)
- ξ : Pull parameter of detection efficiency
- σ_{ξ} : Uncertainty of detection efficiency
- ξ_d^{setB} : Pull parameter of uncommon detection efficiency for data set B only, d = detector (far, near).
- σ_{ξ_d} : Uncertainty of uncommon detection efficiency for data set B only, d = detector (far, near).
- f_r : Pull parameter for the reactor Thermal power and isotope fraction for reactor (r = $1 \sim 6$)
- σ_{f_r} : Uncertainty of the neutrino flux from thermal power for reactor (r = $1 \sim 6$)
- b_d^p : Pull parameter for the accidental, fast neutron, magnitude part of ^{9}Li/^{8}He and ^{252}Cf background, d = detector (far, near), P = data set (Set A, Set B)
- $\sigma_{b_d^p}$: Combined uncertainty for the accidental, fast neutron, magnitude uncertainty of ^{9}Li/^{8}He and ^{252}Cf background, d = detector (far, near), P = data set (Set A, Set B)
- β_d^p : shape uncertainty of ^{9}Li/^{8}He shape, d = detector (far, near)), P = data set (Set A, Set B)
- S_{LH}^d : Pull parameter for the ^{9}Li/^{8}He background shape uncertainty, d = detector (far, near)
- $\sigma_{S_{LH}}^d$: normalized uncertainty for the ^{9}Li/^{8}He Background, d = detector (far, near)

The χ^2 values are calculated separately two data sets A and B because the IBD selection cut and its detection efficiency are different in each data set an the. ^{252}Cf backgrounds are only obtained for data set B. Therefore, the systematic uncertainties are different. The detection efficiency uncertainty is the relative ambiguity between the far and near detectors. Hence, it is located only in terms of the far expected IBD. The uncommon detection efficiencies are the independent

ambiguities in the far and near detectors because they pertain to the statistics of their own data. The uncommon detection efficiencies are too small at the data set A; hence, the uncommon detection efficiencies are applied only to set B. The values of pull parameter ξ_d^{setB} have the fixed value "0" in the data set A term. The reactor pull parameter has only a reactor index no detector index and it commonly located in both the numerator and denominator. That means the correlation between far and near detectors from the reactor uncertainties is taken into account in the χ^2 function. Background uncertainty pull term take into account combined all background uncertainties combined except the shape uncertainty of ^{9}Li/^{8}He. Since, ^{9}Li/^{8}He is estimated with same the ^{9}Li/^{8}He template for both data sets A and B, the shape uncertainty of ^{9}Li/^{8}He is correlated between data sets A and B. For this reason, the shape uncertainty of ^{9}Li/^{8}He are applied separately for data sets A and B.

9.4.2 Fit Result of Rate Only Analysis

The fitting result shows that $sin^2(2\theta_{13}) = 0.087 \pm 0.009(stat.) \pm 0.007(syst.)$, where the the world average value of $|\Delta m^2_{ee}|$ is used Ref. [12]. To obtain the statistical error, we fit to this model with all pull parameters turned off. The systematic error is calculated from following equation once the total error is obtained from the fit result with all pull parameters turned on.

$$\delta^2_{syst.} = \delta^2_{total} - \delta^2_{stat.} \tag{9.9}$$

Since the $|\Delta m^2_{ee}|$ is borrowed from the world average value, the systematic error from the uncertainty of $|\Delta m^2_{ee}|$ needs to be considered. This systematic error is estimated by half the difference of the values of $sin^2(2\theta_{13})$ with $|\Delta m^2_{ee}| \pm \delta|\Delta m^2_{ee}|$. The results are summarized in the following table.

	$\|\Delta m^2_{ee}\| =$ 2.49 $\times 10^{-3}$ eV^2 world average [12]	$\Delta m^2_{ee}\| =$ 2.55 $\times 10^{-3}$ eV^2 $(+\delta_{\|\Delta m^2_{ee}\|})$	$\Delta m^2_{ee}\| =$ 2.43 $\times 10^{-3}$ eV^2 $(-\delta_{\|\Delta m^2_{ee}\|})$	Systematic error from $\|\Delta m^2_{ee}\|$
$sin^2(2\theta_{13})$	0.087	0.086	0.088	0.001

Table 9.3: Systematic error from $|\Delta m^2_{ee}|$

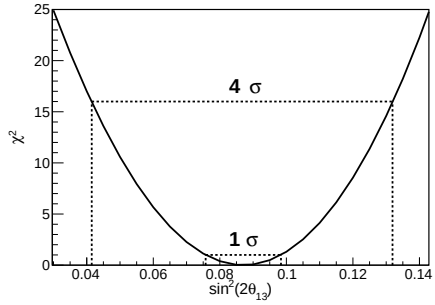

Figure 9.9: χ^2 fitting result of the rate only analysis. 1 σ value contains statistic and systematic uncertainties.

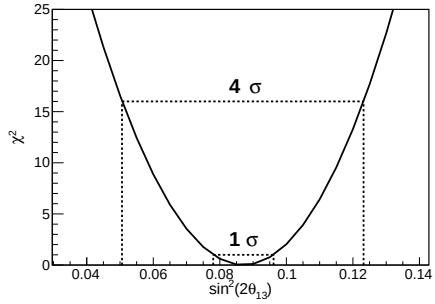

Figure 9.10: The statistics-only χ^2 fitting result of rate-only analysis. 1-σ value contains statistic uncertainty only.

9.5 Rate + Shape Analysis

9.5.1 χ^2 Fitting of Rate + Shape Analysis

The χ^2 for the rate + shape analysis is also based on the pull method described in Ref. [68], and is written as

$$\chi^2 = \sum_{P=SetA,SetB} \sum_{i=1}^{N_{bin}} \left\{ \frac{\frac{N_{obs}^{F,P,i}}{N_{obs}^{N,P,i}} - \frac{N_{exp}^{F,P,i}}{N_{exp}^{N,P},i}}{U^{P,i}} \right\}^2 + \chi^2_{penalty} \tag{9.10}$$

where

$$
\begin{aligned}
N_{exp}^{F,P,i} = & \sum_{r=1}^{6} \left[\left(1 + \xi + \xi_F^{SetB} + f_r\right) \cdot T_{exp}^{F,P,r,i} \right] + \epsilon \cdot \delta E \frac{\partial T_{exp}^{F,P,r,i}}{\partial E} \\
& + \sum_{k=acci,Cf} \left(\frac{\left(\delta B_{shape}^{P,F,k,i}\right)^2}{\sqrt{\sum_i \left(\delta B_{shape}^{P,F,k,i}\right)^2}} \cdot b_{shape}^{P,F,k} \right) \\
& + \sum_{k=acci,Fn,Cf} \left(\delta B_{mag.}^{P,F,k,i} \cdot b_{mag.}^{P,F,k}\right) + \delta B_{LH}^{P,F,i} \cdot b_{LH}^{P,F}
\end{aligned}
\tag{9.11}
$$

$$
\begin{aligned}
N_{exp}^{N,P,i} = & \sum_{r=1}^{6} \left[\left(1 + \xi_F^{SetB} + f_r\right) \cdot T_{exp}^{N,P,r,i} \right] \\
& + \sum_{k=acci,Cf} \left(\frac{\left(\delta B_{shape}^{P,N,k,i}\right)^2}{\sqrt{\sum_i \left(\delta B_{shape}^{P,N,k,i}\right)^2}} \cdot b_{shape}^{P,N,k} \right) \\
& + \sum_{k=acci,Fn,Cf} \left(\delta B_{mag.}^{P,N,k,i} \cdot b_{mag.}^{P,N,k}\right) + \delta B_{LH}^{P,N,i} \cdot b_{LH}^{P,N}
\end{aligned}
\tag{9.12}
$$

$$
U^{P,i} = \frac{N_{obs}^{F,P,i}}{N_{obs}^{N,P,i}} \sqrt{\frac{N_{obs}^{F,P,i} + N_{bkg}^{F,P,i}}{\left(N_{obs}^{F,P,i}\right)^2} + \frac{N_{obs}^{N,P,i} + N_{bkg}^{N,P,i}}{\left(N_{obs}^{N,P,i}\right)^2}} \tag{9.13}
$$

and,

$$
\begin{aligned}
\chi^2_{penalty} = & \left(\frac{\xi}{\sigma_\xi}\right)^2 + \sum_{d=F,N} \left(\frac{\xi_d^{SetB}}{\sigma_{\xi_d}}\right)^2 + \sum_{r=1}^{6} \left(\frac{f_r}{\sigma_{f_r}}\right)^2 + \left(\frac{\epsilon}{\sigma_{cal}}\right)^2 \\
& + \sum_{P,d,k} \left(\frac{b_{shape}^{P,d,k}}{\sigma_{b_{shape}}^{P,d,k}} \right)^2 + \sum_{P,d,k} \left(\frac{b_{mag.}^{P,d,k}}{\sigma_{b_{mag.}}^{P,d,k}} \right)^2 + \sum_{d} \left(\frac{S_{LH}^{d}}{\sigma_{LH}^{d}} \right)^2
\end{aligned}
\tag{9.14}
$$

Here, the parameters are defined as follow.

- $N_{obs}^{d,P,i}$: Number of background subtracted IBD, d = detector (far, near), P = data set (Set A, Set B) in the i^{th} energy bin.
- $N_{bkg}^{d,P,i}$: Number of total background, d = detector (far, near), P = data set (Set A, Set B) in the i^{th} energy bin.

- $N_{exp}^{d,P,i}$: Number of expected IBD, d = detector (far, near), P = data set (Set A, Set B) in the i^{th} energy bin.
- $T_{exp}^{d,P,i,r}$: Number of expected IBD template, d = detector (far, near), P = data set (Set A, Set B), r = Reactor (1∼6) in the i^{th} energy bin.
- ξ : Pull parameter of detection efficiency
- σ_{ξ} : uncertainty of detection efficiency
- ξ_d^{setB} : Pull parameter of uncommon detection efficiency for data set B only, d = detector (far, near)
- σ_{ξ_d} : Uncertainty of uncommon detection efficiency.
- f_r : Pull parameter for the reactor thermal power and isotope fraction for reactor (r = $1 \sim 6$)
- σ_{f_r} : Uncertainty of the neutrino flux from thermal power and isotope fraction for reactor (r = $1 \sim 6$)
- ϵ : Pull parameter for the energy scale uncertainty
- $\delta E \frac{\partial T_{exp}^{F,P,r,i}}{\partial E}$: Uncertainty of energy scale in data set P in far detector in reactor r in the i^{th} energy bin.
- σ_{cal} : Normalized uncertainty of the energy scale uncertainty
- $b_{shape}^{P,d,k}$: Pull parameter for the shape uncertainty of background in data set P in detector d in k^{th} Background.
- $\delta B_{shape}^{P,F,k,i}$: Shape uncertainty for the Background in data set P in detector d in k^{th} background in the i^{th} energy bin.
- $\sigma_{b_{shape}^{P,d,k}}$: Normalized shape uncertainty for the background in data set P in detector d in k^{th} background.
- $b_{mag.}^{P,d,k}$: Pull parameter for the magnitude uncertainty of background uncertainty in data set P in detector d in k^{th} background.
- $\delta B_{mag.}^{P,F,k,i}$: Magnitude uncertainty for the Background in data set P in detector d in k^{th} background in the i^{th} energy bin.
- $\sigma_{b_{mag.}^{P,d,k}}$: Normalized magnitude uncertainty for the background in data set P in detector d in k^{th} background.

- b^{d}_{LH} : Pull parameter for the ^{9}Li/^{8}He background shape, d = detector (far, near)

- $\delta B^{P,d,i}_{LH}$: ^{9}Li/^{8}He shape uncertainty , d = detector (far, near)), P = data set (Set A, Set B) in the i^{th} energy bin.

- $\sigma^{d}_{b_{LH}}$: Normalized shape uncertainty for the ^{9}Li/^{8}He background, d = detector (far, near)

The differences from the rate only χ^2 function originate from calculating the energy bin by bin, taking into account that the energy scale difference and the uncertainties of background are separate shape and magnitude uncertainties. The uncertainties attached to the i^{th} energy bin index are different from each other. To consider this property, the pull term of these uncertainties is normalized and paired with its uncertainty value at the i^{th} energy bin and normalized constraining term σ.

9.5.2 Fit Result of Rate + Shape Analysis

The fitting results obtained from the rate + shape analysis are $sin^2(2\theta_{13}) = 0.082 \pm 0.009(stat.) \pm 0.006(syst.)$ and $|\Delta m^2_{ee}| = 2.62^{+0.21}_{-0.23}(stat.)^{+0.12}_{-0.13}(syst.) \times 10^{-3}$ eV^2 with $\chi^2/NDF = 58.9/66$..

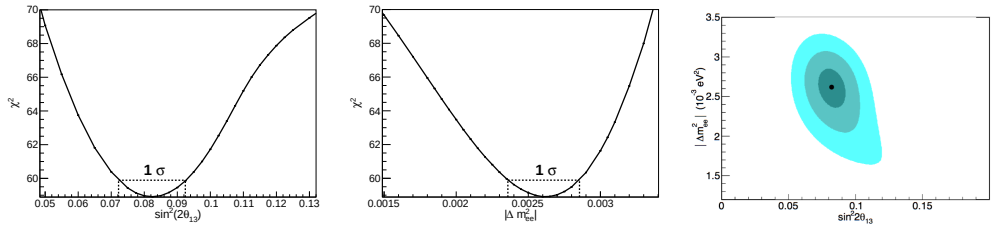

Figure 9.11: The resulting plots of rate and shape analysis with all pull term turned on. The left plot shows minimum χ^2 values at the $sin^2(2\theta_{13})$ value on the X-axis. The middle plot shows minimum χ^2 values at the $|\Delta m^2_{ee}|$ value on the Y-axis. The right plot shows a contour plot with the allowed regions for 1-, 2-, and 3-σ. The σ contains the total error.

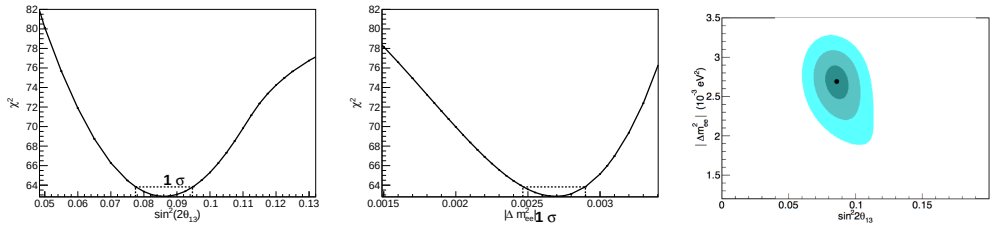

Figure 9.12: The result plots of rate and shape analysis with all terms turned off. The left plot shows minimum χ^2 values at the $sin^2(2\theta_{13})$ value on the X-axis. The middle plot shows minimum χ^2 values at the $|\Delta m^2_{ee}|$ value on the Y-axis. The right plot shows a contour plot with the allowed regions for 1-, 2-, and 3-σ. The σ contains the statistical error only.

9.6 Shape Only Analysis

9.6.1 χ^2 Fitting of Shape Only Analysis

The χ^2 for the shape only analysis is also based on the pull method described in Ref. [68], and is written as

$$\chi^2 = \sum_{P=SetA,SetB} \sum_{i=1}^{N_{bin}} \left\{ \frac{\frac{N^{F,P,i}_{obs}}{N^{N,P,i}_{obs}} - \left(1+\alpha^P\right) \frac{N^{F,P,i}_{exp}}{N^{N,P}_{exp},i}}{U^{P,i}} \right\}^2 + \chi^2_{penalty} \qquad (9.15)$$

The differences from rate + shape χ^2 function are $(1+\alpha^P)$ in the front of the expected term. This $(1+\alpha^P)$ term affect the magnitude information are abandoned.

9.6.2 Fit Result of Shape Only Analysis

The fitting results obtained from the shape only analysis are $sin^2(2\theta_{13}) = 0.066^{+0.042}_{-0.046}(total)$ and $|\Delta m^2_{ee}| = 2.62^{+0.38}_{-0.41}(total) \times 10^{-3}$ eV^2 with $\chi^2/NDF = 58.8/67$.

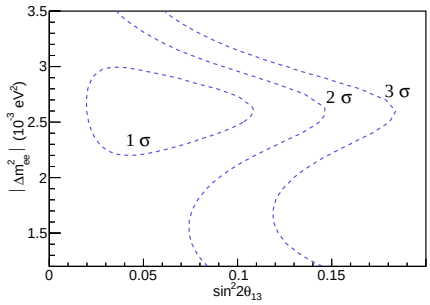

Figure 9.13: The contour plot of shape only analysis with turning on all pull terms with allowed region of 1-, 2-, and 3-σ.

9.7 Summary and Comparison of Experimental Results

9.7.1 Results Summary

RENO has observed energy dependent disappearance of reactor antineutrino by comparing 500 days of data from two identical detectors. The obtained $\sin^2(2\theta_{13})$ and $|\Delta m^2_{ee}|$ are summarized in the Table 9.4, and Figures 9.14, 9.15, and 9.16. Figure 9.14 shows 68.3 %, 95.5 % and 99.7 % confidence region for the neutrino oscillation parameter $\sin^2(2\theta_{13})$ and $|\Delta m^2_{ee}|$. Figure 9.15 shows the observed IBD prompt spectrum in the far detector compared to the expected spectrum for oscillation at the far detector. The expected spectra are obtained by weighting the spectrum at the near detector with the best-fit oscillation and the no-oscillation models. Figure 9.16 shows the measured survival probability of reactor neutrino as a function of an effective baseline L_{eff} over neutrino energy E_ν, in a good agreement with the prediction that is obtained from the observed distribution in the near detector. The new results are reported in Ref. [69].

	$\sin^2(2\theta_{13})$	$\lvert\Delta m^2_{ee}\rvert$ $(\times 10^{-3} eV^2)$
	mean $\pm$ (stat.) $\pm$ (sys.) $\pm$ (tot.)	mean $\pm$ (stat.) $\pm$ (sys.) $\pm$ (tot.)
Rate Only	$0.087 \pm 0.009 \pm 0.007 \pm 0.011$	-
Rate + Shape	$0.082 \pm 0.009 \pm 0.006 \pm 0.010$	$2.62\ ^{+0.21}_{-0.23}\ ^{+0.12}_{-0.13}\ ^{+0.24}_{-0.26}$
Shape Only	$0.066\ ^{+0.042}_{-0.046}$(total)	$2.62\ ^{+0.38}_{-0.41}$

Table 9.4: Measured $\sin^2(2\theta_{13})$ and $|\Delta m^2_{ee}|$

	Rate Only	Rate + Shape	
	$\sin^2(2\theta_{13})$	$\sin^2(2\theta_{13})$	$\lvert\Delta m^2_{ee}\rvert$ $(\times 10^{-3} eV^2)$
Reactor	$\pm$ 0.0028	+ 0.0026 - 0.0028	+ 0.018 - 0.018
Detection efficiency	$\pm$ 0.0029	+ 0.0028 - 0.0029	+ 0.020 - 0.022
Energy Scale	-	+ 0.0026 - 0.0015	+ 0.081 - 0.094
Backgrounds	$\pm$ 0.0054	+ 0.0030 - 0.0028	+ 0.084 - 0.106
Total	$\pm$ 0.0068	+ 0.0055 - 0.0052	+ 0.115 - 0.133

Table 9.5: Systematic errors from uncertainty sources

The systematic uncertainties were studied carefully. The uncorrelated uncertainty of the detection efficiency is 0.2 %. The uncorrelated uncertainty from the reactors is 0.9 %. The energy scale uncertainty between the far and near detectors is 0.15 %. The background uncertainties are 4.7% and 6.7% for the near and far detectors, respectively. The systematic errors from these systematic uncertainties are summarized in Table 9.5. The dominant systematic error source is the background uncertainty. The second dominant systematic error source is the energy scale. The background uncertainties depend on the statistics of the background sample and data so that the systematic error from the background uncertainty and statistical error will be reduced as data increases as a factor of the $\sqrt{n_{data}}$.

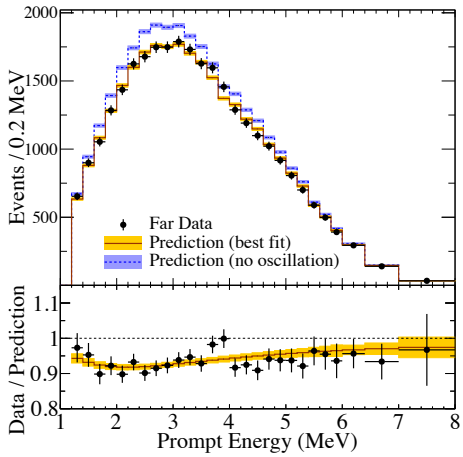

Figure 9.15: Comparison of the observed IBD prompt spectrum in the far detector with the no-oscillation prediction from the observed spectrum in the near detector. The prediction from the best-fit results to oscillation is also shown.

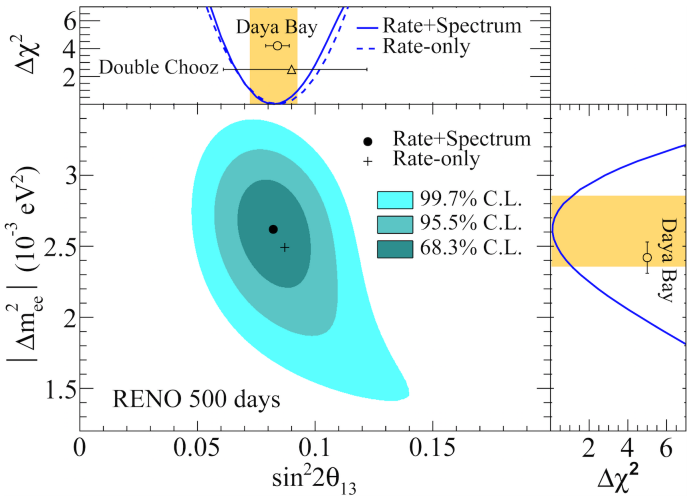

Figure 9.14: Allowed regions of 68.3 %, 95.5 %, 99.7 %. in the $|\Delta m^2_{ee}|$ and $\sin^2(2\theta_13)$. The $\Delta\chi^2$ distributions for distributions for $\sin^2(2\theta_13)$ (top) and $|\Delta m^2_{ee}|$ (right) are also shown. The rate-only result for $\sin^2(2\theta_13)$ is shown by the cross.

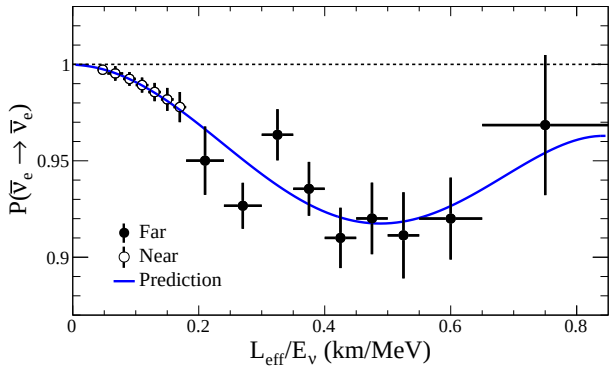

Figure 9.16: Measured reactor neutrino survival probability as a function of L_{eff}/E_ν.

9.7.2 Comparison of Experimental Results

Comparison of our measurement with the previously obtained values of $\sin^2(2\theta_{13})$ is a useful and important check. From the first result of PRL (2012) [6] to the current result [69] as shown in Table 9.6 and Figure 9.17, the systematic error has

been reduced by a factor of 3 and the statistical error is reduced by the amount of data. The $\sin^2(2\theta_{13})$ values obtained have also been reduced because the estimation of backgrounds have changed and using world average value of $|\Delta m^2_{ee}|$ is changed from $2.32\times10^{-3}\text{eV}^2$ (PDG 2012) [70] to $2.49\times10^{-3}\text{eV}^2$ (PDG2014) [12].

	Data Set	$\sin^2(2\theta_{13})$	Stat. Error	Sys. Error	Tot. Error	$\lvert\Delta m^2_{ee}\rvert$
PRL 2012	220 days	0.113	0.013	0.019	0.023	2.32
TAUP 2013	403 days	0.100	0.010	0.012	0.016	2.32
Current Result	500 days	0.087	0.009	0.007	0.011	2.49
PDG 2014	–	0.093	–	–	0.008	2.49

Table 9.6: $\sin^2(2\theta_{13})$ Measurement in RENO.

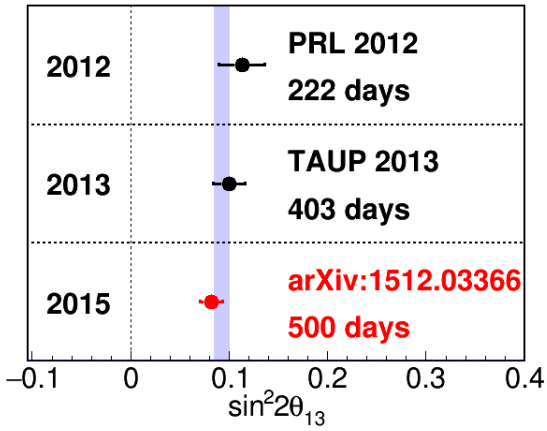

Figure 9.17: Summary of $\sin^2(2\theta_{13})$ Measurement in RENO. The light blue box is $\sin^2(2\theta_{13})$ at PDG 2014.

The results of RENO with 500 days data [69] agree well with the results of Daya Bay [54] and Double Chooz [71],as shown in the following tables and plots. The results of Double Chooze has the lowest-significance results because the those results are from data with only one detector, and Double Chooze could not cancel out correlated uncertainties by comparing two detectors. The Daya Bay results provide the lowest error among the three experiments.

RENO has received improvements in energy calibration, signal selection criteria, and background estimation. These improvements reduce the systematic error of the rate-only $\sin^2(2\theta_{13})$ result from 0.019 in the previously published RENO

result [6] to 0.006.

$\sin^2(2\theta_{13})$	RENO (500 days) [69]	Daya Bay [54]	Double Chooz [71]
Rate Only	0.087 ± 0.011	0.085 ± 0.006	$0.090\ ^{+0.032}_{-0.029}$
Rate + shape	0.082 ± 0.010	0.084 ± 0.005	

Table 9.7: Comparison of the experimental result for $\sin^2(2\theta_{13})$

$\lvert\Delta m^2_{ee}\rvert\ (\times 10^{-3} eV^2)$	RENO (500 days) [69]	Daya Bay [54]	Double Chooz
Rate + shape	$2.62\ ^{+0.24}_{-0.26}$	2.42 ± 0.11	-

Table 9.8: Comparison of the experimental result for $\lvert\Delta m^2_{ee}\rvert\ (\times 10^{-3} eV^2)$

Chapter 10

Summary and Discussion

The RENO experiment is designed to measure the value of neutrino mixing angle θ_{13} and oscillation frequency $|\Delta m^2_{ee}|$ by comparing data from the two identical detectors located near and far from the nuclear reactors. In the first 500-day data 31541 and 290775 IBD candidate events are found at the far and near detectors, respectively. The estimated backgrounds are 4.9% at the far detector and 2.8% at the near detector with respect to the number of observed IBD candidates. The background subtracted IBD spectra shows an excess around 5 MeV relative to the prediction from the reactor spectrum model. This observation indicates a demand for modification of current reactor $\bar{\nu}_e$ model and reconsideration of the reactor anomaly. To avoid this excess problem, a method comparing spectral ratio between observed and expected is used. The far to near spectral ratio of IBD events shows an energy dependent disappearance of reactor $\bar{\nu}_e$ in comparison to the expected far to near ratio. The result obtained using event rate information is

$$\sin^2(2\theta_{13}) = 0.087 \pm 0.009(stat.) \pm 0.007(syst.) \pm 0.011(total), \tag{10.1}$$

where, the world average value of $|\Delta m^2_{ee}| = 2.49 \times 10^{-3}\text{eV}^2$ is used [12]. The method using event rate and shape information obtains

$$\sin^2(2\theta_{13}) = 0.082 \pm 0.009(stat.) \pm 0.006(syst.) \pm 0.010(total). \tag{10.2}$$

This large value of θ_{13} will raise the following round of neutrino experiments to measure CP phase angle. and resolve the neutrino mass hierarchy problem. The main causes of the systematics error of $\delta \sin^2 2\theta_{13}$ are the uncertainties of backgrounds, energy scale, detection efficiency and reactor $\bar{\nu}_e$ flux as summarized in Table 9.5. Because the backgrounds are measured from the data samples, the uncertainties of background estimation will be reduced with the increases of data.

As shown in Fig 10.1, the RENO experiment is expected to get a $\sin^2 2\theta_{13}$ value with a 7% fractional error.

With a measurements from the hydrogen captured IBD data and better understating of systematic uncertainties, the RENO experiment could obtain the results with 5% or less than 5% fractional error. The combining of accelerator beam results and precise $\sin^2 2\theta_{13}$ would be the first step of the finding CP phase angle.

The first $|\Delta m^2_{ee}|$ measurement of the RENO experiment is

$$|\Delta m^2_{ee}| = 2.62^{+0.21}_{-0.23}(stat.)^{+0.12}_{-0.13}(syst.)^{+0.24}_{-0.26}(total). \tag{10.3}$$

The Table 10.1 shows consistent results of the current experiments and powerfully supports the paradigm of three generations of neutrinos. The RENO experiment is expected to determine $|\Delta m^2_{ee}|$ values with a precision of ~5% with 5 years of data. It might provide a tip on the neutrino mass ordering.

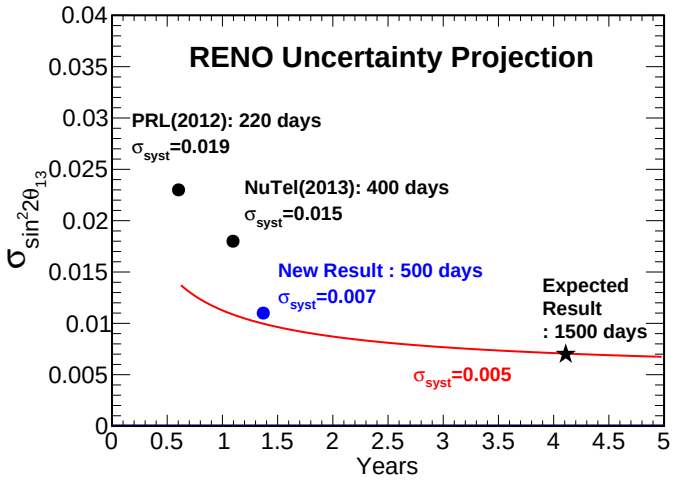

Figure 10.1: Uncertainty projection of RENO

Experiment	Δm^2	Result ($\times 10^{-3}$ eV^2)
RENO [69]	$\lvert\Delta m^2_{ee}\rvert$	$2.62 + 0.24 - 0.26$
Daya Bay [54]	$\lvert\Delta m^2_{ee}\rvert$	2.42 ± 0.11
MINOS [53]	$\lvert\Delta \bar{m}^2\rvert$	$2.50 + 0.23 - 0.25$
T2K [51]	Δm^2_{32} (normal)	2.51 ± 0.10
	Δm^2_{13} (inverted)	2.48 ± 0.10

Table 10.1: Comparison of the current Δm^2 values

The comparison of the current estimation precision to the RENO, the Daya bay and the expected precision to the RENO with 1500 days data are summarized as following table and figure.

$\sin^2(2\theta_{13})$	RENO (500 days) [69]	Expected RENO (1500 days)	Daya Bay [54]
Statistical Error	0.009	0.005	-
Systematic Error	0.006	0.005	-
Total Error	0.01	0.007	0.005

Table 10.2: Comparison of the error of the experimental result for $\sin^2(2\theta_{13})$

$\lvert\Delta m^2_{ee}\rvert$ $(\times 10^{-3} eV^2)$	RENO (500 days) [69]	Expected RENO (1500 days)	Daya Bay [5
Statistical Error	+0.21 - 0.23	+0.12 -0.13	-
Systematic Error	+0.12 - 0.13	+0.10 - 0.12	-
Total Error	+0.24 - 0.26	+0.16 - 0.18	+0.11

Table 10.3: Comparison of error of experimental result for $\lvert\Delta m^2_{ee}\rvert$

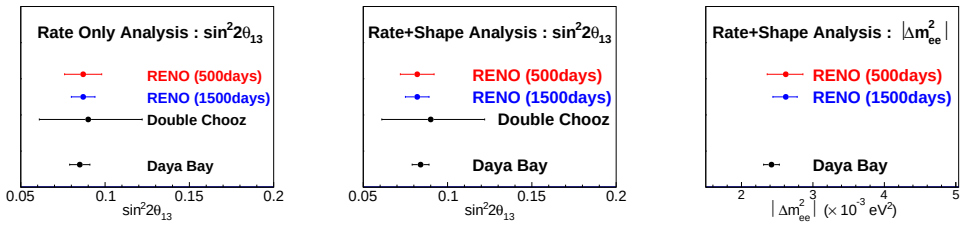

Figure 10.2: Plot for the comparison of the experimental result

Appendix A

PMT Charge Stability

As time goes by, The response of pmt to the unit energy decrease. The main causes of the decreasing response are degradation in attenuation length of Gd-LS as shown Figure A.1. So that some charge correction factor is needed to fix the decreasing energy response problem. The daily charge correction factor for regular run data is derived from p.e. distribution of delayed signal of IBD candidate. The delayed signal of IBD candidates are distribute at the target uniformly. The correction factor from the delayed is mean charge correction for the uniformly distributed events. It is imperfect correction for the calibration source data which is distributed at target center. A additional charge correction factor for source data is needed. The additional charge correction factor is derived from the comparing n-Gd events between IBD candidates and Cf source data and the common decreasing slope of the source data.

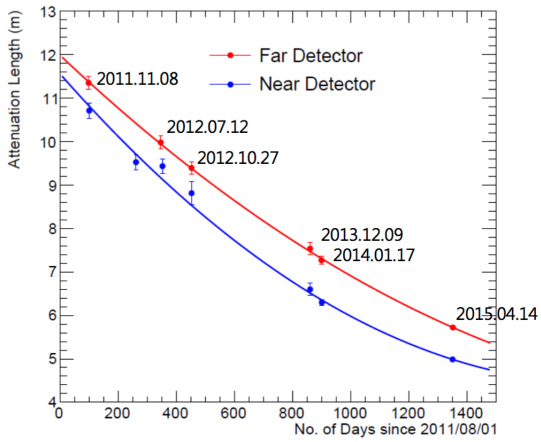

Figure A.1: Stability of Gd-LS Attenuation length. The initial attenuation length (August first 2011) is assumed as 12 m.(same for near and far detector)

A.1 Charge Correction from IBD Delayed Signal

At the opening paragraph of this section, the pmt response is decreasing as time goes. The pmt response is monitored by photo-electron distribution of delayed signal of IBD candidates. Figure A.2 shows the clearly 8 MeV Gd captured neutron events. The IBD candidates are observed around 70 events per day at the far detector and around 700 event per day at the near detector. They could be enough daily monitoring material.

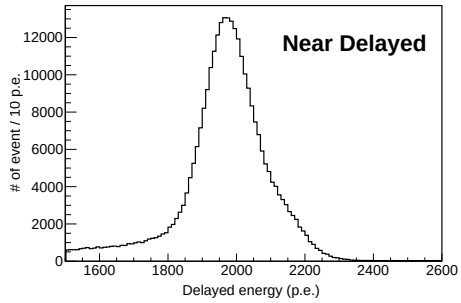

Figure A.2: Photo-electron distribution of delayed signal of IBD candidate. Clearly shown 8 MeV Gd captured neutron events

Figure A.3 shows the degradation of daily base pmt response by observation

of the peak values of delayed. From the Figure A.3, The charge correction factors for each run could be derived from following equation.

$$\text{Correction Factor} = \frac{\text{reference p.e.}}{\text{peak value of delayed}} \tag{A.1}$$

where, reference p.e is 1984.33 p.e. for the near detector and 2036.18 p.e. for the far detector. After applying this correction factor, Figure A.4 shows the response of pmt is well controlled.

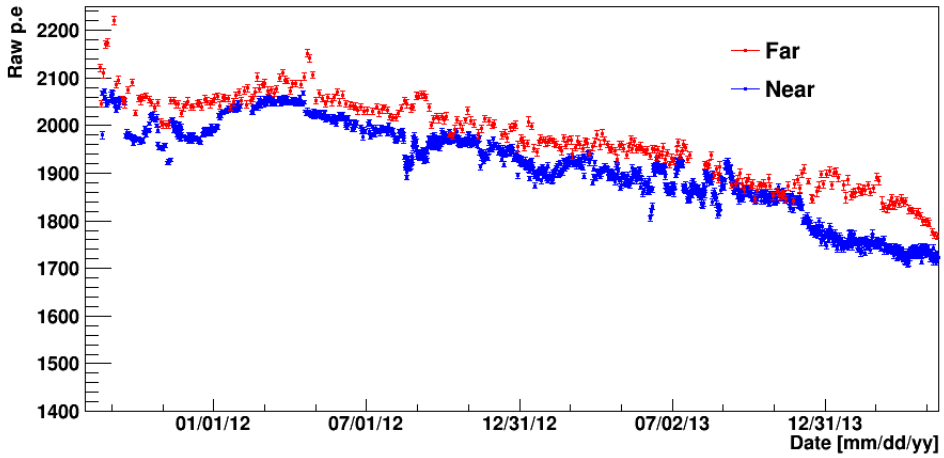

Figure A.3: Time variation of peak value of photo-electron distribution of delayed signal of IBD candidate. The Red point is peak value of p.e. distribution at the far detector. each point is a bunch of 200 IBD candidates ($\sim$ 3 day data). And Blue point is peak value of p.e. distribution at the near detector. each point is a bunch of 300 events($\sim$ 0.5 day data)

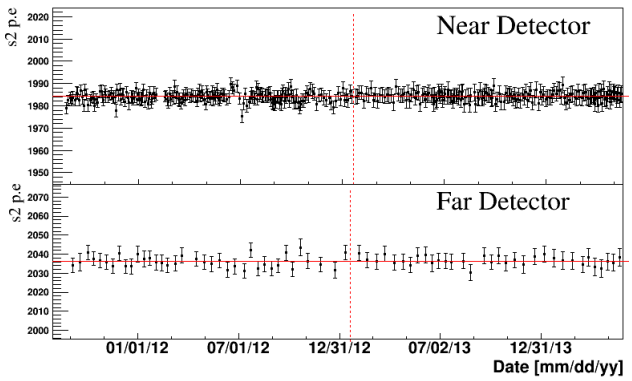

Figure A.4: Time variation of peak value of photo-electron distribution of delayed signal of IBD candidate after correction.

A.2 Charge Correction for Source Data

The pmt response of calibration source data is also decreasing as time goes, even though after correction by correction factor from IBD candidate delayed signal(Equation A.1) as shown Figure A.5.

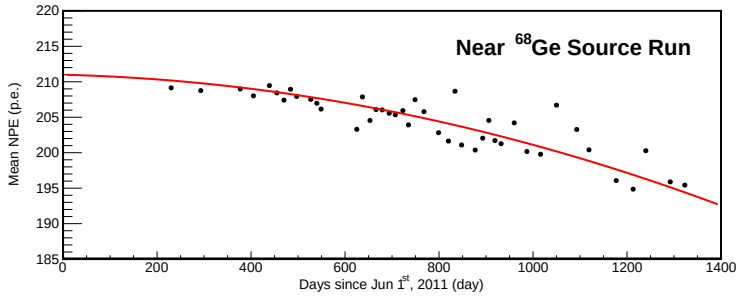

Figure A.5: Time variation of ^{68} Ge source data at the near detector. Black dots are Mean of photo electron distribution of ^{68} Ge source data after applying charge correction from delayed signal of IBD candidate. And red line is guide line. The mean p.e. of ^{68} Ge source data is decreasing as time goes, even though the charge correction factor(Equation A.1 is applied.)

Because the ratio of events at the target center and events that distribute target uniformly is increasing as time goes. Increasing of the ratio is also due to degradation of attenuation length of Gd-LS. Calibration source data is taken at

the center of target. So that calibration source data is distribute target center. It is difference from IBD candidate which is distributed target uniformly. So that the conversion factor for center distributed event to uniform distributed event is needed to calibration energy. This conversion factor is named as center-to-uniform correction factor and defined as following equation.

$$C_{center-to-uniform} = \frac{\text{mean p.e. of uniform distributed delayed signal}}{\text{mean p.e. of center distributed delayed signal}} \quad \text{(A.2)}$$

where the center distributed delayed signal is events in the cylindrical region, height is (-550 mm , 550 mm) and radius is 400 mm, located target center. Figure A.6 shows the center-to-uniform correction factor is increasing as time goes. So that the additional charge correction factor is needed to correct p.e distribution of source data.

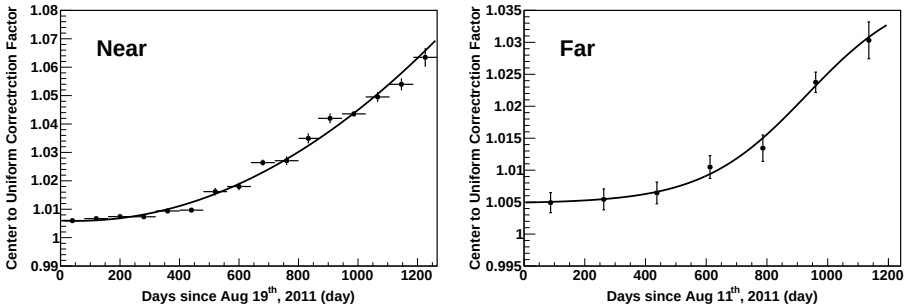

Figure A.6: Time variation of Center-to-Uniform correction factor. The center-to-uniform correction factor is increasing as time goes at the both detector.

The additional charge correction factor for Hydrogen captured neutron events of ^{252}Cf is defined as following equation.

$$C_{n-H}^{additional} = \frac{Q_{n-Gd}^{IBD} \cdot \frac{1}{C_{center-to-uniform}}}{Q_{n-Gd}^{Cf}} \quad \text{(A.3)}$$

where, Q_{n-Gd}^{IBD} is mean p.e. of delayed signal of IBD candidates after applying charge correction factor(Equation A.1). Q_{n-Gd}^{Cf} is mean p.e. of Gadolinium captured neutron event of ^{252}Cf. and $C_{center-to-uniform}$ factor is the value on Nov 2011 that date is chosen as reference date for all charge correction. The additional charge correction factor for n-H events of ^{252}Cf is derived from comparing Gadolinium captured neutron event between IBD candidate and ^{252}Cf. Because

of Gadolinium captured neutron event of IBD candidate (=delayed signal) is uniformly distributed event. In the contrary, Gadolinium captured neutron event of ^{252}Cf is distributed at the center of target. Therefore the term of Center-to-Uniform correction factor is needed. This correction factor is simpler than additional charge correction factor for other source data. Other sources do not have Gadolinium captured neutron event which could be comparing with delayed signal of IBD candidates. Because of this, The additional charge correction factor for other sources is using degradation slope from time variation of mean p.e. of source data and p.e. values from Hydrogen captured neutron event as defined following equation.

$$C_{src,cs}^{additional} = \frac{\overline{Q'_{Cf,n-H}}}{Q_{Cf,n-H}^{ref.} \cdot f_{src,cs}(date)} \tag{A.4}$$

where, $\overline{Q'_{Cf,n-H}}$ = Mean($C_{n-H}^{additional} \cdot Q_{Cf,n-H}$, the degradation slope of source data and ^{137}Cs data is $f_{src,Cs}(date) = 1 + P_1^{src,Cs} \cdot date + P_2^{src,Cs} \cdot date^2$ and $Q_{Cf,n-H}^{ref.} = P_0^{cf} \cdot f_{cf}$(Nov.2011). P_0^{cf} is fitting parameter of Equation A.6.

The degradation slope (=$f_{src,Cs}$) of ^{137}Cs and other sources have different behavior. So that the slopes are derived from different method. Firstly, the slope for the ^{137}Cs(=f_{Cs})is derived from fitting 2nd polynomial(=Equation A.5) on the its own time variation as shown Figure A.7. and the slope of other sources(=f_{src}) is derived from fitting common slope model(=Equation A.6) on the time variation of all the other sources.

$$fittingfunction_{cs} = P_0^{Cs} \cdot f_{Cs} = P_0^{Cs} \cdot (1 + P_1^{Cs} \cdot date + P_2^{Cs} \cdot date^2) \tag{A.5}$$

$$\begin{aligned} fittingfunction_{src} &= (P_0^{Ge} + P_0^{Cf,n-H} + P_0^{Co} + P_0^{Cf,n-Gd}) \cdot f_{src} \\ &= (P_0^{Ge} + P_0^{Cf,n-H} + P_0^{Co} + P_0^{Cf,n-Gd}) \cdot (1 + P_1^{src} \cdot date + P_2^{src} \cdot date^2) \end{aligned} \tag{A.6}$$

The fitting result of the Equation A.5 and Equation A.6 are summarized in the Figure A.7, A.8 and the Table A.1, A.2. And the mean p.e. time variation after correction is shown A.9.

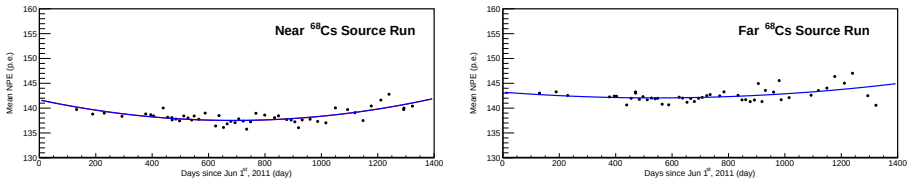

Figure A.7: The degradation slope of ^{137}Cs data. Left side is near detector and right side is far detector.

Parameter	Near	Far
P_0^{Cs}	141.65 ± 0.03	143.21 ± 0.03
P_1^{Cs}	-8.50 $\times 10^{-5}$ ± 5.17 $\times 10^{-7}$	-2.97 $\times 10^{-4}$ ± 4.99 $\times 10^{-7}$
P_2^{Cs}	6.18 $\times 10^{-8}$ ± 3.27 $\times 10^{-10}$	-2.75 $\times 10^{-8}$ ± 3.19 $\times 10^{-10}$

Table A.1: Fitting results of ^{137}Cs time variation

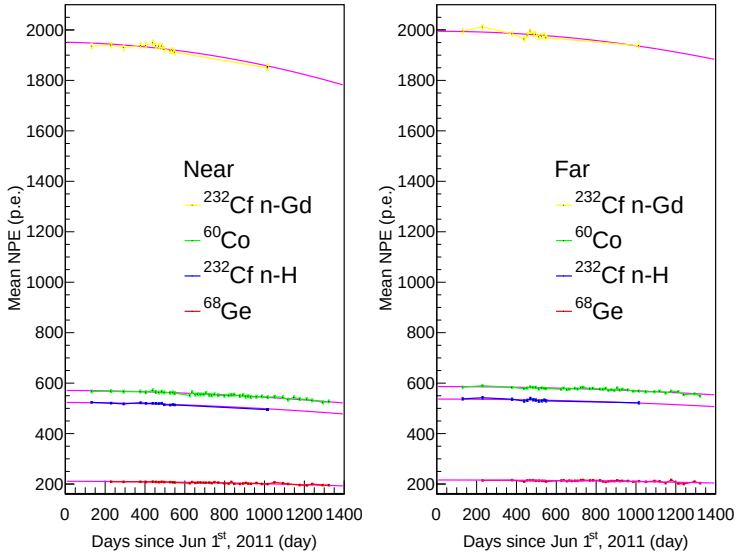

Figure A.8: The common degradation slope of the other sources, Left side is near detector and right side is far detector.

Parameter	Near	Far
P_0^{Ge}	211.00 ± 1.18	216.09 ± 0.52
$P_0^{Cf,n-H}$	523.38 ± 2.59	586.41 ± 0.92
P_0^{Co}	571.03 ± 3.03	586.41 ± 0.92
$P_0^{Cf,n-Gd}$	1951.27 ± 9.61	1994.63 ± 2.65
P_1^{src}	-7.95 $\times 10^{-6}$ ± 1.62$\times 10^{-5}$	-3.70 $\times 10^{-9}$ ± 4.96 $\times 10^{-17}$
P_2^{src}	-3.89 $\times 10^{-8}$ ± 1.15 $\times 10^{-8}$	-2.87 $\times 10^{-8}$ ± 1.74 $\times 10^{-9}$

Table A.2: Fitting results of the other sources time variation

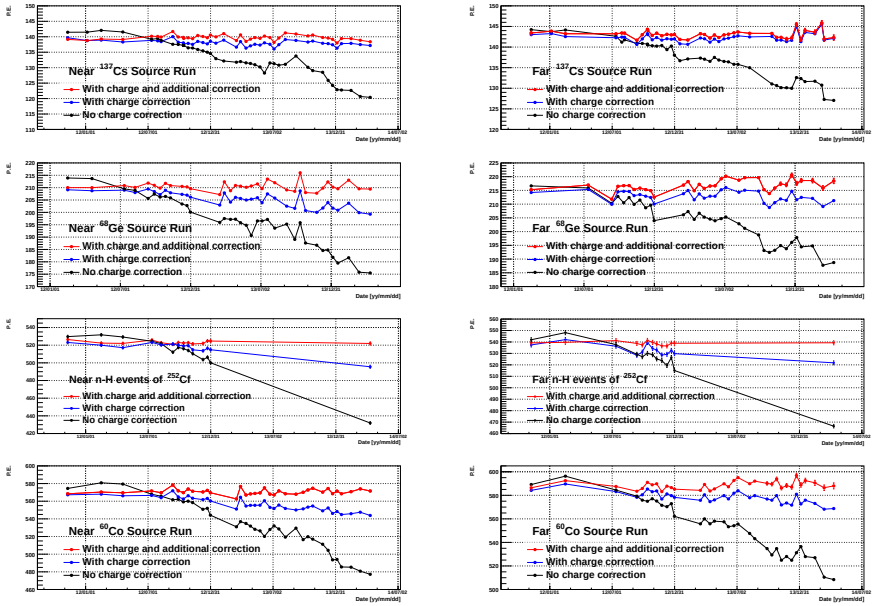

Figure A.9: Comparison of time variation of sources. Left side is near detector and right side is far detector. Black is the time variation of the source data without any charge correction. Blue is the time variation of the source data after applying charge correction. Red is the time variation of the source data after applying charge correction and additional correction. The red shows the stability of source data is well controlled.

Appendix B

Signal Loss from IBD Selection Criteria

B.0.1 Signal Loss from Time Coincidence

We require the coincidence time window for the prompt and delayed event, 2μsec $\sim$ 100μsec. The DAQ process for each channel takes $\sim$1μsec, so below 2μsec, the prompt and delayed event can be mixed like single events. So, we give up the portion of below 2μsec. The mean lifetime of neutron capture by Gd is $\sim$30μsec, so the portion of upper than 100μsec is negligible. If we increase the coincidence time window more than 100μsec, the increased events will be negligible and accidental background will increase. The efficiency for this coincidence time window is 96.20 %.

There is one more inefficiency. The capture time distribution should be exponentially decrease. However, Figure B.1 shows that both Monte-Carlo simulation and final data sample have rapidly increase structure between 2 $\sim$ 13 μsec region. Dashed line is the extrapolation of exponential fitting upper than 13 μsec region. We calculate the difference of extrapolation curve and both measured data spectrum and simulated result to calculate the inefficiency of this region. The inefficiency between 2 $\sim$ 13 μsec capture time is 13.04 % for data and 8.81 % for Monte-Carlo simulation. The difference is 4.23 %, so we subtract this difference to the original efficiency to compensate the difference of data and Monte-Carlo. The final calculated efficiency is therefore 91.07 %. And signal loss from time coincidence is 8.93 %.

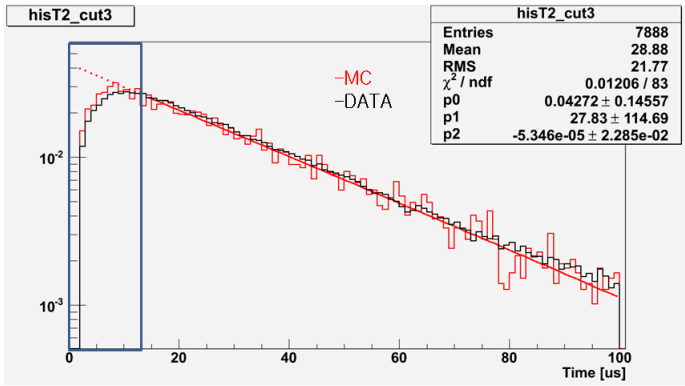

Figure B.1: Capture time distribution of final data sample and Monte-Carlo simulation. There are rapidly increasing structure between 2 $\sim$ 13μsec and dashed line is the extrapolation curve of exponential fitting upper than 13μsec region. The difference of extrapolation curve and capture time distribution is considered to the inefficiency.

B.0.2 Signal Loss from Energy Threshold

Prompt Energy Threshold

The threshold energy of prompt signal for Inverse Beta Decay event is 1.022 MeV, about 250 photo-electrons. However in experiment, we must consider the energy resolution and discriminator efficiency, and so on. So, we need to require more lower energy for prompt signal energy threshold. We decided this energy threshold to 170 photo-electrons. Also, almost whole generated events are passing this criterion. The efficiency of prompt energy cut is 100%, No signal Loss.

Delayed Energy Threshold

The criteria for delayed energy cut is 6 MeV $\sim$ 12 MeV. However, Figure 8.1 shows that there is a long tail below 6 MeV. This portion of event cannot be selected to the Inverse Beta Decay events. Consider this fractional loss, the efficiency for delayed energy cut is 94.14 %. and the loss from delayed energy cut is 5.86 %.

B.0.3 Signal Loss from Spatial Correlation and Removal of Incoming γ-rays and Flashers

In the section 6.3, the γ-ray and flasher removal cut ($Q_{max}/Q_{tot} < 0.07$) does not have any signal loss.

B.1 Equation for Signal Loss from Timing Veto with Muon or Trigger Information

If trigger is within cut time range [0,Δt] relative to the prompt of IBD event, the IBD event is lost by the cut. Because no correlation between the prompt of IBD event and adjacent trigger, Signal loss is just probability that at least one of trigger is within cut time window [0,Δt] relative to the prompt of IBD event and It can be calculated by poisson probability distribution.

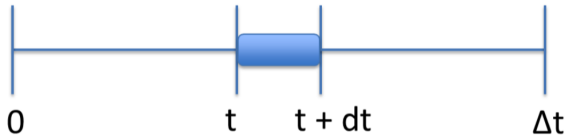

Figure B.2: Signal loss condition: One Trigger is within [t,t+dt]. and no trigger is [0,t].

The probability of signal loss condition that the one trigger is within [t,t+dt] and no trigger is [0,t] is

$$dP = P[(N(t) - N(0)) = 0] \cdot P[(N(t+dt) - N(t)) = 1] = e^{-R_{trg}t} \cdot R_{trg}dt \quad \text{(B.1)}$$

where, $P[(N(t) - N(0)) = 0] = e^{-R_{trg}t}$ and $P[(N(t+dt) - N(t)) = 1] = R_{trg}dt \cdot e^{-R_{trg}dt} \sim R_{trg} \cdot dt \cdot (1 - R_{trg} \cdot dt) \sim R_{trg} \cdot dt$.

And, the total probability of signal loss is

$$P(0, \Delta t) = \int_0^{\Delta t} dP = \int_0^{\Delta t} e^{-R_{trg}t} \cdot R_{trg}dt = 1 - e^{-R_{trg}\Delta t}. \quad \text{(B.2)}$$

The signal loss from Timing veto cut with Muon or Trigger information is calculated by Equation B.2. But there is some modification case by case in the Equation B.2. More details are following section.

B.2 Signal Loss from Muon Veto

The signal loss from muon veto is simply calculated by Equation B.2. The rate of each type muon and the results are summarized following table. The uncertainty of these signal loss is neglect. Because it is calculated from event rate that is order of million and fractional statistical error is order of 10^{-4}%.

Muon Type	Far			Near		
	Energy	Rate (Hz)		Energy	Rate (Hz)	
		set A	set B		set A	set B
A	> 1.5 GeV	0.047	0.045	> 1.6 GeV	0.109	0.100
B	$1.2 \sim 1.5$ GeV	0.082	0.079	$1.5 \sim 1.6$ GeV	0.083	0.074
C	$1.0 \sim 1.2$ GeV	0.159	0.150	$1.4 \sim 1.5$ GeV	0.092	0.083
1	$0.07 \sim 1.0$ GeV	12.853	12.856	$0.07 \sim 1.4$ GeV	117.231	117.011
2	$20 \sim 70$ MeV	0.257	0.260	$20 \sim 70$ MeV	0.787	0.625

Table B.1: Rate of each type muon at data set A and B

Muon Type	Far			Near		
	Veto Time (ms)	Signal Loss (%)		Veto Time (ms)	Signal Loss (%)	
		set A	set B		set A	set B
A	700	3.243	3.113	700	7.341	6.786
B	500	4.018	3.855	400	3.264	2.907
C	200	3.122	2.959	200	1.830	1.645
1	1	1.277	1.277	1	11.062	11.043
2	1	0.023	0.026	1	0.079	0.062
combined	–	11.201	10.782	-	21.642	20.863

Table B.2: Signal loss from muon veto

B.3 Signal Loss from Trigger Timing Veto

Trigger vetos consist of 5 kinds as listed following.

- Any Trigger before 100 μs cut : No any trigger within (-100 μs, 0 μs) of prompt signal.
- Prompt-like Trigger before 300 μs cut : No prompt-like trigger within (-300 μs, 0 μs) of prompt signal.
- Buffer Trigger after 200 μs cut : Zero buffer trigger within (0 μs, 200 μs) of prompt signal.
- Prompt-like Trigger after 1000 μs cut : No prompt-like trigger within (0 μs, 1000 μs) of prompt signal.

- Buffer and Veto Trigger after 200 μs cut : Zero buffer and veto trigger within (0 μs, 200 μs) of prompt signal.

The equations for signal loss of trigger time veto are modified Equation B.2 as described below.

The equation for Signal loss of Any Trigger Before 100 μs Cut

$$Loss_{AnyTrg}^{100\mu s} = 1 - e^{-\left(R_{AnyTrg} - R_{TotalMuon}\right)\cdot 0.0001 sec} \tag{B.3}$$

where, R_{AnyTrg} is rate (Hz) of any trigger. and $R_{TotalMuon}$ is rate(Hz) of all muon. Prompt of IBD candidate is already passed muon veto. There is no muon before the prompt. Therefore effective event rate is $R_{AnyTrg} - R_{TotalMuon}$.

The equation for Signal loss of Prompt-like Trigger Before 300 μs Cut

$$Loss_{P.like}^{300\mu s} = e^{-R_{P.like}\cdot 0.0001 sec} - e^{-R_{P.like}\cdot 0.0003 sec} \tag{B.4}$$

where, $R_{P.like}$ is rate (Hz) of prompt-like trigger. Prompt-like trigger before 300 μs cut overlap the any trigger before 100 μs cut. So that time range (-100 μs, 0 μs) is excluded to avoid over calculation.

The equation for Signal loss of Buffer Trigger After 200 μs Cut

$$Loss_{BufTrg}^{200\mu s} = \frac{\int_0^{100\mu s} f(t') \cdot e^{-\frac{t'}{30\mu s}} dt'}{\int_0^{100\mu s} e^{-\frac{t'}{30\mu s}} dt'} \tag{B.5}$$

where,

$$f(t') = \int_0^{t'} e^{-\left(R_{BufTrg} - R_{prompt}\right)\cdot t} \cdot \left(R_{BufTrg} - R_{prompt}\right) dt + \int_{t'}^{200\mu s} e^{-R_{BufTrg}\cdot t} \cdot R_{BufTrg} dt, \tag{B.6}$$

and R_{BufTrg} is rate (Hz) of buffer trigger. R_{prompt} is rate (Hz) of prompt candidate signal which is the prompt-like trigger with energy range 0.75 $\sim$ 12 MeV. The equation of signal loss for buffer trigger cut is weighted average mean of $f(t')$ with weight is the probability of the time t' which is the moment of getting delayed signal. The effective event rate is difference between the prompt and delayed and after delayed. There is no prompt candidate between the prompt and delayed. If there is prompt candidate between the prompt and delayed, the prompt and delayed could not be IBD candidate pair. So that effective event rate is $R_{BufTrg} - R_{prompt}$ between the prompt and delayed and R_{BufTrg} after delayed.

The equation for Signal loss of Prompt-like Trigger After 1000 μs Cut

$$Loss_{P.like}^{1000\mu s} = e^{-R_{P.like}\cdot 0.0002sec} - e^{-R_{P.like}\cdot 0.001sec} \tag{B.7}$$

where, $R_{P.like}$ is rate (Hz) of prompt-like trigger. Prompt-like trigger after 1000 μs cut overlap the buffer trigger after 200 μs cut. So that time range (0 μs, 200 μs) is excluded to avoid over calculation.

The equation for Signal loss of Buffer and Veto Trigger After 200 μs Cut

$$Loss_{BVTrg}^{200\mu s} = \frac{\int_0^{100\mu s} f(t') \cdot e^{-\frac{t'}{30\mu s}} dt'}{\int_0^{100\mu s} e^{-\frac{t'}{30\mu s}} dt'} \tag{B.8}$$

where,

$$f(t') = \int_0^{t'} e^{-(R_{BVTrg}-R_{TotalMuon})\cdot t}\cdot(R_{BVTrg} - R_{TotalMuon})\, dt + \int_{t'}^{200\mu s} e^{-R_{BVTrg}\cdot t}\cdot R_{BVTrg} dt \tag{B.9}$$

and R_{BVTrg} is rate (Hz) of buffer and veto trigger, $R_{TotalMuon}$ is rate(Hz) of all muon. The equation for signal loss of buffer and veto trigger is also weighted average mean of $f(t')$ with weight is the probability of the time t' which is the moment of getting delayed signal. The effective event rate is difference between the prompt and delayed and after delayed. Because delayed signal is muon veto passed event. So that there is no muon event between prompt and delayed signal. So that effective event rate is $R_{BVTrg} - R_{TotalMuon}$ between the prompt and delayed and R_{BVTrg} after delayed.

Summary of Signal Loss from Trigger Timing Veto

The signal loss from trigger timing veto is calculated equations in previous paragraph. The rate of each event and the results are summarized following table. The uncertainty of these signal loss is neglect. Because it is calculated from event rate that is order of million and fractional statistical error is order of 10^{-4}%.

Event Type	Far Rate (Hz)		Near Rate (Hz)	
	set A	set B	set A	set B
Any Trigger	145.515	143.672	597.283	591.695
Buffer Trigger	77.013	77.407	60.602	57.815
Buffer&Veto Trigger	23.136	23.141	208.617	208.255
Prompt-like Trigger	47.560	50.692	30.428	30.410
Prompt Candidate	39.811	41.336	24.534	25.576
Total Muon	13.398	13.391	118.302	117.893

Table B.3: Rate of each event type at data set A and B

Veto	Far Signal Loss (%)		Near Signal Loss (%)	
	set A	set B	set A	set B
Any Trigger before 100 μs	1.312	1.294	4.677	4.628
Prompt-like Trigger before 300 μs	–	1.004	0.605	0.605
Buffer Trigger after 200 μs	1.424	1.426	1.140	1.082
Prompt-like Trigger after 1000 μs	–	3.934	–	2.389
Buffer&Veto Trigger after 200 μs	–	0.426	–	3.767
Combined	2.718	7.862	6.334	11.929

Table B.4: Signal loss of trigger timing veto at data set A and B. Represented by "–" mean that veto cut does not apply.

B.4 Signal Loss from Removal of ^{252}Cf Contamination

Removal cuts of ^{252}Cf contamination consist of 3 kinds as listed following.

- Hotspot removal cut : No prompt signal in the region $\sqrt{(X-125)^2+(Y-125)^2}$ < 300 mm and - 1700 mm < Z < -1200 mm.
- ΔR-Cf before cut : No prompt-like trigger greater then 3 MeV within (-10 sec, 0 sec) and (0, 400 mm) of prompt signal
- ΔR-Cf after cut : No prompt-like trigger greater then 3 MeV within (0 sec, 10 sec) and (0, 400 mm) of prompt signal

The signal losses for Removal of ^{252}Cf Contamination can not be calculated by Equation B.2. It is not using time information only. So that The signal losses are estimated by measuring contribution of IBD signal in the cut rejected sample as described followings.

Signal Loss of Hotspot Removal Cut

The signal loss of hotspot removal cut is estimated from the ratio of rejected and total IBD candidates at the set A. The Hotspot removal cut rejected of set A are 118 events. and Total IBD candidates of set A are 26310. So there ratio (=118/26310) is 0.00449. Therefore Signal Loss of Hotspot Removal Cut is 0.449%.

Uncertainty of this Signal Loss is estimated from the contribution of IBD candidates at the 18 times over sized region rejected sample by spectral fitting. As shown Figure B.3, The uncertainty is 0.025%.

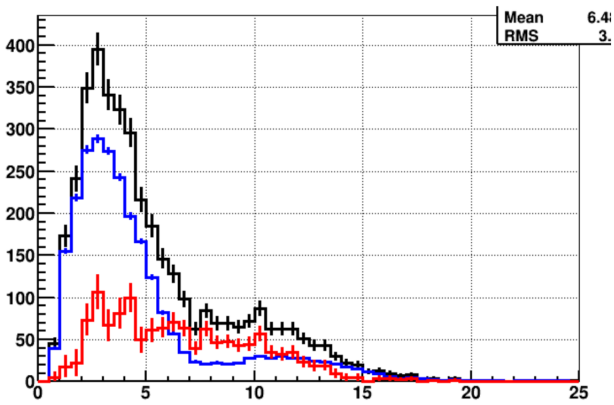

Figure B.3: Estimation of signal loss for Hotspot Removal Cut. The X axis unit of the plot is MeV. Black is Rejected by region R $<$ 900 mm , -1700 $<$ Z $<$ -700 mm which is 18 times larger than original cut region. Blue is fitting result of IBD candidate. And red is difference between black and blue. The fitting error is 0.453%. So that the uncertainty of hotspot removal cut is 0.025% (= 0.453/18).

Signal Loss of ΔR-Cf before and after cut

The signal loss of ΔR-Cf cut is estimated from the contribution of IBD candidate at the cut rejected sample derived from spectral fitting. The fitting results is shown Figure 6.42 and Figure 6.43.

^{252}Cf Removal	Signal Loss (%)	
	Far data set B	Near data set B
Hotspot Removal	0.449 ± 0.025	–
ΔR-Cf before cut	1.146 ± 0.098	2.362 ± 0.046
ΔR-Cf after cut	1.251 ± 0.079	2.179 ± 0.037
Combined	2.821 ± 0.126	4.490 ± 0.06

Table B.5: Signal loss of ^{252}Cf removal cuts at data set B. Represented by "–" mean that cut does not apply.

B.5 Summary of Signal Loss

So far, the signal losses from IBD selection are described. The signal losses could be divided two kinds: One is common signal losses of two detectors and two data set. and the other one is uncommon signal losses of two detectors and two data set. Common signal losses are from time coincidence, energy cut of prompt and delayed, spatial correlation cut and incoming γ-ray and flasher cut. These signal losses have very small varying in the period of set A and set B, and very small difference between far and near detector. So that these common signal losses are assumed same at the far and near detector and time. Uncommon signal losses are from the other selection criteria. The differences are from the event rate varying with time and difference between far and near detector environment such as overburden. The signal losses are summarized in following table. The loss that described by '-' means the cut is not applied that data set. The uncertainty that displayed '-' is too smaller than other loss uncertainties. So It was ignored.

Criteria	Far		Near	
	Loss	Uncertainty	Loss	Uncertainty
Time Coincidence	8.03	0.01	8.03	0.01
Prompt Energy Cut	0	0.01	0	0.01
Delayed Energy Cut	5.86	0.1	5.86	0.1
Spatial Correlation Cut	0	-	0	-
Gamma and Flasher Cut	0	-	0	-
Combined	13.42	0.09	13.42	0.09

Table B.6: Common Signal Loss (%)

Criteria	Far		Near	
	Loss	Uncertainty	Loss	Uncertainty
Muon Veto Cut	11.20	–	21.64	–
Any Trigger before 100 μs	1.312	–	4.677	–
Prompt-like Trigger before 300 μs	–	–	0.605	–
Buffer Trigger after 200 μs	1.424	–	1.140	–
Combined	13.62	–	26.61	–

Table B.7: Signal Loss for data set A (%)

Criteria	Far		Near	
	Loss	Uncertainty	Loss	Uncertainty
Muon Veto Cut	10.78	–	20.86	–
Any Trigger before 100 μs	1.29	–	4.63	–
Prompt-like Trigger before 300 μs	1.00	–	0.61	–
Buffer Trigger after 200 μs	1.43	–	1.08	–
Prompt-like Trigger after 1000 μs	3.93	–	2.39	–
Buffer&Veto Trigger after 200 μs	0.43	–	3.77	–
Hotspot removal	0.45	0.03	–	–
ΔR-Cf before cut	1.15	0.10	2.36	0.05
ΔR-Cf after cut	1.25	0.08	2.18	0.04
Combined	20.12	0.10	33.42	0.04

Table B.8: Signal Loss for data set B (%)

Appendix C

Study of Fast Neutron Background Shape

Spectrum of fast neutron is usually described flat distribution. But we do not know real spectrum of fast neutron. So that we decide to add uncertainty from model (= shape uncertainty). The difference between fitting result with fitting model $0th$ polynomial and $1st$ polynomial treat as a shape uncertainty of fast neutron. To reduce ambiguity of model difference, fast neutron dominant sample is used. Fast neutron dominant sample is the rejected by prompt-like trigger after cut without buffer trigger cut, as shown Figure C.1. Figure C.1 is fitting result plot of fast neutron dominant sample with IBD, 10 MeV, and fast neutron components. The models of Fast neutron are first polynomial and zeroth polynomial. In zeroth polynomial case, Fast neutron dominant sample is fitted with fast neutron component only and fitting range is greater than 22 MeV. And the other case first polynomial, Fast neutron dominant sample is fitted with all three component and fitting range is greater than 1 MeV. Figure C.2 shows the residual fast neutron component that is from subtracting IBD and 10 MeV component from the fast neutron dominant sample. They are still shown flat shape within error range.

The estimated fractional shape uncertainty of fast neutron is 1.25 % for the far detector and 1.20 % for the near detector.

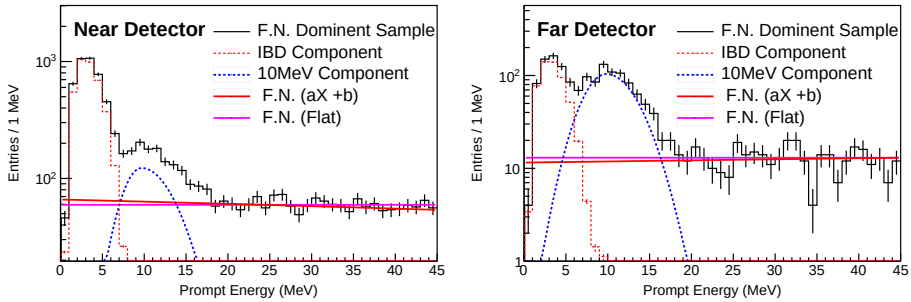

Figure C.1: Estimation of fast neutron shape uncertainty. Left side plot is near detector and right side plot is far detector. Black histogram is fast neutron dominant sample which is the rejected by prompt-like trigger after cut without buffer trigger cut. Red dotted histogram is IBD candidate component which is due to signal loss from prompt-like trigger after veto cut. Blue dotted histogram is a background with around 10 MeV peak which is not yet fully understood. Red line is Fitting result of fast neutron with first order polynomial model and other components and fitting range is greater than 1 MeV. Blue line is Fitting result of fast neutron with zeroth order polynomial model alone and fitting range is greater than 22 MeV.

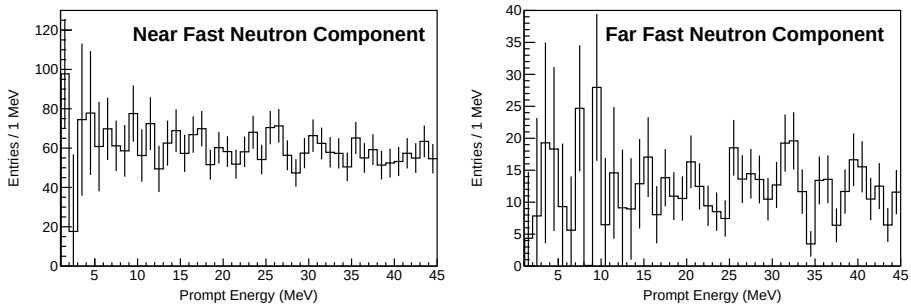

Figure C.2: Energy spectra of Fast Neutron from fast neutron dominant sample. Left side plot is near detector and right side plot is far detector. This histograms are from subtracting IBD and 10 MeV component from the fast neutron dominant sample. So that this histogram is similar to first order polynomial fitting result of fast neutron. But they are still shown flat shape within error range.

Appendix D

Study of ^{9}Li/^{8}He Background Shape

^{9}Li/^{8}He are produced by interaction between cosmic muons and carbon in the detector. ^{9}Li has half life time of 0.178 sec. And ^{8}He has half life time of 0.119 sec. To obtain ^{9}Li/^{8}He shapes, Time correlation between IBD candidate and Muons could be important clue. So that Time distance between IBD candidate and Muons could be fitted following function.

$$f(t) = A \cdot e^{-\frac{t}{\lambda}} + B \cdot e^{-\frac{t}{\tau}} + S \cdot e^{-\frac{t}{T}} \tag{D.1}$$

where, A is amplitude of μ-accidental, λ is mean time of μ-accidental, B and τ is amplitude and mean time of ^{9}Li/^{8}He component, S and T is amplitude and mean time of IBD component.

Figure D.1 shows the Time since muon distribution of IBD candidate. We found 3 time components by multiple exponential function fitting (Equation D.1: Black line of Figure D.1 is named IBD component which has no correlation with muons. Blue line of Figure D.1 is ^{9}Li/^{8}He component which has order of 100 μs of fitted exponential mean time. And unexpected red line is named μ-accidental component which has fitted exponential mean time of 20 μs. To avoid μ-accidental component, ^{9}Li/^{8}He is obtained from sample that has greater than 60 ms of time since muon.

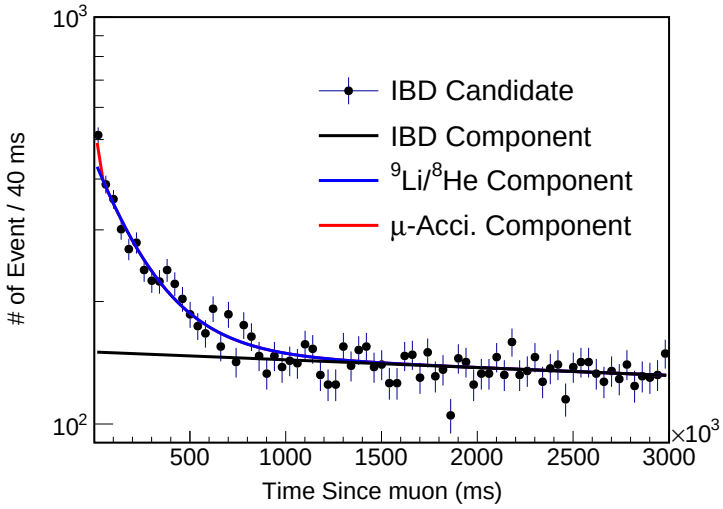

Figure D.1: Time since muon distribution of IBD candidate. Black dot is IBD candidate. Black line is fitting result of IBD component. Blue line is fitting result of ^{9}Li/^{8}He component. And red line is fitting result of μ-accidental component.

The processed of obtaining ^{9}Li/^{8}He shape are listed following.

- Preparing spectra : spectra of IBD component is the IBD candidate which have greater than 1 sec time since high energy muon (far : $>$ 1.5 GeV, near : $>$ 1.6 GeV) . and spectra of IBD + ^{9}Li/^{8}He sample with small amount of μ-accidental is time since muon region 60$\sim$500 ms for far detector and 60$\sim$400 ms for near detector.
- Estimating Contribution of IBD component at IBD + ^{9}Li/^{8}He component by multiple exponential function fitting.
- Obtaining ^{9}Li/^{8}He spectrum by subtracting IBD component with amount that estimated previous step to IBD + ^{9}Li/^{8}He sample.
- Subtraction small amount of μ-accidental to ^{9}Li/^{8}He spectrum.

D.1 Obtaining ^{9}Li/^{8}He Background Shape

As described before, The ^{9}Li/^{8}He background shape of far and near detector are obtained by using a time coincidence of IBD candidate and high energy muon which have long track line in the detector. The ^{9}Li/^{8}He Background Shape is

from the subtraction IBD component to IBD + ^{9}Li/^{8}He sample such as described following equation.

$$N^{i}_{LiHe} = N^{i}_{IBD+LiHe} - \beta \cdot N^{>1sec,i}_{IBD} \tag{D.2}$$

where, i is energy bin index, N^{i}_{LiHe} is the number of ith bin ^{9}Li/^{8}He shape as shown Figure D.4, $N^{i}_{IBD+LiHe}$ is ith bin value of the sample that have either IBD component and ^{9}Li/^{8}He component with the criteria that time coincidence with muon (>1.5 GeV) is within (60, 500 ms) for far detector and time coincidence with muon (>1.6 GeV) is within (60,400 ms) for near detector as shown Figure D.3, Muon energy range and time range are chosen to get the minimum uncertainty of ^{9}Li/^{8}He shape. So that the muon energy range (>1.5 GeV) and time range (60, 500 ms) are chosen for far detector. and muon energy range (>1.6 GeV) and time range (60, 400 ms) are chosen for near detector. $N^{>1sec,i}_{IBD}$ is ith bin value of the sample which have greater than 1 sec time coincidence with high energy muon (far : > 1.5 GeV, near : > 1.6 GeV), and β is scale factor for IBD component. Scale factor β is defined as following equation.

$$\begin{aligned} \beta &= \frac{N^{60\sim500ms}_{IBD}}{N^{>1sec}_{IBD}}, \text{for far detector, with muon (>1.5 GeV)} \\ \beta &= \frac{N^{60\sim400ms}_{IBD}}{N^{>1sec}_{IBD}}, \text{for near detector, with muon (>1.6 GeV)} \end{aligned} \tag{D.3}$$

where,

$$N^{t_0\sim t_1}_{IBD} = \int_{t_0}^{t_1} S \cdot e^{-\frac{t}{T}} dt \tag{D.4}$$

S and T is fitting results of amplitude and mean time of IBD component defined as Equation D.1.

The uncertainty of ^{9}Li/^{8}He shape (Figure D.4) is calculated by following equation.

$$\left(\delta N^{i}_{LiHe}\right)^2 = N^{i}_{IBD+LiHe} + \left(\delta\beta \cdot N^{>1sec,i}_{IBD}\right)^2 + \left(\beta \cdot \sqrt{N^{>1sec,i}_{IBD}}\right)^2 \tag{D.5}$$

The Equation D.5 is derived from simple error propagation. and $\delta\beta$ is taken into account correlated between S and T.

The results of Equation D.2 are shown Figure D.4. But this shape has still small amount of μ-accidental. So It is needed to subtract μ-accidental. Next section will describe about μ-accidental.

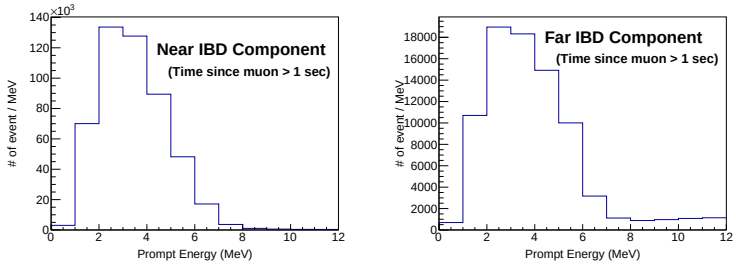

Figure D.2: Spectra of IBD Component (Time since muon $>$ 1 sec). Left side is near detector and right side is far detector. This component have no time correlation with high energy muon(far : $>$ 1.5 GeV, near : $>$ 1.6 GeV).

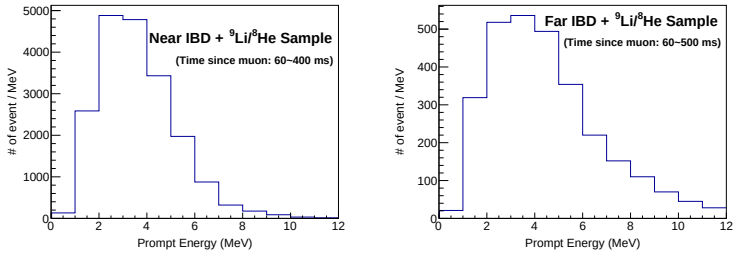

Figure D.3: Spectra of IBD+^{9}Li/^{8}He sample. Left side is near detector and right side is far detector. These samples are collected with the criteria that time coincidence with muon (>1.5 GeV) is within (60, 500 ms) for far detector and time coincidence with muon (>1.6 GeV) is within (60,400 ms) for near detector.

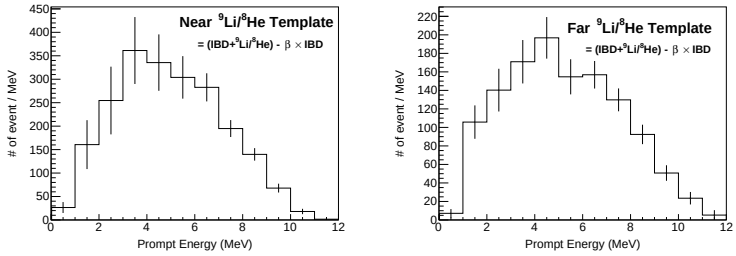

Figure D.4: ^{9}Li/^{8}He shape with small μ-accidental.Left side is near detector and right side is far detector. The ^{9}Li/^{8}He shape is obtained from Equation D.2 using Figure D.2, Figure D.3. But This shape still has small amount of μ-accidental.

D.2 Study of μ-Accidental

We found unexpected component which have short time coincidence with high energy muon. That is μ-accidental component which have 20 ms mean time in the time since muon plot as shown Red line of Figure D.1. The reason that is named μ-accidental, it have time correlation with muons and similar prompt energy and ΔR distribution of accidental. By the way, The ^{12}B/^{12}N also have mean life time of ~20 ms. So that delayed energy spectrum of μ-accidental is similar to ^{12}B/^{12}N energy spectrum as shown D.5.

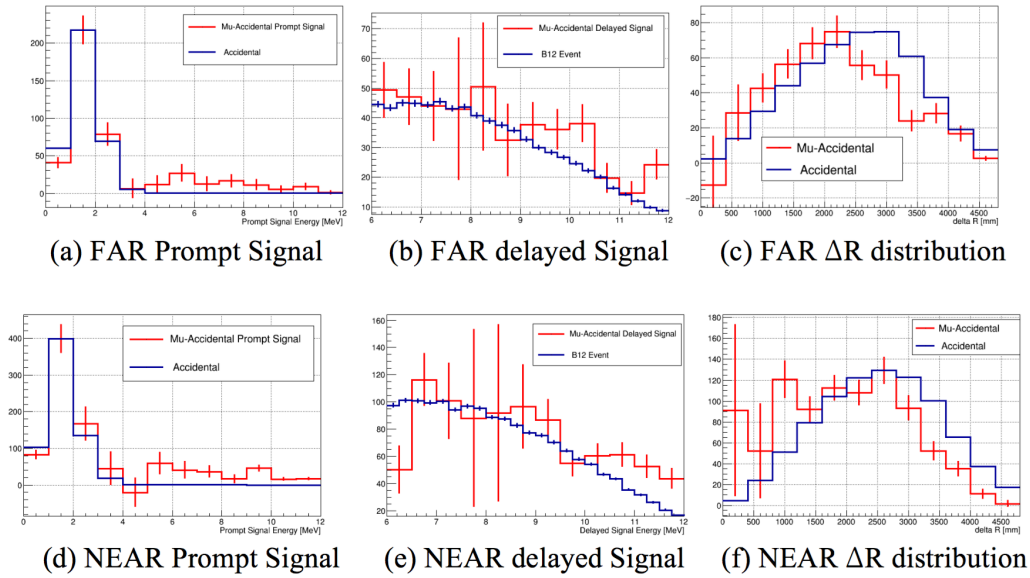

(a) FAR Prompt Signal (b) FAR delayed Signal (c) FAR ΔR distribution

(d) NEAR Prompt Signal (e) NEAR delayed Signal (f) NEAR ΔR distribution

Figure D.5: Properties of μ-accidental. Upper plots are far detector. and lower plots are near detector. Left side plots is prompt energy of μ-accidental and accidental background. Middle plots are delayed energy of μ-accidental and accidental background. And right side plots are distance between prompt and delayed (=ΔR) distribution of μ-accidental and accidental background. These plot shows similarity between μ-accidental and accidental.

As mentioned previous section, ^{9}Li/^{8}He shape (Figure D.4) has small amount of μ-accidental. So that estimation of μ-accidental amount at the ^{9}Li/^{8}He shape (Figure D.4) is needed. and subtraction μ-accidental to ^{9}Li/^{8}He shape. The sample that IBD+^{9}Li/^{8}He(Figure D.3) has two accidental components : IBD-accidental and μ-accidental. IBD-accidental is just simple accidental background which have no time correlation with high energy muons. So that contribution

of IBD-accidental is same in the IBD component(Figure D.2) and sample that IBD+^{9}Li/^{8}He(Figure D.3). Estimation of IBD-accidental is simply ΔR fitting method as shown left side plots of Figure D.6. And estimation of μ-accidental is also ΔR fitting method with constrained IBD-accidental components as shown right side plots of Figure D.6.

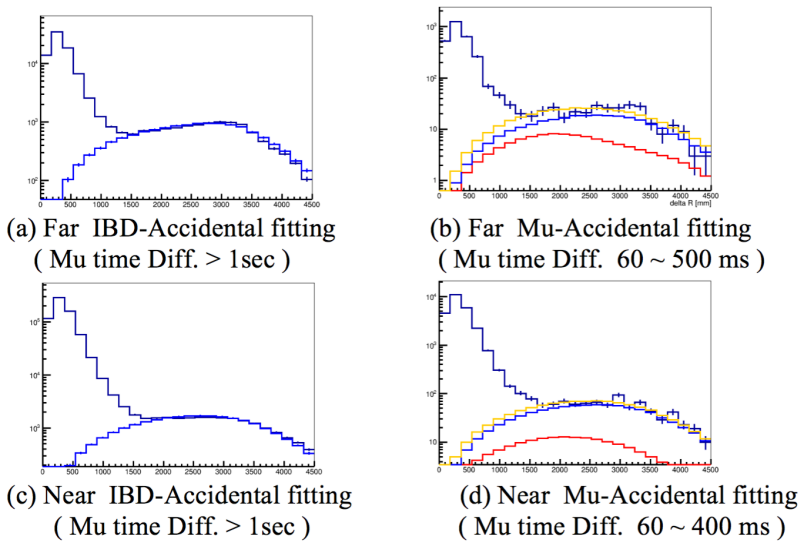

Figure D.6: Estimation of μ-accidental. X axis is distance between prompt and delayed(=ΔR), Y axis is the number of IBD candidate. Upper plots are far detector and lower plots are near detector. Left side plot is estimation of IBD-accidental which is normal accidental does not have time correlation with muons. Blue is fitting results of IBD-accidental. and purple histogram is IBD candidate which have greater than 1 sec of time since muon. Right plot is estimation of μ-accidental. Purple histogram is IBD candidate which have (60$\sim$500 ms) of time since muon for far detector and (60$\sim$400 ms) of time since muon for near detector. Blue is constrained fitting result of IBD-accidental. Red is fitting result of μ-accidental. and Orange is sum of two accidentals.

The result of μ-accidental is 33.28 $\pm$ 6.14 for far detector and 33.74 $\pm$ 8.65 for near detector. So the μ-accidental subtracted ^{9}Li/^{8}He shape shapes are shown following figure.

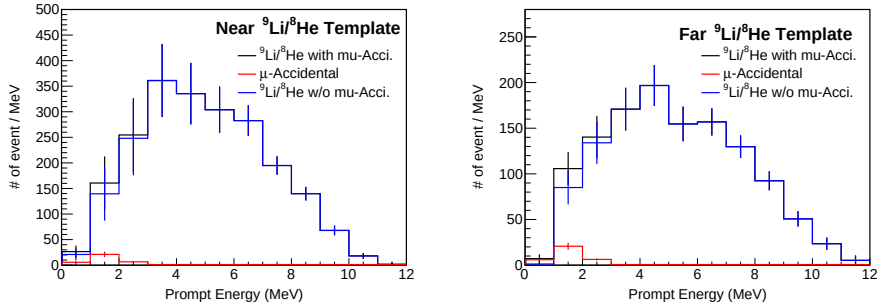

Figure D.7: Spectra of μ-accidental subtracted ^{9}Li/^{8}He. Left side is near detector and right side is far detector. Black is ^{9}Li/^{8}He shape with small amount of μ-accidental. Red is μ-accidental. Blue is μ-accidental subtracted ^{9}Li/^{8}He shape.

D.3 Summary of ^{9}Li/^{8}He Background Shape

so far, the study of ^{9}Li/^{8}He Background Shape is described. ^{9}Li/^{8}He shapes are derived from time correlation between IBD candidates and high energy muons. Muon energy range and time range are chosen to get the minimum uncertainty of ^{9}Li/^{8}He shape. The results for the study of ^{9}Li/^{8}He Background Shape are summarized in following table.

	Far	Near
Prompt Energy	$0 \sim 12$ MeV	$0 \sim 12$ MeV
Muon Energy	> 1.5 GeV	> 1.6 GeV
Time since muon	$60 \sim 500$ ms	$60 \sim 400$ ms
Mean Time of IBD component	22.7 ± 0.15	10.50 ± 0.02
Mean Time of LiHe component	249.65 ± 18.9	357.38 ± 53.95
Number of IBD+^{9}Li/^{8}He	2867	19295
Number of IBD (>1sec)	81954	495257
$\beta\times$ IBD (>1sec)	1632.85 ± 10.25	17147.6 ± 41.46
μ-accidental	33.28 ± 6.14	33.74 ± 8.65
Number of ^{9}Li/^{8}He without μ-accidental	1200.87 ± 53.93	2113.67 ± 141.40

Table D.1: Summary table of ^{9}Li/^{8}He study.

Appendix E

Study of ^{252}Cf Background Shape

The backgrounds due to ^{252}Cf are not yet fully understood. But we found various components of the backgrounds due to ^{252}Cf contamination from Cf removal cut rejected sample. The founded six component of the backgrounds due to ^{252}Cf contamination are summarized following lists.

- 1 MeV-a Component from any trigger before cut rejected sample.
- 1 MeV-b Component from ΔR-Cf before cut rejected sample.
- 2.2 MeV Hydrogen captured neutron component from any trigger before cut rejected sample.
- 7.9 MeV Gadolinium captured neutron component from any trigger before cut rejected sample.
- 8 MeV Component from hotspot removal cut rejected sample.
- 12 MeV Component from ΔR-Cf after cut rejected sample.

The shape of backgrounds due to ^{252}Cf contamination could be reconstructed by estimating remaining amount of each components in the final sample. For the study, Data set B and C of far detector are used. Because Data set B and C are severe contaminated by ^{252}Cf.

E.1 Six Components of ^{252}Cf Background

As mentioned previous, backgrounds due to ^{252}Cf contamination consist of 6 components. Figure E.1 shows six ^{252}Cf background components. 3 components (1

MeV-a, 2.2 MeV, 7.9 MeV) are found from any trigger before cut rejected sample. 2.2 MeV and 7.9 MeV components are well known Hydrogen or Gadolinium captured neutron event, and 1 MeV-a component has unknown origin. And the other 3 components (1 MeV-b, 8 MeV, 12 MeV) are found from Cf removal cuts. 1 MeV-b component is rejected from ΔR-Cf before cut. and 12 MeV component is rejected from ΔR-Cf after cut. lastly the 8 MeV component is rejected from hotspot removal cut.

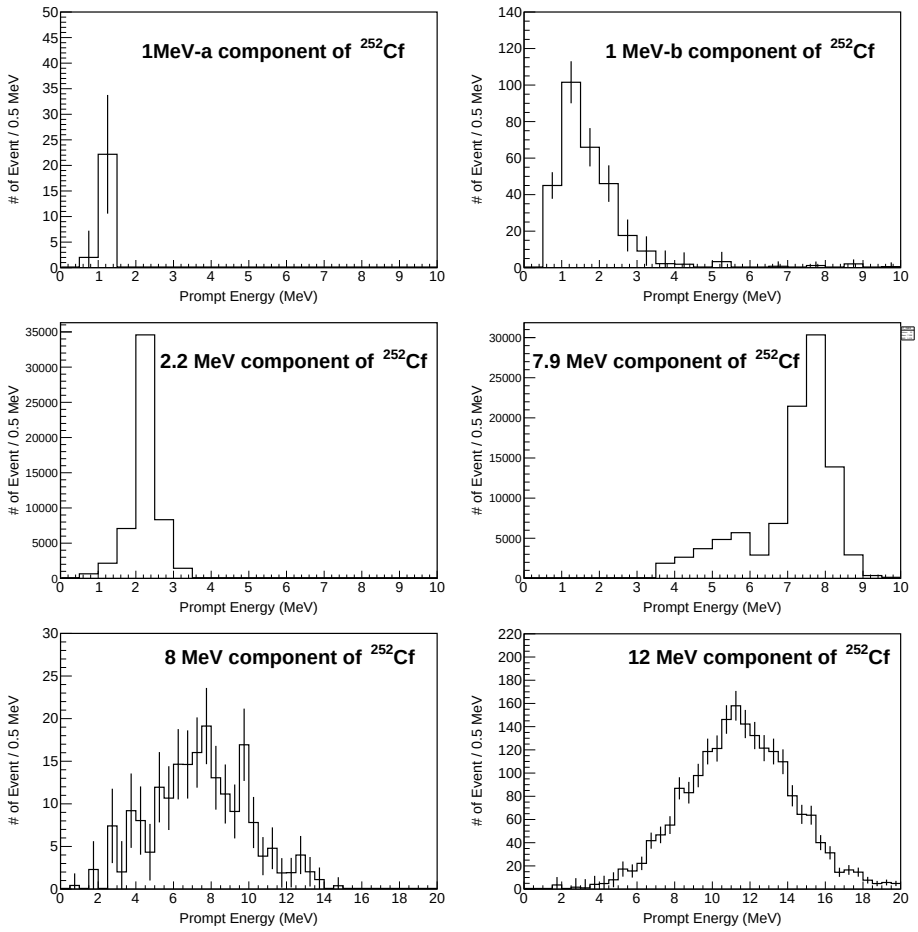

Figure E.1: Spectra of Six ^{252}Cf background components.

E.2 Estimation of Remaining ^{252}Cf Components

As mentioned previous section, To reconstruct shape of ^{252}Cf backgrounds,The remaining ^{252}Cf components in the final sample of data set A and B are estimated. And than Sum of these component with estimated remaining value is the reconstructed shape of ^{252}Cf backgrounds. Following sections will mention about how estimate remaining of each components.

E.2.1 The Components from Any Trigger Before Cut Rejected

The components from any trigger before cut rejected are 1 MeV-a, 2.2 MeV and 7.9 MeV component. The remaining in the final cut passed IBD candidate sample of the data set B and C are estimated from saturation function fitting of rejected each three components with varying cut time windows. Figure E.2 shows estimation of rejected each three components (upper left side plot) and estimation of remaining components in the final cut passed sample. Upper left side plot of Figure E.2 is estimation of rejected three components by spectral fitting with 3 components and IBD component to any trigger before cut rejected samples. This fittings are executed with various cut time window of any trigger before cut. And a saturated rejected value is remaining component in the final cut passed sample. Each rejected component have saturation value as shown Figure E.2. The fitting results of saturation value for 1 MeV-a component is 19.24 $\pm$ 16.88. Error of 1 MeV-a component is taken into account shape error and fitting error of saturation point. The fitting results of saturation value for 2.2 MeV component is 162.97 $\pm$ 52.14. Error of 2.2 MeV component is calculated with saturation fitting error only. shape error is neglect. Because it is too small. The fitting results of saturation value for 7.9 MeV component is 14.60 $\pm$ 9.72. Error of 7.9 MeV component is also calculated with saturation fitting error only. It has same reason.

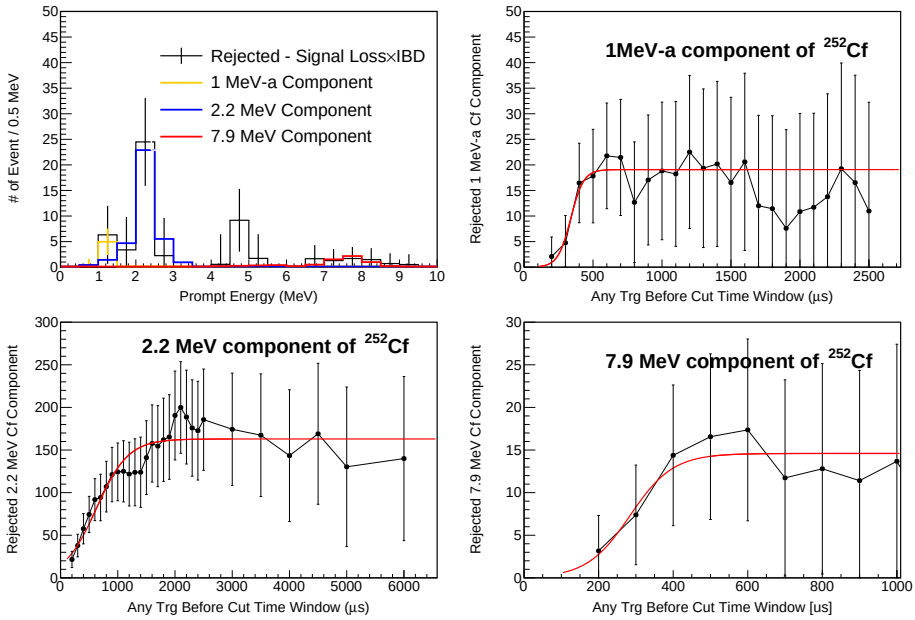

Figure E.2: Estimation of remaining components from any trigger before cut rejected. Upper left side plot is estimation of 3 components at the any trigger rejected sample. Black Histogram is subtraction of rejected and signal loss times IBD candidates. Orange is fitting result of 1 MeV-a component. Blue is fitting result of 2.2 MeV component. Red is fitting result of 7.9 MeV component. Upper right side plot is estimation of remaining 1 MeV-a components by fit with saturation model. Lower left side plot is estimation of remaining 2.2 MeV components. And lower right side plot is estimation of 7.9 MeV components. X axis of these three plots is any trigger cut time windows. Y axis of these three plots is rejected each component estimated from rejected fitting results such as upper left side plot. The saturated values of each components are the remaining of the final sample.

E.2.2 1 MeV-b Component

Unfortunately, remaining 1 MeV-b component could not be estimated. So that the 1 MeV-b component is estimated indirect way using subtraction expected IBD and known backgrounds to iBD candidate of data set B and C (= expected ^{252} Cf shape). The six components are fitted together into the expected ^{252}cf shape. And then the remaining 1 MeV-b component is obtained. But this method has problems. One is largest error from statistical error of the IBD candidate. And using expected shape what this analysis want observed is disturb observation of

IBD candidates. To minimize these problems, only 1 MeV-b component is chosen from this method. Figure E.3 shows the fitting results of estimating 1 MeV-b component with expected cf shape. The remaining 1 MeV-b component in the final sample is 215.47 ± 106.14.

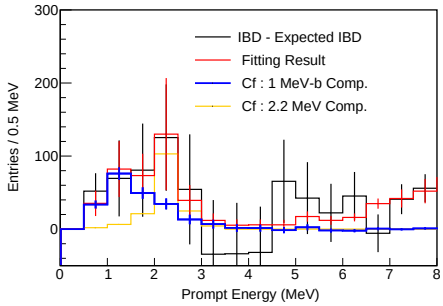

Figure E.3: Estimation of remaining 1 MeV-b component. Black histogram is subtraction of Expected IBD and known background to IBD candidate that means expected cf shape at the data set B and C (=expected cf shape). Blue is spectral fitting result of 1 MeV-b component. and Orange is fitting results of 2.2 MeV component. And red is fitting result of all component.

E.2.3 8 MeV Component

Remaining 8 MeV component could be estimated from tails of hotspot events at the outside of cut region as shown Figure E.4. Left side plot of Figure E.4 is Z distribution of IBD candidate in the horizontal cut region. This distribution is fit with flat function and gaussian function. The gaussian tail in the outside of cut region is the remaining 8 MeV component. Right side plot of Figure E.4 is R^2 distribution of IBD candidate in the vertical cut region. This distribution is fit with flat function and exponential function. The exponential tail in the outside of cut region is the remaining 8 MeV component, too. The results of remaining 8 MeV component is 12.37 ± 13.07 from right side of Figure E.4, and 7.10 ± 13.36 from left side of Figure E.4. So the total remaining 8 MeV component is 19.47 ± 18.69.

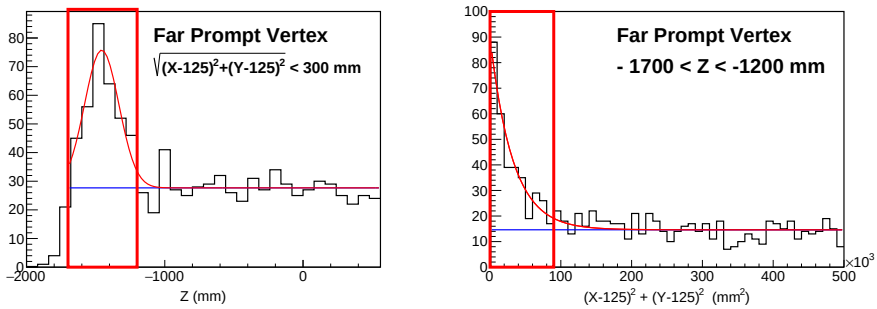

Figure E.4: Estimation of remaining 8 MeV component. Left side is Z distribution of IBD candidate in the horizontal cut region. Red Box is cut region. Blue line is fitting result of normal events. Red line is fitting results of hotspot events. the tails are in the outside of cut region. It could be remaining 8 MeV component. And Right side plot is R^2 distribution of IBD candidate in the vertical cut region. The tails are also in the outside of cut region. So that these tails could be also remaining 8 MeV component.The remaining 8 MeV component is tail of hotspot events from fitting results.

E.2.4 12 MeV Component

Remaining 12 MeV component could be estimated from spectral fitting with fast neutron and 12 MeV component to final cut passed iBD candidate sample as shown Figure E.5. The fitting result of remaining 12 MeV component is 172.76 $\pm$ 9.78.

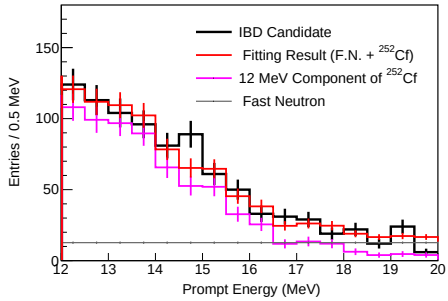

Figure E.5: Estimation of remaining 12 MeV component. Black histogram is final cut passed IBD candidate of data set B and C. Gray line is fast neutron. Blue is fitting result of 12 MeV component. Red line is fast neutron + 12 MeV component.

E.3 summary

So far, the six components of Backgrounds from ^{252}Cf are described. Each remaining at the final samples are estimated with over calculated error and summarized following Table E.1. And the total sum of six remaining components is shape of backgrounds from ^{252}Cf as shown Figure E.6.

Component	Remaining (0.75∼8 MeV)
1 MeV-a	19.08 ± 16.88
1 MeV-b	215.37 ± 106.14
2.2 MeV	162.97 ± 52.14
7.9 MeV	14.60 ± 9.72
8 MeV	21.06 ± 18.81
12 MeV	172.76 ± 9.78
Combined	605.63 ± 121.84

Table E.1: Summary table of remaining ^{252}Cf components

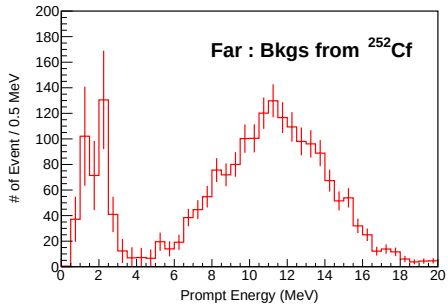

Figure E.6: The shape of backgrounds from ^{252}Cf. This plot is sum of six remaining components.

Appendix F

Estimation of Baseline between Reactors and Detectors

The baseline between reactors and detectors is relative distance from center of the each reactor core and to the center of detectors. The center of detector is center of target as shown Figure F.1. And the center of reactor is center of reactor fuel as shown Figure F.2. So the baseline between reactors and detectors is defined as relative distance from the center of reactor fuel to the center of detector target. Absolute values of baseline and X, Y, Z position of detector and reactor are not shown this thesis. Because the coordinates of reactor is national secret. So that in this thesis, only the uncertainties of baseline and X, Y, Z position are shown.

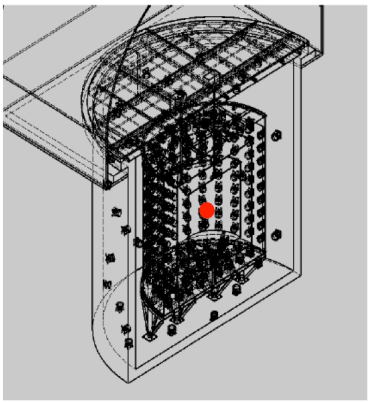

Figure F.1: Center of the detector. side is center of detector. It is defined as a center of target.

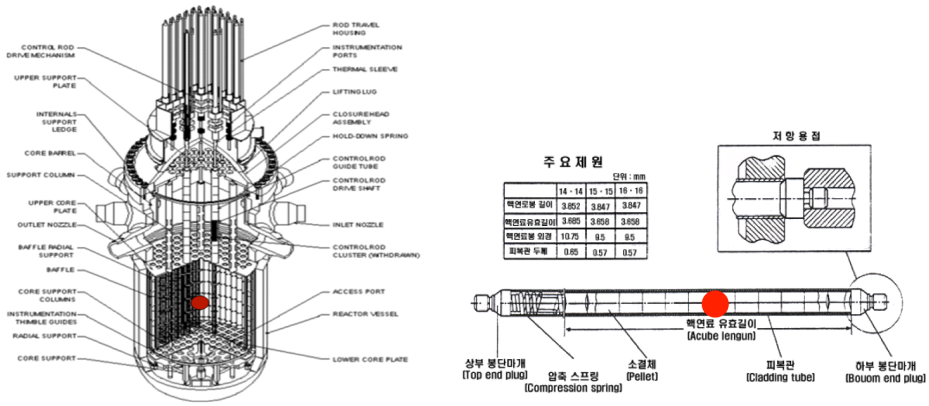

Figure F.2: Center of reactor. Left side is plot of reactor center. It is defined as a center of reactor fuel. Right side is schematic of fuel rod. The z of center point is defined red point in the plot that is center of acube lengun.

Baseline is a parameter of expected flux as shown Equation 3.8. So that uncertainty of baseline is also source of systematic error of θ_{13} and $\left|\Delta m^2_{ee}\right|$. To calculation the systematic uncertainties due to the position uncertainties of reactor and detector, Monte-Carlo simulation is used. Assuming that gaussian probability distribution, vary the position of each reactor by $x_i \rightarrow x_i + G(0, \Delta x_i)$ and calculate the flux.

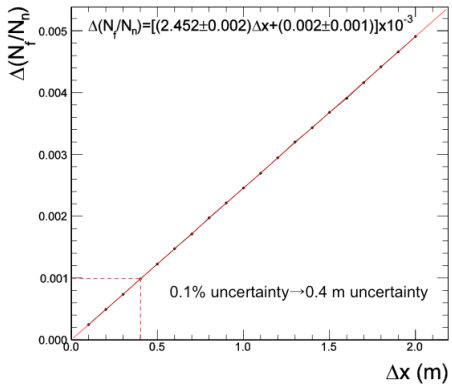

Figure F.3: Uncertainty of far to near ratio due to baseline uncertainty estimated by Monte-Carlo simulation

The results of Monte-Carlo simulation is shown Figure F.3. It shows to keep

the far to near ratio uncertainty below 0.1%, the position uncertainty in each axis needs to be below 40 cm (assuming much smaller position uncertainty for detectors). The uncertainty 0.1% of far to near ratio is negligible compared the uncertainty 0.5% from reactor thermal power and the uncertainty 0.7% from fission fraction. So the systematic error of baseline is needed to have below 40 cm.

The position of the reactors and detectors are measured by difference company and difference time. So they need connection work between measurements. The X and Y position of detector center is measured by open traverse method. Firstly, Sam-Kyung E&C surveyed from the reference point of the plant to CP3 or CP6 which are points in front of detector tunnel) And next, Asis E&C surveyed from the CP3 or CP6 to detector center as shown Figure F.4. The uncertainties of open traverse survey can not be estimated. But uncertainties of closed traverse survey could be estimated. The maximum uncertainty of closed traverse survey is 8 times of surveying machine uncertainty. So we assumed uncertainties of X and y position of detector center is 8 times of measurement uncertainties of surveying machine (Leica TPS800).

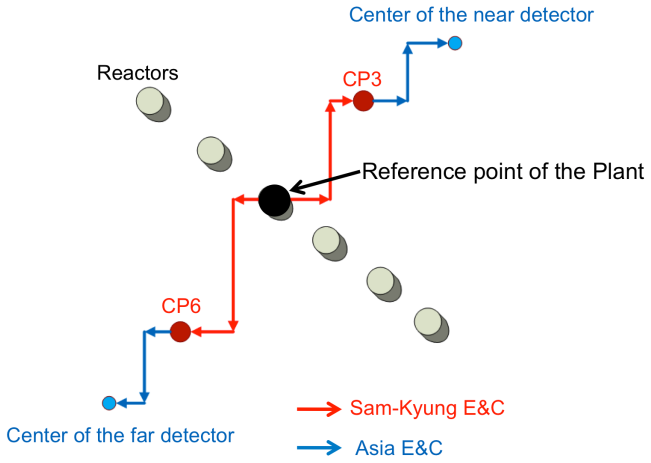

Figure F.4: Conceptual plot of survey for X and Y position of detector center. Red arrow is survey by the Sam-Kyung E&C from the reference point of the plant to CP3 or CP6 which are points in front of detector tunnel before the detector construction. Blue arrow is survey by the Asia E&C from the CP3 or CP6 to center of the far detector after completion of tunnel construction. The X and Y position of detector center are from combined these two results.

Surveying of Z position is also measured independent of the plant. So It need to connection between reference points of reactors and detecter. This work is measured by Soobong construction from the reference point of the plant(BM NO1) to reference point of the far detector as shown Figure F.5. We decided that uncertainty of Z position is upper limit of acceptable levels from the building law.

Figure F.5: Satellite map of survey route for Z position of detector center. Red line is survey route by the Soobong construction from level reference point (BM NO1) of the plant to reference point of the detector.

The coordinates of reactors are determined by GPS to a precision of within 3 cm and provided by KHNP. So that all uncertainties of positioning information are summarized in Table F.1. It shows the uncertainties of positioning is below 20 cm. And the uncertainties of baseline is also below 40 cm. So that the systematic error due to baseline is neglect in this analysis.

	Reactor	Far detector	Near detector
δx	3.0	7.8	11.9
δy	3.0	6.4	9.4
δz	3.0	2.0	1.1
δr	5.2	10.3	15.2

Table F.1: Uncertainty of center points

Appendix G

Optimization of MC Parameter

G.1 Motivation

When we obtain pe-to-MeV conversion function, we use center-to-uniform correction factor , that is, the ratio of number of photo electrons observed by uniform source and center source. And we have noticed that this ratio is different between data and MC. In case of MC, the uniform-to-center ratio (uniform/center) is less than '1' while the uniform-to-center ratio derived from data is greater than '1' as shown in Figure G.1. The values in horizontal axis in Figure G.1 are the distance from the target surface. '0' is defined as target surface and bigger minus value is more distant from target surface toward center. We have checked many MC parameters and found that the attenuation length can affect the uniform-to-center ratio. Figure G.2 shows that p.e. of ^{60}Co source MC decrease with attenuation length decreasing. The horizontal axis values indicate the level of attenuation length decreasing relative to the previous MC, which is used for analysing previous results data sample (220 day data). We can see the level of p.e. decreasing is not same between center source and uniform source. When attenuation length is large, uniform-to-center is less than 1. However, when attenuation length decrease, uniform-to-center becomes larger than 1. That means the attenuation length set in our MC is not correctly tuned for data. So we try to tune attenuation length of MC by comparing uniform-to-center with that of data.

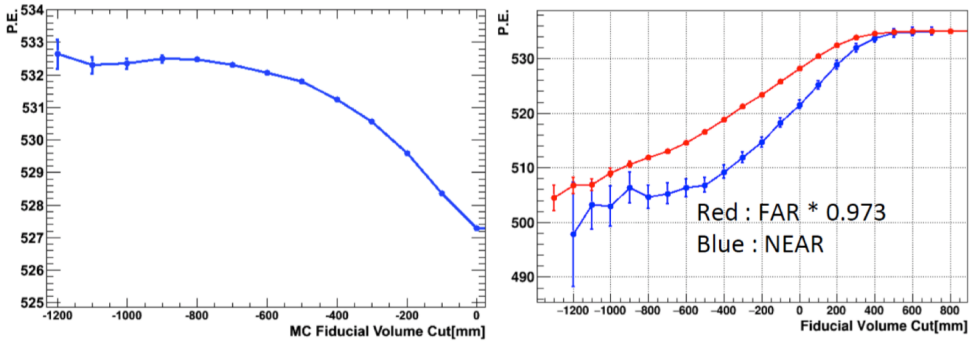

(a) 2.223 MeV gamma MC (b) n-H data

Figure G.1: Photo electron vs. volume cuts of n-H event. Left hand side plot is for 2.223 MeV gamma MC and right side plot is for n-H data

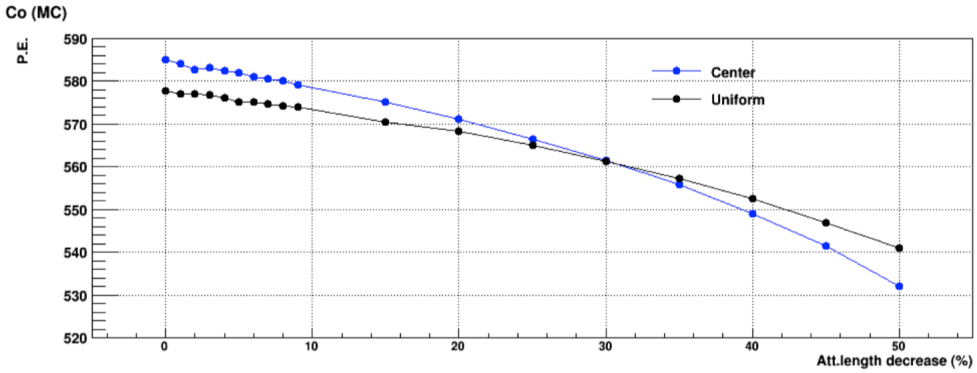

Figure G.2: Photo electron vs. Gd-LS attenuation length for ^{6}0Co MC at center and uniform

G.2 Tuning MC parameters

Our motivation to tune MC parameters began from necessity to tune Gd-LS attenuation length. However, if we change Gd-LS attenuation length, p.e. is changed and then we also need to change Gd-LS light yield to compensate the p.e. change from attenuation length tuning. In case of light yield, we tried to tune it by comparing p.e. of Co source between data and MC. So we have to satisfy the following requirement during our MC parameter tuning.

- uniform-to-center should be consistent between n-Gd data and n-Gd MC

- p.e. of target Co source should be consistent between data and MC at 0 day
- p.e. of gamma catcher Co source should be consistent between data and MC at 0 day

We proceed MC tuning in the following order.

- Step 0. Gd-LS attenuation length tune
  Gd-LS attenuation length is tuned by comparing uniform-to-center of n-Gd data and n-Gd MC.
- Step 1. Gd-LS light yield tune
  Gd-LS light yield is tuned by comparing p.e. of Co source between data and MC at 0 day. However, if we adjust Gd-LS light yield here, the uniform-to-center between data and MC, which was tuned at 0 step, becomes discrepant. So this discrepancy in uniform-to-center is tuned again in the next step.
- Step 2. LS light yield tune
  LS light yield not only affect the events in gamma catcher but also events in target because some of gamma produced in target spill out to gamma catcher region. So here, we tried to match uniform-to- center of n-Gd data and n-Gd MC by tuning LS light yield and at the same time we tried to match p.e of Co source data and MC in gamma catcher. If we cannot satisfy all the requirements of MC parameter tuning mentioned above upto this step, we go to next step to tune LS attenuation length.
- Step 3. LS attenuation length tune
  If there is still some discrepancy between data and MC until step2, we try to match it by tuning LS attenuation length.

G.2.1 Gd-LS attenuation length tune

Gd-LS attenuation length is tuned by comparing uniform-to-center of n-Gd data and n-Gd MC. Uniform-to-center is obtained by looking at p.e. as a function of cylindrical volume cut as shown in Figure G.3. The graph in Figure G.3 is for n-Gd MC, which Gd-LS attenuation length is decreased by 45%. relative to the default value in our MC. The values in horizontal axis are the distance from the target surface. '0' is defined as target surface and bigger minus value is more distant from target surface toward center. As for the p.e. of uniform n-Gd event, we can take the p.e value at '0'. To obtain p.e of center n-Gd events, we have to select events in small volume around center. However, we cannot do that because of

limited statistics. Instead we predict p.e. for any volume cut by fitting the graph in Figure G.3. In MC, we can generate n-Gd events whose vertex is at target center and compare what volume cut corresponds to the p.e. of center events. According to the result using the MC shown in Figure G.3, the p.e. at -1000 mm volume cut gives similar p.e. from center events. In general, however, this is not true because MC with other parameters may give different result. Anyway, for consistency between data and MC, we need to apply the same method of measuring uniform-to-center. Here, we apply -1000 mm volume cut to both data and MC to obtain p.e. from center events. However, we can choose any other volume cut criteria for center instead of -1000 mm as long as we keep consistency between data and MC. Figure G.5 shows the graph like that of Figure G.3 but for 500 days near and far data. As mentioned, we take p.e value at -1000 mm volume cut as center events and 0 mm cut as uniform events. The uniform-to-center ratios we obtained this way are 1.00785 +/- 0.00028 for near data and 1.00602 ± 0.00091 for far data. As uniform-to-center is obtained for data, we try to tune Gd-LS attenuation length of MC by looking uniform-to-center of MC for various Gd-LS attenuation length. Figure 6 shows center-to-uniform vs. Gd-LS attenuation length of MC and the allowed band from data is indicated for far (left) and near (right). The horizontal axis values are the relative Gd-LS attenuation length (%) to the default value set in our MC. By looking at this graph, we tuned Gd-LS attenuation length as -43.7% for far MC and -44.5% for near MC.

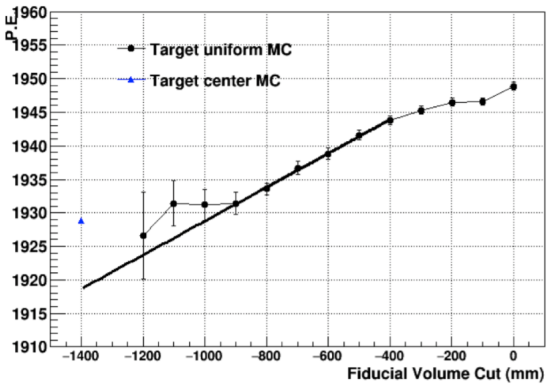

Figure G.3: Photo electron vs. cylindrical volume cut for IBD n-Gd MC, which attenuation length is decreased by 45% relative to the default value in our MC

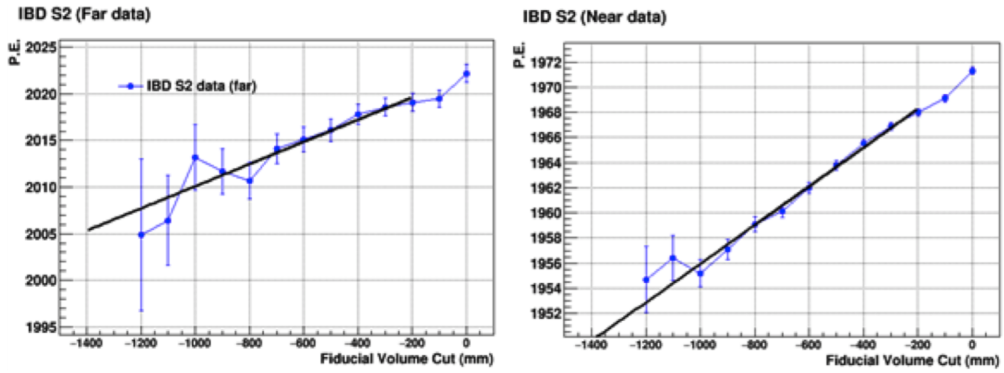

Figure G.4: Photo electron vs. cylindrical volume cut for 500 days far (left) and near (right) IBD n-Gd data, respectively.

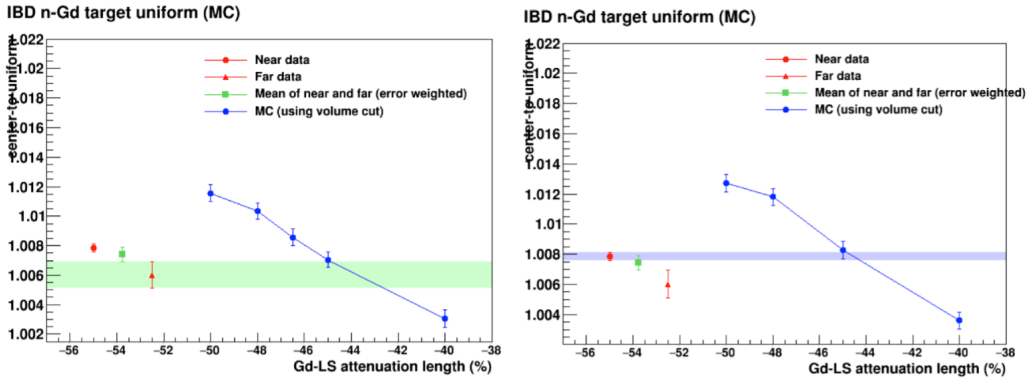

Figure G.5: Photo electron vs. cylindrical volume cut for 500 days far (left) and near (right) IBD n-Gd data, respectively.

G.2.2 Gd-LS light yield tune

In previous section, we decreased Gd-LS attenuation length from default value. Then it changes not only uniform-to-center but also decreases number of photo electrons. In default MC, we had tuned light yield so that number of photo electrons of Cs MC and far Cs source data agree. However, now the p.e. of source MC and data do not agree since we changed Gd-LS attenuation length. So we try to tune Gd-LS light yield by looking at p.e. of Co source. The p.e. of Co source data taken at 8.November.2011 is 589.144 ± 0.102 for far detector. And we found

that if we increase Gd-LS light yield by 9% relative to the default value, the p.e of far Co MC becomes 588.824 ± 0.115 and this agree with data. For near MC Gd-LS light yield tune, we also had a look at p.e of Co source as a function of Gd LS light yield. Figure G.6 shows p.e. of near Co source MC vs. Gd-LS light yield. The black dot is near Co source data. By comparing with that of data, we have tuned near Gd-LS light yield as +8.5% increase relative to default value.

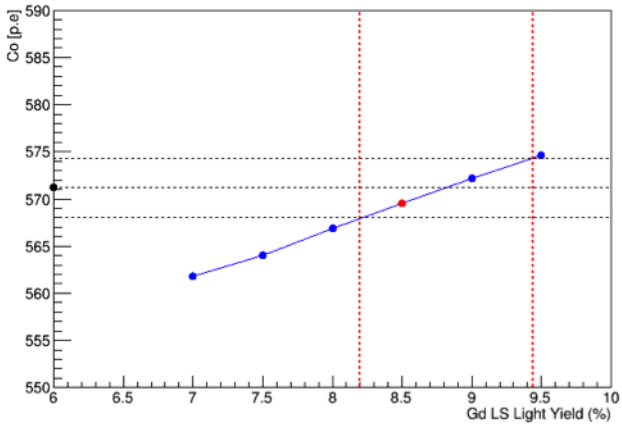

Figure G.6: Photo electron of near Co source MC vs Gd-LS light yield. The black dot is near Co data and black horizontal dot is the uncertainty of data

G.2.3 LS light yield tune

In previous section, we have tuned Gd-LS light yield. However, due to the change of Gd-LS light yield, the uniform-to-center of MC is affected. So we need to match uniform-to-center of MC to that of data again. In this step, we try to match it by tuning LS light yield. At the same time, we try to match p.e. of Co source MC generated at gamma catcher to the p.e. of Co data taken at gamma catcher region. Figure G.7 shows that uniform-to-center vs. LS light yield (left) and p.e. of gamma catcher Co source vs. LS light yield (right) for far MC. The black dot and horizontal black dotted line are data and its uncertainty for far. In this graph, we found that 4% increase of LS light yield from the default value can match uniform-to-center of data and at the same time p.e. of gamma catcher Co source data for far. Likewise, we tried to tune near LS light yield. Figure G.8 is similar plot to but for near MC and we found that if we increase near LS light yield by 7% compared to default value, we can match uniform-to-center and p.e of gamma catcher Co data at that same time.

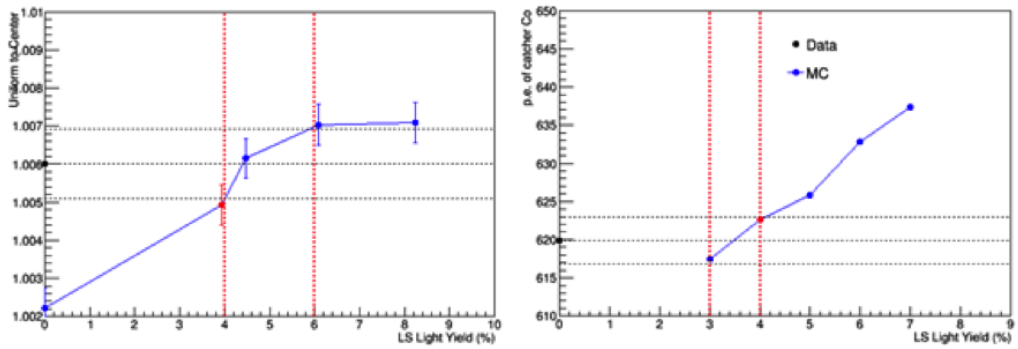

Figure G.7: (FAR MC) Uniform-to-center vs. LS light yield (left). Photo electron of gamma catcher Co source vs. LS light yield (right). The black dot and horizontal dotted line are data and its uncertainty

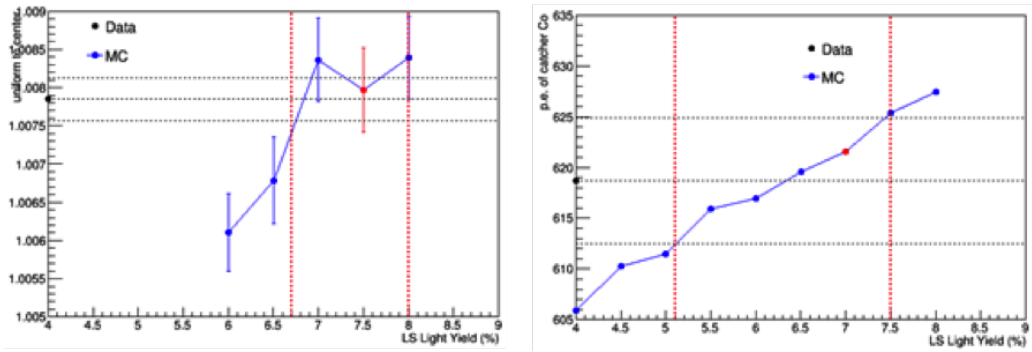

Figure G.8: (NEAR MC) Uniform-to-center vs. LS light yield (left). Photo electron of gamma catcher Co source vs. LS light yield (right). The black dot and horizontal dotted line are data and its uncertainty

G.2.4 LS attenuation length tune

Until previous sections we could successfully satisfy all the requirement of MC tune mentioned in the beginning of section G.2 So we do not have to change LS attenuation length.

G.2.5 Summary for tuned MC parameters

We have found that our attenuation length in MC was not tuned correctly. So we have tuned it by comparing uniform-to-center with that of data using n-Gd events. And light yield is also tuned to compensate the p.e change by tuning Gd-LS attenuation length. Finally, we have tuned the MC parameters for 500 days of data for near and far, respectively. Table G.1 summarize the tuned MC parameters

	Near MC	Far MC
Default Light Yield	9075	9285
Tuned Light Yield	Gd-LS LY: +8.5% LS LY : +7%	Gd-LS LY: +9% LS LY : +4%
Gd-Ls attenuation Length	-44.50%	-43.70%

Table G.1: Summary of tuned MC parameters for 500 days data

Appendix H

Measurement of Birks Constant

The Birks constant of the RENO is measured via light output of the LS due to the recoiled electron which is Compton scattered with γ-ray from ^{137}Cs source. Figure H.1 shows a schematic of the experimental setup.

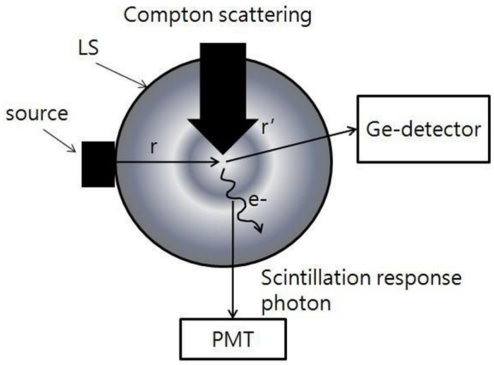

Figure H.1: Experimental setup for Birks constant.

The γ-ray emitting from the ^{137}Cs can be scattered with electron, transmit energy to electron, and then be measured its energy. The energy of the recoiled electron can be calculated following equation.

$$E_e = E_\gamma - E_{\gamma'} = 662\text{KeV} - E^{Ge-det.}_{measured}, \tag{H.1}$$

where, E_e is the energy of the recoiled electron, E_γ is the energy of the γ-ray before scattered, well known energy of 662 KeV. $E_{\gamma'}$ and $E^{Ge-det.}_{measured}$ is the energy of the

γ-ray after scattered, measured by Ge-detector. The Ge-detector was calibrated by γ-ray of 551 KeV from the ^{22}Na and γ-ray of 662 KeV from the ^{137}Cs, as shown in Fig. H.2.

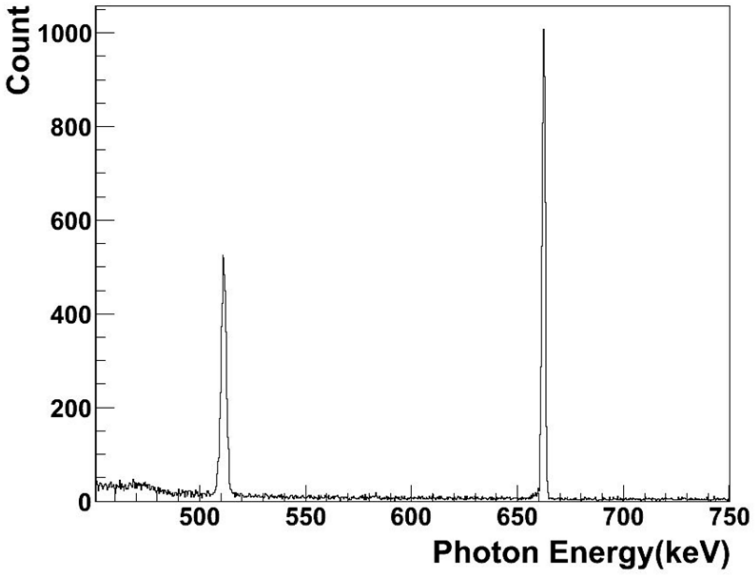

Figure H.2: Calibration of the Ge-detector. The detector is calibrated by using two energy peak from γ-ray of 551 KeV from the ^{22}Na source and γ-ray of 662 KeV from the ^{137}Cs source.

The recoiled electron can move in the LS or GdLS and forced the LS or GdLS to emit scintillating light. The scintillating light is collected by PMTs. Therefore, Light yield of LS or GdLS is measured by the PMT. The relation between the light yield of LS or GdLs and electron energy are shown in Fig. H.3. The region enclosed two red lines of the left plot of the Fig. H.3 shows selected data. The data are divided each 2.5 KeV-energy of the electron, as shown in the right plot of Fig. H.3. From the each sliced data, the PMT count histogram are made. Gaussian fitting result from the histogram, shown in Fig. H.4, means the light yield of the LS or GdLS at the sliced electron energy bin. From the this results, the relation between the light yield and the recoiled electron energy are obtained, as shown in Fig. H.5.

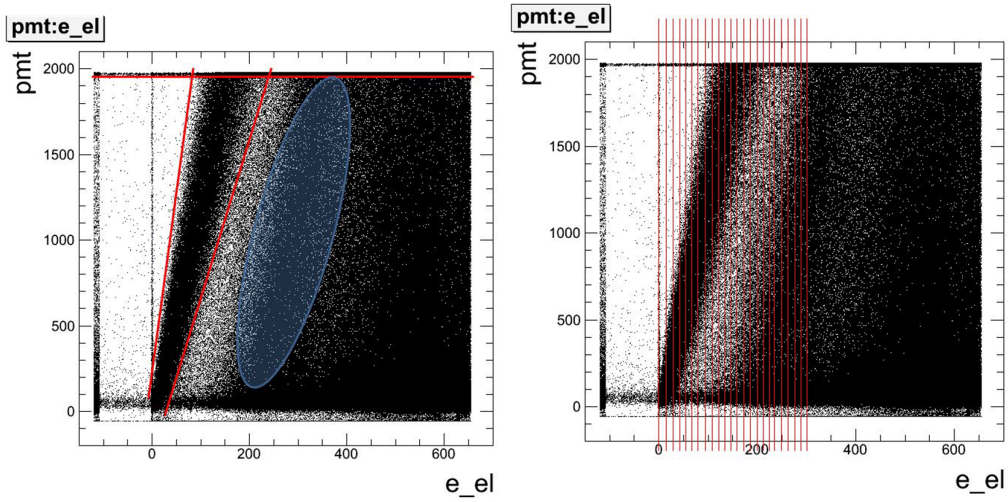

Figure H.3: PMT ADC count vs energy of the recoiled electron. The region enclosed two red lines of the left plot shows the selection region. The region inside of blue circle of the left plot shows a dim hill which is the inefficiently measured energy of the γ-ray due to compton scattering of the γ-ray in the ge-detector. The regions between the red lines of the right plot shows split data with same energy distance of 2.5 KeV.

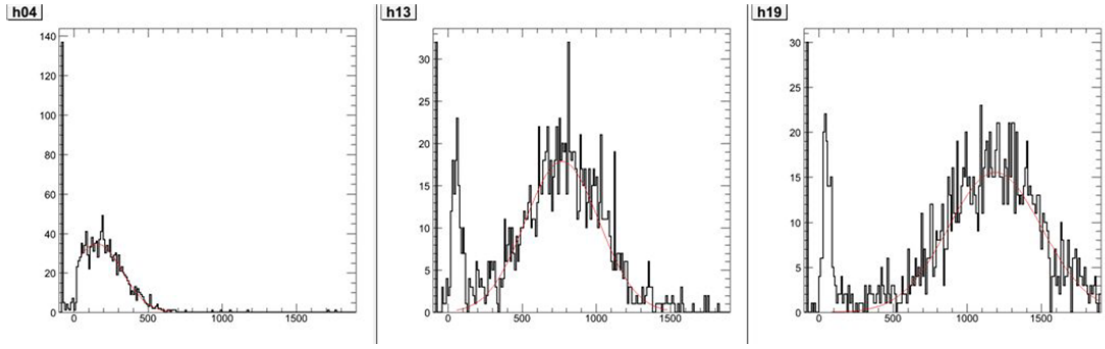

Figure H.4: Fitting results of pMT ADC(light yield) for each bin. The fitting function is Gaussian. From the this results, the light yield of LS or GdLS at the energy bin are obtained.

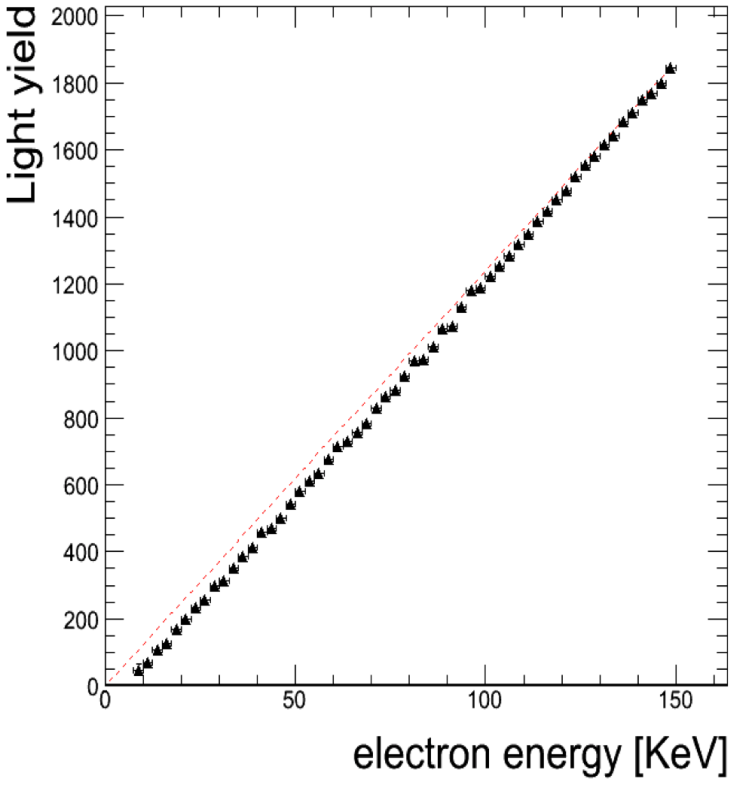

Figure H.5: Light yield vs the energy of the recoiled electron. The dotted line is guide line. The deviation between dotted line and data point means non linearity of the LS light yield.

So far, all data for measuring Birks constant k_B are ready. The fitting function to get k_B is described as following,

$$L = a \cdot \int \frac{1}{1 + k_B \frac{dE}{dx}} dE + b, \tag{H.2}$$

where, a, k_B and b are free parameters. The parameter a means the relative scintillation efficiency. and the parameter b means the offset of the data. The $\frac{dE}{dx}$ term means a stoping power of the LS or GdLS, is calculated from Berger & Seltzer Equation [73] and shown in Fig. H.6. The measurement result of the birks constant k_B is shown in Fig. refgkb and Table H.1.

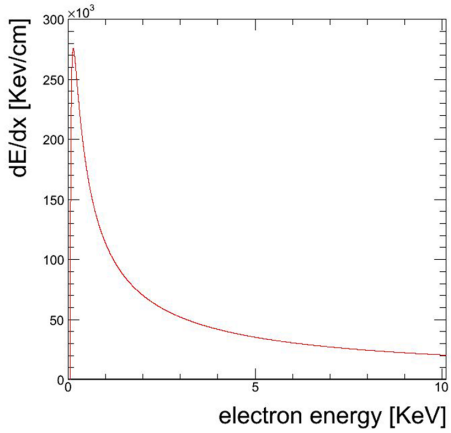

Figure H.6: Stoping power of electron in the LS. This plot is calculated from Berger & Seltzer Equation [73].

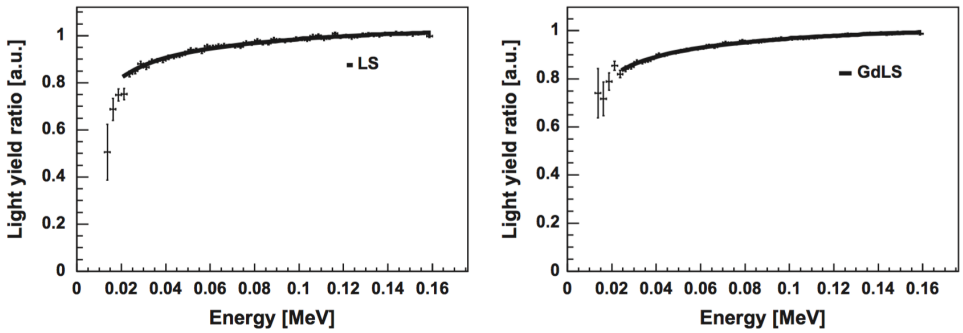

Figure H.7: Fraction of measured light yield and energy as a function of energy in LS and GdLS. The left plot shows the LS. And the right plot shows the GdLS. The black line shows the fitting result [32].

	k_B (cm/MeV)
LS	0.0117±0.0003
GdLS	0.0124±0.0004

Table H.1: Measured birks constant of LS and GdLS

Bibliography

[1] B. Pontecorvo, Sov. Phys. JETP **7** (1958) 172.

[2] Z. Maki,M. Nakagawa, and S. Sakata, Prog. Theor. Phys. **28** (1962) 870.

[3] Y. Fukuda *et al.*, (Super-Kamiokande Collaboration), Phys. Rev. Lett. **81** (1998) 1562-1567.

[4] Q.R. Ahmad *et al.*, (SNO Collaboration), Phys. Rev. Lett. **87** (2001) 071301

[5] Q.R. Ahmad *et al.* (SNO Collaboration), Phys. Rev. Lett. **89** (2002) 011301.

[6] J.K. Ahn *et al.* (RENO Collaboration), Phys. Rev. Lett. **108** (2012) 191802.

[7] F.P. An *et al.* (Daya Bay Collaboration), Phys. Rev. Lett. **108** (2012) 171803.

[8] Y. Abe *et al.* (Double Chooz Collaboration), Phys. Rev. Lett. **108** (2012) 131801.

[9] B. Pontecorvo, Zh. Eksp. Theo. Fiz. **34**, 247 (1957).

[10] B. Pontecorvo, Zh. Eksp. Theo. Fiz. **34**, 247 (1957).

[11] R. N. Mohapatra *et al.*,"Theroy of Neutrino:A white paper" (2005), hep-ph/0510213.

[12] Olive KA, *et al.* (Part. Data Group) Chin. Phys. C 38:090001 (2014).

[13] C.L. Cowan Jr., F. Reines, F.B. Harrison, H.W. Kruse, and A.D. McGuire, Science, vol. **124**, no. 3212, (1956) 103104.

[14] K. Eguchi *et al.* (KamLAND Collaboration), Phys. Rev. Lett. **90** (2003) 021802.

[15] T. Araki *et al.* (KamLAND Collaboration), Phys. Rev. Lett. **94** (2005) 081801.

[16] H. Kwon *et al.* Phys. Rev. D**24** 1097, (1981).

[17] J. Vuilleumier *et al.* Phys. Lett. B**114** 298, (1982).

[18] G. K. *et al.* Phys. Lett B**138** 449, (1984).

[19] G. Zacek *et al.* Phys. Rev. D**34** 2621, (1986).

[20] A. Afonin *et al.* JETP Lett. **41** 435, (1985).

[21] A. Afonin *et al.* JETP Lett. **45** 247, (1987).

[22] A. Afonin *et al.* JETP Lett. **54** 253, (1991).

[23] G. Vidyakin *et al.* JETP Lett. **59** 390, (1994).

[24] B. Ackhar *et al.* Phys. Lett. B**338** 383, (1994).

[25] Chooz Collaboration, M. Apollonio *et al.* Phys. Lett. B**420** 397, hep-ex/9907037, (1998).

[26] Palo Verde Collaboration, F. Boehm *et al.* Prog. Part. Nucl. Phys. **40** 253, (1998).

[27] Palo Verde Collaboration, F. Boehm *et al.* Phys. Rev. D**64** 112001, (2001).

[28] Palo Verde Collaboration, Boehm, *et al.*, Physical Review Letters **84** (2000) 3764

[29] Palo Verde Collaboration, Boehm, *et al.*, Physical Review D **62** (2000) 072002.

[30] Chooz Collaboration, M. Apollonio, *et al.*, European Physical Journal C **27** (2003) 331;

[31] Yeh M, Garnov A, Hahn RL. Nucl. Instrum. Methods A **578**:329 (2007).

[32] Park JS, *et al.* (RENO Collab.) Nucl. Instrum. Methods A **707**:45 (2013).

[33] Beriguete W, *et al.* Nucl. Instrum. Methods A **763**:82 (2014).

[34] V. I. Kopeikin, Preprint Kurchatov Institute of Atomic Energy, Moscow IAE-4305/2 (1998).

[35] K. Schreckenbach, G. Colvin, W. Gelletly, and F. Von Feilitzsch, Phys. Lett. B **160**, 325 (1985).

[36] A. A. Hahn *et al.*, Phys. Lett. B **218**, 365 (1989).

[37] H. V. Klapdor and J. Metzinger, Phys. Rev. Lett. **48**, 127 (1982).

[38] P. Vogel, G. K. Schenter, F. M. Mann, and R. E. Schenter, Phys. Rev. C **24**, 1543 (1981).

[39] P. Huber and T. Schwetz, Phys. Rev. D **70**, 053011 (2004)

[40] P. Vogel and J. Engel, Phys. Rev. D **39**, 3378 (1989)

[41] Vogel P. Phys. Rev. D **29**:1918 (1984)

[42] Vogel P, Beacom JF. Phys. Rev. D **60**:053003 (1999)

[43] D. H. Wilkinson, Nucl. Phys. A**377**, 474 (1982).

[44] C. Bemporad, G. Gratta, and P. Vogel, Rev. Mod. Phys. **74**, 297 (2002)

[45] H. Nunokawa, S. Parke, and R. Zukanovich Funchal, Phys. Rev. D **72**, (2005) 013009.

[46] K. Anderson *et al.*, "White paper report on using nuclear reactors to search for a value of $\theta 13$" (2004), hep-ex/0402041.

[47] Members of the APS Multi-Divisional Neutrino Study, "The Neutrino Matrix" (2004).

[48] M. Freund, P. Huber and M. Lindner, Nucl. Phys. B**615**, 331-357 (2001).

[49] http://home.kias.re.kr/MKG/h/reno50

[50] Kettell S, *et al.* arXiv:1307.7419 [hep-ex] (2013)

[51] Abe K, *et al.* (T2K Collab.) Phys. Rev. Lett. **112**:061802 (2014)

[52] K. Abe *et al.* (T2K Collaboration), Phys. Rev. D **88**, 032002 (2013); K. Abe *et al.* (T2K Collaboration), Phys. Rev. Lett. **112**, 061802 (2014).

[53] P. Adamson *et al.* (MINOS Collaboration), Phys. Rev. Lett. **107**, (2011) 181802; P. Adamson *et al.* (MINOS Collaboration), Phys. Rev. Lett. **110**, (2013) 251801.

[54] F.P. An *et al.* (Daya Bay Collaboration), Phys. Rev. Lett. **112**, (2014) 061801; F.P. An *et al.* (Daya Bay Collaboration), Phys. Rev. Lett. **115**, (2015) 111802.

[55] F. Elisei, *et al.*, Nuclear Instruments Methods in Physics Research Section A **400** (1997) 53;G. Alimonti, *et al.*, Nuclear Instruments & Methods in Physics Research

[56] Y. Ding, *et al.*, Nuclear Instruments Methods in Physics Research Section A **522** (2007) 439.

[57] http://www.isuchemical.com.

[58] J.S. Park, *et al.*, New Physics **58** (2009) 62.

[59] Y. Ding *et al.*, Nucl. Instrum. Meth. A **584**, 238 (2008).

[60] T. Mueller at. al., Phys. Rev. C **83**, 054615 (2011).

[61] P. Huber, Phys. Rev. C **84**, 024617 (2011)

[62] Yu.V.Klimov, Atomic Energy, Vol.**76**,No.2 (1994)

[63] Improving Pressurized Water Reactor Performance Through Instrumentation: Application Case of Reducing Uncertainties on Thermal Power, EPRI, Palo Alto, CA: 2001. 1001470

[64] ANC: A Westinghouse Advanced Nodal Computing Code, Westinghouse Report WCAP-10965-P-A(P) (1996)

[65] T. Hagner *et al.*, Astropart. Phys. **14**, 33 (2000).

[66] http://www.ezag.com

[67] Liangjian, *et al.* Nucl. Instrum. Methods A **564**:1 471-474 (2006) .

[68] G. L. Fogli, L. Lisi, A. Marrone, D. Montanino, and A. Palazzo, Phys. Rev. D **66**, 053010 (2002).

[69] J.H. Choi *et al.* (RENO Collaboration), arXiv:1511.05849 [hep-ex] (2015)

[70] J. Beringer *et al.* (Particle Data Group), Phys. Rev. D**86**, 010001 (2012).

[71] Y. Abe *et al.* (Double Chooz Collaboration), arXiv:1406.7763 [hep-ex] (2014)

[72] See a talk given by Larstem Heeger at UW undergraduate colloquium in Feb. 27, 2013

[73] S.M. Seltzer, M.J. Berger, Int. J. Appl. Radiat. Isot. **33**:11, 1189-1218 (1992)

국문초록

Observation of Energy and Baseline Dependent Reactor Neutrino Disappearance in the RENO Experiment

최원국
물리천문학부 물리학전공
서울대학교 대학원

The Reactor Experiment for Neutrino Oscillation (RENO) 는 2011년 8월부터 data를 받기 시작했다. RENO는 중성미자 섞임각 θ_{13} 과 질량 제곱의 차이 $|\Delta m^2_{31}|$ 과 $|\Delta m^2_{32}|$ 의 가중평균인 $|\Delta m^2_{ee}|$ 를 측정하기 위해 설계되었다. RENO의 실험 장소는 서울에서 280 km 떨어진 영광의 한빛 원자력 발전소이다. 여기는 6개의 원자로가 동일한 거리로 일렬로 나열되어 있고, 이 실험은 원자로 중심으로 부터 294 m 떨어진 곳에 근거리 검출기, 1384 m 떨어진 곳에 원거리 검출기를 두어 사용한다. 6개 원자로부터 나오는 중성미자양으로 가중평균한 거리는 근거리검출기는 408.6 m , 원거리 검출기는 1444.0 m 이다. 2011년 8월 부터 2013년 1월까지 500 일 분량의 Data를 분석하여 원거리에서는 31541, 근거리에서는 290775 개의 중성미자 이벤트 후보를 골라냈으며 백그라운드비율은 원거리 4.9%, 원거리는 2.8% 이다. 측정된 선행이벤트의 스펙트럼이 현재 가장 많이 사용하고 있는 이론으로 예측한 선행이벤트의 스펙트럼에 비해 5 MeV 부근에서 높게 나타났다. 이 초과분은 원자로 열출력에 비례하므로 백그라운드가 아니라 원자로에서 온 중성미자 이벤트이다. 이 문제점을 피해나가기 위해 원거리 / 근거리 비율을 기준으로 분석하여 거리와 중성미자 에너지에 따른 중성미자 사라짐을보았고, 에너지 스펙트럼과 양으로부터 $\sin^2 2\theta_{13} = 0.082 \pm 0.009(stat.) \pm 0.006(syst.)$ 과 $|\Delta m^2_{ee}| = \left[2.62^{+0.21}_{-0.23}(stat.)^{0.12}_{-0.13}(syst.)\right] \times 10^{-3}\mathrm{eV}^2$ 를 측정하였다. 정확한 θ_{13} 의 측정값이 가속기 기반의 중성미자실험의 결과와 합치게 된다면 Lepton의 CP 위상각을 측정하는데 중요한 단서가 될 수 있다.